

INFLUENCE OF STRESS, UNDERCUTTING, BLASTING AND TIME ON OPEN STOPE STABILITY AND DILUTION

A Thesis Submitted to the College of
Graduate Studies and Research
in Partial Fulfillment of the Requirements for the Degree of
Doctor of Philosophy
in the Department of Civil and Geological Engineering
University of Saskatchewan
Saskatoon

By

Jucheng Wang

© Copyright Jucheng Wang, August 2004. All rights reserved.

PERMISSION TO USE

In presenting this thesis in partial fulfillment of the requirements for a Postgraduate degree from the University of Saskatchewan, I agree that the Libraries of this University may make it freely available for inspection. I further agree that permission for copying of this thesis in any manner, in whole or in part, for scholarly purposes may be granted by the professor or professors who supervised my thesis work or, in their absence, by the Head of the Department or the Dean of the College in which my thesis work was done. It is understood that any copying or publication or use of this thesis or parts thereof for financial gain shall not be allowed without my written permission. It is also understood that due recognition shall be given to me and to the University of Saskatchewan in any scholarly use which may be made of any material in my thesis.

Requests for permission to copy or to make other use of material in this thesis in whole or part should be addressed to:

Head of the Department of Civil and Geological Engineering
University of Saskatchewan
Saskatoon Saskatchewan, Canada
S7N5A9

ABSTRACT

This thesis presents the results of open stope stability and dilution research which focused on evaluating and quantifying stress, undercutting, blasting and exposure time and their effect on open stope stability and dilution.

Open stope mining is the most common method of underground mining in Canada. Unplanned stope dilution is a major cost factor for many mining operations. Significant advances in empirical stability and dilution design methods have improved our ability to predict probable dilution from open stoping operations. However, some of the factors that influence hanging wall dilution are either ignored or assessed in purely subjective terms in existing designs. This thesis attempts to quantify these factors, from a geomechanics perspective, to assist in predicting and minimizing dilution.

A comprehensive database was established for this study based on two summers of field work. Site geomechanics rock mass mapping and classification were conducted and case histories were collected from Cavity Monitoring System (CMS) surveyed stopes from Hudson Bay Mining and Smelting Co. Ltd. (HBMS) operations.

The stope hanging wall (HW) zone of stress relaxation was quantified based on extensive 2D and 3D numerical modelling. Stress relaxation was linked to the stope geometry and the degree of adjacent mining activity.

The influence of undercutting on stope HW stability and dilution was analysed using the case histories collected from HBMS mines. An undercutting factor (UF) was developed to account for the undercutting influence on stope HW dilution. Numerical simulations were conducted to provide a theoretical basis for the undercutting factor. A relationship

was observed between the degree of undercutting, expressed by the UF term and the measured dilution.

Many factors can significantly and simultaneously affect a blast performance, which may result in blast damage to stope walls. Major blasting factors which influence stope HW stability were identified. The influence of blasting on stope HW stability and dilution was evaluated based on the established database.

The HBMS database, Bieniawski's stand-up time graph, as well as Geco mine case histories were used to evaluate the influence of exposure time on stope stability and dilution. Relating increased mining time to increased dilution allows the mining engineer to equate mining delays to dilution costs.

Each of the factors assessed in this study was studied independently to assess its influence on stope dilution, based on the HBMS database. The factors influencing dilution often work together, so a multiple parameter regression model was used to analyze the available parameters in the HBMS database.

The findings of this research greatly improve an engineer's ability to understand and to predict the influence of mining activities and stoping plans on hanging wall dilution.

ACKNOWLEDGEMENTS

I would like to thank my supervisors Dr. D. Milne, Dr. M. Reeves and my Ph.D. supervision committee members for their continuous invaluable guidance during my research and the completion of the thesis.

I also would like to thank the Callinan Mine, Ruttan Mine and Trout Lake Mine of Hudson Bay Mining and Smelting Co. Ltd. who allowed me to collect data and provided me with valuable assistance for the study. Special thanks go to Mr. G. Allen, M. Yao, K. Pawliuk and M. Willet for their assistance with my field work.

The following organizations deserve thanks for their much appreciated financial support:

- Hudson Bay Mining & Smelting Co. Ltd.,
- The Natural Sciences and Engineering Research Council of Canada (NSERC),
- The University of Saskatchewan,
- The Department of Civil and Geological Engineering at the University of Saskatchewan,
- The Department of Geological Sciences at the University of Saskatchewan.

Appreciation is extended to all the people who gave me precious assistance and suggestions, and to my proofreaders.

Finally, I would like to thank my wife Wei Gu for her patience and encouragement throughout the research. Thanks to my two daughters Tina and Nita for making me enjoy my lovely family.

TABLE OF CONTENTS

PERMISSION TO USE	i
ABSTRACT	ii
ACKNOWLEDGEMENTS	iv
TABLE OF CONTENTS	v
LIST OF TABLES	xii
LIST OF FIGURES	xiv
LIST OF PHOTOS	xxiii
CHAPTER 1. INTRODUCTION	1
1.1 Background	1
1.2 Objective of the Research	4
1.3 Thesis Overview	7
CHAPTER 2. OPEN STOPE STABILITY AND DILUTION DESIGN	
METHODS	10
2.1 Introduction	10
2.2 Analytical Methods for Excavation Design	11
2.2.1 Stress Driven Failure	11
a). Kirsch's Equation – A 2D Analytical Method for Estimating Stress.	11
b). Mohr-Coulomb Failure Criterion	13
c). Hoek and Brown Failure Criterion	15
2.2.2 Gravity Driven Failure	16
a). Kinematic Failure.	17
b). Beam Failure.	17
c). Plate Failure	21
d). Voussoir Beam Failure	22

2.2.3 Gravity Derived Stress Relaxation Failure	30
2.3 Empirical Open Stope Stability and Dilution Design Methods	30
2.3.1 NGI Classification System, Q and Modified Q, Q'	31
2.3.2 Stability Number, N and Modified Stability Number, N'	37
2.3.3 Shape Factor, Hydraulic Radius and Radius Factor.....	39
2.3.4 Empirical Stability Graph Design Methods	40
2.3.5 Empirical Dilution Design Methods	44
2.4 Numerical Design Methods	44
2.4.1 Finite Element Methods (FEM).....	47
2.4.2 Boundary Element Methods (BEM).....	48
2.5 Summary	49
 CHPATER 3. BACKGROUND ON FIELD SITE DATA	 51
 3.1 Introduction	 51
3.2 General Mine Information	52
3.2.1 Trout Lake Mine	52
3.2.2 Callinan Mine	53
3.2.3 Ruttan Mine	53
3.3 Mine Geology	53
3.3.1 Regional Geology	53
3.3.2 Mine Geology	56
a). Callinan Mine	56
b). Trout Lake Mine	58
c). Ruttan Mine	60
3.4 Rock Mass Classification	60
3.4.1 Methodology.....	60
3.4.2 Joint Sets Information	62
3.4.3 RQD Estimating	63
3.4.4 Joint Quantification Parameters, J_n , J_r , J_a , J_w , and SRF	63
3.4.5 NGI Q system rock Mass Classification	65

3.5 Quantifying Dilution with the Cavity Monitoring System	68
3.5.1 Cavity Monitoring System Survey and Data Manipulating	68
3.6 Summary	70
 CHAPTER 4. EMPIRICAL DATABASE AND DESCRIPTION	71
4.1 Empirical Database	71
4.2 Database Descriptions	74
4.2.1 General	74
4.2.2 Stope Geometry	74
4.2.3 Stope HW Modified Stability Number N'	78
4.2.4 Undercutting of Stope Hanging Walls	79
4.2.5 Drilling and Blasting	80
4.2.6 Stope Stress Situation before Mining	85
4.2.7 CMS Surveyed HW Dilution	85
4.2.8 Open Stope Exposure Time	87
4.3 Summary	88
 CHAPTER 5. DILUTION FACTOR AND DILUTION PREDICTION ERROR ..	90
5.1 Dilution Design Graph	90
5.2 Dilution Factor	92
5.3 Dilution Prediction Error	93
5.4 Summary	95
 CHAPTER 6. INFLUENCE OF STRESS ON OPEN STOPE HANGING WALL STABILITY AND DILUTION	96
6.1 Introduction	96
6.1.1 Stress Related Failure	97
6.1.2 Empirical Assessment of Hanging wall Stress Conditions	98

6.2 Stress Relaxation	99
6.3 Assessment of Opening Geometry and Relaxation Extent	101
6.3.1 Hydraulic Radius and Radius Factor	101
6.3.2 Quantifying the Relaxation Zone	102
6.4 Previous Modelling Studies	103
6.5 Current Modelling Studies	105
6.5.1 Modelling Geometries and Input Parameters	105
6.5.2 Modelling Study of rectangular Hanging Wall Geometries	107
6.5.2.1 Comparison with Previous Modelling Studies	115
6.5.3 Relationship between Radius Factor, Stress Ratio K and the Depth of Relaxation for 2D Tunnel Geometries	116
6.5.4 Modelling Study of Disc Shaped Geometries	119
6.5.5 Discussion of the Modelling Results	123
6.5.6 Proposed Application of the ELRD to RF Relationships	129
6.6 Relating Mining Activity, Stress State and Dilution	132
6.7 Summary	141

CHAPTER 7. INFLUENCE OF UNDERCUTTING ON STOPE STABILITY AND DILUTION

7.1 Introduction	143
7.2 Quantifying Hanging Wall Undercutting	146
7.3 Interaction of Undercutting and Stress.....	148
7.4 General Interaction of Undercutting on Stability and Dilution.....	158
7.5 Case History Assessment	159
7.5.1 Stress Influence	159
7.5.2 Abutment Loss Influence	161
7.5.3 Case History Example	163
7.6 Summary	166

CHAPTER 8. INFLUENCE OF BLASTING ON STOPE HANGING WALL STABILITY AND DILUTION	167
8.1 Introduction	167
8.2 Blasting Background	168
8.3 Methods of Assessing Blast Damage	171
8.3.1 Peak Particle Velocity Method	171
8.3.2 Blast Damage Consideration in Hoek and Brown Failure Criterion	173
8.3.3 Visual Inspection and CMS Survey Methods	174
8.4 Factors Influencing HW Blast Damage and Dilution	174
8.4.1 Rock Mass Properties	176
8.4.2 Drillhole Design	177
8.4.3 Explosive Type	179
8.4.4 Wall Control Methods	179
8.4.5 Explosive Distribution	180
8.4.6 Initiation Sequence, Explosive Per Delay and Availability of Free Surface	181
8.4.7 Drillhole Deviation	181
8.5 Database Assessment of Blast Parameters and Dilution	183
8.5.1 Drillhole Pattern versus Stope HW Dilution	184
8.6 Summary	192
 CHAPTER 9. INFLUENCE OF STOPE EXPOSURE TIME ON HANGING WALL STABILITY AND DILUTION	 194
9.1 Introduction	194
9.2 Mechanism of Time Influence on Stability and Dilution	196
9.3 Influence of Exposure Time on the HBMS Database	199
9.4 Complementary Data on the Influence of Exposure Time	203
9.4.1 Stand-up Time Graph Analysis	203
9.4.2 Geco Mine Case History Study	206

9.5 Summary	206
CHAPTER 10. STATISTICAL ANALYSIS OF EMPIRICAL DATA	208
10.1 Introduction	208
10.2 Parameters in the Statistical Analysis	208
10.3 Multiple Parameter Statistical Analysis	209
10.4 Stepwise Multiple Parameter Regression Analysis	215
10.5 Graphical Presentation of the Statistical Analysis Results	221
10.6 Comparison of the Empirical and Statistical Analysis of the HBMS	
Database	224
10.7 Summary	226
CHAPTER 11. CONCLUSION AND RECOMMENDATIONS	229
11.1 Establishment of a Comprehensive Database	229
11.2 Quantifying Stress Relaxation as a Factor Influencing HW Dilution	230
11.3 Influence of Undercutting, Blasting and Exposure Time on Open Stope	
HW Dilution	232
11.3.1 Influence of Undercutting on Open Stope HW Dilution	233
11.3.2 Influence of Blasting on Open Stope HW Stability and Dilution	234
11.3.3 Influence of Stope Exposure Time on Open Stope HW Stability and	
Dilution	235
11.4 Statistical Evaluation of the Factors Influencing Open Stope Stability and	
Dilution	236
11.5 Summary and Assessment of Findings	238
11.6 Recommendations for Future Research	239
REFERENCES	240

APPENDIX I. BRIEF DESCRIPTION OF INDIRECT BOUNDARY ELEMENT METHOD (BEM) -FICTITIOUS STRESS METHODS.....	248
1. Introduction	248
2. Assumptions for the Application of the Method	248
3. The Principle of Indirect BEM	250
APPENDIX II. HBMS DATABASE	255
APPENDIX III. VARIATION OF THE DEPTH OF THE RELAXATION ZONE WITH LOCATION ON THE SURFACE EXPRESSED AS THE EFFECTIVE RADIUS FACTOR	273

LIST OF TABLES

Table 2.1 Classifications of rock mass quality based on Q	33
Table 2.2 Classification of individual parameters used in the NGI Q classification system	34
Table 3.1 Rock Mass Classification at Callinan, Trout and Ruttan Mines	67
Table 4.1. Example stope summary sheet	73
Table 4.2. Stope location category.....	85
Table 4.3. Summary of the database parameters.....	84
Table 6.1. Modelling geometry (HW) configurations	112
Table 6.2. Modelled results showing the depth of relaxation at the centre of a stope HW for rectangular shaped HWs.....	107
Table 6.3. Modelled results of ELRD for rectangular shaped HW	115
Table 6.4. Examine 2D geometries modelled	117
Table 6.5. Maximum relaxation depth and ELRD for tunnel span geometries	117
Table 6.6. Modelling geometries for disc shaped openings.....	119
Table 6.7. Relaxation depth at the centre of HW	123
Table 6.8. ELRD for disc shaped stope HW modelling results.....	123
Table 6.9. Stress situation modelled results	135
Table 7.1. Calculated UF for test case Examine 3D model stope	152
Table 7.2. ELRD _{uc} modelled results for test case Examine 3D model stope	156
Table 8.1. Peak Particle Velocity threshold damage levels	172
Table 8.2. Hoek and Brown failure criterion m and s constants values	175

Table 9.1. Influence of stand-up time on stability and effective classification values (10m span) based on the RMR Stand-up Time Graph	205
Table 10.1. Parameters included in analysis and descriptive statistics	209
Table 10.2. Correlations between parameters	212
Table 10.3. Multiple parameter regression coefficients	214
Table 10.4. Variables Entered/Removed	217
Table 10.5. Stepwise multiple parameter regression coefficients	218
Table 10.6. Comparison between empirical and statistical analysis (stepwise results)	226

LIST OF FIGURES

Figure 1.1. Dilution definition	3
Figure 1.2. Factors affecting open stope stability and dilution.....	5
Figure 2.1. Definition of stresses in polar coordinates used in Kirsch's equations	13
Figure 2.2 Mohr Coulomb failure criterion.....	14
Figure 2.3. Hoek and Brown failure criterion	16
Figure 2.4. Deflection of a simple beam	19
Figure 2.5. Illustration of parameters.....	19
Figure 2.6. Voussoir block theory	23
Figure 2.7. Voussoir arch failure modes	26
Figure 2.8. General solutions for beam (infinite depth) and square plate	28
Figure 2.9. Stress factor A for stability graph analysis	38
Figure 2.10. Determination of joint orientation factor B for stability graph analysis	38
Figure 2.11. Determination of gravity adjustment factor C for stability graph analysis	39
Figure 2.12. Mathews Stability Graph.....	41
Figure 2.13. Modified stability graph.....	42
Figure 2.14. Modified stability graph with support	43
Figure 2.15. Empirical dilution approach.....	45
Figure 2.16. ELOS dilution design method.....	46
Figure 3.1. Mines location map	52
Figure 3.2. Generalized regional geology of the Flin Flon area	55
Figure 3.3. Longitudinal view of Callinan Mine orebody	57
Figure 3.4. Longitudinal view of Trout Lake Mine orebody.....	59

Figure 3.5. Longitudinal view of Ruttan Mine orebody	61
Figure 3.6 Illustration of joint set orientation mapping	62
Figure 3.7 Trout Lake Mine major joints planes stereonet plot.....	64
Figure 3.8 Callinan Mine major joints planes streonet plot.....	64
Figure 3.9 Example rock mass classification recording sheet	66
Figure 3.10. Schematic illustration of the typical CMS set-up.....	69
Figure 4.1. Rock mechanics database structure	72
Figure 4.2. Isometric of a typical open stope	75
Figure 4.3. Stope strike length distribution	75
Figure 4.4. Stope height distribution	76
Figure 4.5. Stope hanging wall hydraulic radius (HR) distribution	76
Figure 4.6. Stope hanging wall dip distribution	77
Figure 4.7. Stope width distribution	77
Figure 4.8. Distribution of modified stability number N'	79
Figure 4.9. Distribution of overcut drifts undercutting	81
Figure 4.10. Distribution of undercut drifts undercutting	82
Figure 4.11. Drillhole size distribution	83
Figure 4.12. Drillhole pattern distribution	84
Figure 4.13. Distribution of powder factor.....	84
Figure 4.14. Distribution of stope location categories	86
Figure 4.15. Stope HW ELOS distribution	86
Figure 4.16. Stope exposure time distribution	87
Figure 5.1. Dilution design graph	91
Figure 5.2. Illustration of obtaining dilution factor	92
Figure 5.3. Illustration of accuracy of current dilution design on Callinan Mine and Trout Lake Mine case histories.....	94
Figure 5.4. Comparison between actual ELOS and Dilution Graph predicted ELOS for the HBMS database	95

Figure 6.1. Rock fractures forming rock blocks within the rock mass with a 1 m long scale	98
Figure 6.2. Deflection of streamlines around a cylindrical obstruction	100
Figure 6.3. Schematic illustrating of model geometries modeled by Clark (1998) ...	104
Figure 6.4. ELOS vs. HR	104
Figure 6.5. Schematic illustration of the numerical modelling geometry	106
Figure 6.6. σ_1 predicted using Examine3D; example plot for a 40x40x10m stope with K=2.0.....	109
Figure 6.7. σ_2 predicted using Examine3D; example plot for a 40x40x10m stope with K=2.0.....	110
Figure 6.8. σ_3 predicted using Examine3D; example plot for a 40x40x10m stope with K=2.0.....	111
Figure 6.9. The depth of relaxation at the centre of the stope HW vs. radius factor for different stress ratios for rectangular shaped stope HWs	112
Figure 6.10. The depth of relaxation at the centre of the stope HW vs. hydraulic radius for different stress ratios for rectangular shaped stope HWs.....	113
Figure 6.11. ELRD vs. radius factor for different stress ratios for rectangular shaped stope hanging walls	114
Figure 6.12. ELRD vs. HR for different stress ratios for rectangular shaped stope hanging walls.....	114
Figure 6.13. Relaxation depth at middle height of side-walls vs. RF for K=1.5, 2.0 and 2.5	118
Figure 6.14. Variation of ELRD with radius factor for tunnel side walls	118
Figure 6.15. σ_1 predicted using Examine3D; example plot for a 20 m diameter disc shaped stope with K=2.0	120
Figure 6.16. σ_2 predicted using Examine3D; example plot for a 20 m diameter disc shaped stope with K=2.0	121
Figure 6.17. σ_3 predicted using Examine3D; example plot for a 20 m diameter disc shaped stope with K=2.0	122

Figure 6.18. The depth of relaxation at centre of the stope vs. radius factor for different stress ratios for disc shaped stope hanging walls	124
Figure 6.19. ELRD vs. radius factor plot with three stress regimes for circular shaped surfaces.....	124
Figure 6.20. Overall comparison of depth of relaxation at the centre of stope HW versus RF for different shaped models for three stress regimes	125
Figure 6.21. Overall comparison of depth of relaxation at the centre of stope HW versus HR for different shaped models for three stress regimes	125
Figure 6.22. Overall comparison of ELRD vs. RF for different shaped models for three stress regimes	126
Figure 6.23. Overall comparison of ELRD vs. HR for different shaped models for three stress regimes	126
Figure 6.24. Variation in hydraulic radius and radius factor for a constant 100 metre span and increasing length	128
Figure 6.25. Design graph of depth of relaxation at the centre of stope HW surface based on RF	129
Figure 6.26. Design graph of depth of relaxation at the centre of stope HW surface based on HR	130
Figure 6.27. ELRD design graph based on RF	130
Figure 6.28. ELRD design graph based on HR	131
Figure 6.29. Comparison of modelled values of ELRD with ELOS on Clark's dilution graph for $K=2.0$	133
Figure 6.30. Stope categories showing adjacent mining configurations	134
Figure 6.31. Modelled stress ratio change for the stope categories (K initial = 1.3).....	136
Figure 6.32. ELRD estimate for stope stress categories (solid lines are modelled and dashed lines are inferred from the modelled results)	136
Figure 6.33. CMS measured ELOS versus stope categories plot	137
Figure 6.34. Actual ELOS minus dilution factor against stope stress category case history plot	138

Figure 6.35. Actual ELOS minus dilution factor against stope stress category for the cases with $N' < 10$ (31 cases)	139
Figure 6.36. Actual ELOS minus dilution factor versus the stope stress category for the cases with $DF > 1.0$ (37 cases)	139
Figure 6.37. Dilution prediction error ($ELOS_{act.} - DF$) against the estimated ELRD cases history plots (88 cases)	140
Figure 6.38. Dilution prediction error ($ELOS_{act.} - DF$) against the estimated ELRD cases history plots for the cases with the $N' < 10$ (29 cases)	141
Figure 7.1. Percentage of undercutting (UC) and the undercutting depth from the HBMS database.....	144
Figure 7.2. Schematic illustration of instability caused by undercutting	145
Figure 7.3. Stope isometric showing the undercutting parameters	148
Figure 7.4. Distribution of the calculated UF values for the HBMS database (150 cases)	149
Figure 7.5. Schematic showing influence of undercutting on stope relaxation	149
Figure 7.6. Stress relaxation zone (shaded) around a stope with no undercutting	150
Figure 7.7. Stress relaxation zone (shaded) around a stope with 5 metres of undercutting	151
Figure 7.8. Effect of undercutting on stress relaxation modelling model	151
Figure 7.9. Examine 3D σ_3 plot for the stope geometry without undercutting with $K = 2$	153
Figure 7.10. Examine 3D σ_3 plot for the stope geometry with 1.5m average undercutting with $K = 2$	154
Figure 7.11. Examine 3D σ_3 plot for the stope geometry with 3m average undercutting with $K = 2$	155
Figure 7.12. Example plots of ELRD versus average depth of undercutting (for a 40x30x5 m stope)	157
Figure 7.13. Example plots of additional ELRD due to undercutting versus average depth of undercutting (for a 40x30x5m stope)	157

Figure 7.14. Schematic cross section showing the zones of undercutting influence	158
Figure 7.15. Additional ELRD due to undercutting that can be expected for the 6 stope stress categories (for a typical HBMS stope geometry with a HR of 8.6m)	160
Figure 7.16. $ELRD_{total}$ versus the actual dilution minus the dilution factor case history plots (88 cases)	160
Figure 7.17. $ELRD_{total}$ versus the actual dilution minus the dilution factor case history plots for the cases with $N' < 10$ (29 cases)	161
Figure 7.18. Comparison between UF and dilution in excess of predicted values ...	162
Figure 7.19. UF versus average dilution in excess of predicted values	162
Figure 7.20. UF/ N' versus ELOS prediction error case history plot	163
Figure 7.21. Plane view of stope drifts layout and undercutting (shaded areas)	164
Figure 7.22. Drilling cross section showing CMS surveyed overbreak profiles and undercutting	165
Figure 8.1. First stage of explosive /rock interaction	169
Figure 8.2. Later stages of explosive/rock interaction	170
Figure 8.3. Schematic illustration of the effect of burden on explosives fired in rock	178
Figure 8.4. Cross section showing the drillhole deviation orientations.....	182
Figure 8.5. Plane view showing surveyed drillhole deviation along strike	183
Figure 8.6. Drillhole size versus actual ELOS case history plots.....	184
Figure 8.7. Drillhole size versus actual ELOS minus DF case history plots.....	185
Figure 8.8. Powder factor versus actual ELOS case history plots.....	185
Figure 8.9. Powder factor versus actual ELOS minus DF case history plots.....	186
Figure 8.10. Definition of parallel drillhole pattern.....	187
Figure 8.11. Definition of fanned drillhole pattern	187
Figure 8.12. Schematic Illustration of drillhole deviation	188
Figure 8.13. Histograms showing the influence of parallel and fanned drillhole pattern on stope dilution	189

Figure 8.14. Individual cases showing the influence of parallel and fanned drillhole patterns on stope dilution	189
Figure 8.15. Comparison between two drillhole patterns on HW dilution for Callinan Mine	191
Figure 8.16. Comparison between two drillhole patterns on HW dilution for Trout Lake Mine	191
Figure 8.17. Drillhole pattern versus undercutting factor	192
Figure 9.1. CMS surveyed progressive caving with time	195
Figure 9.2. Stand-up time guidelines	195
Figure 9.3. Schematic illustration of time dependent stress redistribution	198
Figure 9.4. Stope exposure time case histories.....	200
Figure 9.5. CMS measured ELOS versus exposure time case history plots	201
Figure 9.6. Histogram plot of average ELOS prediction error versus stope exposure time	201
Figure 9.7. Stope exposure time versus ELOS prediction error case history plots	202
Figure 9.8. Stope exposure time divided by N' versus ELOS prediction error case history plots	203
Figure 9.9. Manipulating the N' change for the ELOS increase on Clark's (1998) dilution graph	205
Figure 10.1. Histogram of regression standardized residual.....	215
Figure 10.2. Comparison between CMS measured ELOS and multiple parameter regression model calculated ELOS	216
Figure 10.3. Histogram of standardized residual for stepwise analysis	219
Figure 10.4. Comparison between CMS measured ELOS and the most influence parameter regression model calculated ELOS	220
Figure 10.5. Comparison between the models shown in Figure 2 and Figure 4	220
Figure 10.6. The model design lines for the average T and UF values with case histories plots.....	222

Figure 10.7. Illustration of the influence of stope exposed time (T) on hanging wall ELOS (ELOS=1.0m)	223
Figure 10.8. Illustration of the influence of undercutting factor (UF) on stope hanging wall ELOS (ELOS=1.0m)	223
Figure 10.9. Example interpretation of dilution graph (dilution graph with the HBMS data plotted)	225
Figure 10.10. The model design lines for the average T and UF values with case history data and Clark's dilution design lines	227
Figure I-1. Idealized diagram showing the transition from intact rock to a heavily jointed rock mass with increasing sample size	249
Figure I-2. The problem to be solved	251
Figure I-3. Traction on potential boundary before excavation	251
Figure I-4. Negative tractions representing effects of excavation	252
Figure I-5. The approach of solving of the problem – superposition	252
Figure I-6. Illustration of numerical model	254
Figure III-1. An irregular stope back showing the calculated ERF value and RF value	274
Figure III-2. Effective Radius Factor (ERF) values along centre lines of a 40m x 40m surface	276
Figure III-3. Effective radius factor changes with the distance change along axes for a 40m x 40m rectangular surface	276
Figure III-4. Depth of relaxation along axes of a 40m x 40m square shaped surface corresponding to distance (from centre of the surface) and ERF	277
Figure III-5. ERF values along two mutual perpendicular axes, measured at 5 meters intervals, for a 40m x 100m rectangular surface	277
Figure III-6. ERF changes with the distance from the surface center along two axes for a 40m x 100 m rectangular surface	278

Figure III-7. Depth of relaxation along the long axis of a 40 x100m ² rectangular shaped surface corresponding to distance from the centre or ERF	278
Figure III-8. Depth of relaxation along the short axis of a 40x100m ² rectangular shaped surface corresponding to distance from the centre or ERF	278

LIST OF PHOTOS

Photo 9.1. Illustration of instability caused by stress redistribution process.....	197
---	-----

CHAPTER 1

INTRODUCTION

1.1 Background

This thesis focuses on the influence of stress, undercutting, blasting and exposure time on open stope hanging wall stability and dilution (in this thesis, dilution refers to the unplanned dilution from a stope hanging wall). Open stope mining is a non-entry mass-production mining method and the most commonly practiced mining method in Canada. Open stope instability and ore dilution are important factors which can create significant additional operating expenses for underground mines. Dilution is defined as waste rock which mixes with ore, reducing or diluting the grade. Dilution directly increases the costs of production (i.e., cost per unit weight of metal mined). Understanding and controlling dilution are important factors for reducing mining costs. The costs of dilution are significant and increase the cost of both the mining and milling operations.

The direct costs associated with dilution are primarily due to physically handling additional waste materials. These costs consist of mucking, tramming, crushing, hoisting and milling of waste rock, as well as the additional demands for backfilling. Anderson and Grebence (1995) and Dunne et. al (1996) reported that the typical costs for mining, milling and administration to handle the waste materials are approximately \$30-40/tonne. In 2000, Hudson Bay Mining & Smelting Co. Ltd. reported that their direct cost of dilution was about \$20/tonne (Yao et al., 1999). Anderson et al. (1995) reported that the cost of dilution at the Golden Giant Mine (Hemlo Gold Mines Inc) is approximately \$5.4 million per year (\$38/tonne at a mining rate of 3000 tonnes/day, 14% dilution). These per tonne dilution costs can amount to a very high annual expense.

The indirect costs are harder to quantify, but are typically associated with instability. Oversized waste rock caused by dilution can result in significant indirect cost. Oversize may cause plugged drawpoints, secondary blasting, lost access to ore and lost ore resource, lengthy mucking time and equipment damage. However, the most serious cost of dilution is the cost resulting from ore being displaced by waste within the mine/mill circuit. Open stope instability and dilution can seriously increase expenses for a mining operation.

Scoble and Moss (1994) defined the total dilution as the sum of the planned dilution and unplanned dilution. Figure 1.1 shows this definition of dilution. Planned dilution is the non-ore material (below cutoff grade) that lies within the designed stope boundaries (mining lines). Unplanned dilution is additional non-ore material, which is derived from rock or backfill outside the stope boundaries (mining lines). Unplanned dilution is predominately due to blast overbreak and sloughing of unstable walls. Unplanned open stope dilution is a measure of stope instability. Planned dilution can be controlled by optimizing the mining method and mining design, while unplanned dilution can create excessive mining costs.

Many factors, such as rock mass condition, stope geometry, in-situ stress condition, blasting, stope exposure time and geological structures influence stope stability and dilution. Experience based empirical methods (Mathews et al., 1981; Pakalnis, 1986; Potvin et al., 1988; Milne 1997; Clark, 1998) and computer based numerical methods (e.g., Finite element methods, boundary element methods) exist for predicting stope stability and dilution. Both general design approaches ignore some important factors that influence hanging wall dilution. Empirical methods do not adequately account for stope hanging wall geometry, blasting, exposure time and stresses. Numerical methods can adequately assess opening geometry and stresses. However the influence of blasting,

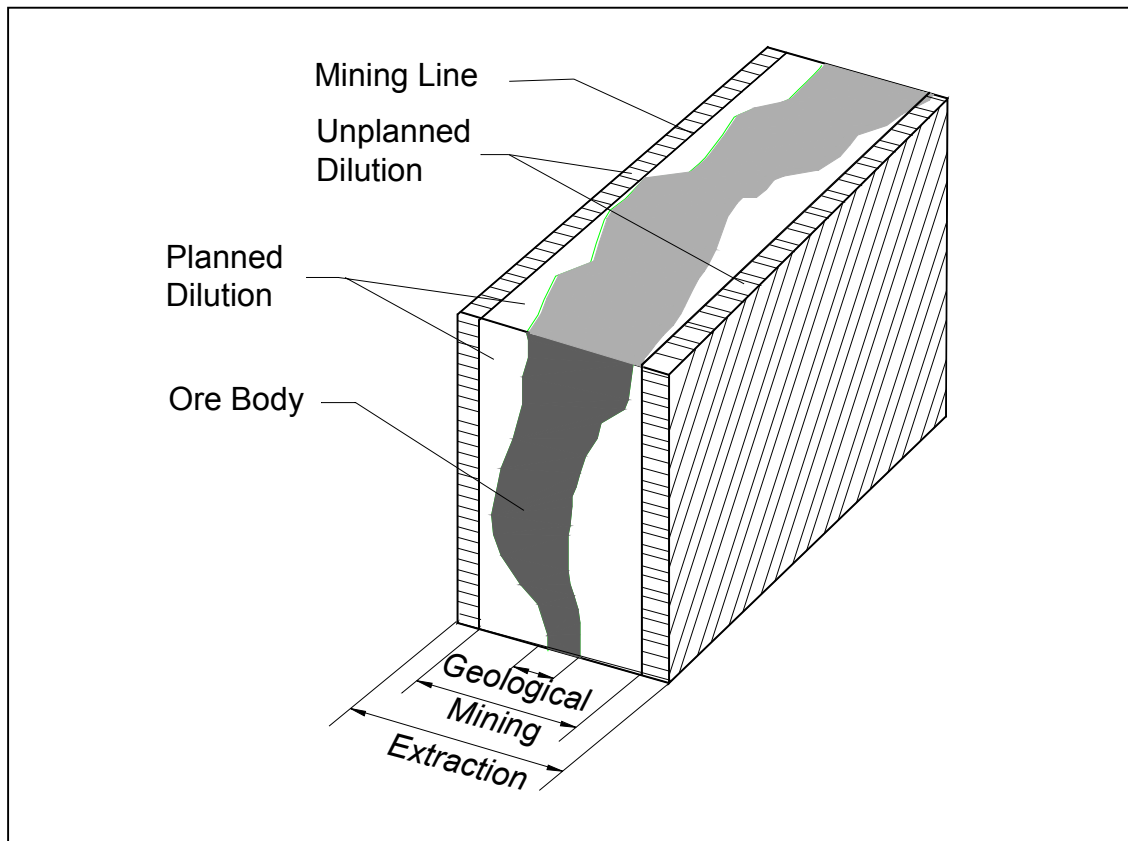


Figure 1.1. Dilution definition (after Scoble & Moss, 1994)

exposure time and the overall rock mass strength properties are not easily assessed due to the difficulty of obtaining realistic input data. These factors may have a significant effect on stope instability and dilution.

This research project is mainly based on the collection and analysis of a large number of case histories from field-collected data at Hudson Bay Mining and Smelting (HBMS) operations. The analysis of this large number of case histories could not practically be undertaken by computer modelling of each case. The complex opening geometry would be very time consuming to model and many of the factors influencing stability and dilution, such as exposure time and blasting influences, cannot be easily modelled. An empirical approach, coupled with selective numerical modelling, has been followed to take advantage of the strong points of both general approaches to analysis. An existing empirical method of estimating stope dilution (Clark, 1998) has formed the initial basis of the empirical approach for data analysis. Figure 1.2 shows the general factors

influencing open stope dilution, as well as those factors that form a key part of this research.

1.2 Objectives of the Research

The overall objectives of this research project are to:

- Improve the understanding of factors which control open stope stability and dilution
- Quantify the factors, which are poorly accounted for or ignored by existing empirical design methods, and
- Provide better guidelines for designing stable open stopes with minimum dilution

The general approach taken for this research was to collect a large number of case histories documenting hanging wall dilution. Information on the rock properties and mining conditions were related to measured hanging wall dilution to determine guidelines for estimating dilution. The Cavity Monitoring System (CMS) instrument was used to measure the excavated stope geometry. This instrument is described in detail in Section 3.5.

Two full summers of fieldwork were conducted at the Callinan, Trout Lake and Ruttan Mines of Hudson Bay Mining and Smelting Co. Ltd. The main goal of the fieldwork was to collect field data pertaining to dilution. Systematic underground site mapping and rock mass classification were conducted at the mines. A comprehensive database was established for the study based on stope mining data, rock mass mapping and classification data as well as survey data on the open stope geometry. Based on the database and site observations, it has been recognized that stress, undercutting and blasting, as well as stope exposure time, have a significant effect on stope stability and ore dilution, in addition to the factors that had been incorporated by existing empirical design methods. These factors are ignored (e.g., undercutting, blasting and exposure time factors) or not adequately accounted for (e.g., stress factor) in current design approaches. The proposed research is directed toward quantifying the

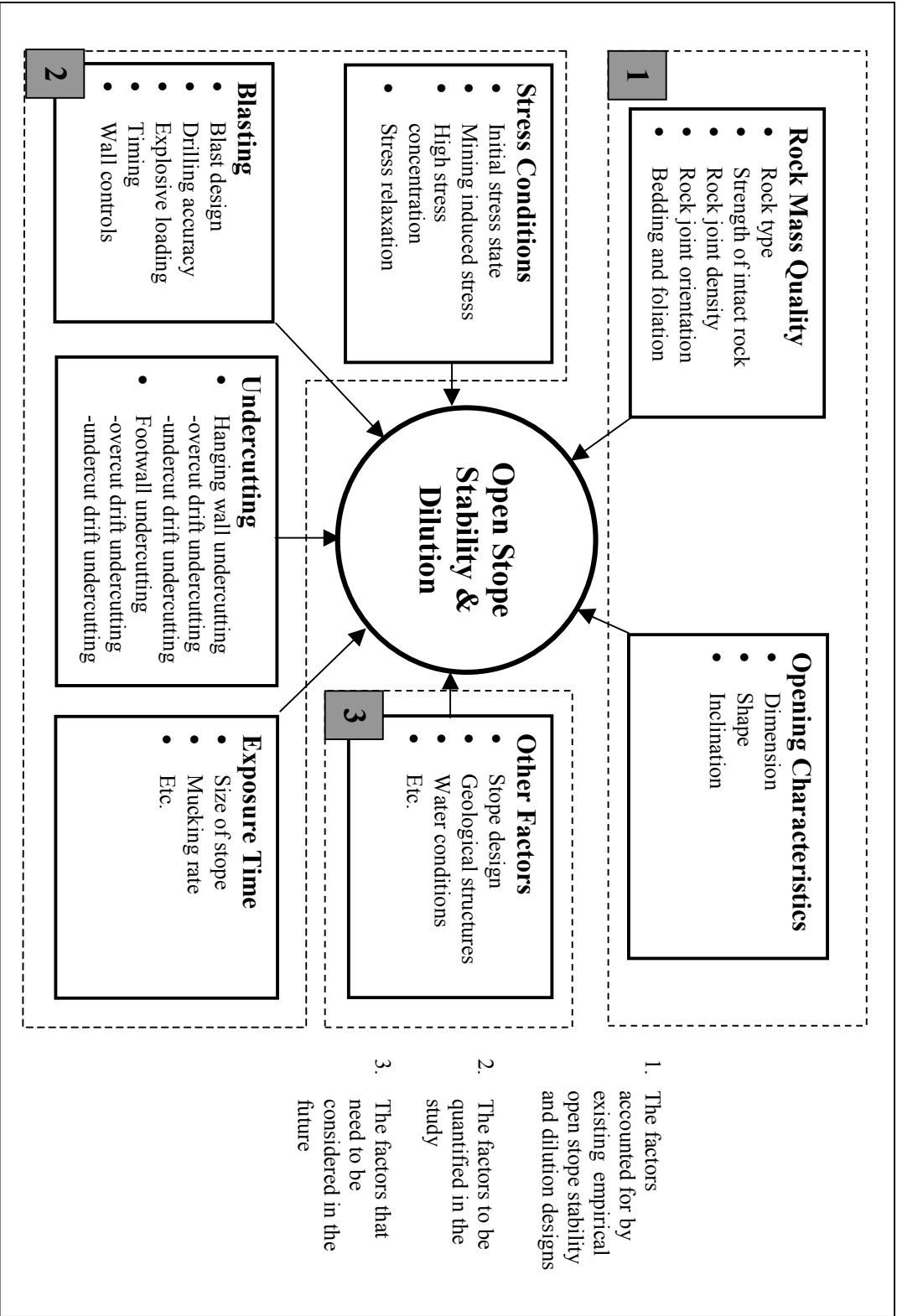


Figure 1.2. Factors affecting open stope stability and dilution

influence of these factors. More specifically, the objectives of this research are described as follows:

a) Quantify the influence of stress on open stope stability and dilution

Stress can have a significant effect on stope stability and dilution. Open stope hanging wall (HW) instability is influenced by the size of the stress relaxation zone on the stope HW. Without clamping (confining) stresses, the jointed rock mass may fall towards the excavated stope void due to gravitational force. The size of the relaxation zone on a stope hanging wall is directly related to the in-situ stress conditions. This can have a significant influence on stope stability and dilution. Some stopes may lie in a stress shadow zone that has a lower stress state, while other stopes may lie in an area of higher stresses. Typical stope configurations have been numerically modelled in this project to analyze stress effects. The effect of the pre-mining stress state on stope stability and dilution has been assessed.

b) Quantify the influence of undercutting on open stope stability and dilution

Undercutting in this study is defined as the stope overcut and the undercut drifts that are cut into the stope hanging wall. Undercutting also has a significant effect on stope stability and dilution. Undercutting the stope hanging wall on both overcut and undercut drifts is a well recognized factor which contributes to hanging wall instability and dilution. In many mines, undercutting the hanging wall degrades the integrity of the rock mass, as it breaks along continuous foliation or bedding planes parallel to the stope hanging wall contact, reducing stability. This undercutting also increases the zone of distressed or relaxed rock that may potentially fall into the open stope as dilution. The effect of undercutting on stope stability and dilution has been quantified in this project using case history analysis, as well as 2D and 3D numerical modelling.

c) Evaluate the effect of blasting on open stope stability and dilution

There are many factors that may affect blast performance. In general, a good blast is

one that will maximize ore recovery and fragmentation, and minimize waste dilution into the ore. Attempts have been made by researchers to quantify the effect of blasting on stope stability and dilution. Success has been limited due to the complexity of the problem. Factors influencing stope hanging wall blast damage include the properties of the rock mass (ore) being blasted and the hanging wall rock mass, explosive properties, drillhole design, drilling accuracy, explosive distribution, and initiation sequence. The effect of blasting on stope stability and dilution is complicated and is assessed based on the collected empirical data.

d) Evaluate the influence of stope exposure time on open stope stability and dilution

The length of an opening exposure time has been recognized as a factor influencing open stope stability and dilution. When an open stope is made in a pre-stressed rock, the stress field is disturbed. The magnitude and orientation of stresses in the vicinity of the stope will change to reach a new state of equilibrium. At the stope abutments, high stress concentrations occur. Stress relaxation or tensile stresses will be induced in the stope hanging wall and footwall. In the high compressive stress concentration abutments, the rock mass will undergo deformation and shearing. This will cause stress shedding farther away from the opening which will in turn increase the hanging wall and footwall zone of relaxation. The deformation will not stop until a new equilibrium is reached. During this new equilibrium formation process, the accumulated deformation increases with the exposure time. The HBMS mines' database and the complementary data from stand-up time graph (Bieniawski 1976) and Geco Mine have been used in this project to analyse the effect of exposure time on stope stability and dilution.

1.3 Thesis Overview

The thesis, organized into 11 chapters, is focused on assessing the influence of stress, undercutting, blasting and exposure time on open stope hanging wall stability and dilution. The following is an overview of the thesis:

Chapter 1 provides background information on the research, the objectives and the scope of the study.

Chapter 2 briefly reviews open stope stability and dilution related literature. The review includes theoretical rock/rockmass failure (stress driven failure, gravity driven failure) along with open stope stability and dilution design methods (analytical design methods, empirical design methods and numerical design methods).

Chapter 3 introduces the mines from which the case histories were collected. The case histories were collected from Trout Lake Mine, Callinan Mine and Ruttan Mine of Hudson Bay Mining and Smelting (HBMS) Ltd. Mine geology, rock mass properties, mining method, stope survey information, mine dilution control practice, and data collection are briefly presented.

Chapter 4 presents the database information and the initial database analysis. The database includes 150 case histories from HBMS mines. Each case history includes a CMS survey and a summary of the mining information. The summary includes rock mass classification, stope geometry, stress in terms of stope location situation, drilling and blasting, undercutting parameters, and data on the measured dilution.

Chapter 5 defines two new terms used in the research: dilution factor (DF) and dilution prediction error (DPE). More detailed information on the dilution design graph (Clark, 1998) is also presented.

Chapter 6 examines the effects of stress on open stope hanging wall stability and dilution. Stress relaxation is recognized as one of the major causes of open stope HW instability and dilution. With an estimate of the initial stress condition, different mine designs and mining sequences can create different induced stress conditions. This will influence the stress relaxation zone on the stope HW. 2D and 3D computer numerical modelling was conducted to aid the assessment of the influence of stress on the stope HW relaxation zone. Case histories were also used to analyze stope stress conditions.

Chapter 7 examines the effects of undercutting on HW stability and dilution. Both theoretical and numerical analyses were conducted to evaluate and quantify the influence of undercutting on HW dilution. Case histories were used to link undercutting with measured stope hanging wall dilution.

Chapter 8 looks at the effects of blasting on HW stability and dilution. Factors which can cause HW damage or overbreak are identified. The factors considered are drillhole drilling accuracy (drillhole deviation), slot location, explosive and its distribution, initiation sequence, and wall control techniques. With current blasting techniques, it was found that drillhole deviation is a major factor influencing HW instability. Case histories with drillhole deviation survey data and surveyed stope dilution were used to analyze the effects of drillhole deviation on HW instability.

Chapter 9 analyses the stope exposure time influence on open stope hanging wall stability and dilution. The database established from HBMS mines' case histories, the stand-up time graph (Bieniawski 1976) and history cases from Geco Mine were used.

Chapter 10 describes the statistical analysis of the empirical database. The statistical analysis was conducted to assess the factors influencing open stope stability and dilution and to verify the approaches discussed in previous chapters.

Chapter 11 presents the conclusions of the research. Recommendations for future research are suggested.

CHAPTER 2

OPEN STOPE STABILITY AND DILUTION DESIGN METHODS

2.1 Introduction

This chapter is a brief review of open stope stability and dilution related literature. The review is focused on the design techniques related to open stope stability and dilution.

Three general design methods exist for underground excavation design. These are:

- Analytical methods
- Empirical methods
- Numerical modelling methods

Analytical design methods work on the basic engineering design approach of determining material strength and loads on the material, and then applying a failure criterion to estimate stability. Empirical design methods are based on extensive engineering empirical data. Design lines or design criteria are estimated from the analysis of field data coupled with engineering judgement and case histories. Numerical modelling methods are used to simulate the induced stress distribution around an opening. Using the simulated stress situation, the stability of an excavation can be estimated by applying failure criteria based on the material strength properties.

2.2 Analytical Methods for Excavation Design

In rock engineering, failures generally occur in three categories (Milne, 1997): stress driven failure, gravity driven failure and a combination of stress and gravity driven failure. These general three types of failure mechanisms and corresponding design methods are reviewed in this chapter.

2.2.1 Stress Driven Failure

When the magnitude of applied stress exceeds the material strength, failure will occur. Stress related failure can be compressive or tensile. The failure caused by tensile stress will be discussed in section 2.2.3. Compressive stress driven failures can occur in underground structures such as pillars and open stope abutments where induced stresses concentrate around excavations. Stress driven failure design considers the strength properties of the rock or rock mass and the stress regime. A number of different failure criteria have been developed in the past (Coulomb, 1776; Griffith, 1921; Griffith, 1924; Bieniowski, 1974; Hoek and Brown, 1980) for the critical state rocks have for compressive stresses. These failure criteria are usually based on the study of the strength of intact rock. Correction factors or high safety factors are often used to reflect the weaker fractured rock mass properties. Most failure criteria are limited to areas of high stress, and have had limited use in rock mechanics. In rock engineering, the widely accepted failure criteria are Mohr-Coulomb failure criterion (Coulomb, 1776) and Hoek and Brown failure criterion (Hoek and Brown, 1980), which are discussed in this section. The stresses can be estimated using analytical methods or numerical modelling methods. The Kirsch equations are useful for estimating stresses for circular geometries and are discussed in this section. Numerical modelling methods are more numerous and are discussed later in this chapter.

a). Kirsch's Equation – A 2D Analytical Method for Estimating Stress

One of the first solutions for the two-dimensional distribution of stresses around an

opening in an elastic body was published in 1898 by Kirsch. The solution predicts stress concentrations for a simple cross-sectional shape, a circular hole forming an infinitely long tube within an infinite medium. Kirsch's equations are expressed relative to a system of polar co-ordinates. The stresses are defined in terms of the tractions acting on the faces of an element located at a radius r and a polar angle θ (Hoek and Brown, 1980)(Figure 2.1). Kirsch's Equations are as follows:

$$\begin{aligned}\sigma_{rr} &= \frac{\sigma_v}{2} \left[(1+K)(1 - \frac{a^2}{r^2}) - (1-K)(1 + \frac{3a^4}{r^4} - \frac{4a^2}{r^2}) \cos 2\theta \right] \\ \sigma_{\theta\theta} &= \frac{\sigma_v}{2} \left[(1+K)(1 + \frac{a^2}{r^2}) + (1-K)(1 + \frac{3a^4}{r^4}) \cos 2\theta \right] \\ \sigma_{r\theta} &= \frac{\sigma_v}{2} (1-K)(1 - 3\frac{a^4}{r^4} + 2\frac{a^2}{r^2}) \sin 2\theta\end{aligned}\tag{2.1}$$

where,

σ_{rr} is the radial stress,

$\sigma_{\theta\theta}$ is the tangential stress,

$\sigma_{r\theta}$ is the shear stress,

σ_v is the original vertical stress,

σ_h is the original horizontal stress,

K is the ratio of horizontal stress to vertical stress ($K=\sigma_h/\sigma_v$),

θ is the polar angle measured counter-clockwise from positive x-axis,

a is radius of the hole, and

r is the distance from the hole centre.

Kirsch's equations show that the magnitudes of stresses around the opening are related to the magnitude of the far field stress, the ratio of horizontal to vertical stress, the dimensions of the opening and the distance from the opening. The radial and shear stresses are zero on the excavation boundary. The tangential stress has a larger value on the boundary perpendicular to the minor principal stress (i.e., at $r = a$, $\theta = \pi/2$) and has a smaller or tensile stress (e.g., when $K \geq 3$) on the boundary perpendicular to the major principal stress (i.e. at $r = a$, $\theta = 0$).

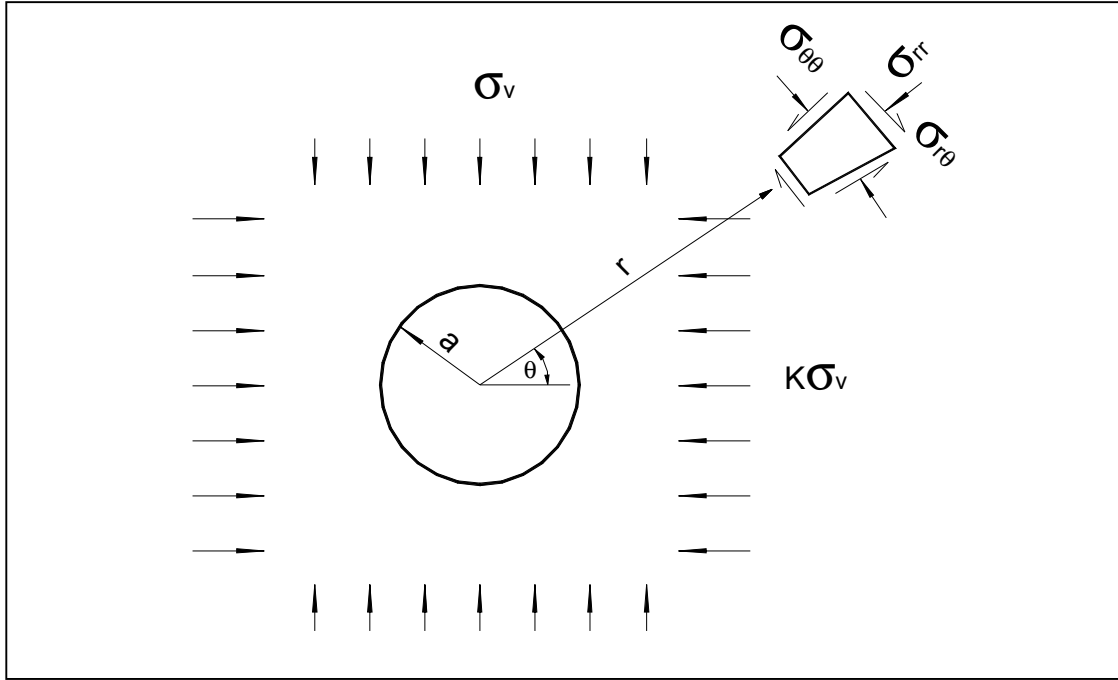


Figure 2.1. Definition of stresses in polar coordinates used in Kirsch's equations (after Brady & Brown, 1993)

b). Mohr-Coulomb Failure Criterion

It was observed that when a rock is being compressed, it will fail in shear. Coulomb (1776) postulated that the shear strength of rock is made up of two parts: a constant cohesion and a normal stress-dependent frictional component. The failure criterion takes into account the increased strength of the rock with increasing confinement. Figure 2.2 shows the criterion with a tensile cut-off. This tensile cut-off shows the Mohr-Coulomb envelope line extended to the tensile region up to the point where σ_3 becomes equal to the uniaxial tensile strength of rock $-T_0$. The minor principal stress can not be less than $-T_0$.

The Coulomb failure criterion is expressed as:

$$\tau = \frac{1}{2}(\sigma_1 - \sigma_3) \sin\left(\frac{\pi}{2} + \phi\right) \quad (2.2)$$

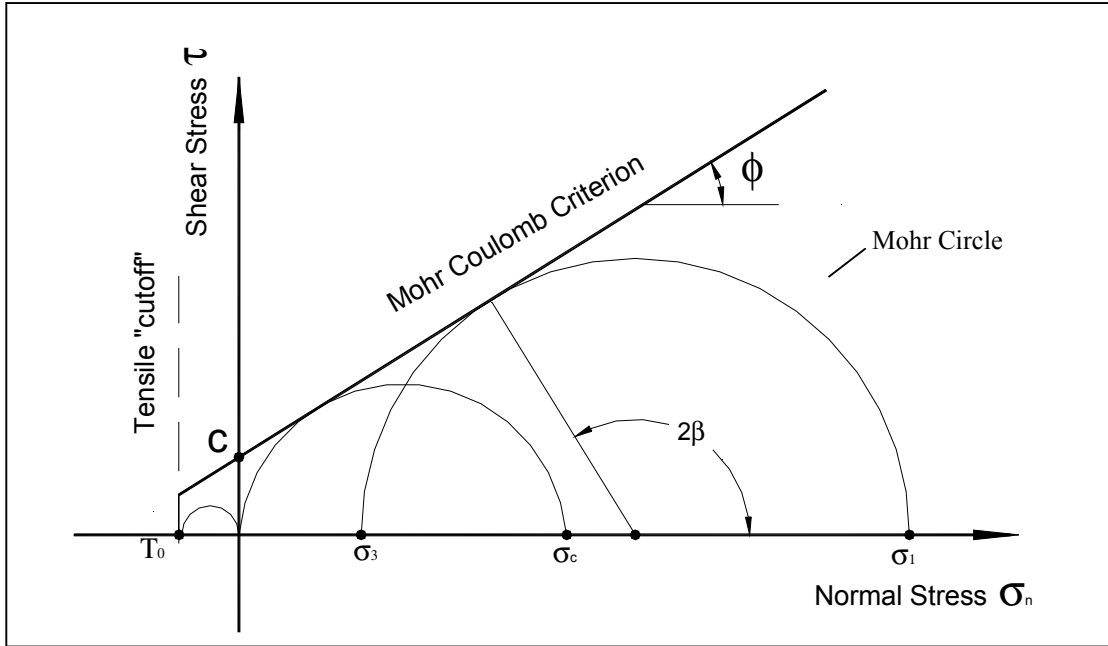


Figure 2.2. Mohr Coulomb failure criterion (after Goodman, 1989)

$$\text{or } \tau = \frac{1}{2}(\sigma_1 - \sigma_3) \sin 2\beta \quad (2.3)$$

where,

τ = shear strength;

σ_1 = maximum principal stress;

σ_3 = minimum principal stress; and

ϕ = angle of internal friction.

$$\beta = 45^\circ + \phi/2$$

The criterion in the compressive region also can be expressed in term of the maximum principal stress σ_1 by the following equation:

$$\sigma_1 = \sigma_c + \sigma_3 \left(\frac{1 + \sin \phi}{1 - \sin \phi} \right) \quad (2.4)$$

where, σ_c = unconfined compressive strength.

c). Hoek and Brown Failure Criterion

Hoek and Brown (1980) developed an empirical relationship for the peak failure stress for a range of confining stresses. Two constants, m and s , were introduced to account for rock mass strength properties. The constants m and s are determined based on the rock type, rock mass classification and rock mass properties. This relationship is expressed as:

$$\sigma_1 = \sigma_3 + \sqrt{m\sigma_3\sigma_c + s\sigma_c^2} \quad (2.5)$$

where,

σ_1 is the maximum principal stress;

m and s are constants dependent on rock type and rock mass classification.

Figure 2.3 shows the failure curve for given m and s values. The advantage of this failure criterion is that it can be tied to a rock mass classification value, RMR (rock mass rating)(Bieniawski, 1976) or Q (Barton, 1974), which takes rock mass properties into account rather than only intact rock properties. The disadvantage of the criterion is that it is a purely empirical concept with no basis in fundamental theory.

For open stope mining, stress concentration can occur in pillars, hanging wall abutments, and footwall abutments. If the concentrated stress exceeds the strength of the rock mass, failure occurs. The failure of pillars or stope abutments could cause instability in an open stope. In this case, the above failure criteria can be used to analyse the stability of the open stope. For stope hanging walls, which are usually in a state of low compressive or tensile induced stress, the tensile portion of the Hoek and Brown failure criterion is not reliable since it was developed mainly from compressive experiments. Stope hanging walls consist of jointed rock masses which have very low or negligible tensile strength. Rather than induce failure, tensile stresses loosen the rock mass making it more susceptible to gravity induced instability.

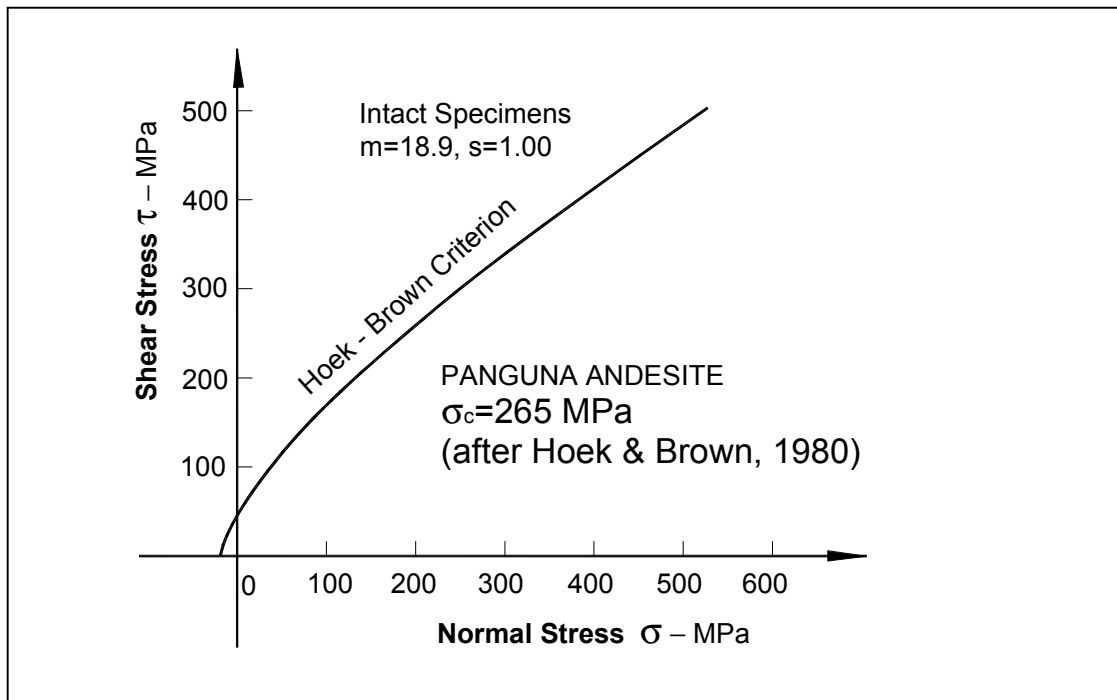


Figure 2.3. Hoek and Brown failure criterion (after Hoek & Brown, 1980)

2.2.2 Gravity Driven Failure

Gravity driven failure considers the dead weight of the material considered for design and the rock mass strength properties. Gravity driven failure designs include kinematic failure, beam theory, plate theory, and Voussoir arch beam theory. Beam and plate theories originate from civil engineering and treat the immediate surface of an opening as a continuous structure. Voussoir arch theory is also borrowed from civil engineering and looks at the transmission of vertical gravity loading to a horizontal thrust onto the opening abutment. Kinematic failure design looks at the jointed nature of the rock mass and determines what block or wedge geometries can fall into an opening. These gravity driven failure design methods are sometimes used in underground excavations. However, the assumptions required for some of these design methods make them of limited value. The following sections briefly discuss these design methods with emphasis placed on the limiting assumptions required.

a). Kinematic Failure

Kinematic failure is sometimes called structurally controlled failure or wedge failure. It is a relatively common failure mode in underground hard rock mines. For a block of rock to fall free from the roof or the side walls of an excavation, it is necessary that the block should be separated from the surrounding rock mass by at least three intersecting structural discontinuities. Failure can occur by sliding along one or more of the planes in the case of a wedge on a wall or the back. The frequency, condition, and orientation of the jointing combined with the size of the excavation, determines the size of potential wedges (Goodman, 1989). The stress level around the excavation and joint condition can also influence the stability of a wedge. However, most design procedures assume the immediate back to be in a relaxed or low stress state. The potential wedge size and location can be determined by detailed rock mass mapping. Based on mapping data, the potential wedge can be analysed by modelling (Carvalho, et al., 1992-95) or stereonet analysis. The kinematic design method is primarily used for entry-type excavations such as tunnels. Discontinuities can often realistically be mapped at a scale of tunnel excavations. Open stoping is a non-entry excavation method with typically very large excavations. It is hard to get realistic joint information and joint strength properties at the scale of an open stope. For this reason a kinematic approach is rarely used for an open stope excavation design.

b). Beam Failure

Much of the following discussion was taken from Obert and Duval (1967) and Saada (1974). For rock engineering purposes the flexure of beams can be presented by an approximate theory based on the following assumptions.

1. The beam is straight and the length to its other dimension (either thickness or width) ratio is larger than 8;
2. The beam is prismatic and has a longitudinal plane of symmetry;

3. The beam material is continuous, homogeneous, isotropic, and linear elastic;
4. Loads are applied normally to the longitudinal axis of the beam and in the plane of symmetry;
5. Plane sections in an unloaded beam remain planar during flexure;
6. The deflection of the beam is assumed to be in the form of a circular arc of radius R and deflections and slopes are small enough so that the curvature C is given by

$$C = \frac{1}{R} = \frac{\frac{d^2 u_2}{dx_1^2}}{\left[1 + \left(\frac{du_2}{dx_1}\right)^2\right]^{3/2}} \approx -\frac{d^2 u_2}{dx_1^2} \quad (2.6)$$

(See Figure 2.4).

where,

C = beam deflection curvature;

R = beam deflection circular arc radius;

du_2 = displacement increment in x_2 direction;

dx_1 = distance increment in x_1 direction.

Based on the above assumptions, the beam deflection curvature C, deflection slope $\theta(x_1)$ and stresses can be calculated by the following equations (Figure 2.4 & 2.5):

$$\text{Deflection Curvature} \quad C = \frac{1}{R} \approx \frac{d^2 u_2}{dx_1^2} = -\frac{M_{13}}{EI_{33}} \quad (2.7)$$

$$\text{Deflection Slope} \quad \theta(x_1) = \frac{du_2}{dx_1} \quad (2.8)$$

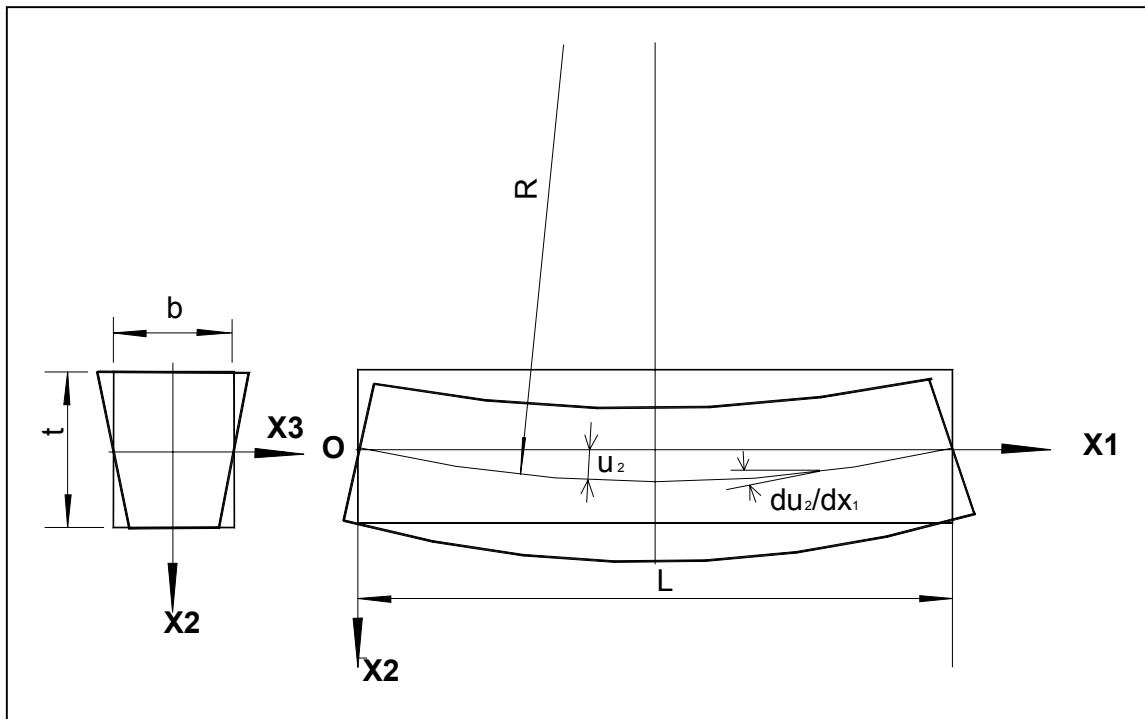


Figure 2.4. Deflection of a simple beam (after Obert & Duval, 1967)

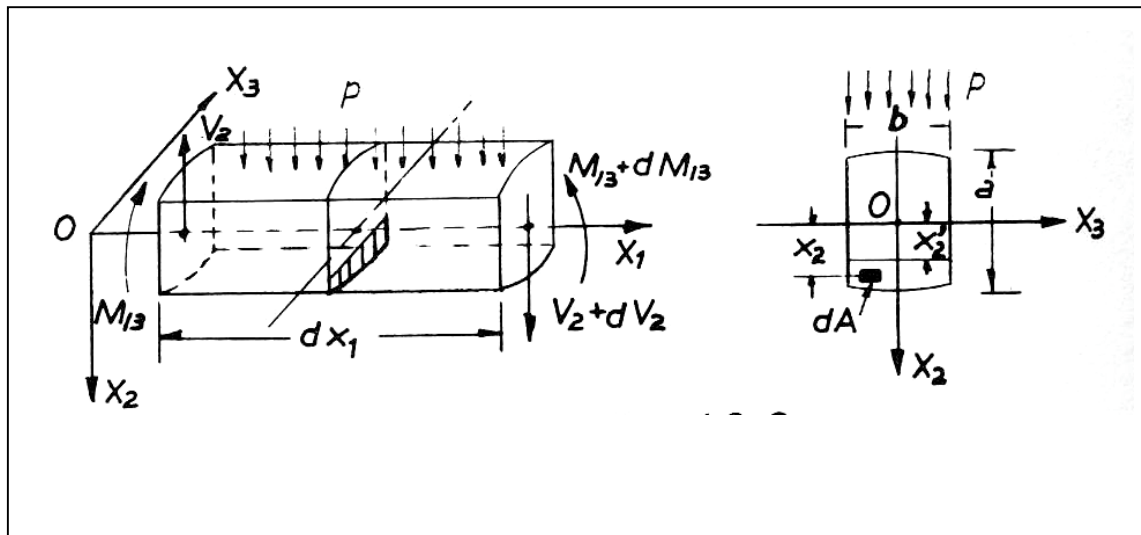


Figure 2.5. Illustration of parameters (from Obert & Duval, 1967)

$$\sigma_{11} = \sigma_{11}(x_1, x_2) = \frac{M_{13}x_2}{I_{33}} \quad (2.9)$$

$$\sigma_{12}(x_1, x_2) = \frac{V_2}{I_{33}b} \int_{x_2}^a x_2 dA = \frac{V_2 Q_3}{I_{33}b} \quad (2.10)$$

$$\sigma_{22} = \sigma_{33} = \sigma_{13} = \sigma_{23} = 0 \quad (2.11)$$

where,

M_{13} = bending moment about the OX_3 axis on the face normal to OX_1 ;

E = material Young's Modulus;

I_{33} = moment of inertia of the section about the OX_3 axis;

$\theta(x_1)$ = deflection slope in OX_1 direction;

Q_3 = static moment of the area A about the OX_3 axis;

σ_{11} , σ_{12} , σ_{22} , σ_{33} , σ_{13} and σ_{23} are stresses;

V_2 = shear force in X_2 direction.

The beam theory best applies to tunnel roof (flat) conditions in a bedded or laminated rock mass. In this case, the tunnel span is equal to a beam length and the beam thickness is set to the bedding spacing.

Under downward loading, the maximum deflection is at the middle length of the beam. The top half of the beam is in compression and the bottom half of the beam is in tension.

The stability of a beam can be determined by calculating whether a beam's stresses and deformation are within the allowable strength or deformation ranges of the beam material. The allowable deformation range can be determined by the strength of the beam material and the material properties such as Young's modulus E and Poisson's ratio ν .

The major flaw with this design approach is the assumption that the rock mass can

mobilize tensile stresses. The presence of cross joints (joints other than those parallel to the span) make it impossible for tensile stresses to be mobilized since the joints break the rock continuity. This design method is not usually used for open stope stability design.

c). Plate Failure

As with beam theory, some assumptions are required for the application of this theory. These assumptions are (Obert and Duval, 1967):

1. A plate is a straight and flat rectangular surface whose width is at least more than four times of the thickness and whose length is equal to or greater than its width.
2. The plate material is homogenous, isotropic, and linear elastic.
3. The maximum deflection of the plate is less than half of its thickness.
4. All loads are applied normal to the plate.
5. When the plate deflects the central plane remains unstressed.
6. Vertical straight lines remain straight after flexure but become inclined.

Consider a thin rectangular plate of length b , width a , and thickness t with built-in edges in all four sides and loaded by its own weight. The maximum deflection and stress are given by (Obert and Duval, 1967):

$$\text{Maximum Deflection } (\eta)_{\max} = \frac{\alpha \gamma a^4}{Et^2} \quad (2.12)$$

$$\text{Maximum Stress } (\sigma)_{\max} = \frac{6\beta \gamma a^2}{t} \quad (2.13)$$

where,

α and β = coefficients based on the plate length and width ratio for a Poisson's ratio of 0.3

γ = unit weight of the plate material

a = plate width

E = Young's modulus

t = plate thickness

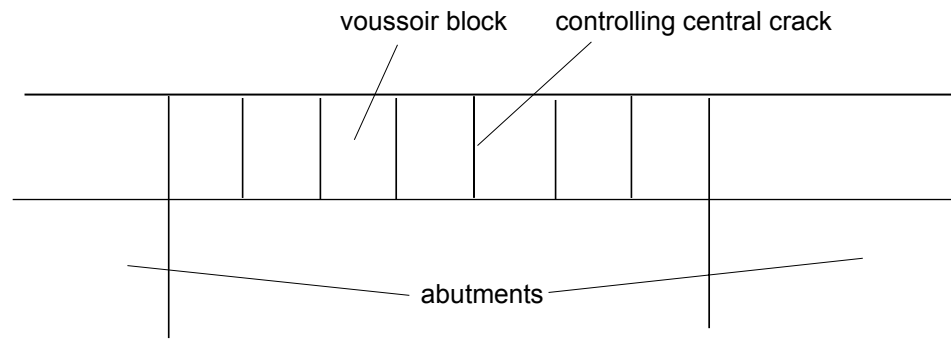
The stability of the plate then can be estimated based on the maximum induced stress and the strength of the intact rock. As with the beam design method, the major flaw with this design approach is the assumption that the rock mass can mobilize tensile stresses (which requires that the beam material is continuous, homogeneous, isotropic, and linear elastic). The presence of cross joints (joints other than parallel to the plate) makes it impossible for tensile stresses to be mobilized.

d). Voussoir Beam Failure

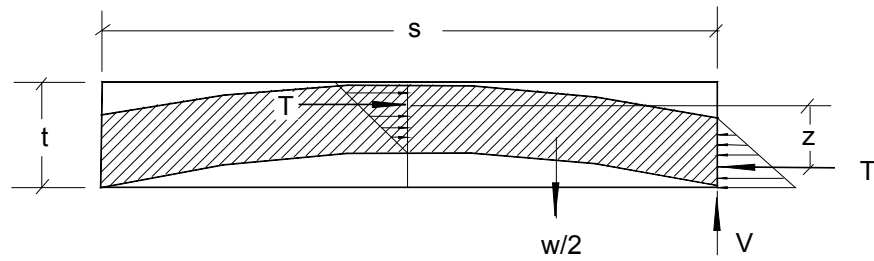
For both beam and plate deflection, the lower part of the member is in tension and the top part is in compression. The fractured nature of rock mass usually makes it difficult to mobilize any tensile loads in the back of an excavation. Evans (1941) was the first to consider analyzing stope backs as discrete blocks as in a masonry or Voussoir arch. It has long been recognized that arching can greatly increase the load bearing capacity of a beam. The Voussoir beam model was modified by Beer and Meek (1982) and is illustrated in Figure 2.6. A linear arch with vertical joints has also been studied by Stimpson (1989) and by Sepehr and Stimpson (1988). The concept illustrated in this figure is that the line of lateral thrust within such an arch, when traced on the beam span, approximates a parabolic arch.

Voussoir beam theory makes the following assumptions (Brady & Brown, 1985):

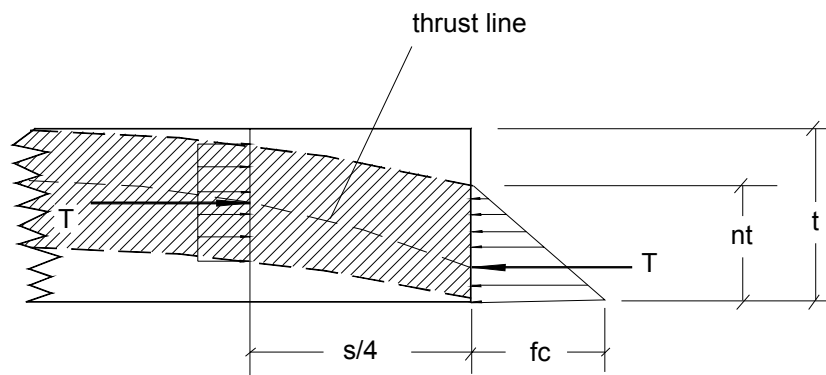
- The rock mass is assumed to be cut by linear discontinuities trending along strike, such that the back can be assumed to be composed of discrete blocks;
- It is assumed that there is no horizontal compressive stress in the back transferred from the surrounding rock; and,
- No tensile strength develops between individual blocks (cohesion = 0).



(a) Voussoir block excavation roof



(b) Parabolic arch developed in roof



(c) Line of thrust in beam to abutments

Figure 2.6. Voussoir block theory (after Brady and Brown, 1985)

Because the solution to the problem is indeterminate, two assumptions are required for the analysis. First, the line of thrust is assumed to be parabolic, and secondly, the load distribution at the centre of the beam and the abutment contact is assumed to be triangular (Figure 2.6(b)). The triangular end load operates over a length nt where,

$$n = 1.5 \left(1 - \frac{z}{t} \right) \quad (2.15)$$

where,

n = lateral load to depth ratio

z = arch height

t = beam thickness

Applying moment equilibrium around the centroid of the half beam yields:

$$\frac{\gamma}{8} t S^2 = \frac{f_c n t z}{2} \quad \text{or,} \quad f_c = \frac{\gamma S^2}{4 n z} \quad (2.16)$$

where,

f_c = the maximum longitudinal compressive stress

γ = unit weight of beam

S = horizontal span of beam

Assuming that the shape of the thrust arch acting in the beam is parabolic, the arc length L , can be expressed by:

$$L = S + \frac{16z^2}{3S} \quad (2.17)$$

where,

L = arc length of parabolic thrust profile

z = height of arch

The resultant force acts through the centre of each force distribution, so the initial moment arm for f_c is given by:

$$Z_o = t - \frac{2nt}{3} \quad (2.18)$$

where,

Z_o = initial moment arm of f_c

t = beam thickness

The average longitudinal stress in the beam is estimated by considering the stresses in the quarter span of the beam, as shown in Figure 2.6(c). At a distance $S/4$ from the abutment, the stress distribution is uniform over the arch depth. The average longitudinal stress f_{av} for this quarter of the beam, and hence for the entire beam, is given by:

$$f_{av} = \frac{1}{2} f_c \left(\frac{2}{3} + \frac{n}{2} \right) \quad (2.19)$$

An explicit solution for the loading in the beam and beam deformation is not possible. An iterative procedure is required, which begins with assuming a value for the initial load to depth ratio, n . An initial value of $n=0.5$ will normally produce a stable solution. The procedure involves calculating sequentially f_c , f_{av} , L , z , and n . The process is repeated with the load to depth ratio n , used to calculate f_c . Iterations continue until stable load to depth ratios are obtained.

Beer and Meek (1982) identified three possible failure modes for Voussoir arches (Figure 2.7). The following is taken from Beer and Meek (1982):

- Crushing at the hinges formed in the upper portion of the centre of the beam and at the lower abutment contacts;
- Shear at the abutment when the limiting shear resistance T is less than the required abutment vertical reaction force V , ($W/2$); and,
- Buckling of the roof beam with increasing eccentricity of lateral thrust giving rise to a snap-through mechanism.

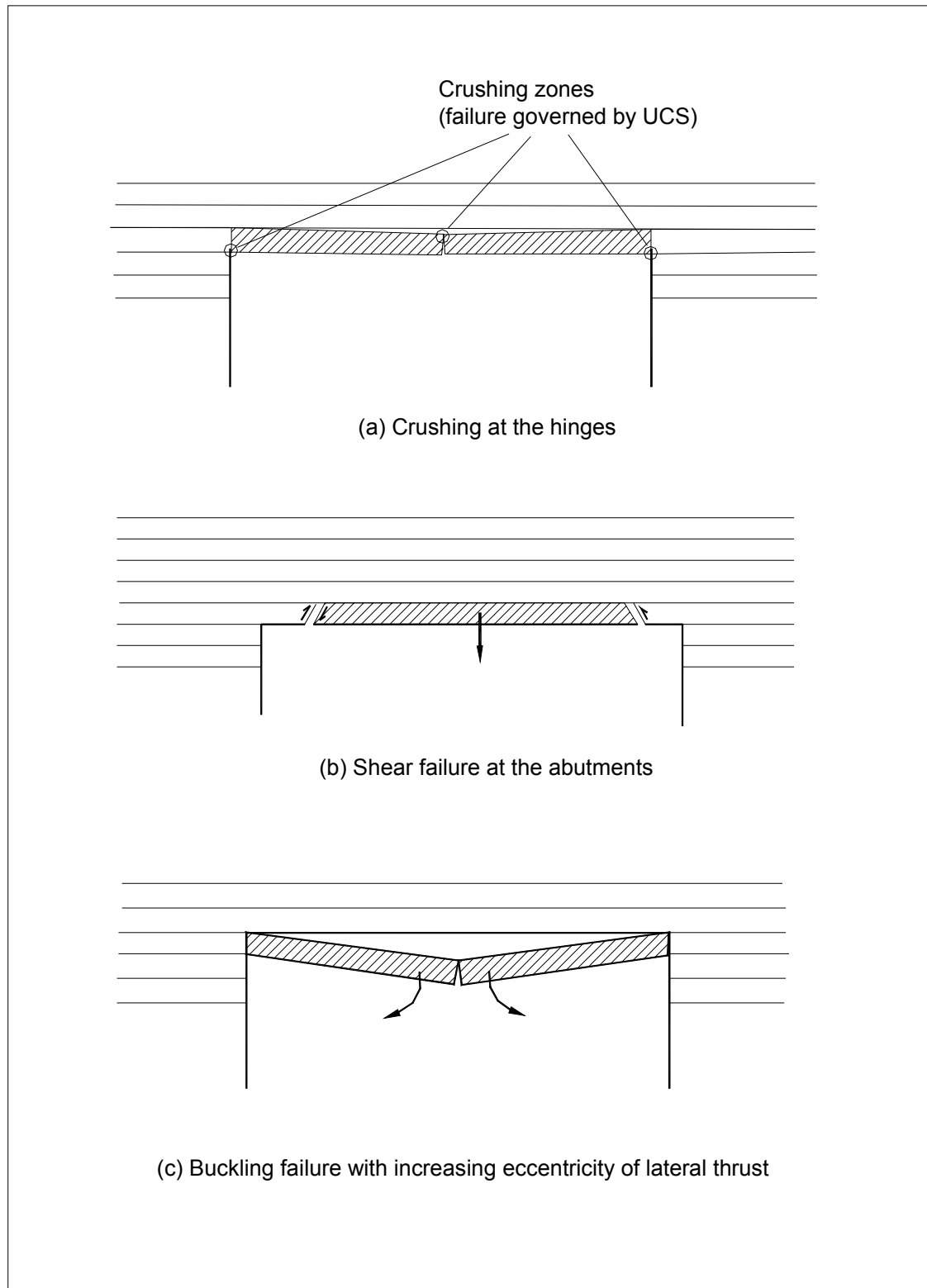


Figure 2.7. Voussoir arch failure Modes (after Beer and Meek, 1982)

Crushing or compressive failure is analyzed by comparing the maximum longitudinal compressive stress f_c to the uniaxial compressive strength of the beam. The factor of safety (F) against compressive failure of the beam is then:

$$F = \frac{UCS}{f_c} \quad (2.20)$$

The factor of safety against shear failure is defined by the frictional resistance to shearing divided by the shear stress caused by the weight of the beam. The resistance to shearing is given by:

$$F = T \tan \phi = \frac{f_c n t (\tan \phi)}{2} \quad (2.21)$$

The abutment shear force (V) is:

$$V = \frac{W}{2} = \frac{\gamma S t}{2} \quad (2.22)$$

The factor of safety (FS) against shear failure at the abutments is given by:

$$F_s = \frac{f_c n}{\gamma S} \tan \phi \quad (2.23)$$

Buckling failure will occur when the moment arm z becomes negative; that is, when the centroid of the centre force distribution is lower than the abutment lateral force distribution. A check should be made in the iteration procedure described above to determine if z is negative and, therefore, if buckling failure occurs.

A solution can be obtained for a square stope surface for any inclination and for any material specific gravity (Brady and Brown, 1985). These general solutions are expressed as graphs shown in Figure 2.8. To use these graphs, the effective specific gravity, normalized rock mass modulus and the normalized compressive strength (UCS') must be calculated. Finally the maximum stable span for a beam can be found

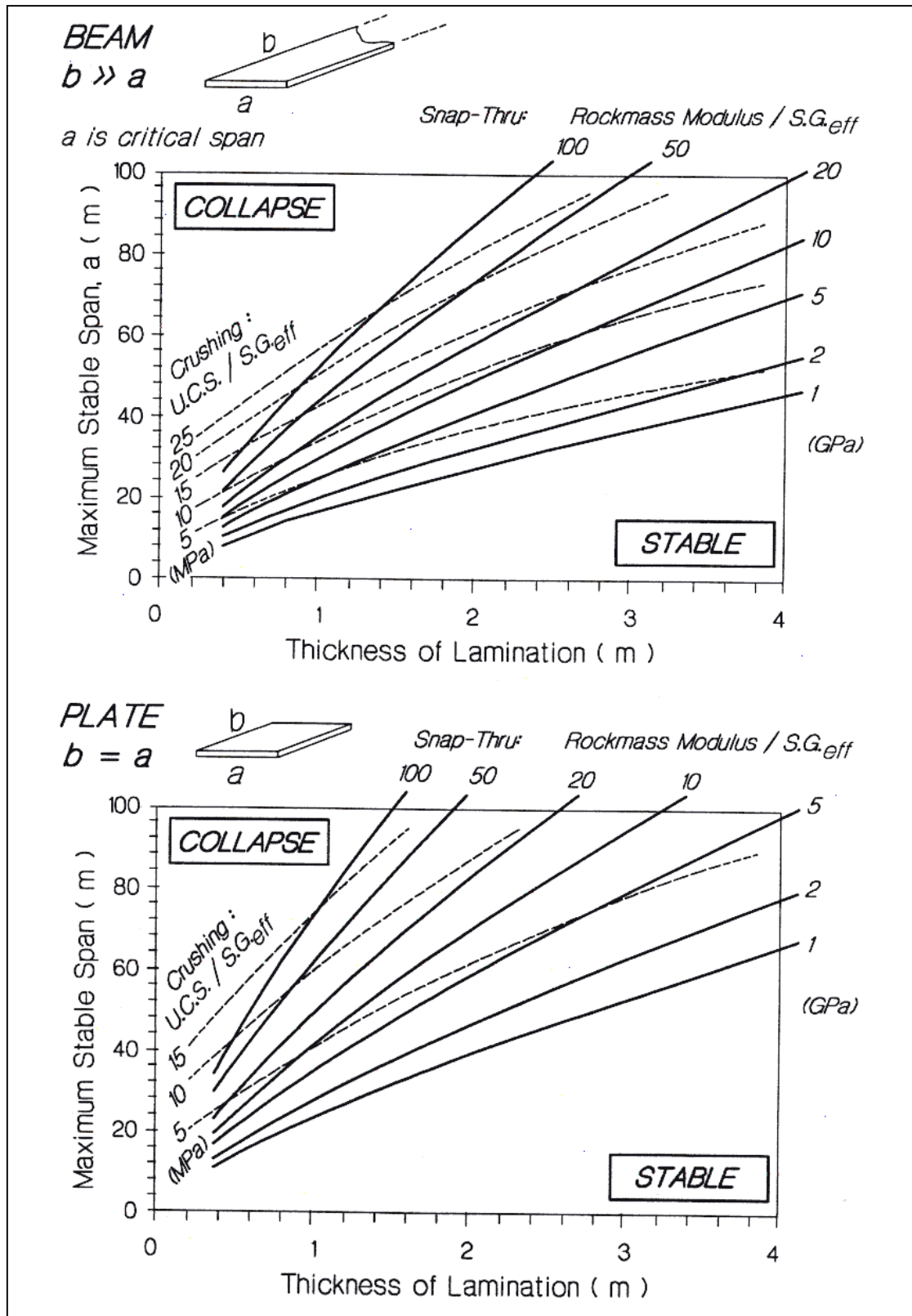


Figure 2.8. General solutions for beam (infinite depth) and square plate (from Hutchinson and Diederichs, 1996)

from the assumed thickness of lamination (beam height). The span used in the analysis is the shorter span.

The effective specific gravity ($S.G._{eff}$), normalized rock mass modulus E' and the normalized compressive strength (UCS') are calculated as follows (Hutchinson and Diederichs, 1996):

$$S.G._{eff} = S.G. \times \cos \alpha \quad (2.24)$$

$$UCS' = UCS / S.G._{eff} \quad (2.25)$$

$$E' = E / S.G._{eff} \quad (2.26)$$

where,

$S.G.$ = specific gravity of rock mass

$S.G._{eff}$ = effective specific gravity

α = wall dip

UCS' = normalized compressive strength of the rock

UCS = uniaxial compressive strength of rock

E' = normalized rock mass modulus

E = rock mass modulus (parallel to excavation surface)

The required input parameters and the 2D nature of this approach make the Voussoir beam theory difficult to apply to open stope HW design. It is difficult to estimate the thickness of the assumed beam, rock mass modulus and other input parameters for a blast damaged, jointed rock mass. Factors such as joint strength, orientation and spacing significantly influence hanging wall stability and are not accounted for in the Voussoir analysis. This approach is interesting, however, it cannot be effectively applied to field conditions.

2.2.3 Gravity Driven Stress Relaxation Failure

Stress relaxation (zero or tensile stress) around the surface of an excavation is one of the major factors causing excavation instability. When an excavation is made in a pre-stressed rock, the magnitude and orientation of stresses in the vicinity of the excavation will be changed. Following the creation of the excavation, the surface of the excavation (especially large surfaces) may become de-stressed (relaxed). Within the de-stressed area, a zone of relaxation or a zone of tensile stress may exist. “Since intact rock has a very low tensile strength and discontinuities have no strength in tension, tensile stress is not likely to build up in a rock mass medium. Instead, tensile stresses will open existing joints or induce new cracks through intact rock, creating a zone of relaxation. Inside this zone of relaxation, individual rock blocks have more freedom to move because they are unconfined and thus become more sensitive to gravitational forces” (Potvin, 1988). The jointed rock mass in the relaxed zone on the side walls and the back of an excavation may fall off due to gravity. Instability in an underground excavation is closely related to the zone of relaxation (Clark, 1998; Diederichs & Kaiser, 1999; Kaiser et al., 1997, Martin et al., 2000). Instability problems in open stope mining typically occur in this relaxation zone.

The stress relaxation zone can be analyzed by numerical modelling methods. The stress relaxation numerical modelling is described in Section 6.4.

2.3 Empirical Open Stope Stability and Dilution Design Methods

Empirical open stope design methods can be divided into two main categories: stability design methods and dilution design methods. Many empirical design methods have been developed to incorporate open stope stability and dilution. Mathews et al. (1981) developed the Mathew’s Stability Design Method for open stopes. However, the initial database for developing the design method had a small number of case histories. Potvin et al. (1988) modified the Mathews’ Stability Design Method by redefining some of the rating adjustment factors and by adding more case histories. Nickson modified the

stability graph in 1992 and added additional case histories. Pakalnis (1986) developed a dilution approach from a joint study at the HBMS Ruttan Mine. Clark (1998) developed a new dilution design method based on the format of the stability graph. Rock mass classification is a key input for these empirical design methods.

2.3.1 NGI Classification System, Q and Modified Q, Q'

The NGI (Norwegian Geotechnical Institute) Q classification system was developed by Barton et al. (1974) based on a study of a large number of underground excavation case histories. The Q system is a multivariate system based on six parameters. It is a means of classifying rock masses with respect to in situ parameters including rock mass quality, joint condition, water and stress state. Q is defined by:

$$Q = \left(\frac{RQD}{J_n} \right) \times \left(\frac{J_r}{J_a} \right) \times \left(\frac{J_w}{SRF} \right) \quad (2.27)$$

where:

RQD = the Rock Quality Designation and is calculated as the ratio of the sum of the length of all the pieces of core greater than 10 cm to the total length of the core run. The RQD is expressed as a percentage and ranges from 0 to 100%. 0 to 25% shows a very poor rock quality and 90% to 100% indicates an excellent rock quality. RQD also can be estimated from exposed rock mass wall jointing or from a volumetric joint count.

J_n = joint set number.

J_r = joint roughness number. *J_r* describes the large and small scale surface texture of the critical joint set.

J_a = joint alteration number. *J_a* describes the surface alteration and frictional resistance of the critical joint set.

J_w = joint water reduction factor. *J_w* accounts for the destabilizing effect of high water pressure and of joint washout by water inflow.

SRF = stress reduction factor. SRF modifies Q to account for high in situ stresses which may cause compressive failure of rock and also accounts for highly fractured ground. Either condition results in a higher value of SRF and therefore a lower value of Q .

The Q value can range from 0.001 to 1000. Barton et al. (1974) proposed the rock mass categories based on the evaluation of Q as shown in Table 2.1. In hard rock mines, Q typically ranges from 0.1 to 100. The factors which make up Q are shown in Table 2.2.

The Q classification system has been used with a great deal of success in the design of tunnels in rock (Barton et al., 1992). The parameter SRF , however, becomes redundant when the classification system is used for the estimation of rock mass properties for the purpose of analytical or numerical modelling for design. Stress loading conditions are accounted for during the design calculations. The modified Q' has been proposed to allow the separate assessment of stress conditions.

$$Q' = \frac{RQD}{J_n} \times \frac{J_r}{J_a} \times J_w \quad (2.28)$$

Where, SRF is set to 1.0 which is equivalent to a moderately clamped but not over stressed rock mass.

In addition, in most deep underground hard rock mining environments, the excavations are relatively dry (not considering transient mine water flow from drilling and backfilling). J_w , therefore can also be set to 1.0. In this case, the modified classification system Q' is expressed as:

$$Q' = \frac{RQD}{J_n} \times \frac{J_r}{J_a} \quad (2.29)$$

Table 2.1. Classifications of rock mass quality based on Q (Barton et al., 1974)

Tunnelling Quality Index Q	Rock Mass Description
0.001 – 0.01	Exceptionally Poor
0.01 – 0.1	Extremely Poor
0.1 – 1	Very Poor
1 – 4	Poor
4 – 10	Fair
10 – 40	Good
40 – 100	Very Good
100 – 400	Extremely Good
400 - 1000	Exceptionally Good

For Q (or Q') classification, the rock mass to be considered should be initially divided into geologically or geomechanically distinct zones (e.g., hanging wall granite, hanging wall schist, ore zone, main fault zone, etc.). Each zone should be classified separately.

Q' is used along with several other factors (accounting for stress, jointing and gravity) to determine the stability number N (which was used in Mathews' stability graph, Mathews et al., 1981) and modified stability number N' (which is used in the modified stability graph method (Potvin, 1988; Nickson, 1992) and in the dilation design graph (Clark, 1998) for dimensioning of open stopes in mining. The stability number N and modified stability number N' are reviewed in the next section.

Table 2.2. Classification of individual parameters used in the NGI Q classification system (Hoek & Brown, 1980)

Description	Value	Note
1. ROCK QUALITY DESIGNATION	RQD	
A. Very poor	0 – 25	1. Where RQD is reported or measured as ≤ 10 (including 0), a nominal value of 10 is used to evaluate Q.
B. Poor	25 – 50	
C. Fair	50 – 75	2. RQD intervals of 5, i.e. 100, 95, 90 etc are sufficiently accurate
D. Good	75 – 90	
E. Excellent	90 – 100	
2. JOINT SET NUMBER	Jn	
A. Massive, no or few joints	0.5 – 1.0	1. For intersections use $(3.0 \times Jn)$ 2. For portals use $(2.0 \times Jn)$
B. One joint set	2	
C. One joint set plus random	3	
D. Two joint sets	4	
E. Two joint sets plus random	6	
F. Three joint sets	9	
G. Three joint set plus random	12	
H. Four or more joint sets, random, heavily jointed 'sugar cube', etc	15	
J. Crushed rock, earthlike	20	
3. JOINT ROUGHNESS NUMBER	Jr	
a. Rock wall contact and b. Rock wall contact before 10 cms shear		
A. Discontinuous joints	4	1. Add 1.0 if the mean spacing of the relevant joint set is greater than 3m. 2. Jr = 0.5 can be used for planar, slickensided joints having lineations, provided the lineations are orientated for minimum strength.
B. Rough and irregular, undulating	3	
C. Smooth, undulating	2	
D. Slickensided, undulating	1.5	
E. Rough or irregular, planar	1.5	
F. Smooth, planar	1.0	
G. Slickensided, planar	0.5	
c. No rock contact when sheared.		
H. Zone containing clay minerals thick enough to prevent rock wall contact	1.0	
J. Sandy gravelly or crushed zone thick enough to prevent rock wall contact	1.0	

Table 2.2 (continued)

4. JOINT ALTERATION NUMBER	Ja	ϕ_r (Approx.)	
<i>a. Rock wall contact</i>			
A. Tightly healed, hard, non-softening, impermeable	0.75	-	1. Values of ϕ_r , the residual friction angle, are intended as an approximate guide to the mineralogical properties of the alteration products, if present.
B. Unaltered joint walls, surface staining only	1.0	(25° - 35°)	
C. Slightly altered joint walls non-softening mineral coatings, sandy particles, clay-free disintegrated rock, etc	2.0	(25° - 30°)	
D. Silty-, or sandy-clay coatings, small clay-fraction (non-softening)	3.0	(20° - 25°)	
E. Softening or low friction clay mineral coatings, i.e. kaolinite, mica. Also chlorite, talc, gypsum and graphite etc., and small quantities of swelling clays. (Discontinuous coatings, 1-2mm or less in thickness)	4.0	(8° - 16°)	
<i>b. Rock wall contact before 10 cms shear.</i>			
F. Sandy particles, clay-free disintegrated rock etc	4.0	(25° - 30°)	
G. Strongly over-consolidated, non- softening clay mineral fillings (continuous, < 5mm thick)	6.0	(16° - 24°)	
H. Medium or low over-consolidation, softening, clay mineral fillings, (continuous, < 5mm thick)	8.0	(12° - 16°)	
J. Swelling clay fillings, i.e. montmorillonite (continuous, <5mm thick). Values of Ja depend on percent of swelling clay-size particles, and access to water	8.0 – 12.0	(6° - 12°)	
<i>c. No rock wall contact when sheared.</i>			
K. Zones or bands of disintegrated	6.0		
L. or crushed rock and clay (see	8.0		
M. G,H and J for clay conditions)	8.0 – 12.0	(6° - 24°)	
N. Zones or bands of silty or sandy clay, small clay fraction, (non-softening)	5.0		
Q. Thick, continuous zones or	10.0 – 13.0		
P. bands of clay (see G, H and	13.0 – 20.0	(6° - 24°)	
R. J for clay conditions)			

Table. 2.2 (continued)

5. JOINT WATER REDUCTION FACTOR		J _w	Approx. water pressure (kgf/cm ²)	
A. Dry excavations or minor inflow, i.e. < 5 lit/min, locally	1.0	<1.0	1. Factors C to F are crude estimates. Increase J _w if drainage measures are installed. 2. Special problems caused by ice formation are not considered.	
B. Medium inflow or pressure, occasional outwash of joint fillings	0.66	1.0 - 2.5		
C. Large inflow or high pressure in competent rock with unfilled joints	0.5	2.5 – 10.0		
D. Large inflow or high pressure, considerable outwash of fillings	0.33	2.5 – 10.0		
E. Exceptionally high inflow or pressure at blasting, decaying with time	0.2 – 0.1	>10		
F. Exceptionally high inflow or pressure continuing without decay	0.1 – 0.05	>10		
6. STRESS REDUCTION FACTOR		SRF		
a. Weakness zones intersecting excavation, which may cause loosening of rock mass when tunnel is excavated.				
A. Multiple occurrences of weakness zones containing clay or chemically disintegrated rock, very loose surrounding rock (any depth)			10.0	
B. Single weakness zones containing clay, or chemically disintegrated rock (excavation depth < 50m)			5.0	
C. Single weakness zones containing clay, or chemically disintegrated rock (excavation depth > 50m)			2.5	
D. Multiple shear zones in competent rock (clay free), loose surrounding rock (any depth)			7.5	
E. Single shear zones in competent rock (clay free), (depth of excavation < 50m)			5.0	
F. Single shear zones in competent rock (clay free), (depth of excavation > 50m)			2.5	
G. Loose open joints, heavily jointed or 'sugar cube' (any depth)			5.0	
b. Competent rock, rock stress problems				
	σ _v /σ ₁	σ _t /σ ₁		
H. Low stress, near surface	>200	>13	2.5	
J. Medium stress	200 - 10	13-0.66	1.0	
K. High stress, very tight structure (usually favorable to stability, may be unfavorable for wall stability)	10-5	0.66-0.33	0.5-2	
L. Mild rock burst (massive rock)	5-2.5	0.33-0.16	5-10	
M. Heavy rock burst (massive rock)	<2.5	<0.16	10-20	
c. Squeezing rock, plastic flow of incompetent rock under the influence of high rock pressure				
N. Mild squeezing rock pressure			5-10	
O. Heavy squeezing rock pressure			10-20	
d. Swelling rock, chemical swelling activity depending upon presence of water				
P. Mild swelling rock pressure			5-10	
R. Heavy swelling rock pressure			10-20	

2.3.2 Stability Number, N and Modified Stability Number, N'

The stability number (N) (Mathews et al., 1981) and modified stability number (N') (Potvin, 1988) are used to quantify the rock mass and loading condition. They are based on the same equation, but the weighting factors (A, B, & C) used in the calculations differ. For current stability design methods (Potvin, 1988; Potvin et al., 1989; Nickson, 1992) and dilution design (Clark, 1998), the modified stability number N' is used. The modified stability number N' is defined as:

$$N' = Q' \times A \times B \times C \quad (2.30)$$

Where

N' = modified stability number

Q' = modified tunnelling quality index (NGI) with $SRF = 1$.

(Barton, 1974, see section 2.3.1.1)

A = stress factor

B = joint orientation factor

C = gravity factor

The values for A, B and C are determined graphically as show in Figure 2.9, 2.10 and 2.11.

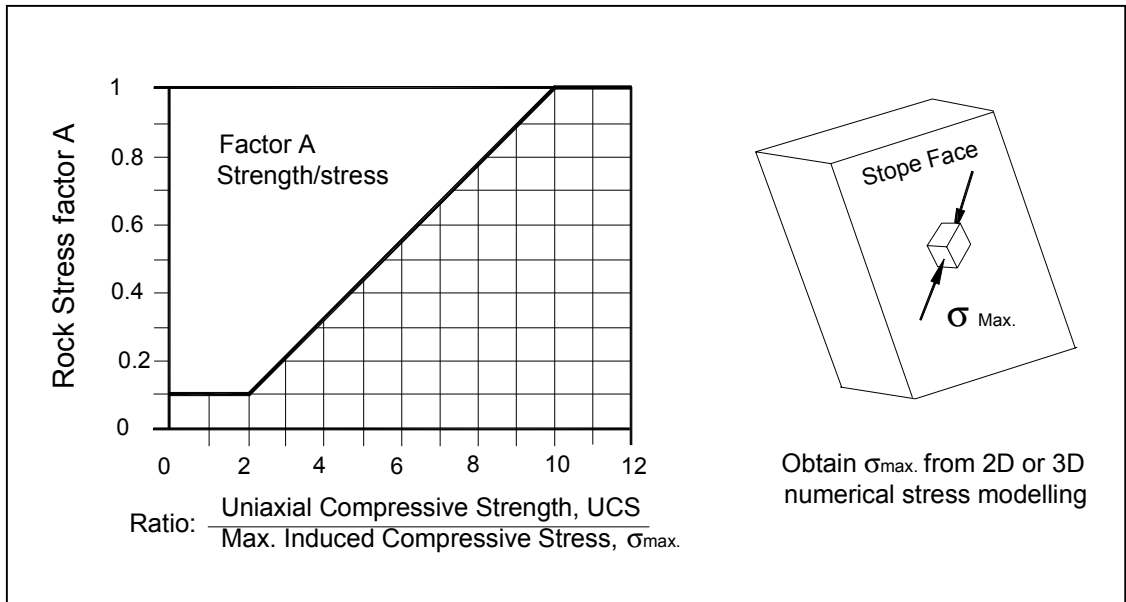


Figure 2.9 Stress factor A for stability graph analysis (after Potvin, 1988)

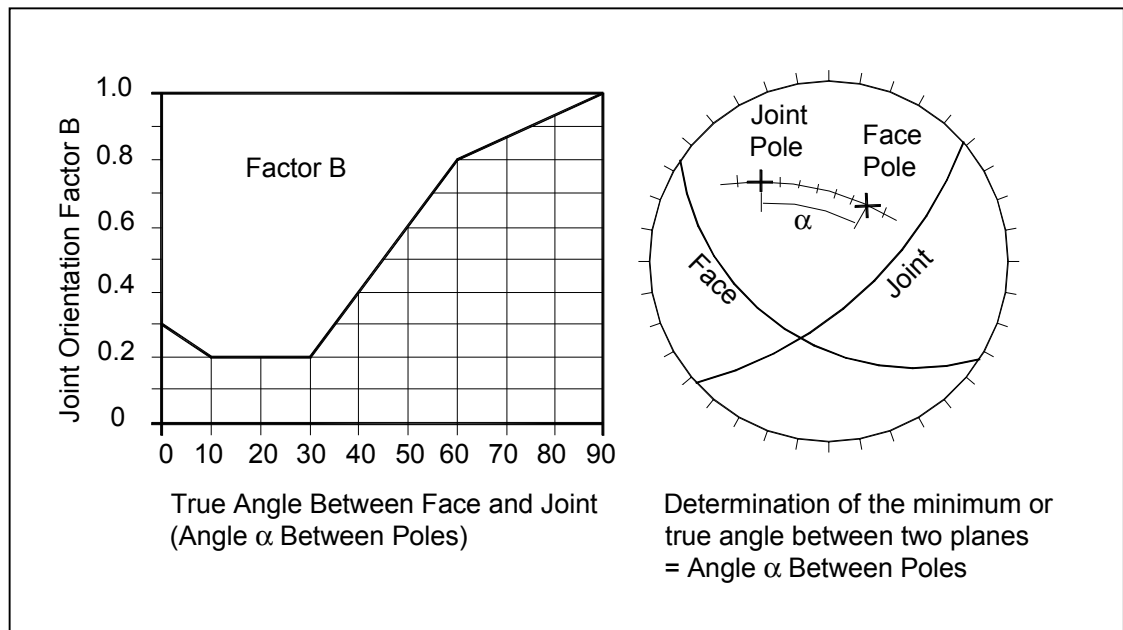


Figure 2.10 Determination of joint orientation factor B for stability graph analysis (after Potvin, 1988)(from Hutchinson and Diederichs, 1995)

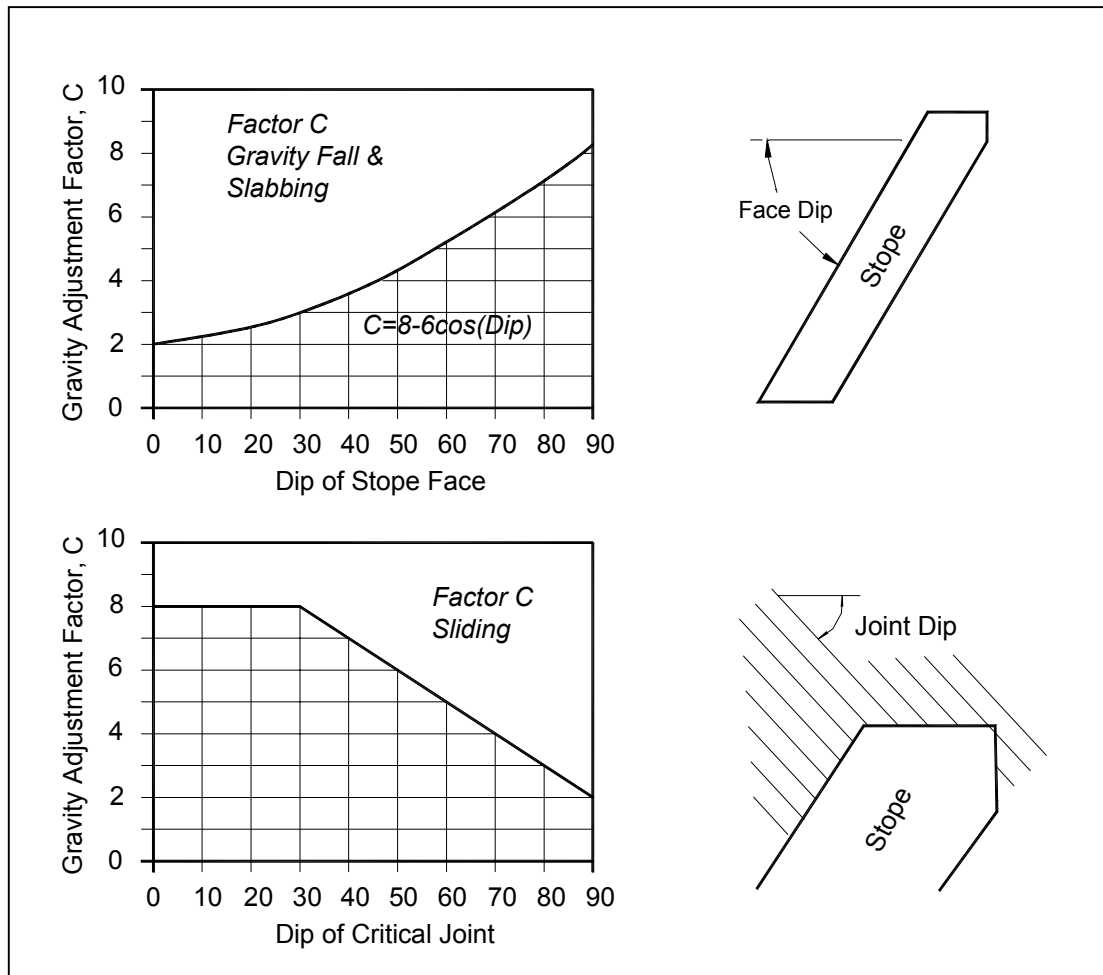


Figure 2.11 Determination of gravity adjustment factor C for stability graph analysis (after Potvin, 1988)

2.3.3 Shape Factor, Hydraulic Radius and Radius Factor

The shape factor is frequently used in mine design and to quantify excavation surface geometry. The shape factor is another word for hydraulic radius (HR). The hydraulic radius (HR) term was initially used in fluid dynamics to relate fluid flow in square pipes to flow in circular pipes, and has been used in empirical design techniques since 1977

(Laubscher). The HR is calculated by dividing the area of a stope surface by the perimeter of that surface.

$$HR = \frac{\text{Area of the Surface}}{\text{Perimeter of the Surface}} \quad (2.31)$$

Radius factor (RF)(Milne, 1997) is another term used to quantify the geometry of the wall of an opening. RF is a parameter that is a function of the average distance from the centre of a wall to the abutments.

RF is expressed as:

$$RF = \frac{0.5}{\frac{1}{n} \sum_{\theta=1}^n \frac{1}{r_{\theta}}} \quad (2.32)$$

where:

r_{θ} = distance from any point within a surface to the abutments at angle θ , and

n = number of rays measured to the surface edge.

The hydraulic radius and radius factor terms have been successfully related to stope stability and dilution (Milne, 1996; Clark, 1997; 1998). For a circular surface, the RF equals HR. The RF is about 1.1 times of HR for a square surface, due to the increased distance to the abutment in the corners (Milne, 1996).

2.3.4 Empirical Stability Graph Design Methods

Except for Pakalnis' dilution design approach, which uses Rock Mass Rating (RMR) as the rock mass quantification parameter, most empirical stability and dilution design approaches use a stability number N or modified stability number N' , which is based on the NGI Q classification. The N' value includes a stress factor, a joint orientation

factor, and a gravity factor. It is plotted against an excavation surface geometry factor HR (Hydraulic Radius). These design methods are empirical techniques to graphically estimate the stability of the walls of underground openings based on the rock mass classification parameters, stress condition and surface geometries.

The stability graph method for open stope design was initially proposed by Mathews et al. (1981). This method uses a stability number N to determine stable excavation dimensions. A graph relating the stability number (N) versus shape factor (S) or hydraulic radius (HR) was presented delineating zones of “Potentially Stable,” “Potentially Unstable,” and “Potentially Caving” (Figure 2.12).

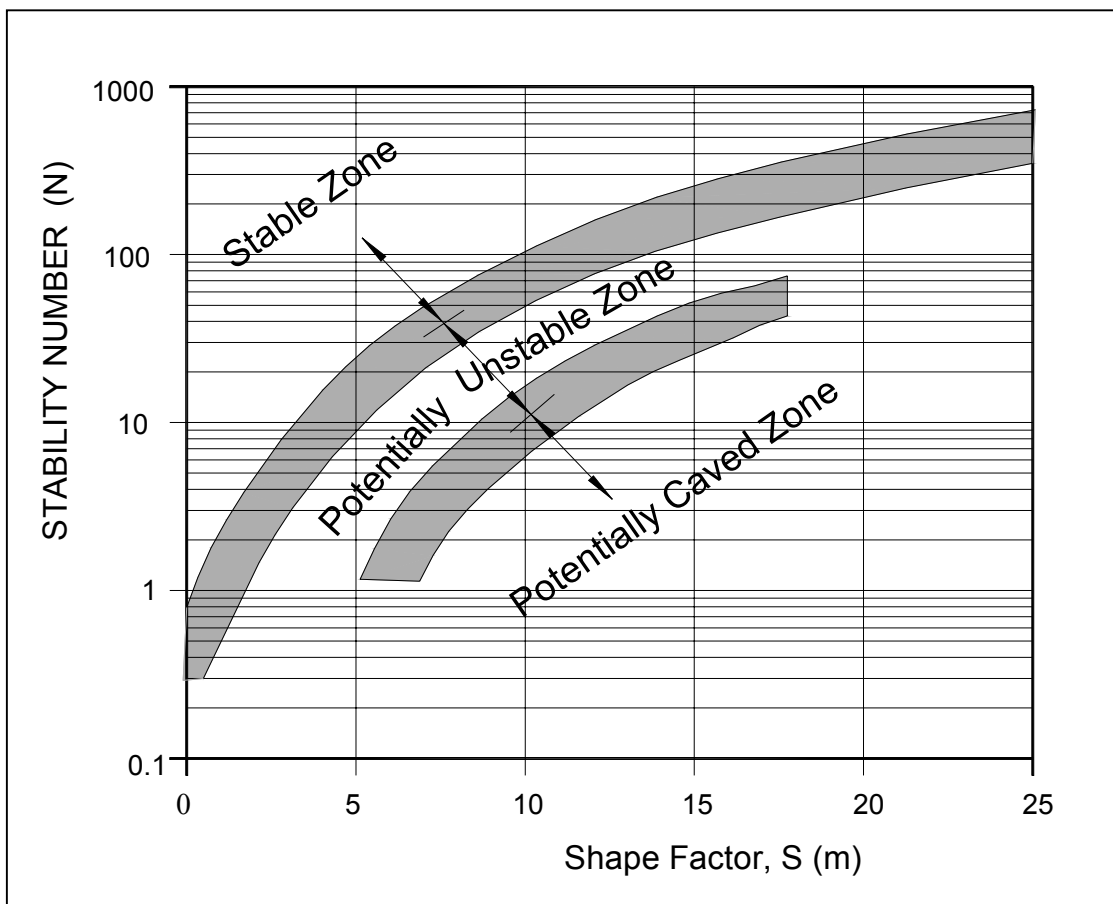


Figure 2.12 Mathews Stability Graph (after Mathews et al., 1981)

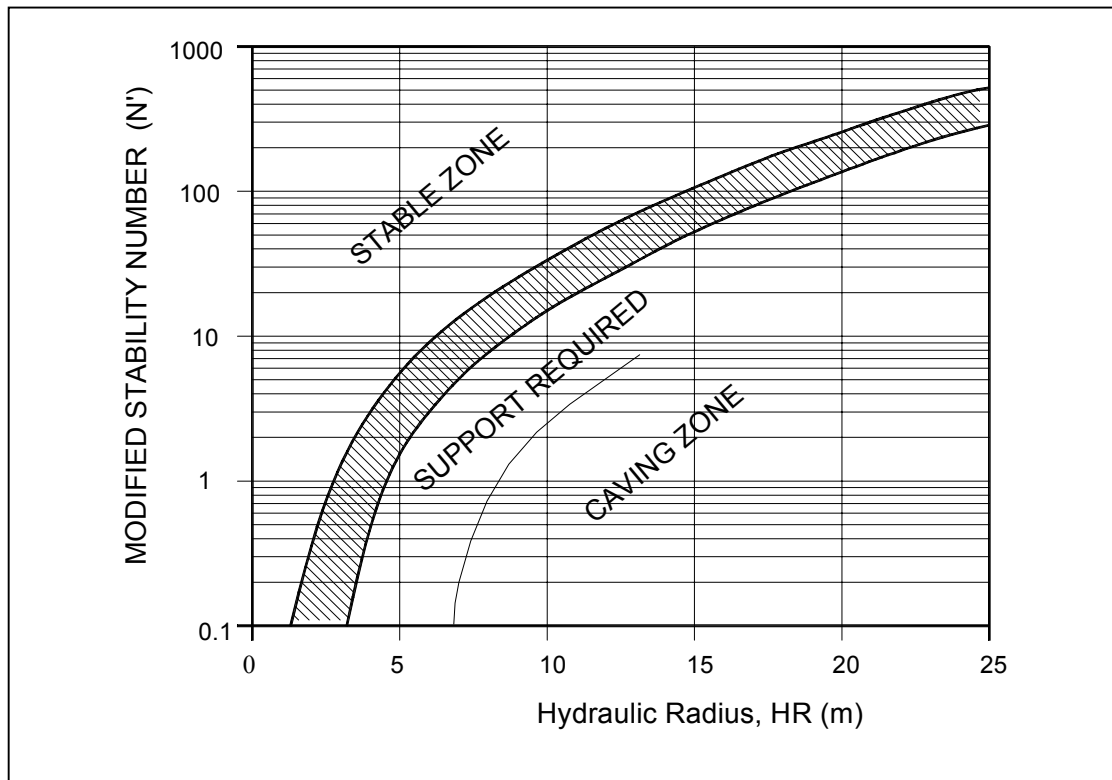


Figure 2.13 Modified stability graph (after Potvin and Milne, 1992)

Potvin (1988) modified Mathews design method by using 242 case histories (176 unsupported, 66 supported) and by redefining some of the adjustment factors, which resulted in the use of a modified stability number N' . Potvin's modified method has become known as the modified stability graph method (Figure 2.13). The influence of cable bolt support was re-examined by Potvin & Milne (1992) and by Nickson (1992) who added additional 59 case histories to the database and, reanalysed the support required for based on statistics. Two new cable bolt design zones were introduced (Figure 2.14).

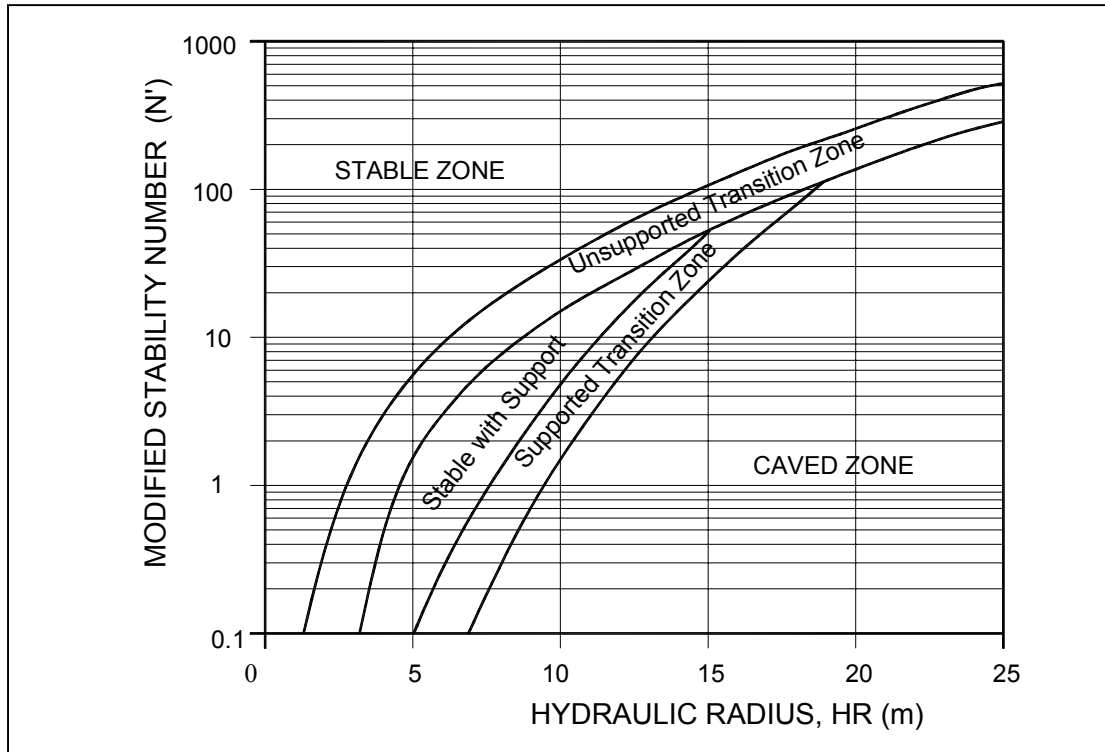


Figure 2.14 Modified stability graph with support (after Nickson, 1992)

A drawback to the stability design methods is the use of qualitative terms such as stable, unstable and caved to describe the various design zones. These zones cannot be quantified in terms of the degree of dilution. There are some limitations when using the stability design methods which include:

- The qualitative descriptions of slope stability only provide a general indication of dilution,
- Some important factors that may affect open slope stability and dilution are ignored such as undercutting of slope walls, drilling and blasting. The stress factor is also poorly accounted for, and,
- Slope width is not taken into account. “Stable” for a 10 m wide slope may be acceptable from a dilution perspective. For a 3 m wide slope, in which a small amount of slough can significantly dilute the ore, the same “stable” description may not be appropriate.

2.3.5 Empirical Dilution Design Methods

Pakalnis (1986) developed a dilution approach based on case histories from the HBMS Ruttan Mine (Figure 2.15). It differs from other methods in that an estimate of sloughing or dilution is given in percent rather than as a stable or unstable assessment. This method is not used by industry. However, it is an early attempt to quantify dilution. Clark (1998) developed a new dilution design method based on the format of the modified stability graph and expressed the slope stability as a dilution estimate. A new term called ELOS (Equivalent Linear Overbreak/Slough) is used to quantify dilution in the design. The ELOS is defined as the average depth of overbreak or slough from the slope wall of concern. The design was based on 47 open slope case histories from 6 different Canadian mines. The dilution design uses three nearly parallel curves to quantify the possible dilution in terms of metres of ELOS. Four zones are presented: $ELOS \leq 0.5$ m, $0.5 < ELOS \leq 1.0$ m, $1.0 < ELOS \leq 2.0$ m and $ELOS > 2.0$ m. The dilution graph is given in Figure 2.16. The dilution design method is a great improvement for open slope dilution estimation; however, neither dilution design method specifically considers the influence of stress, undercutting, drilling and blasting or time.

2.4 Numerical Design Methods

With advances in numerical modelling methods and computer technology, numerical modelling has become a powerful tool for underground opening design. Two general categories of numerical methods available for underground excavation design include differential methods and integral methods. Finite element methods (FEM) and boundary element methods (BEM) are the most common methods for these two categories, respectively. Both 2D and 3D commercial computer programs are available such as Examine 2D (2D Boundary Element Code, Curran & Corkum, 1994), Phases (Finite Element Code, 2D, Carvalho et al., 1991), Map3D (Wiles, 1995) and Examine 3D (Curran & Corkum, 1993)(both are 3D Boundary Element Codes). All these programs can be used for determining induced stresses around underground

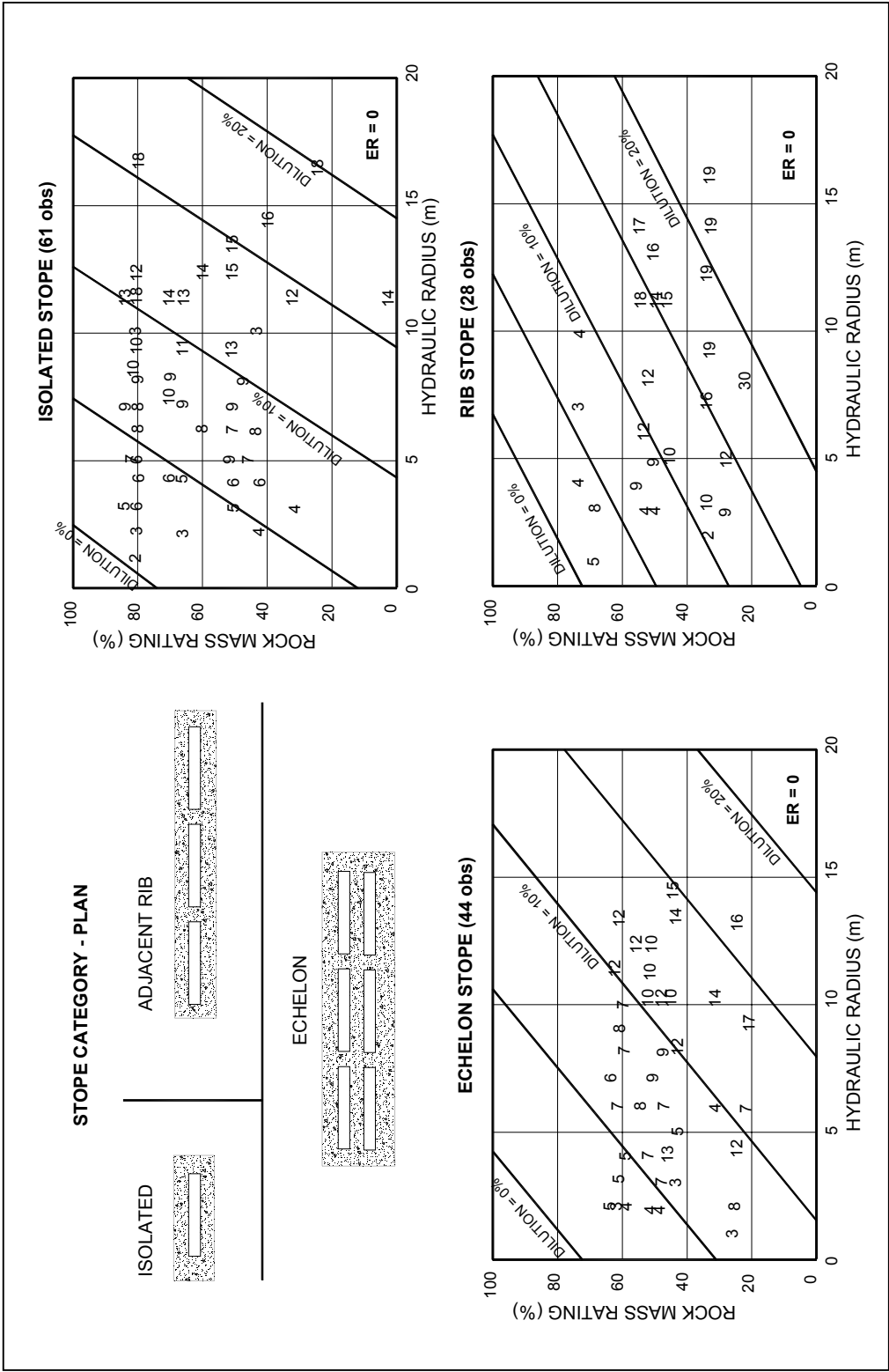


Figure 2.15 Empirical dilution approach (after Pakalnis, 1986)

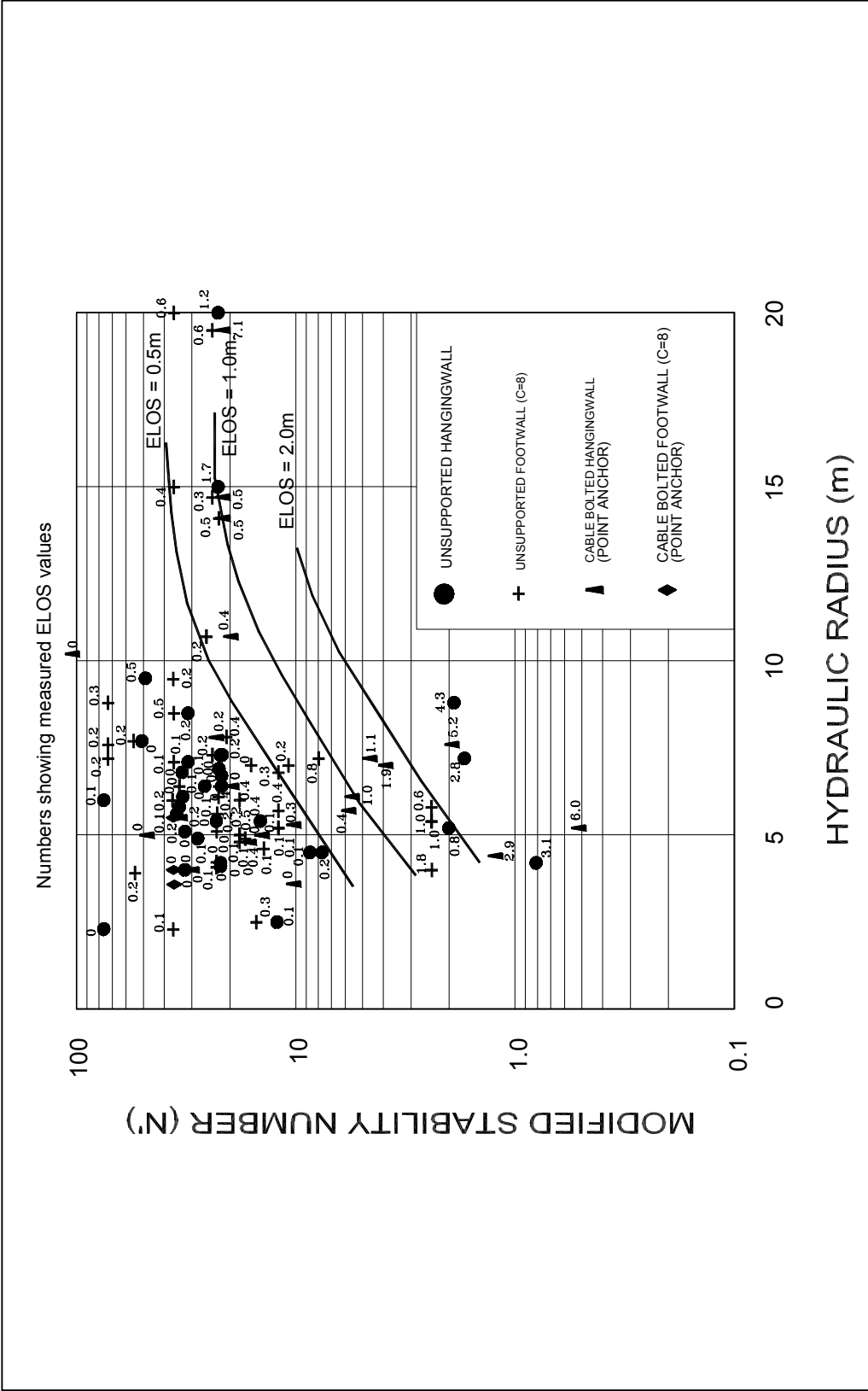


Figure 2.16 ELOS dilution design method (Clark, 1998)

excavations. Failure criteria, as discussed in Section 2.2, are usually coupled with stress analysis to provide an estimate of stability.

Numerical modelling can be used to assist open stope stability and dilution studies by analysing the induced stress state (e.g., high induced stress failure or gravity failure due to stress relaxation).

The following sections briefly discuss the finite element methods (FEM) and boundary element methods (BEM), along with their advantages and disadvantages.

2.4.1 Finite Element Methods (FEM)

The solution of differential equations, implemented using finite element methods, essentially involves dividing the problem domain into small finite ‘elements’ of various shapes (triangles or rectangles in 2D cases and tetrahedrons or ‘bricks’ in 3D cases) held together at the ‘nodes’ which are the corners of elements (Pande et al., 1990). The problem then may be solved based on approximations to the connectivity of elements, and continuity of displacements and stresses between elements (Brady & Brown, 1993), together with its boundary conditions, and to the satisfaction of both compatibility and equilibrium constraints.

The advantage of the FEM is that non-linear and heterogeneous material properties may be readily accommodated. Each element can have different material properties.

The major disadvantage of the FEM is that the outer boundary of the problem domain is defined arbitrarily, and discretisation errors occur throughout the domain. Considerable work is required in preparing data for a problem. This is particularly crucial in 3D problems. In general, for simple isotropic, homogeneous materials, the FEM requires more computation time than the BEM.

2.4.2 Boundary Element Methods (BEM)

The boundary element method solves problems in stress in terms of surface values of the field variables of traction and displacement (Brady & Brown, 1993). As its name suggests, only the problem boundary is defined and discretised. Two types of the BEM exist – direct boundary element methods and indirect boundary element methods. The direct boundary element method uses the weighted residual approach to obtain the governing equations to formulate boundary elements (Gipson, 1987). The indirect boundary element method uses fictitious stresses on the boundary to formulate boundary elements (Crouch & Starfield, 1983). Direct boundary element methods are used to solve limited, simple problems (i.e., half plane problems in civil engineering and beam problems in structural engineering). For underground excavations, the indirect boundary element method (fictitious stress method) is widely used. 3D (Examine 3D, Curran & Corkum, 1993) and 2D (Examine 2D, Curran & Corkum, 1994) boundary element programs were used in this research. More details concerning the fictitious stress method used by these programs are given in Appendix I.

The advantage of the BEM is that it models the far field boundary condition correctly, restricts discretisation errors to the problem boundary, and ensures a fully continuous variation of stress and displacement throughout the whole medium (Brady and Brown, 1985). The method is very efficient in computing time. The disadvantage is that its advantages are largely restricted to application involving linear and homogeneous materials (Crouch & Starfield, 1983).

The accuracy of numerical design is dependent upon the input parameters. Unlike man-made engineering materials such as steel, rock material properties vary widely. Consequently, defining the correct input parameters for a jointed rock mass is often difficult in modelling underground excavations in rock masses. The stress state around an opening is closely related to the opening size, geometry, and adjacent openings rather than the rock mass strength properties. If reasonably representative rock mass properties assumptions can be made, numerical modelling can be used for open stope

stress simulation. A failure criterion must then be applied before numerical modelling can be considered a design approach.

2.5 Summary

Analytical design methods concentrate in two areas: stress driven failure and gravity driven failure. Stress driven failure analysis studies the interaction between stress and strength of the material. This approach assumes that when the magnitude of an applied stress exceeds the strength of the material, failure will occur. Good examples of stress driven failure design methods are the Mohr-Coulomb failure criterion for intact material and the Hoek and Brown failure criterion for rock masses. In open stope mining, the pillars between stopes and the abutments of the stope hanging wall and footwall are usually places of high stress concentration. These failure criteria can be used to analyze the stability of pillars and the abutments. Gravity driven failure concerns failure due to the influence of gravity. Gravity driven failure design methods include kinematic analysis, beam theory, plate theory, and Voussoir arch beam theory. The kinematic analysis method is used for specific cases of structurally controlled failure or wedge failure. Beam theory, plate theory, and Voussoir arch theory were developed for civil engineering. Due to limiting assumptions upon which these methods are based, the irregular nature of a rock mass (that make it difficult to estimate input parameters), and the characteristics of open stopes, it is difficult to apply these approaches to open stope stability analysis.

The empirical open stope stability and dilution design methods are widely used by many mines. Both stability design methods and dilution design methods account for rock mass properties, gravity, and open stope geometry, but poorly account for stress effects on open stope hanging walls. They also ignore some factors that may have a significant influence on open stope stability and dilution such as undercutting, blasting, stope hanging wall curvature, etc.. The purpose of this research is to quantify the influence of stress, undercutting and blasting on open stope stability and dilution. The influence of exposure time is also assessed in the study.

Numerical modelling plays an important role in open stope hanging wall stability and dilution design. Stress relaxation is recognized as one of the major causes of open stope hanging wall instability and dilution, and numerical modelling methods provide the means for estimating the zone of relaxation. The difficulty in defining and obtaining realistic rock mass input parameters, however, makes numerical design methods often difficult to implement. For this reason an empirical design approach has been chosen, in conjunction with limited stress modelling, to assess stope hanging wall dilution at operating mines. The next section provides some background on the mining operations used for the data collection.

CHAPTER 3

BACKGROUND ON FIELD SITE DATA

3.1 Introduction

Mining case histories played an important role in the research conducted. Field data was collected from Hudson Bay Mining and Smelting Co. Ltd (HBMS) mines and a comprehensive database was established for the study. This chapter provides the basic information on mining, geology, and rock mass classification from which the database was derived.

Mining case histories were collected from Cavity Monitoring System (CMS) surveyed stopes at Callinan Mine, Trout Lake Mine and Ruttan Mine. The CMS is a laser survey instrument that can be extended into an open stope on a long boom to obtain the actual open stope profile. The CMS is described at the end of this chapter.

All three mines are operated by HBMS and all use the open stope mining method. Callinan and Trout Lake mines are located in the Flin Flon area. Callinan Mine is located about 1km north of the Flin Flon town centre and Trout Lake Mine is located about 5km northeast of the town. Ruttan mine is located in northern Manitoba, 760km north of Winnipeg and 20km east of the town of Leaf Rapids. Figure 3.1 shows the mine location map. This chapter gives basic background on the mine sites studied.

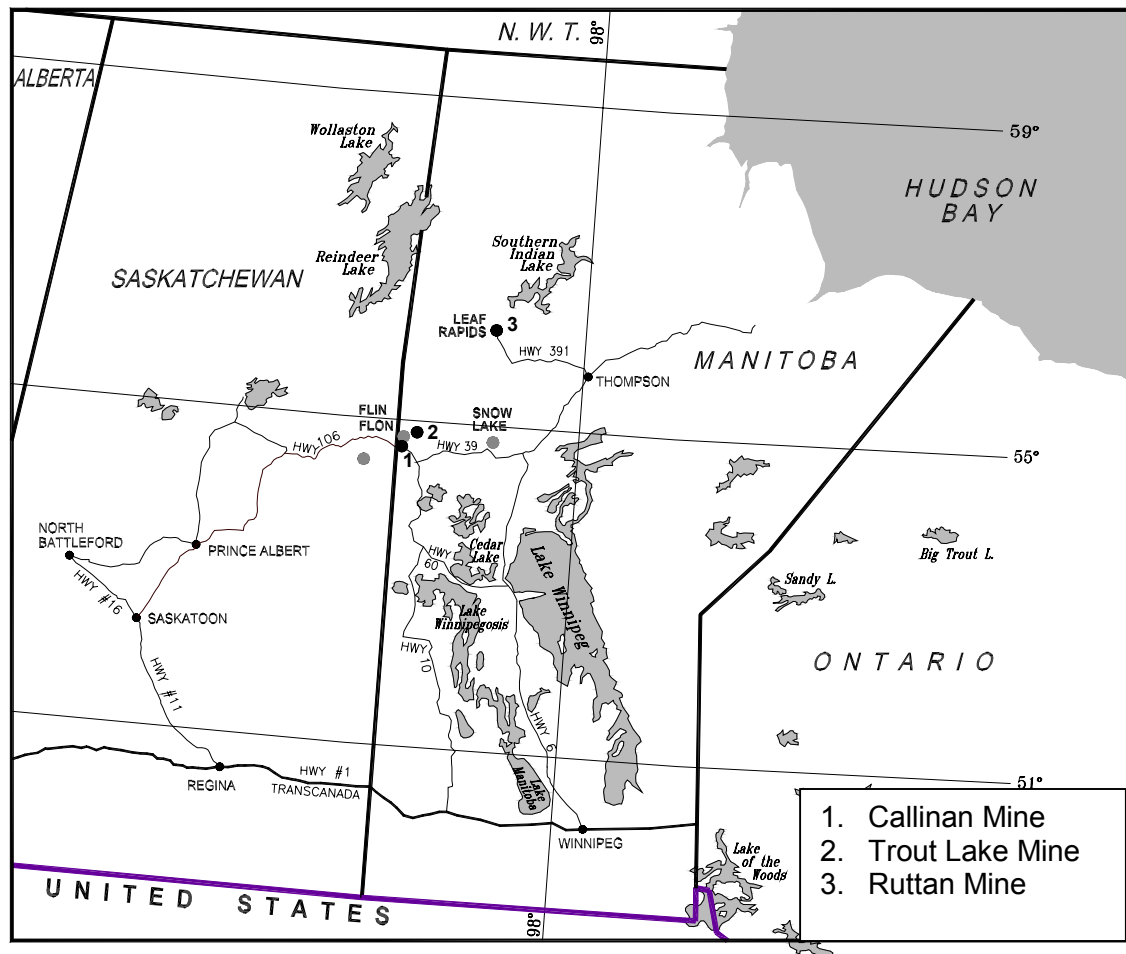


Figure 3.1. Mine location map

3.2 General Mine Information

3.2.1 Trout Lake Mine

The Trout Lake volcanogenic massive copper-zinc sulphide deposit was discovered in 1976 (Syme and Bailes, 1993). Production at the mine began in 1981 under a joint venture involving HBMS, Granges Exploration and Manitoba Mineral Resources, with mining occurring in two main ore zones, the “north” zone and “south” zone (Willet, 2002). Initial mining was carried out using the cut-and-fill method. As mining depth increased, the mine production was switched to open stope mining. During the period of database collection, the ore was extracted by longhole blasting and the stopes were filled after mucking (excavating).

3.2.2 Callinan Mine

The Callinan ore body is a typical volcanogenic massive sulphide-type copper-zinc deposit (Syme and Bailes, 1993). The ore body was discovered by diamond drilling from the Flin Flon Mine in the early 1980's and production started in 1990. The Flin Flon Mine is about 1.5km south of the Callinan Mine and it started in 1930 and closed in 1992. The mine uses open stoping methods. Similar to Trout Lake Mine, the Callinan Mine ore is extracted by longhole blasting and the stopes are filled after they are mucked out.

3.2.3 Ruttan Mine

The Ruttan Mine ore is a multiple lens, steeply dipping ($\sim 70^\circ$) en-echelon copper-zinc deposit (Pakalnis, 1986). At the time of data collection, the mine was preparing to close and mine production was conducted by mining the remaining pillar stopes. The mine used open stoping with delayed backfill. Due to the short mine life remaining, few case histories were included in the database for this research.

3.3 Geology

3.3.1 Regional Geology

The Callinan and Trout Lake deposits are located within the Flin Flon-Snow Lake Volcanic Belt (Ko, 1986) (Figure 3.2). This area in northern Manitoba and Saskatchewan is one of the most productive base metal regions in Canada. Since 1912, as many as fifteen economic deposits have been discovered in this belt. The Callinan and Trout Lake ore bodies are typical volcanogenic exhalative massive sulphide-type copper-zinc deposits and are associated with episodes of rhyolitic magmatism in the otherwise basalt dominated stratigraphy (Syme and Bailes, 1993). The deposits comprise a number of stacked or en-echelon concordant massive sulphide lenses underlain by stringer sulphides. The deposits are conformable to the host stratigraphy.

The ore zones in both mines vary from 2 to over 20m in thickness. The Trout Lake ore body is generally steeper dipping (65° to 70°) than the Callinan deposit (40° to 55°).

The Amisk and Missi Groups outcrop in the Flin Flon area. The Amisk Group volcanic arc strata are composed of a thick (7000m) sequence of massive to pillowed basalt and andesite flows associated with greywackes, and mudstones (Stauffer, 1990). The Amisk strata are unconformably overlain by the Missi Group which comprises a thick (3000m) sequence of continental (alluvial and fluvial) sediments (sandstones to conglomerates)(Stauffer, 1990).

The following information was taken from Syme and Bailes (1993). At Callinan and Trout Lake mines, the dominant rock assemblage comprises a thick sequence of massive to pillowed mafic flows and pyroclastics. These are overlain by massive rhyolite flows and sericitized quartz-phyric fragmental rhyolites that are intruded by sills and dykes ranging in composition from quartz-phyric diorite to gabbro. The ore host rock is a sericitized quartz-phyric fragmental rhyolite. This thick rhyolite unit constitutes the hanging wall and footwall. The massive sulphide ore is underlain by a disconformable chloritic hydrothermal alteration zone developed in the footwall. These units trend northwest-southeast and dip 50°-60° to the north-east.

Much of the following was taken from Speakman et al. (1976). The Ruttan orebody is a copper-zinc rich massive sulphide deposit contained within a sequence of proterozoic volcanic rocks and their derived sediments. Ruttan is located within the Snow Lake belt of Manitoba. This geologic province is characterized by two east-west trending volcanic arc belts, the Wasekwan Group to the north and the Amisk Group to the south. The Wasekwan Group consists of a conformable sequence of volcanic flows, tuffs, agglomerates, breccias and volcanoclastic sediments. Overlying this package of rocks are the shallow water sediments of the Sickle Group.

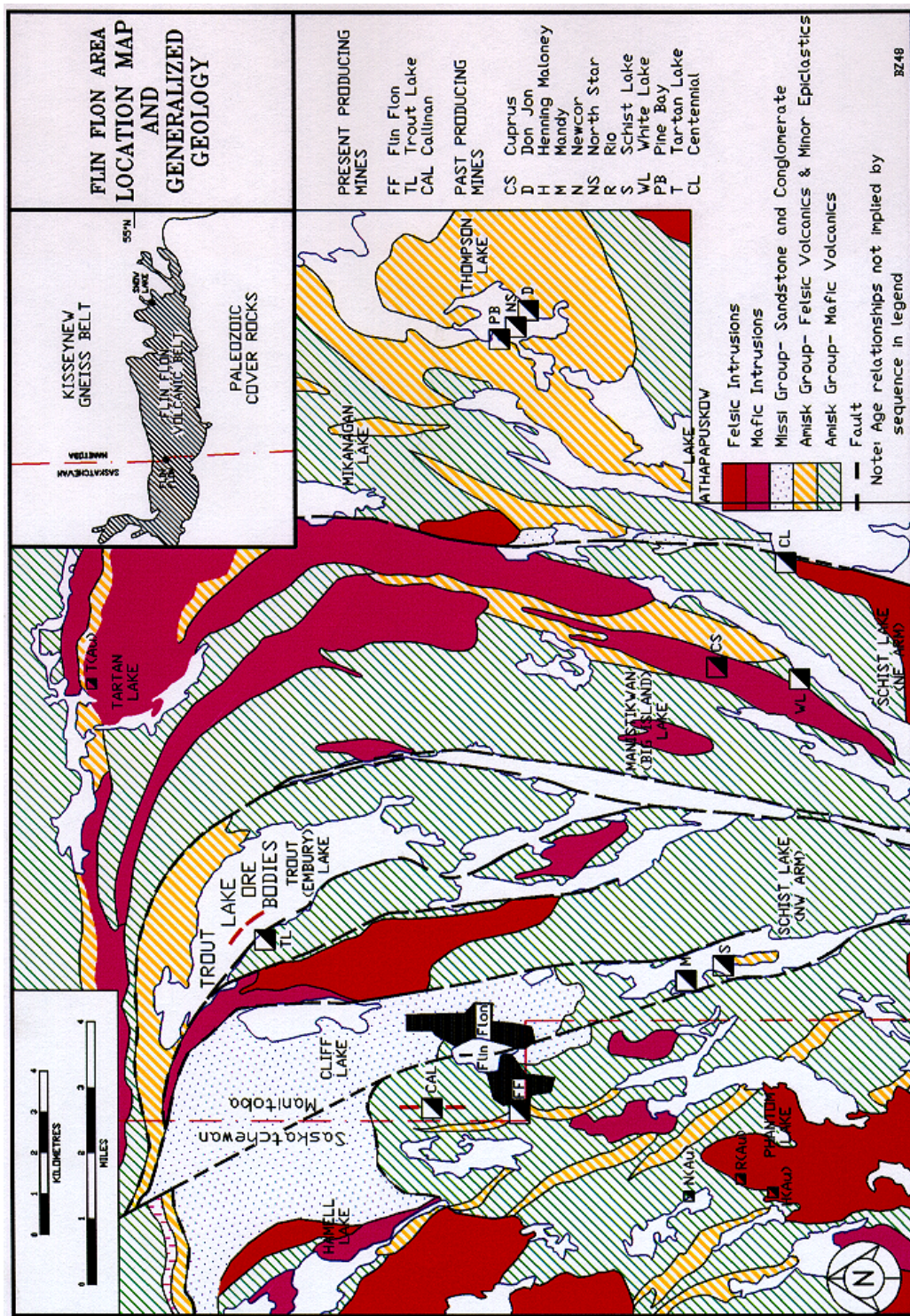


Figure 3.2. Generalized regional geology of the Flin Flon area (from Ko, 1986)

3.3.2 Mine Geology

The geology in the immediate stope hanging wall exercises a controlling influence on the stope hanging wall and dilution. The presence of weak alteration material such as chlorite, sericite and other weak material significantly decreases the rock mass strength and increases the potential for hanging wall dilution.

a). Callinan Mine

Much of the Callinan Mine geology information was taken from Anon (1990). The Callinan ore deposit straddles the Manitoba - Saskatchewan border and is conformable with the host stratigraphy, which strikes to the north and dips to the east. The ore body consists of multiple lenses of massive sulphide hosted in three distinct zones (south, east and north). These lenses are hosted in two distinct quartz phyric rhyolites. The upper, or Flin Flon Mine horizon, and the lower felsic units, are separated by approximately 100m of intermediate basalt flows and breccia. Each felsic unit hosts several lenses.

The south zone lies within the lower felsic unit. The sulphide lenses generally occur towards the stratigraphic top of the rhyolite. The hanging wall often has chlorite talc schist alteration and the footwall rocks are locally sericitized. This weak alteration interval significantly weakens the overall hanging wall strength. The sulphide lenses are dominated by fine-grained pyrite. The lenses appear massive, with no significant zoning. The upper quartz phyric felsic unit contains the lenses of the North and East Zones, and varies from 6 to 91m in thickness. Both zones exhibit similar characteristics, and the ore lenses dip between 40° and 60° (Figure 3.3).

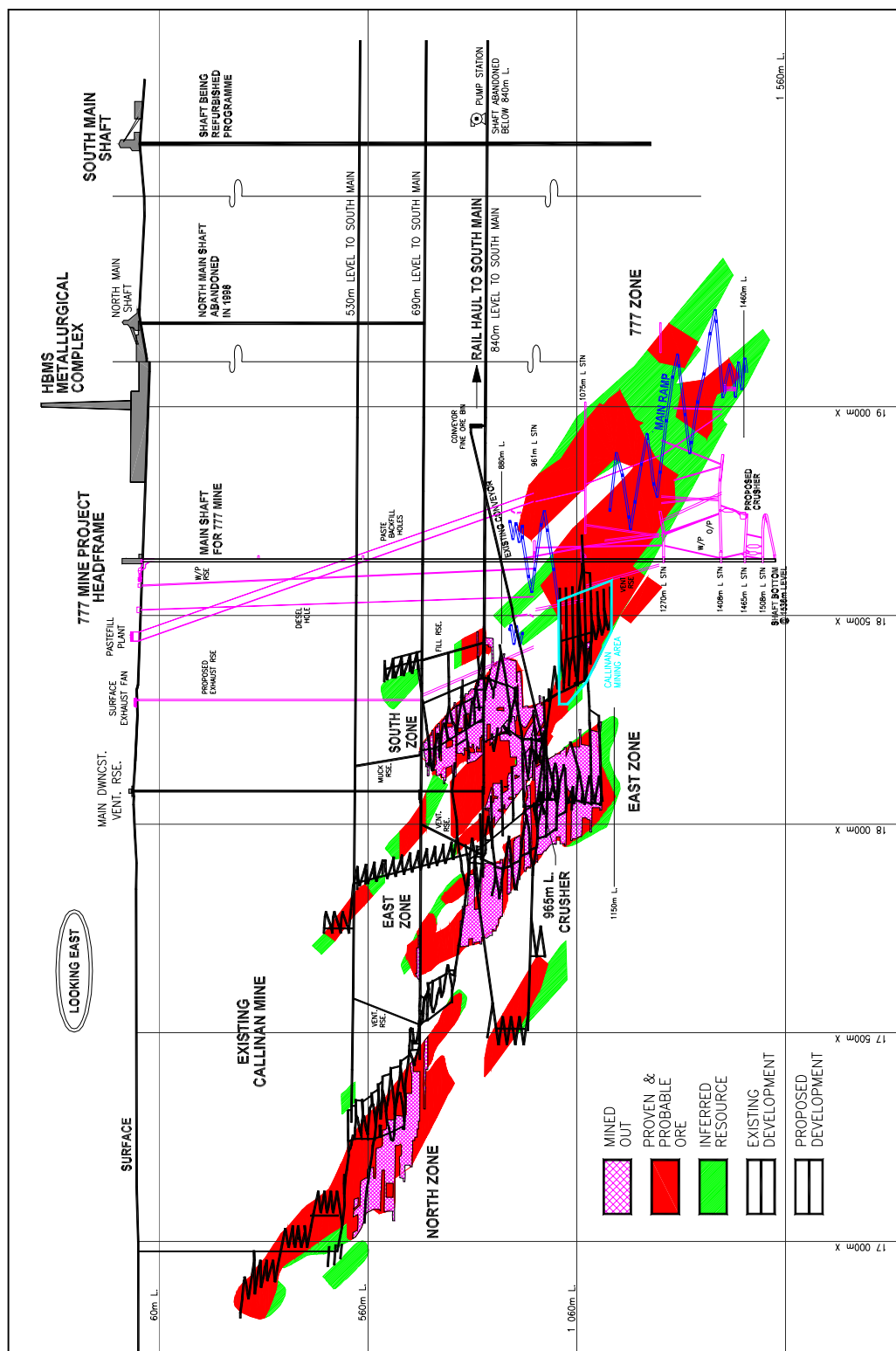


Figure 3.3. Longitudinal view of the Callinan Mine orebody (HBMS, 2001a)

b). Trout Lake Mine

The Trout Lake deposit subcrops beneath 20 to 40m of water and overburden below Trout Lake (Figure 3.4). The following geology summary has been taken from Graaf (1998a). The Trout Lake copper-zinc sulphide deposit comprises massive and stringer sulphides, which occur within the following generalized stratigraphic sequence (from top to bottom):

- Intrusive Rocks
- Hanging wall Graphitic Argillite >600 meters
- Hanging wall Sericitized Quartz-Phyric Fragmental Rhyolite 40-100 meters
- Mafic Flow 10-50 meters
- Host Sericitized Quartz-Phyric Fragmental Rhyolite 140-210 meters
- Footwall Graphitic Argillite 90-130 meters
- Rhyolite Flow >180 meters

The rhyolite flow is a massive homogeneous unit. It is moderately foliated and cut by numerous joints and quartz-carbonate veins. The contact with the overlying graphitic argillite is sharp. The footwall graphitic argillite is a black, fine grained, laminated, sheared rock. The host sericitized quartz-phyric fragmental rhyolite (locally called quartz porphyry) has sharp contacts with the underlying footwall graphitic argillite and the overlying mafic flow. The andesitic, mafic flow is located about 20 to 50m above the ore zone. It separates the overlying hanging wall quartz porphyry (rhyolite) from the host unit. The hanging wall quartz porphyry is barren, but otherwise very similar to the host unit above the ore zone. The hanging wall graphitic argillite is very similar to the footwall graphitic argillite. In the mine area, several sills and dykes ranging from diorite to gabbro intersect the volcanic strata. The intrusives trend northwest and are 10-15m thick near the ore zones.

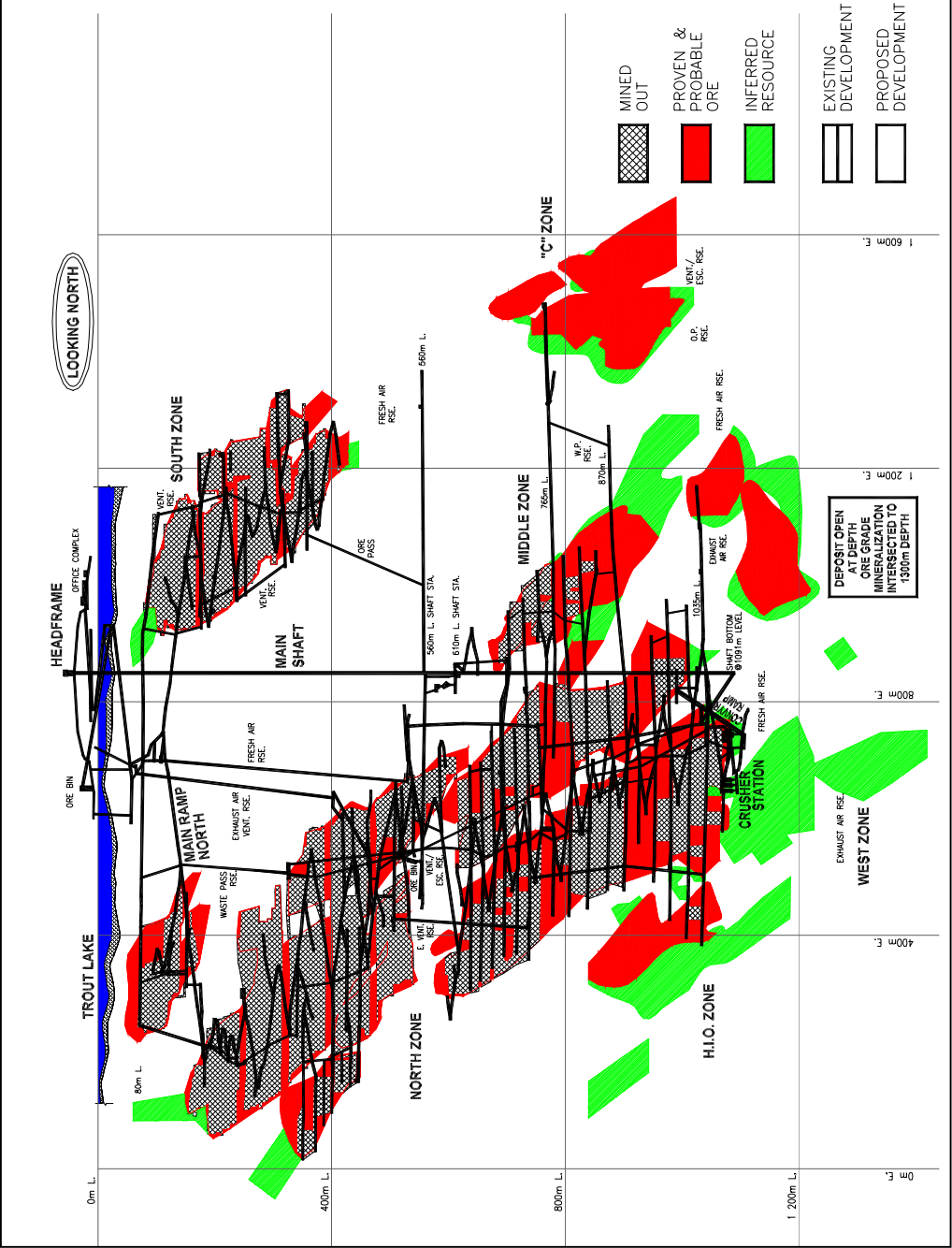


Figure 3.4. Longitudinal view of the Trout Lake Mine orebody (HBMS, 2001b)

The orebody is parallel to the stratigraphy, has a very sharp contact with the hanging wall rock and a diffuse contact with the footwall altered rock (chloritized quartz-phyric, fragmental rhyolite and chlorite schist) within the host rhyolite. Shearing and folding from dynamic metamorphism deformed the ore body laterally and vertically into its irregularly pinching and swelling shape.

c). Ruttan Mine

The Ruttan mine orebody comprises nine ore lenses all subparallel in attitude and en-echelon in nature (Pakalnis, 1986). The orebody strikes N70°E, dips 70°SE and plunges 70° to the east. The maximum dimensions of the ore zone are 120 metres wide by 700 metres long. An abandoned open pit lies immediately above the underground workings to a depth of 210 metres. Figure 3.5 shows the longitudinal view of the Ruttan Mine orebody. Ruttan Mine was closed in May 2002.

3.4 Rock Mass Classification

3.4.1 Methodology

Rock mass site mapping and classification were conducted at Callinan and Trout Mines. The Ruttan mine rock mass classification data was obtained from the mine site rock mechanics engineer. At the Callinan Mine and Trout Lake Mine, rock mass mapping and classification was conducted in the ore lenses, in the overcut drifts and in the undercut drifts when access to stope hanging walls was available. The overcut and undercut drifts define the stope height and are made for stopes access. At the Ruttan mine, rock mass mapping and classification was done for each individual stope. At all three mines, the Q classification system was used. The Q classification system is described in Section 2.3.1.

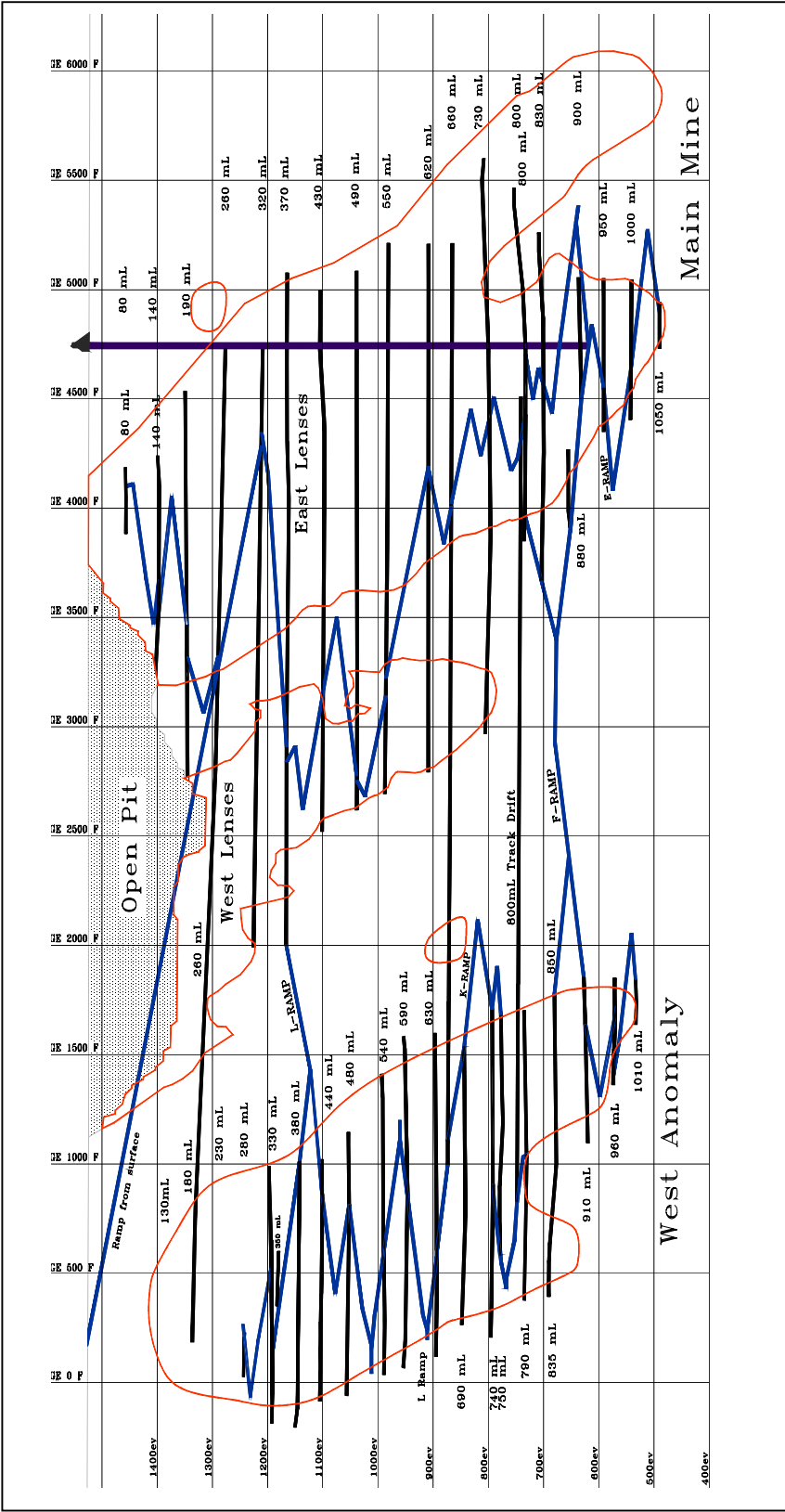


Figure 3.5. Longitudinal view of the Rutan Mine orebody (HBMS, 2001c)

The information collected and recorded from the rock mass mapping includes:

- rock type
- estimated strength of the intact rock, UCS, MPa
- measurements of joints strike direction and dip; spacing; JRC (joint roughness coefficient); amplitude per metre, and estimated numbers of joints per cubic metre
- estimating of joint set number, J_n
- estimating of joint set roughness, J_r
- estimating of joint set alteration number, J_a
- evaluating of joint water reduction factor, J_w

3.4.2 Joint Sets Information

Joint sets information is an important input parameter for rock mass classification. The rock joint characteristics on the stope HW were carefully mapped and recorded.

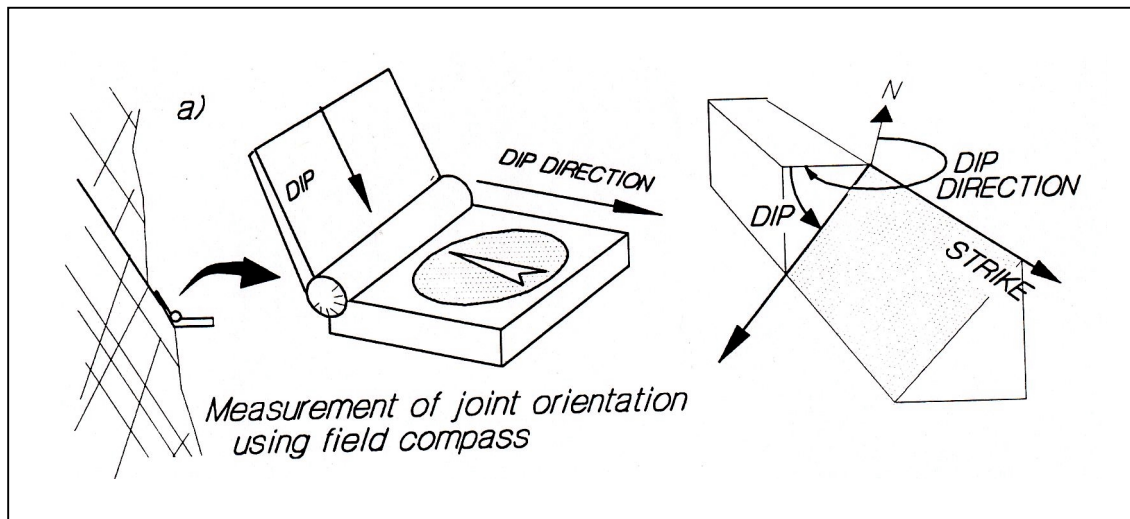


Figure 3.6 Illustration of joint set orientation mapping (from Hutchinson and Diederichs, 1996)

The major joint sets were firstly identified. A compass was used to record the orientation of joints in the HW (Figure 3.6). The average spacing of individual joint set, as well as the joint surface condition such as roughness, alteration and water conditions were recorded.

Figure 3.7 and Figure 3.8 show the stereonet plots of the major joints mapped from Callinan and Trout Lake mines, respectively. Trout Lake Mine has three major joint set plus some random jointings with one joint set parallel to the stope HW. Callinan Mine also has three major joint sets plus random with one set near parallel to the HW. The rock mass classification information at Ruttan Mine was supplied directly from site rock mechanics engineer. No joint orientation data are available for Ruttan Mine.

3.4.3 RQD Estimating

The RQD for the jointed rock mass was estimated from the number of joints present per cubic metre, called the Volume Joint Count, J_v . The RQD values were then calculated by the following equation (Palmström, 1985, 1995):

$$RQD = 115 - 3.3J_v \quad (3.1)$$

3.4.4 Joint Quantification Parameters, J_n , J_r , J_a , J_w , and SRF

The J_n (joint set number), J_r (joint roughness number), J_a (joint alteration number), J_w (joint water reduction number), and SRF (surface stress reduction factor) are joint quantification parameters and are used for the calculation of the NGI rock mass classification Q. These parameters were obtained during the site rock mass mapping and classifications by using Table 2.2 in Section 2.3.1.

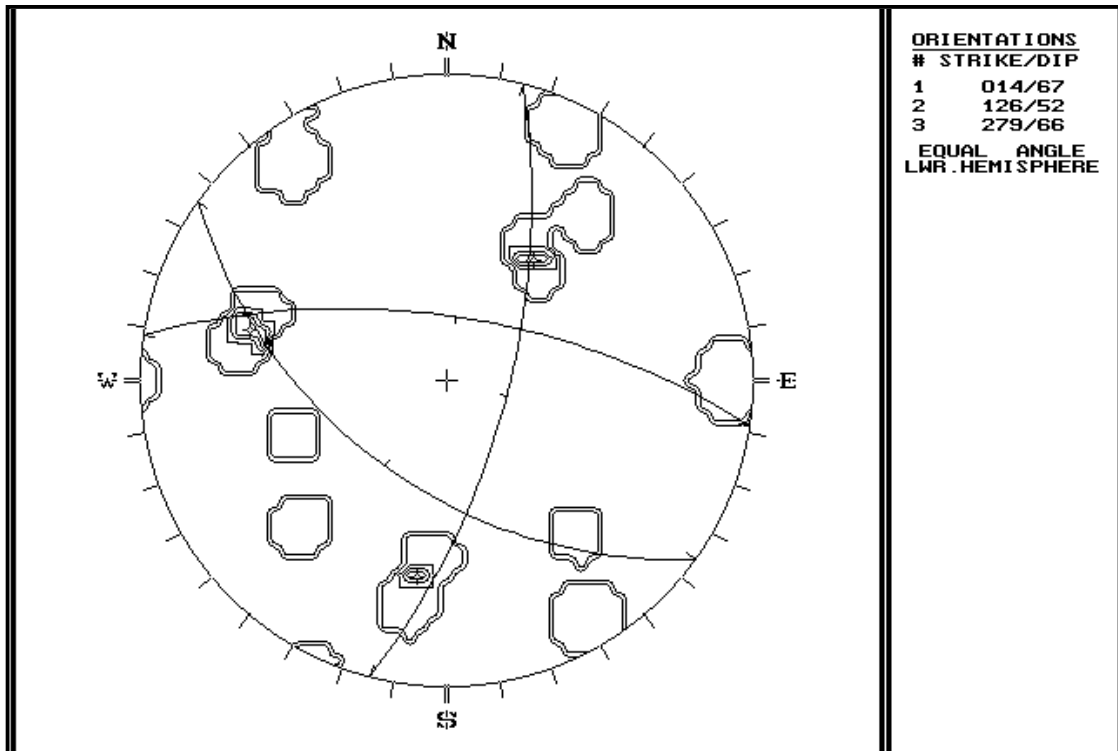


Figure 3.7 Trout Lake Mine major joints planes stereonet plot (14 observations)

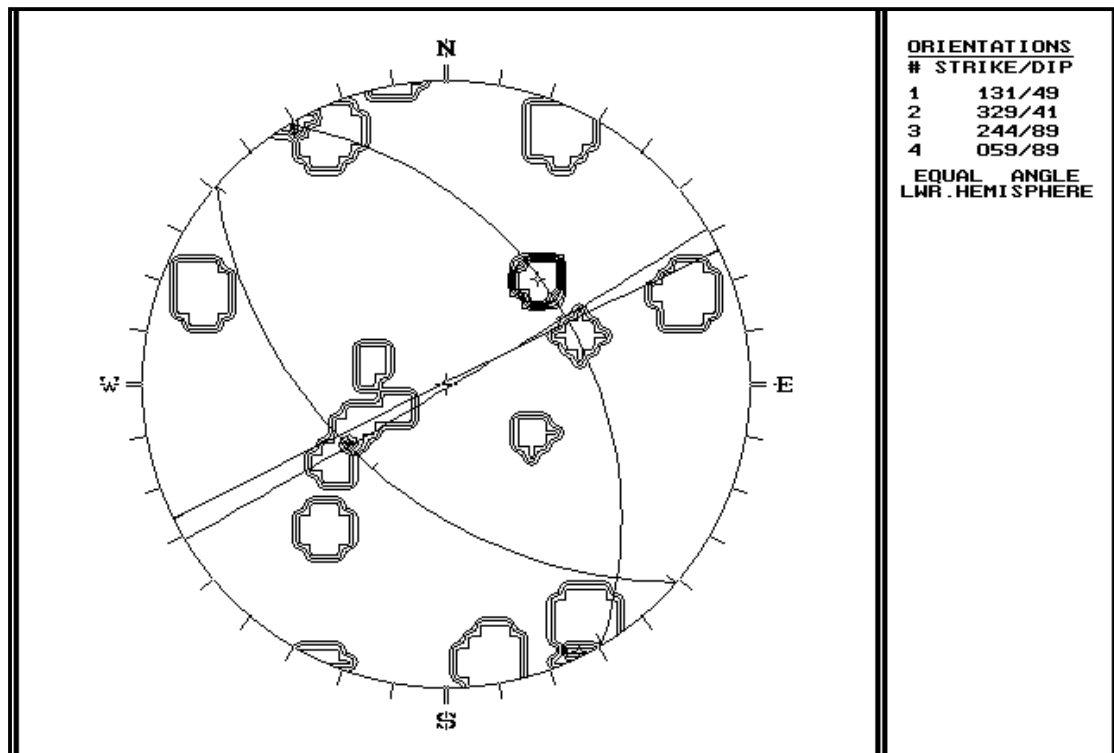


Figure 3.8 Callinan Mine major joints planes stereonet plot (15 observations)

3.4.5 NGI Q System Rock Mass Classification

Upon obtaining the stope HW rock mass classification parameters, the NGI Q classification number was calculated by using Equation 2.27. A detailed explanation of Equation 2.27 is given in Section 2.3.1.

$$Q = \left(\frac{RQD}{J_n} \right) \times \left(\frac{J_r}{J_a} \right) \times \left(\frac{J_w}{SRF} \right) \quad (2.27)$$

A rock mass classification recording sheet was used for recording data and for the calculation of Q. The RMR rock mass rating was also calculated. Figure 3.9 shows an example rock mass classification recording sheet. Mapping and classification work was conducted on site as part of this research.

Table 3.1 presents the rock mass classification values for each mine. In a few cases access was not available and mapping data were obtained from mine personnel (Mike Yao). These areas are indicated in Table 3.1. Generally, the Callinan Mine has better HW rock mass quality (Q' ranges from approximately 4 to 24), Trout Lake Mine has a poorer rock mass quality (Q' ranges from approximately 5 to 7) and the Ruttan Mine rock mass quality is between that of the Callinan and Trout Lake Mine (Q' ranges from approximately 4 to 15).


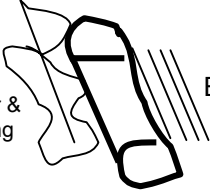
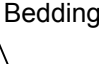
Rock Mass Classification Recording Sheet					
Site: 9292 HW		Collected by: J.W. & M. B.		Date: 1/06/00	
Description of sample area: Rebar support only. Holes have drilled for cable bolting. Bedding planes.					
Rock type		Strength		Sketch	
		~80Mpa			
Structure Data		Set A	Set B	Set C	Set D
Strike/Dip		120/55	20/65		
Average Spacing (m)		0.15	1		
JRC		8	14		
Amp/m		1.5cm	10cm		
Estimated No. of Joints/m ³		10			
RMR₇₆ Classification	Value	Rating	Q' Classification		
RQD	79	17	RQD		79
Intact Rock Strength	80	7	Joint Set No.		6
Joint Spacing	0.15	10	Joint Roughness No.		1.5
Joint Condition	S.R.	12	Joint Alteration		4
Water Conditions	Dry	10	Joint Water Reduction		1
			Stress Reduction		1
RMR		56	Tunnelling Quality Q		4.9
Other Notes: <div style="display: flex; justify-content: space-around; align-items: center; margin-top: 20px;">  <div style="text-align: center;">  <p>Shear & Folding</p> </div> <div style="text-align: center;">  <p>Bedding</p> </div> </div>					

Figure 3.9 Example rock mass classification recording sheet

Table 3.1. Rock mass classification at Callinan, Trout and Ruttan Mines

Mine	Lens	Stope Mapped	Rock Type (HW)	RQD	Jn	Jr	Ja	Q'
Trout Lake Mine	C#2	765C2-2	Sh'd QP Rhy	85	6	1.5	4	5.3
	#5	Mike Y.	Talc Chl Sch	87	9	1.5	2.3	6.3
	#7	950HIO	Arg. Rhy	72	6	1.5	3	6.0
	#8	9285	Chl. Frag. QP Rhy	88	9	1.5	2	7.3
	#9	7891	Chl. Frag. QP Rhy	75	9	1.5	2	6.3
	#9	9291	Chl. Frag. QP Rhy	82	6	1.5	4	5.1
	#9	9292	Chl. Frag. QP Rhy	79	6	1.5	4	4.9
	#10	Mike Y.	Gr. Arg. Rhy-Sil QP	87	9	1.5	2	7.3
	#11	92112	Sh'd QP Frag. Rhy	82	6	1.5	4	5.1
	#12	92124	Ser. QP Rhy	87	6	1.5	4	5.4
Callinan Mine	North	545-3N	Dio/QP	89	6	2	2	14.8
	EHW #1	825mL	Dio	85	6	2.5	1.5	23.6
	EHW #2	825mL	QP	78	6	2	1.5	17.3
	EHW #5	825mL	Dio	93	6	2	1.5	20.7
	E HW #7	910C74	Qp	85	6	1.5	1.5	14.2
	East	CM Data	QP/Dio	80	9	2	1	17.8
	777 #1 lens	1080mL	Frag. QP, Tuff, Sh'd QP	84	9	1.5	2	7.0
	777 #2 lens	1100-11 , 1080-11	QP, Chl, Schist	69	9	1.5	3	3.8
Ruttan Mine	WA2	630-4B2	Rhy,Sed,Sch	85	6	2.5	3	11.8
	WA2	540-12.5B	Intru, M.Sulp, chl/talc sch	80	9	1	1	8.9
	WA1	440-0B2	Rhy, Intru, M.Sulp	83	6	1.5	2	10.4
	MM3	1050-29J6		84	6	1.5	2.5	8.4
	MM2	550-28JS	Rhy, Sed, Intru, Sch	87	6	1.4	2.8	7.3
	WA1	440-1B2	Rhy, Sed, Intru	80	6	1.5	5	4.0
	WA2	590-14B	Intru, Chl/Talc Sch	92	6	2	2	15.3
<p>Notes:</p> <div> <div>Arg. = Argillite</div> <div>Chl = Chlorite</div> <div>Dio = Diorite</div> <div>Frag = Fragmented</div> <div>Gr = Grey</div> <div>Intru = intrusive</div> <div>M.Sulp = massive sulphide</div> </div> <div> <div>QP = Quartz Phyric</div> <div>Rhy = Rhyolite</div> <div>Sch = Schist</div> <div>Sed=Sediments</div> <div>Ser = Sericite</div> <div>Sh'd = Sheared</div> <div>Sil = Siliceous</div> </div>								

3.5 Quantifying Dilution with the Cavity Monitoring System

Since the development of the Cavity Monitoring System (CMS), dilution has become a quantifiable parameter that can be used as an indicator of design efficiency. The foundation of the dilution analysis is based on the ability to obtain accurate dilution information. The development of the Cavity Monitoring System (CMS) has made this possible. For this study, the empirical database was established based on CMS surveyed stope case histories. The CMS was developed jointly by the Noranda Technology Centre (NTC) and Optech Systems. Examples of applications of this system can be found in Miller et al. (1992a, 1992b), Pakalnis et al., (1995a, 1995b) and Mah et al. (1996).

3.5.1 Cavity Monitoring System Survey and Data Manipulating

The CMS is comprised of four major components:

- a. Motorized laser scanning unit
- b. Portable controller and controller case with built-in data logger and CPU
- c. Support package
- d. Data reduction software

The first three components of the CMS are the hardware which is used to perform the survey and to record the survey data. The data reduction software is used to download the surveyed data to a computer and manipulate the data. Figure 3.10 shows the typical CMS set-up.

The main component is the laser scanning unit which utilizes a two beam laser system for distance measurements. It is housed in a motorized fork assembly that is capable of rotating the scanning unit a full 360° about the boom axis and inclines up to 135° about the pivot axis (NTC & Optech, 1997).

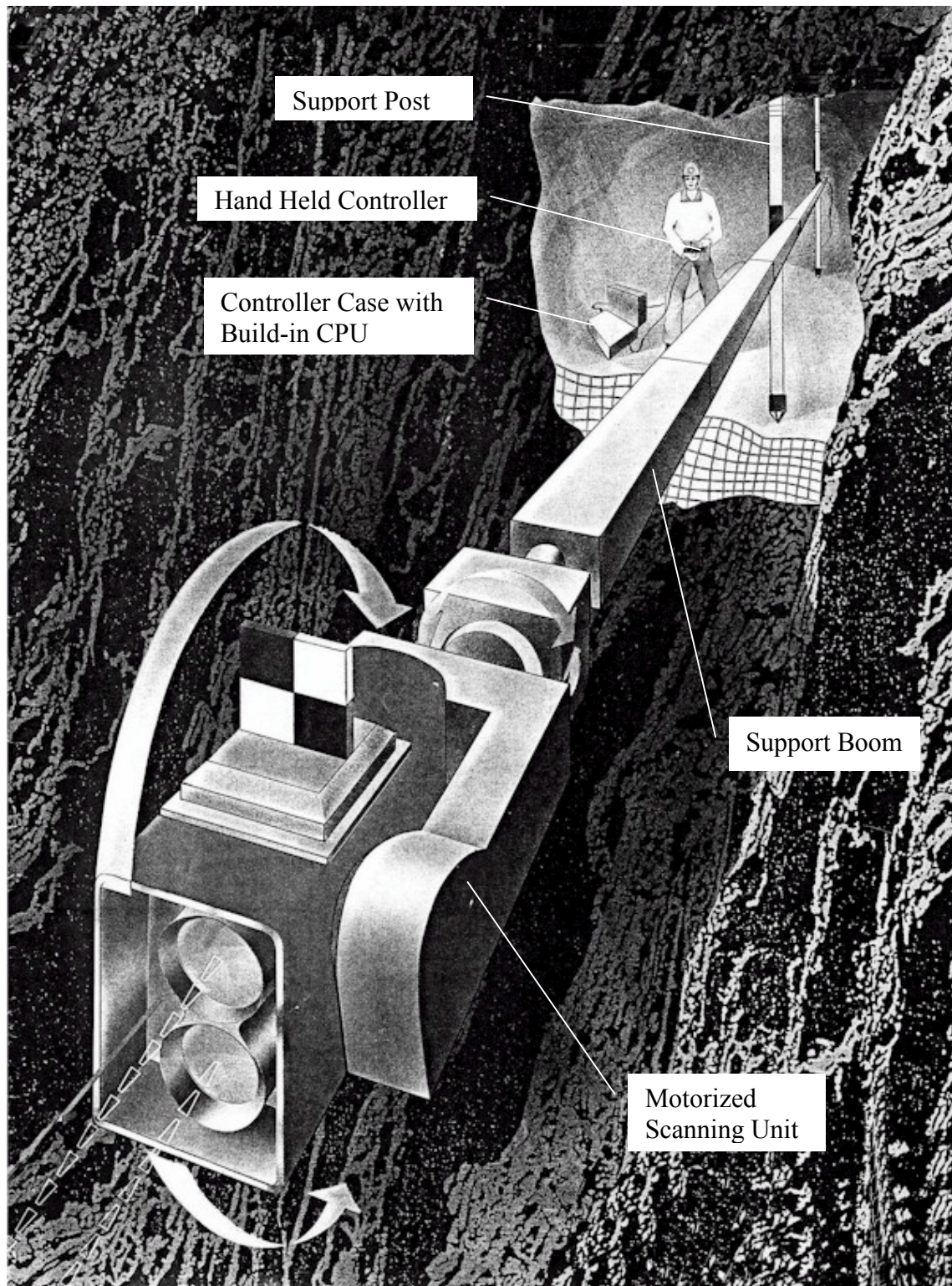


Figure 3.10 Schematic illustration of the typical CMS set-up (after NTC and Optech, 1997)

The portable controller enables the operator to program the survey and remotely activate the laser scanning unit. The controller case houses the data logger, CPU and battery. The support package consists of a 10 metre segmented boom and two adjustable posts that brace the system to the sill and back.

The software is used to download data from the CMS and create a 3D mesh file in DXF format. The DXF file format is a CAD vector format. It is designed to allow the exchange of vector information between different CAD applications. The DXF files can be imported into AutoCAD (Autodesk Inc., 1982-1997) for further processing.

A typical CMS operation involves suspending the CMS scanning unit in an underground opening (Figure 3.6), using the remote hand held controller to program and control the survey, followed by surface office data processing. Once the data are downloaded, the software can be used to create a 3D mesh and cut cross sections (slices) along any desired orientations (this includes coordinate information).

The cut sections can then be imported into AutoCAD and overlain with stope designs. The dilution/slough and underbreak on each section can be calculated by comparing the CMS surveyed section with each stope design section.

3.6 Summary

Empirical methods are site specific, and site conditions used to develop empirical relationships must be documented. In this chapter, the basic information on the mines used in the study was reviewed. This information includes geographical location of the mines, mining methods corresponding to the case histories, mine geology and rock mass classification. The CMS tool accurately measures the actual dilution. The composition of the CMS tool, the setup and its operation were also reviewed.

CHAPTER 4

EMPIRICAL DATABASE AND DESCRIPTION

4.1 Empirical Database

Based on stope mining information, mapping and rock mass classification as well as CMS survey data, a comprehensive empirical database was established for this research. The database includes most of the CMS surveyed stopes from Callinan Mine, Ruttan Mine and Trout Lake Mine. The database consists of 150 case histories, which include 45 cases from Callinan Mine, 8 cases from Ruttan Mine, and 97 cases from Trout Lake Mine. The following information was included in the database:

- General stope information
- Stope geometry
- Rock mass properties and classification
- Undercutting (U/C) information
- Adjacent mining activity information
- Drilling parameters
- Blasting information
- Time between blasting and the CMS survey, and
- CMS survey data calculations.

Figure 4.1 shows the overall database structure. The information shown in the database structure was collected for each stope case history. Table 4.1 shows an example stope summary sheet. These data collection sheets were developed and the information on each stope was collected as part of this research project. The mine is continuing to use these summary sheets for their current mining. Appendix II shows the simplified rock mechanics database for the three mines.

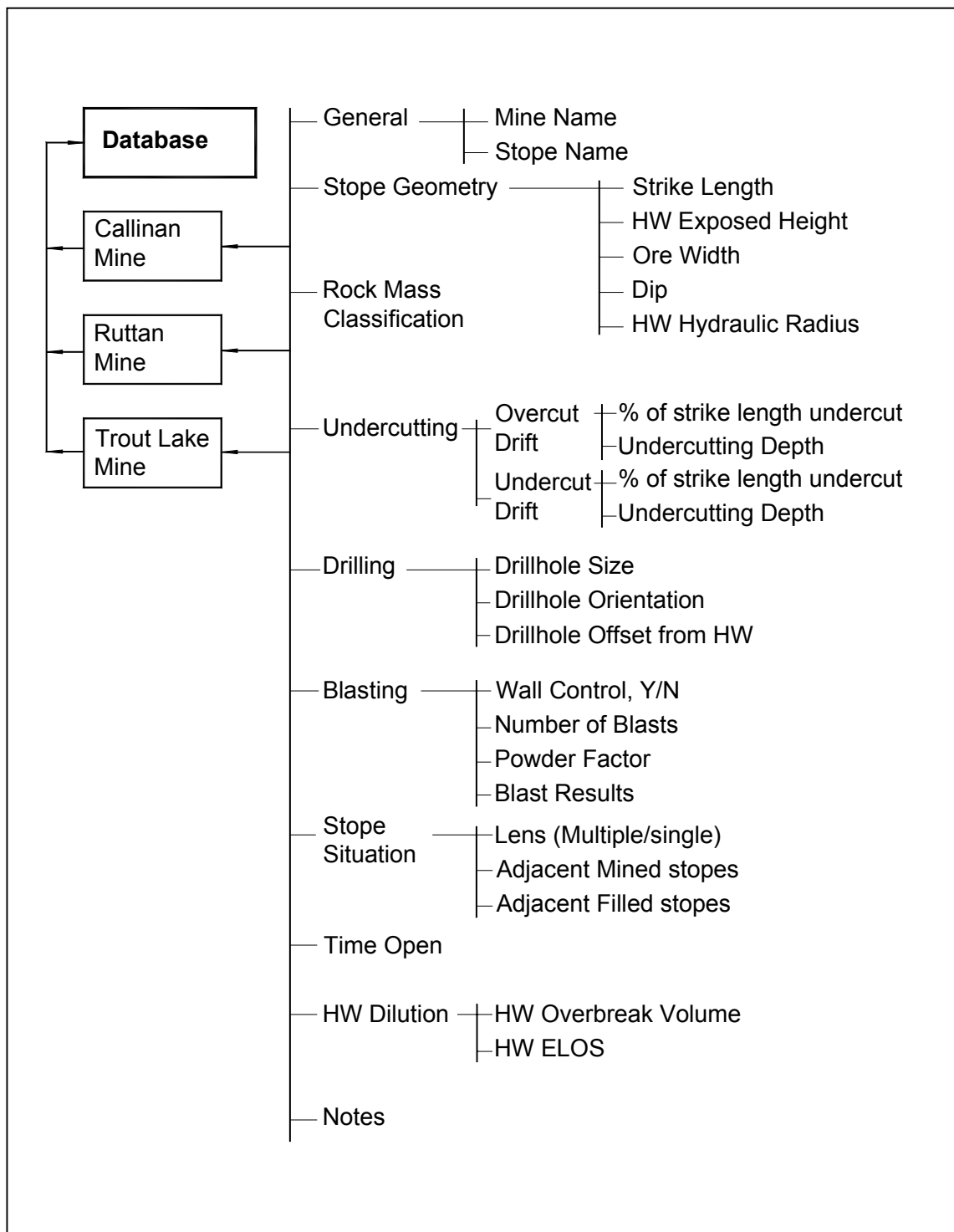


Figure 4.1. Rock mechanics database structure

Table 4.1. Example stope summary sheet

Trout Lake 810-N10-4 STOPE SUMMARY				
General	Strike Length		20.3	m
	HW Exposed Height		34.0	m
	Hydraulic Radius (HR)		6.4	m
	Dip		56	Degrees
	Ore Width		3.9	m
	N'		7.1	
Under Cutting	Under Cut Drift	% of U/C along strike	0%	
		max. U/C	0.0	m
		avg. U/C	0.0	m
	Over Cut Drift	% of U/C along strike	0%	
		max. U/C	0.0	m
		avg. U/C	0.0	m
Blasting	Drillhole Design	parallel (p) or fanned (f) / hole size (inch)	f / 3"	
	Drillhole Offset from HW	max. / min. / avg.	n/a	
	Wall Control	yes / no	y	
	Number of Blasts	slot / main	2 / 1	
	Powder Factor		0.4	kg/ton
	Blast Results	good / average / poor	a	
Stope Situation	Lens	multiple / single	m	
	Adjacent Mined	above / below / one side / both sides	b / os	
	Filled Adjacent Stopes	above / below / one side / both sides	b / os	
Time Open	Time between Major Blast and CMS		40	days
HW Dilution	O/B Volume		731.6	m ³
	ELOS		1.06	m
Note: No U/C, may have a stress problem since the stope is situated adjacent to a large mined area				

4.2 Database Description

4.2.1 General

The database gathered provides the raw data for this dilution study. Any empirical design guidelines developed from this study will have limitations. Empirical design methods are only applicable for conditions similar to those from which the method was derived. It is, therefore, important to have a good understanding of the database for proper application of the design method.

The following sections give a detailed description of the distribution of the data from the case histories.

4.2.2 Slope Geometry

The slope geometry has a significant influence on the stability and the dilution that can be expected from a slope hanging wall. It can be anticipated that a larger slope hanging wall will experience greater instability and corresponding hanging wall dilution. The open slope geometry parameters collected include strike length, exposed HW height, hydraulic radius (HR) of the HW, dip of the HW, and ore width. Figure 4.2 shows an isometric sketch of a typical open stope. The histograms in Figure 4.3 to Figure 4.7 show the distribution of values defining the slope geometry for all of the case histories. A statistical summary is given in Table 4.3 at the end of this chapter.

In general, slope strike length ranges from 11 to 57 m, in which about 80% of the stopes have a strike length between 17 and 30 m. The slope hanging wall exposed heights range from 10 to 85m, with about 70% of the stopes between 29m to 41m. The HR ranges from 3 to 12.6 m, with approximately 75% of the cases between 6m to 9m. The stope HW dip ranges from 24° to 89°, with 75% of the stopes dipping between 48° to 75°. Stope ore width range from 1.9 to 52m, with about 85% of widths between 4m to 12 m.

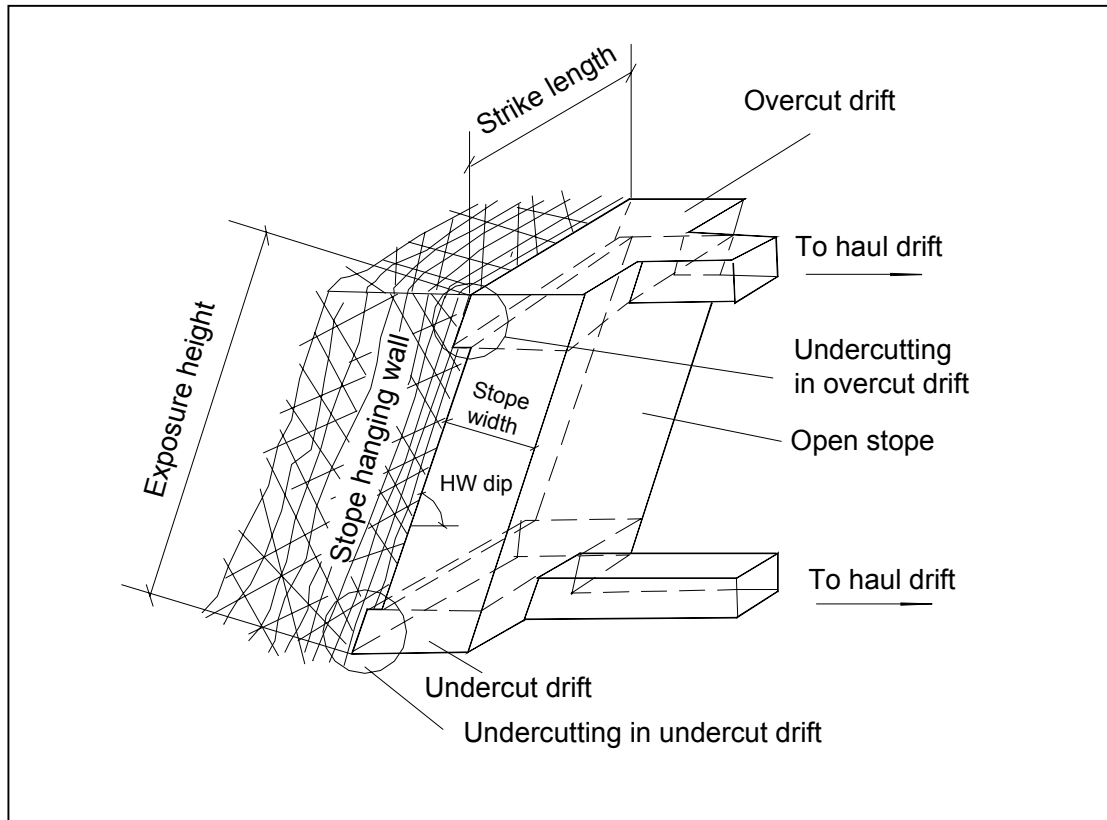


Figure 4.2. Isometric of a typical open stope (after Hutchinson & Diederichs, 1996)

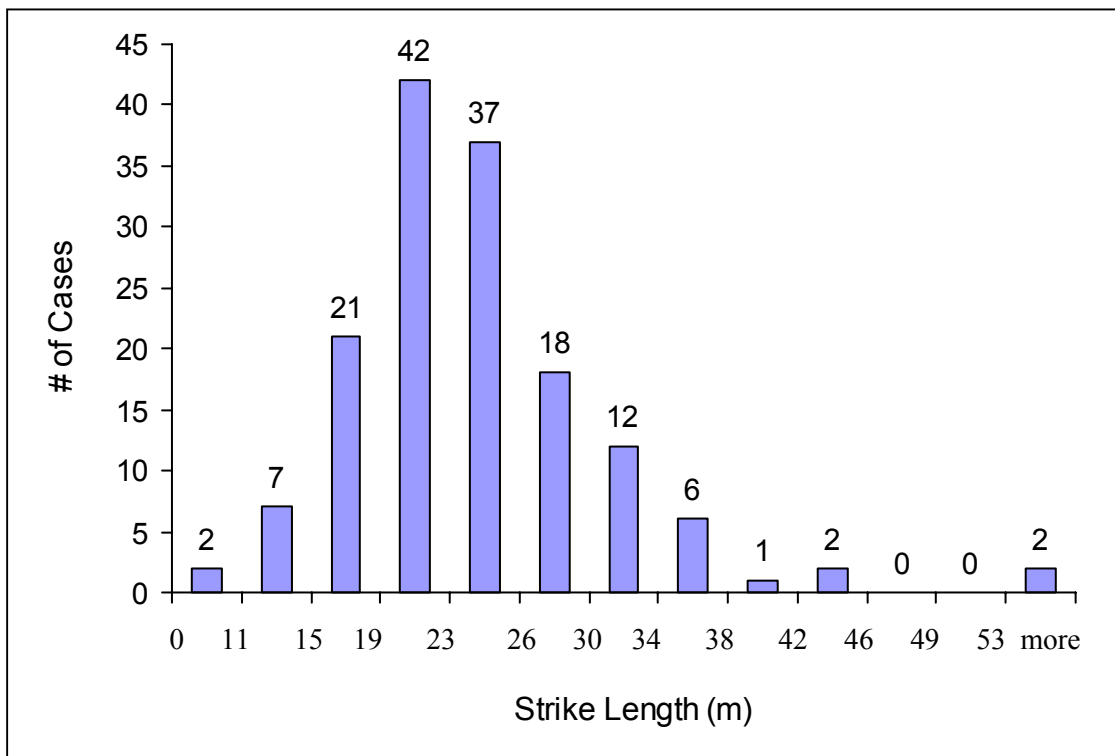


Figure 4.3. Stope strike length distribution

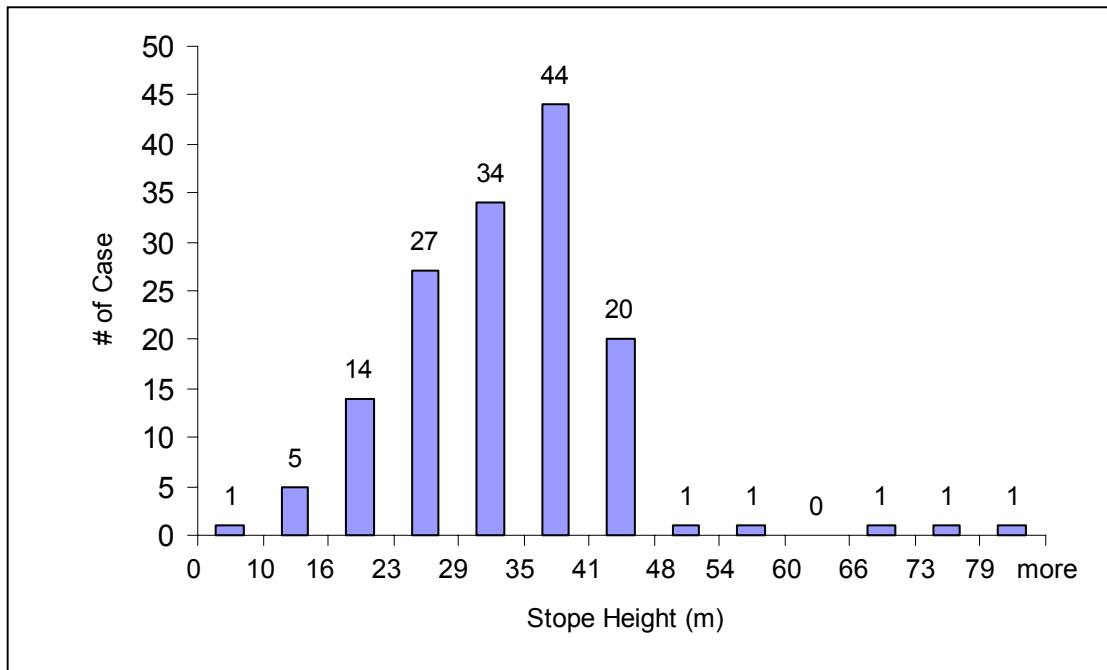


Figure 4.4. Stope height distribution

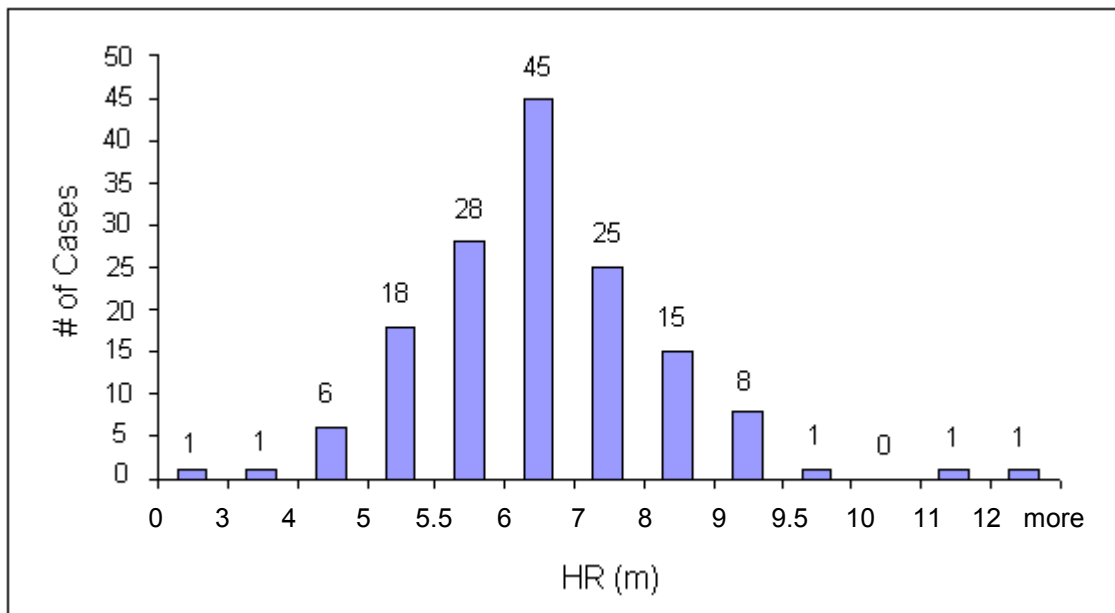


Figure 4.5. Stope hanging wall hydraulic radius (HR) distribution

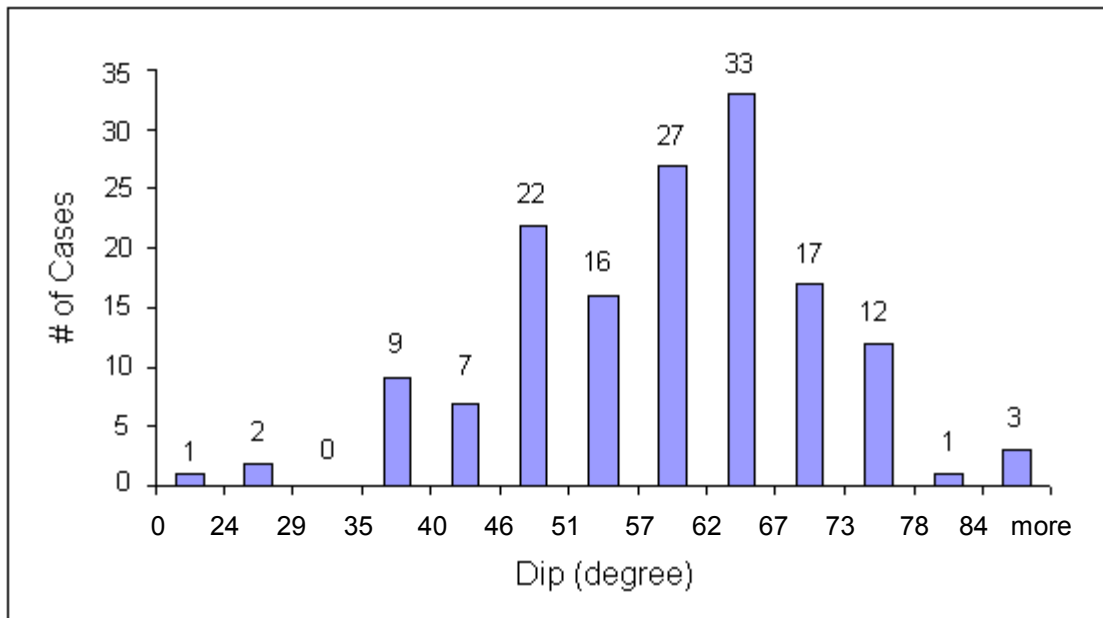


Figure 4.6. Stope hanging wall dip distribution

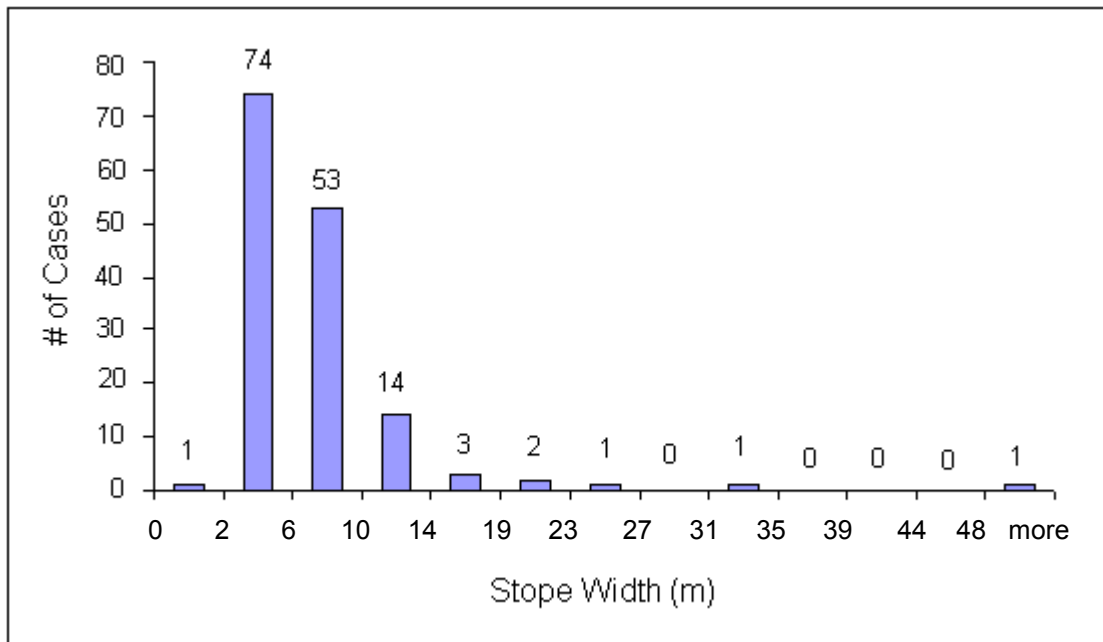


Figure 4.7. Stope width distribution

4.2.3 Stope HW Modified Stability Number N'

The Modified Stability Number N' is used to assess the overall stability of the hanging wall rock (section 2.3.2). The N' value is based on the modified NGI “ Q' ” classification system (Section 2.3.1). The modified stability number N' is calculated from:

$$N' = Q' \times A \times B \times C \quad (2.30)$$

where

N' = modified stability number

Q' = modified tunnelling quality index (NGI) with SRF = 1.

(Barton et al., 1974, Section 2.3.1)

A = stress factor

B = joint orientation factor

C = gravity factor

For a large open stope HW, the HW can be assumed to be in a low stress state or a state of stress relaxation. The stress factor A is set to 1.0 (Figure 2.9). Field mapping indicated that almost all the stope HW foliation is parallel to the HW surface. According to the chart modified by Potvin (1988), a joint orientation factor $B = 0.3$ is assigned (Figure 2.10 in Chapter 2). The gravity factor C is calculated by the formulation of $C = 8 - 6\cos\alpha$, where α is the dip of the stope HW.

The modified stability number N' for the case histories in the database range from 2.9 to 60, with 50% of the values in between 10 and 15. Figure 4.8 shows the stope hanging wall modified stability number N' distribution.

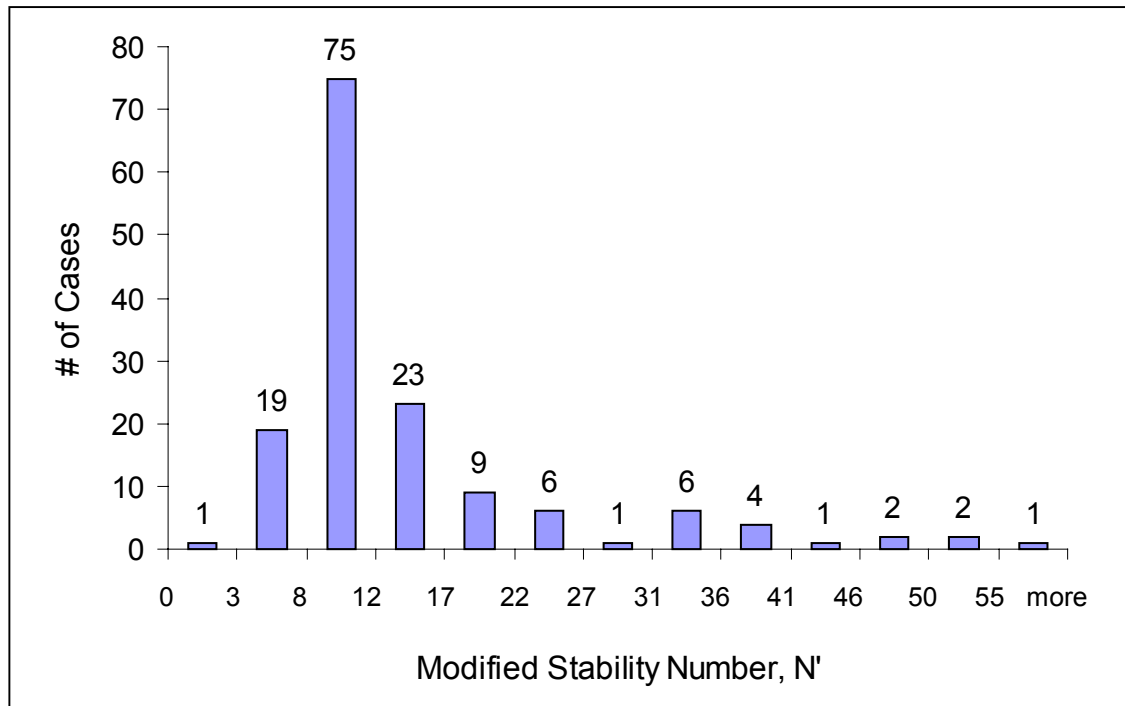


Figure 4.8. Distribution of the modified stability number N'

4.2.4 Undercutting of the Stope Hanging Walls

Undercutting of the hanging wall occurs when the drift does not accurately follow the ore / waste contact and moves into the waste hanging wall rock. Undercutting the hanging wall, or cutting into the hanging wall waste rock, breaks the integrity of the rock beam that often makes up the immediate hanging wall rock. Experience has shown that undercutting the hanging wall reduces stability and increases dilution. Stope hanging wall undercutting information is included in the database. The information on undercutting includes: percentage of undercutting along strike and the corresponding average depth into the hanging wall.

The database shows that about 74% of case histories have some undercutting (111 out of 150 cases). The database also shows that the undercut drift has more undercutting than the overcut drift (in both terms of percentage of undercutting along strike and average depth of undercutting). Along the undercut drift, additional cutting into the hanging wall can occur if the stope below has been mined. Sloughing or significant

dilution in the stope below can cause a significant amount of hanging wall undercutting to the undercut drift of the stope above.

On the overcut drifts, about 40% of the cases cut into the stope hanging wall. In the majority (66%) of these cases, the undercutting depth is in the range of 0.5m to 1.6m. Figure 4.9 shows the distribution of overcut drift undercutting into the hanging wall.

Along the undercut drifts, approximately 65% of the cases undercut the stope hanging wall. The majority of these undercutting cases have an average undercutting depth of 1m to 3m. Figure 4.10 shows the distribution of undercutting for the undercut drift.

4.2.5 Drilling and Blasting

Drilling and blasting of the ore can significantly damage the rock left in the stope. Some degree of stope dilution can be attributed to blast damage and this research project included effects to quantify this amount.

Drilling and blasting parameters are difficult to incorporate into the database. In many cases, very limited data are available on important mining factors such as borehole deviation. The parameters included in the database are: drillhole size, drillhole orientation, drillhole offset from the HW, powder factor and whether or not wall control blasting techniques were applied. The expected influence of these variables on hanging wall dilution is discussed briefly. More detail on blasting is given in Chapter 8. Drillhole size determines the explosive distribution. Generally, smaller hole size provides a better explosive distribution than larger, more widely spaced holes, however smaller drillhole size usually results in more hole deviation, which is a major cause of wall damage. Six different drillhole sizes were used in the database. The most frequently used drillhole size was the 3" diameter, which account for 38% of all the cases. The second most frequently used drillhole sizes were 2.5" and 4.5", which account for 22% and 23% of all the cases, respectively. Figure 4.11 shows the drillhole size distribution.

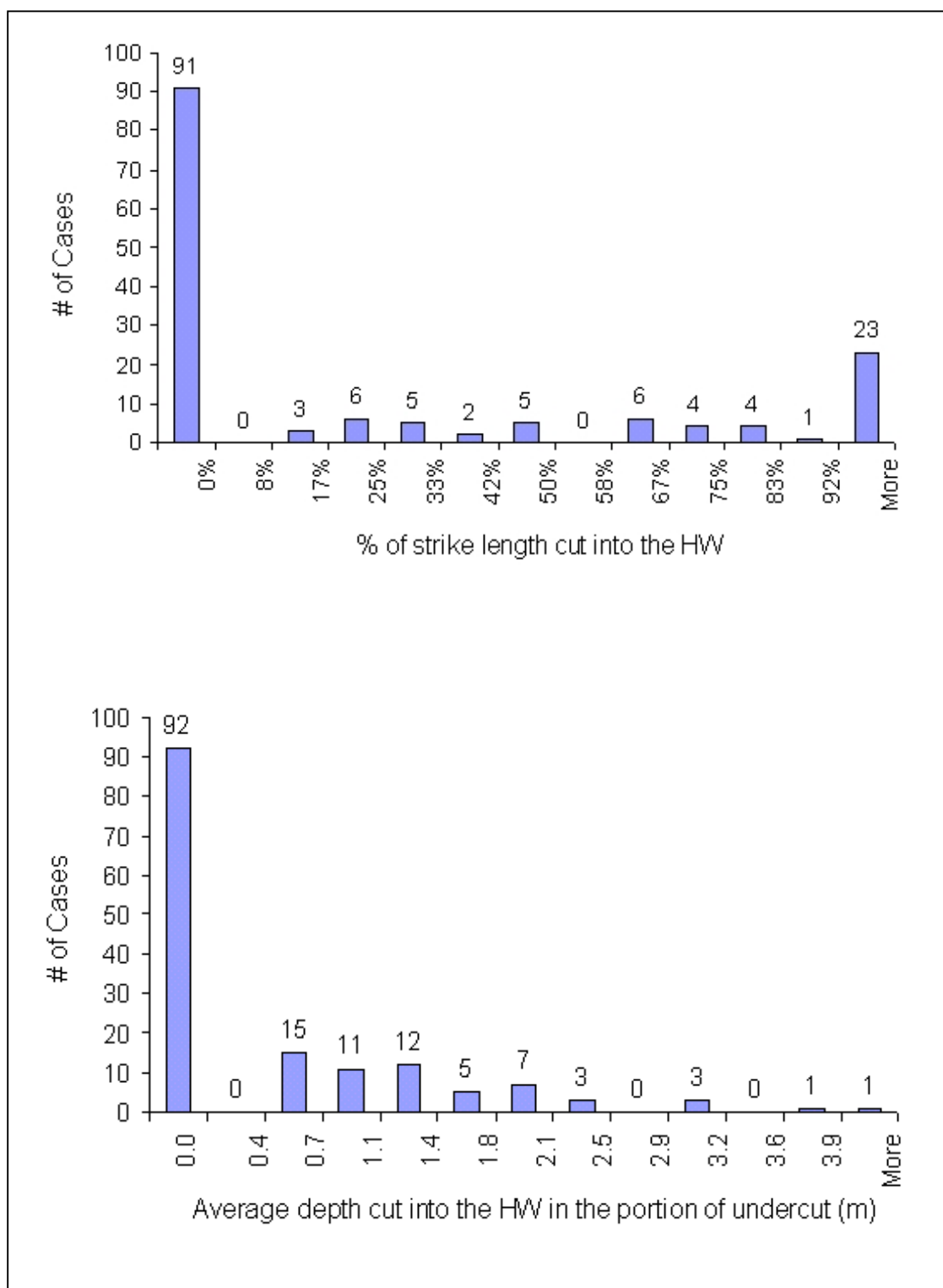


Figure 4.9. Distribution of overcut drift undercutting

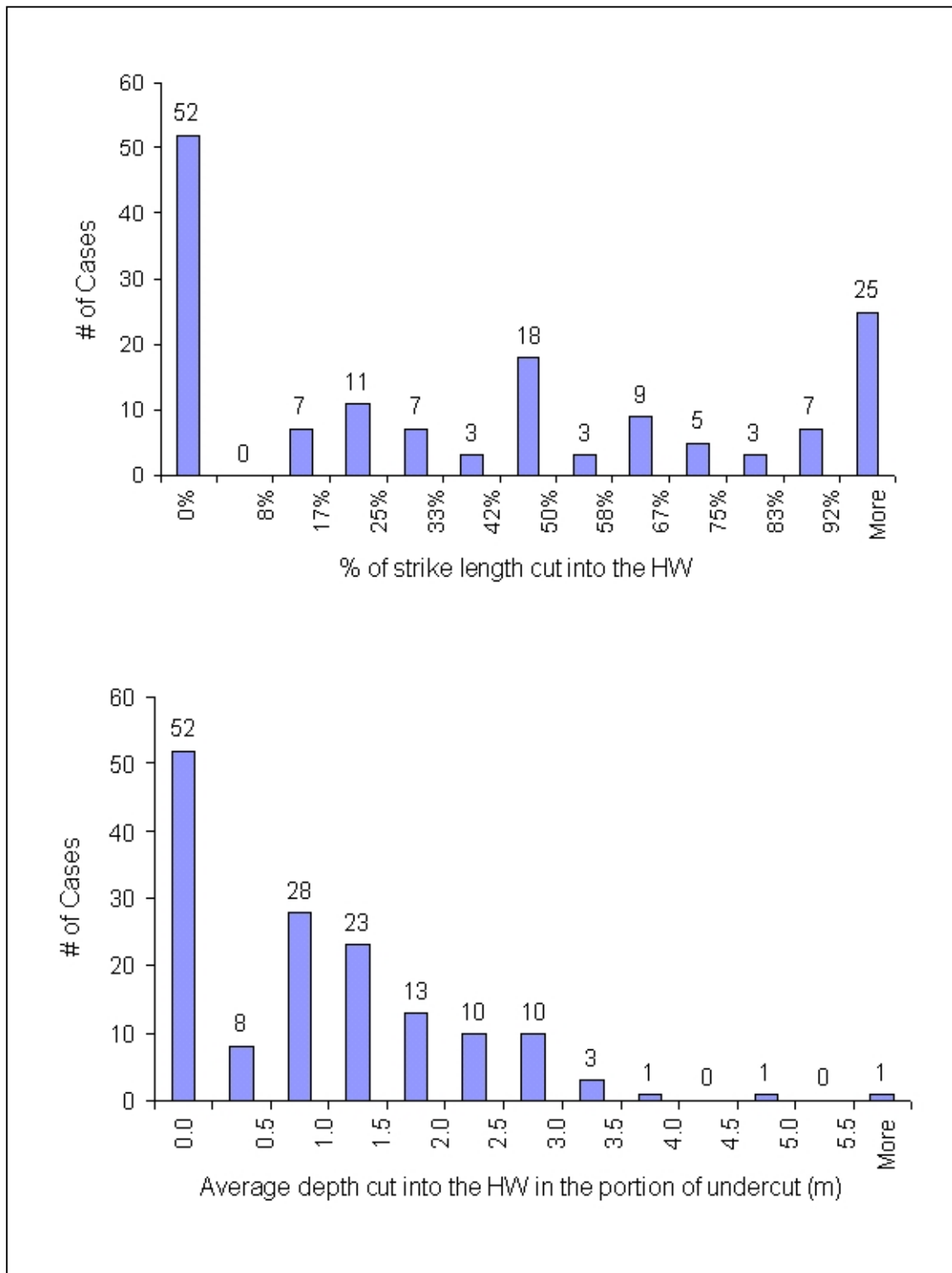


Figure 4.10. Distribution of undercut drift undercutting

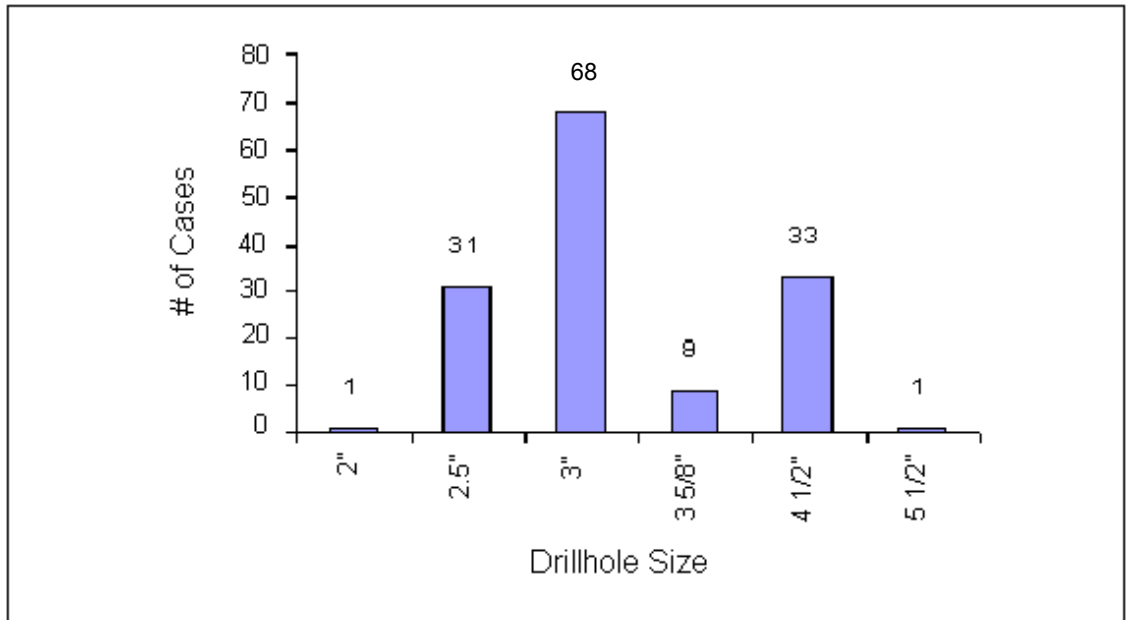


Figure 4.11. Drillhole size distribution

Drillhole orientation refers to the orientation of the holes closest to the hanging wall / ore contact relative to the stope hanging wall. The drillhole orientation was classified into two categories: Fanned and parallel. In the database for the cases with drillhole orientation information (142 cases), about 59% of the cases had a fanned orientation (84 out of 142 cases) and 41% of the cases had a parallel orientation (58 out of 142 cases). Figure 4.12 shows the drillhole pattern histogram.

Except for a few cases, almost all stopes applied various wall control techniques to control blast damage to stope walls.

The powder factor (PF) is the expression of average pounds of explosive used to break one cubic metre of ore in a stope. The database shows that 80% of the case histories had a PF of 0.7 to 1.4 lbs/tonne. Figure 4.13 shows the PF distribution.

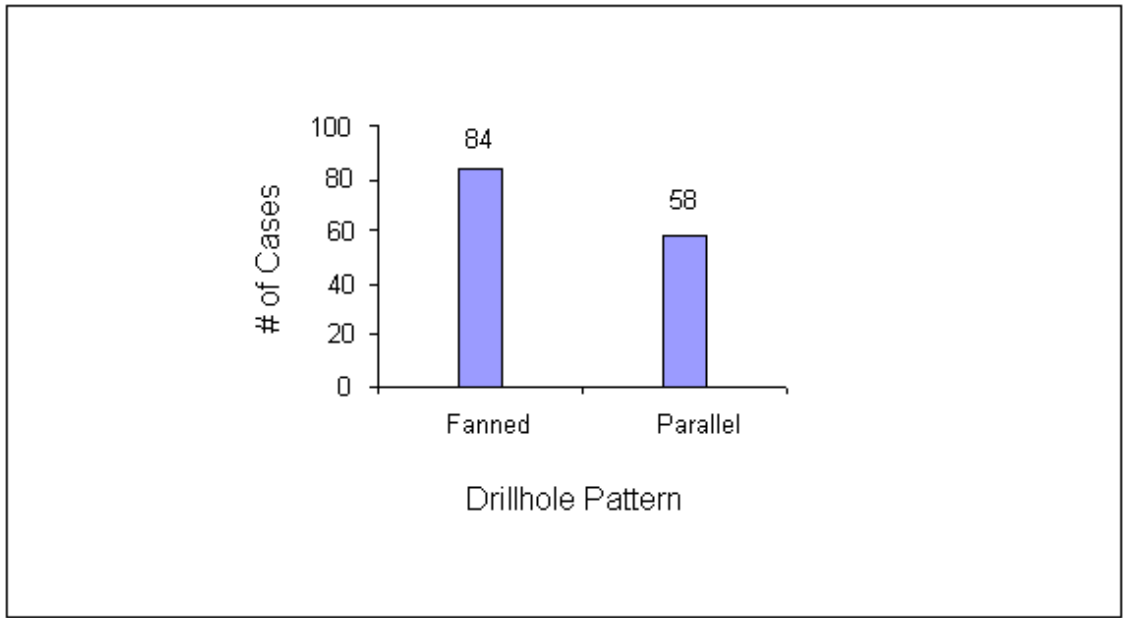


Figure 4.12. Drillhole pattern distribution

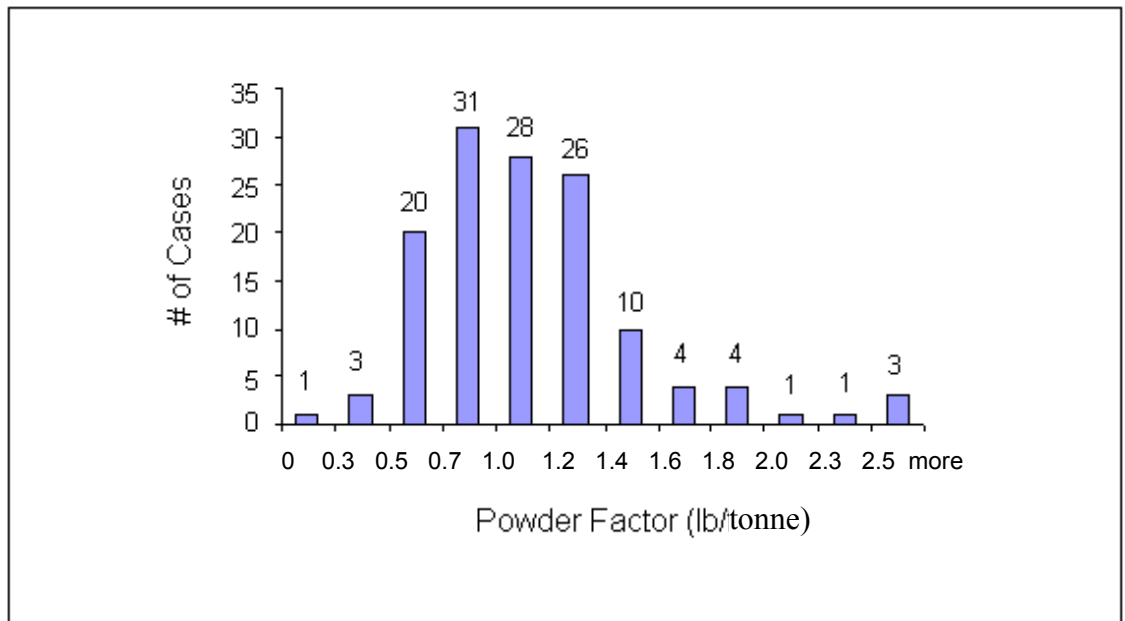


Figure 4.13. Distribution of powder factor

4.2.6 Stope Stress Situation before Mining

After mining, the hanging wall of a stope is in a state of low stress or relaxation. The extent of this zone of relaxation is influenced by the stress situation before mining. The stope stress situation is controlled by the mine's original, or virgin, stress condition, the stope geometry and the stope location relative to adjacent mined stopes. Different stope locations and different mining sequences create different pre-mining in-situ stresses for each stope. The stope location relative to adjacent mined stopes was classified into 6 general categories as described in Table 4.2. More detailed stope stress situation and stope location category descriptions are given in Chapter 6.

Table 4.2. Stope location category

Category	Stope location
1	Isolated stope
2	One side mined
3	Below mined
4	Below & both sides mined
5	one side & below mined
6	above, below & one side mined

The database showed that categories 5 and 2 are the most common stope location configurations, which represent approximately 73% of all the case histories. Figure 4.14 shows the distribution of stope location categories.

4.2.7 CMS Surveyed HW Dilution

CMS surveyed HW dilution is the excessive overbreak dilution outside of the stope HW design line (Figure 1.1). In the database, the stope HW dilution is expressed as equivalent linear overbreak/slough (ELOS), which is the average depth of overbreak/slough from the stope HW. The database shows that the stope HW CMS surveyed ELOS ranges from 0 to 10m. 36% of cases have less than 0.5m ELOS, 24% of cases have ELOS between 0.5 to 1.0m, 25% have 1.0 to 2.0m of ELOS, and 16% have ELOS more than 2.0m. Figure 4.15 shows the Stope HW ELOS distribution.

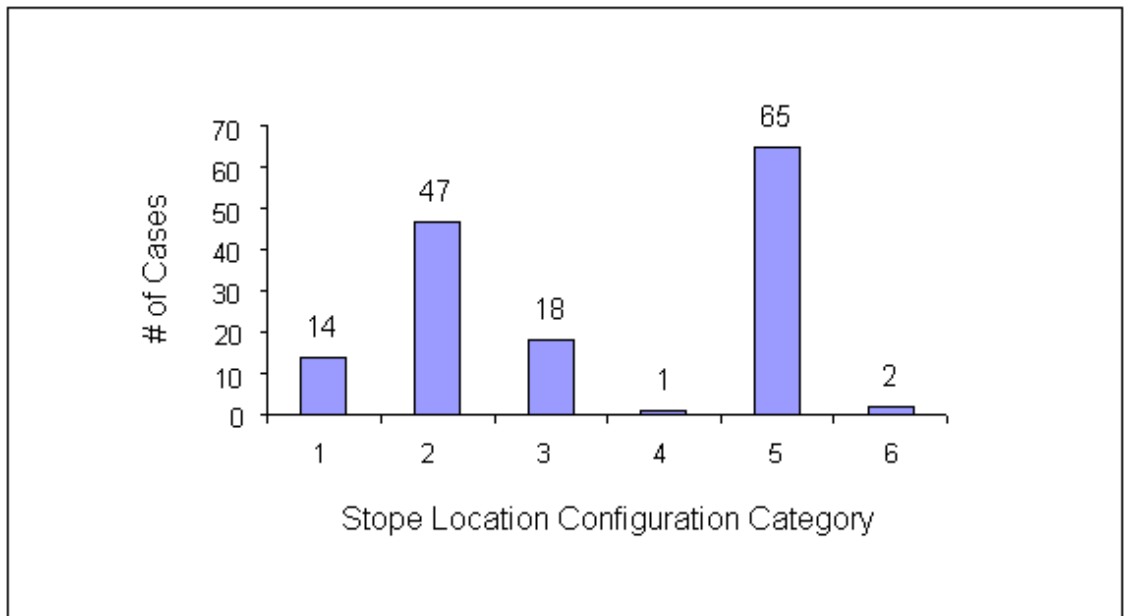


Figure 4.14. Distribution of stope location categories.

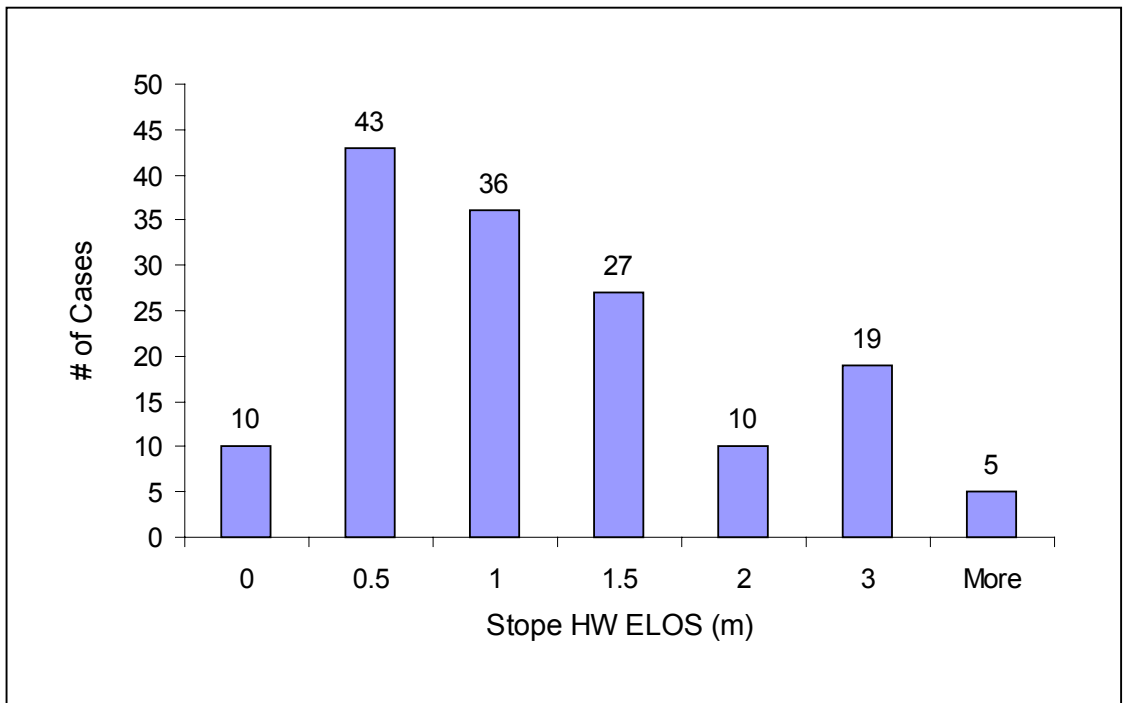


Figure 4.15. Stope HW ELOS distribution

4.2.8 Open Stope Exposure Time

The open stope exposure time is defined as the number of days between the first main blast and the CMS survey date, which usually is conducted at the end of the stope mucking.

For most of the stopes included in the database for this study, the stope exposure time ranges from as little as 4 days to as many as 300 days. Eighty four percent (84%) of case histories have a stope exposure time less than 60 days. Figure 4.16 shows a stope exposure time histogram.

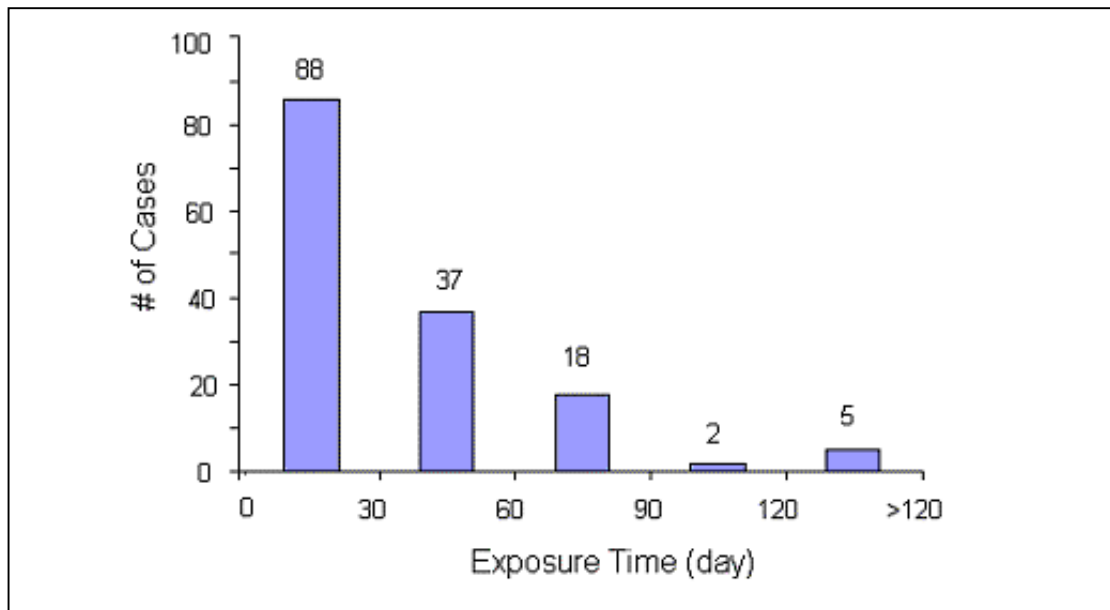


Figure 4.16. Stope exposure time distribution

4.3 Summary

The database consists of 150 CMS surveyed open stope case histories. It contains a wide range of open stope information with a focus on stress, undercutting and blasting parameters. The main database parameters are summarized in Table 4.3. When comparing the behaviour of new case histories, it is important to realize that any relationship derived from this research will only be valid within the range of stoping properties in this database.

The next chapter looks at the stoping database in more detail and compares measured dilution values to predicted dilution based on the dilution graph design method (Clark, 1998).

Table 4.3. Summary of the database parameters

Database parameter	Max. Value	Min. Value	Avg. Value	Majority of population range
Stope strike length, L	57.0 m	11.0 m	23.9 m	15 – 30 m (78%)
Stope HW exposed height, H	85.0 m	10.0 m	33.9 m	23 – 41 m (70%)
HW hydraulic radius	12.6 m	3.0 m	6.7 m	4.6 – 7.8 m (77%)
Ore width	52.0 m	1.9 m	7.5 m	2.0-10.0 m (85%)
Dip	89°	24°	58.9°	46° – 73° (77%)
Stope stability number N'	60.0	2.9	14.8	7.8 – 12.4 (50%)
% of UC in overcut drift	100%	0	30%	0 (61%)
Avg. depth of UC in overcut drift	4.3 m	0	0.5 m	0.4 – 1.4 m (66%)
% of UC in undercut drift	100%	0	40%	0-50% (65%)
Avg. depth of UC in undercut drift	6.0 m	0	1.0 m	0.5 – 1.5 m (52%)
Drillhole size	5 ½"	2"	3"	3" & 4 ½" (71%)
Drillhole orientation	Parallel and fanned			(41% & 59%)
Number of blasts to create stope	10	1	4	
Powder factor	2.7 lb/t	0.3 lb/t	1.1 lb/t	0.5 – 1.4 lb.t (80%)
CMS ELOS	5.6 m	0.0	1.0 m	0 – 1.5 m (77%)

CHAPTER 5

DILUTION FACTOR AND DILUTION PREDICTION ERROR

Two new terms are introduced in this research: the dilution factor (DF) and dilution prediction error (DPE). Both the DF and DPE terms are based on the dilution design graph (Clark, 1998).

5.1 Dilution Design Graph

The empirical dilution graph (Clark, 1998) method is currently the most commonly used approach to estimate the average metres of dilution from open stope hanging walls. The dilution design graph (Figure 5.1) is based on the modified stability graph (Potvin, 1988; Nickson, 1992) and 47 open stope case histories from 6 Canadian mines. The design graph was developed based on engineering judgement and empirical data and was justified by a neural network analysis and statistical methods. The design graph expresses the degree of stability as the average metres of slough (ELOS) that can be expected to fail from the hanging wall. An estimate of dilution is determined by plotting the modified stability number N' versus the hydraulic radius of the stope wall being assessed. This method includes an assessment of the hanging wall geometry, rock quality Q' , stress, joint orientation and surface orientation. The method ignores or poorly accounts for many factors which influence stope dilution. Clark and Pakalnis (1997) listed some of these factors as irregular wall geometry, undercutting of stope walls, blasthole diameter, blasthole length and layout, blasthole offset, stope life, and number of blasts. It is also recognized that stress is poorly accounted for in the dilution graph design method. In all of the case histories in both the Potvin (1988) and Nickson (1992) databases for stope stability, the hanging walls were assessed as being in a state

of relaxation and the stresses were not considered to affect stability. In the current HBMS database, all the stope hanging walls have also been assessed to be in a state of relaxation. This does not allow for differentiating between stress conditions for the hanging wall case histories. Clark and Pakalnis (1997) and Potvin (1988) suggest that a relaxed hanging wall stress state may not be the best condition for stability.

The dilution graph method does not account for all of the factors influencing dilution and it cannot therefore be expected to accurately estimate dilution. A term called the dilution factor is introduced to represent the ELOS estimate obtained from the dilution graph.

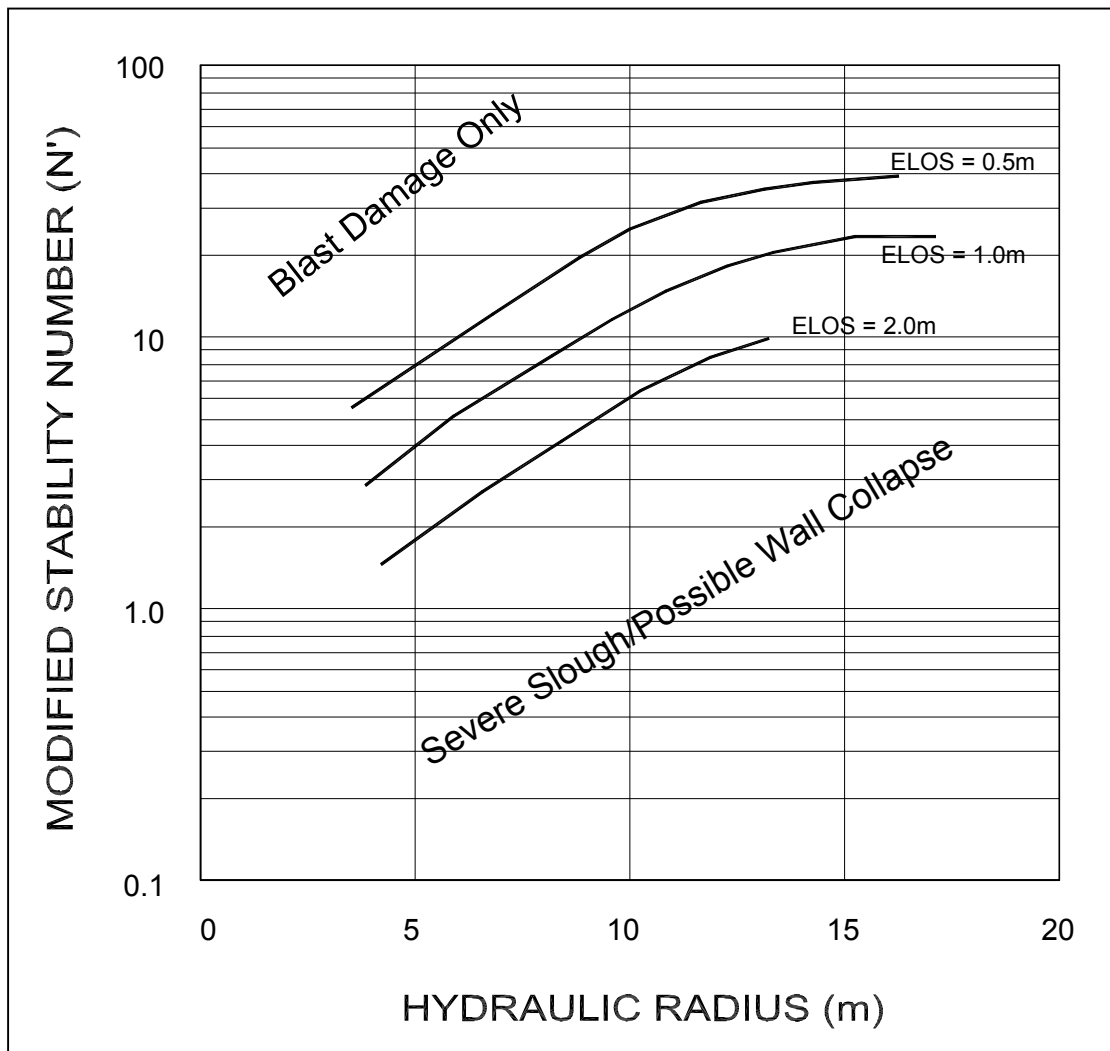


Figure 5.1. Dilution design graph (after Clark, 1998)

5.2 Dilution Factor

The dilution factor (DF) is defined as the ELOS predicted from the dilution design graph based on the slope surface modified stability number N' and hydraulic radius HR. Figure 5.2 illustrates how the dilution factor is obtained. The dilution design zone between design lines of ELOS = 0.5 m and 1.0 m as well as between ELOS = 1.0 m and 2.0 m are divided into even divisions. The estimated value is defined as the DF parameter. For example, consider a slope hanging wall surface with a modified stability

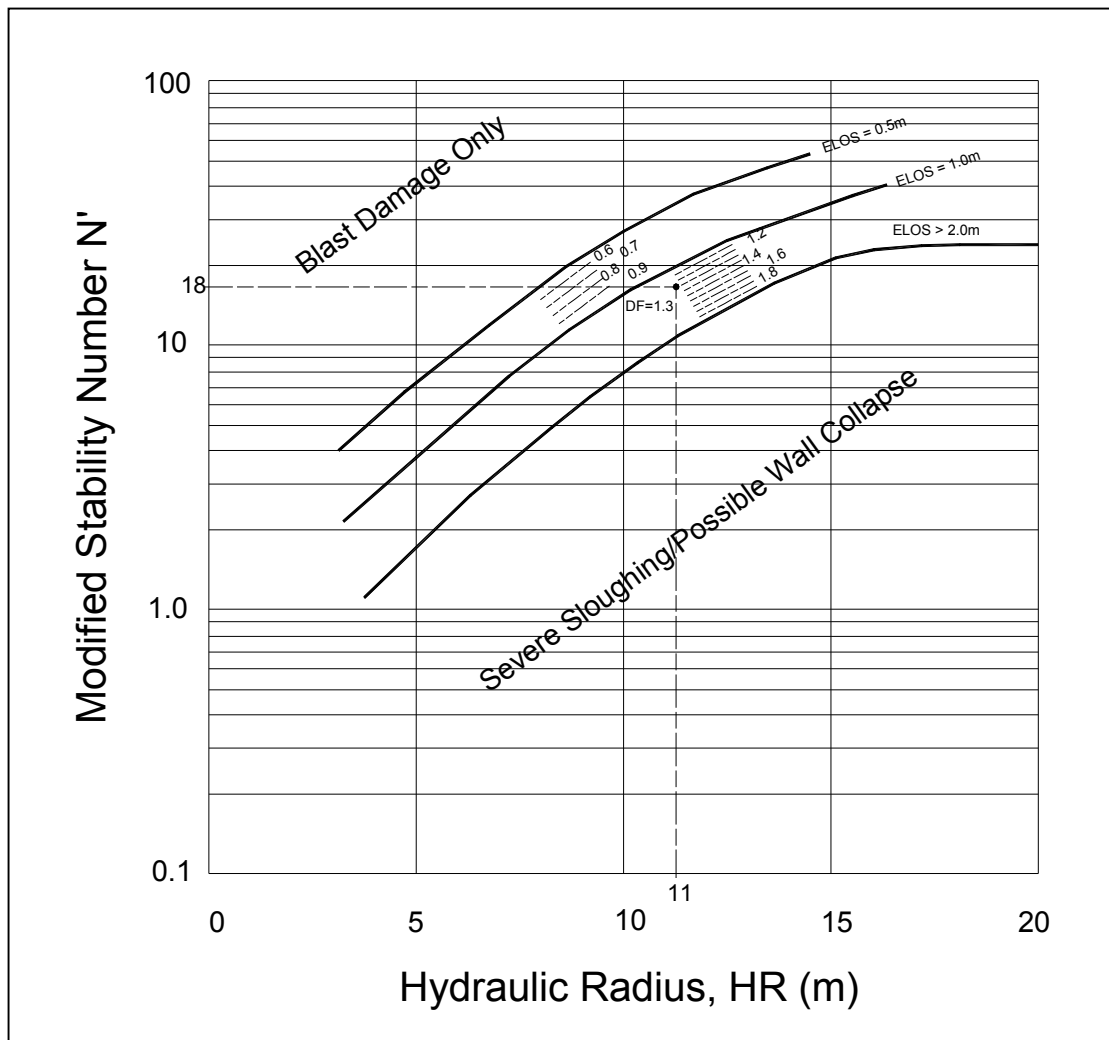


Figure 5.2. Illustration of the procedure for obtaining dilution factor

number N' of 18 and hydraulic radius HR of 11 m. A DF of 1.3 can be determined by reading the value from the intersection of N' and HR coordinates. The DF represents the stope surface average depth of overbreak/slough prediction base on the surface N' and HR values. The actual stope ELOS may differ from the DF value.

5.3 Dilution Prediction Error

The dilution prediction error (DPE) is defined as the difference between the actual ELOS value and the predicted ELOS value (DF). For example, if a stope hanging wall has $N'=18$ and $HR = 11$ ($DF = 1.3$ m), and an actual stope hanging wall average depth of dilution of 1.6 m, the stope hanging wall $DPE = 1.6 - 1.3 = 0.3$ m.

As mentioned, there are many reasons why the dilution graph method may not be accurate for estimating dilution at a specific mine. Since the Ruttan mine was at the end of its operating life during the data collection phase of this project, only the data from Callinan and Trout Lake Mines were analyzed using the dilution graph. Figure 5.3 shows the accuracy of the current dilution design graph on the case histories from Callinan Mine and Trout Lake Mine. The case histories are broken into four categories based on the range of actual or measured equivalent linear overbreak/slough (ELOS) minus ELOS predicted from the dilution design graph. This is another way of expressing the DPE value. These four categories are:

- a). $DPE \text{ or } ELOS |actual-predicted| < 0.5$ m (circles);
- b). $0.5 \text{ m} \leq DPE \text{ or } ELOS |actual-predicted| < 1.0$ (squares);
- c). $1.0 \text{ m} \leq DPE \text{ or } ELOS |actual-predicted| < 2.0$ m (triangles);
- d). $DPE \text{ or } ELOS |actual-predicted| \geq 2.0$ m (diamonds).

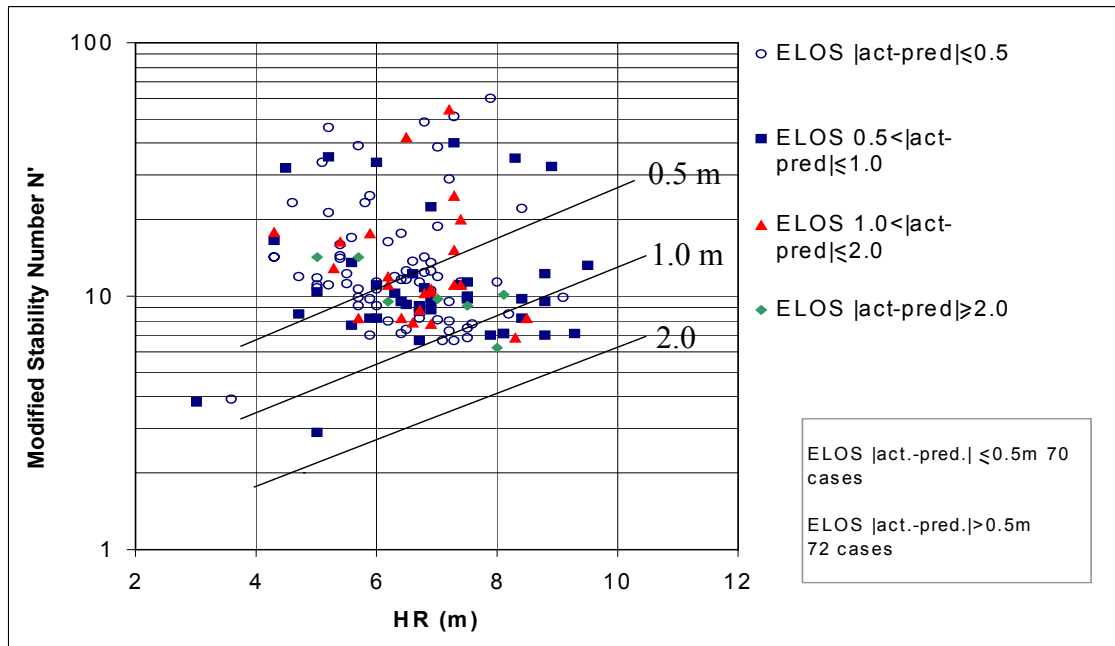


Figure 5.3. Illustration of the accuracy of current dilution design methods on the Callinan Mine and Trout Lake Mine case histories

The plot shows that over 50% of the case histories had average depths of slough that disagreed with the predicted depths of slough from the dilution graph by more than 0.5 metres (DPE > 0.5m). Figure 5.4 more clearly shows the dilution prediction error for the HBMS database assessed using the dilution graph. It is not surprising that there is a significant discrepancy between the actual and predicted depths of hanging wall slough. The dilution graph is based on the conditions encountered in Clark's database. It either ignores or poorly accounts for many factors which influence stope dilution. The stress factor, undercutting factor, and blasting factor are among these. The dilution graph is, however, a very valuable tool for combining many of the factors known to contribute to dilution and representing these factors as a single number or dilution estimate. This graphically determined dilution factor is a reasonable estimate of depths of slough for the average conditions of stress, undercutting and blasting that existed for the original dilution graph database. These conditions will vary for individual stope case histories.

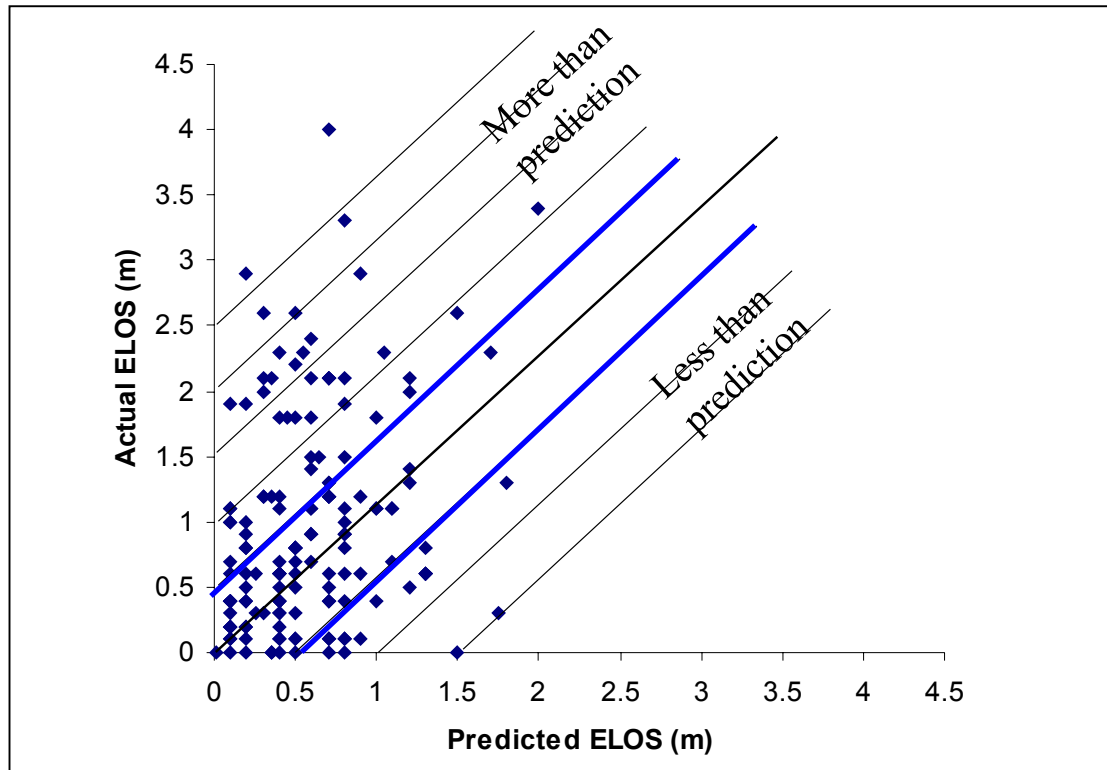


Figure 5.4. Comparison between actual ELOS and Dilution Graph predicted ELOS for the HBMS database

5.4 Summary

The dilution factor (DF) is the predicted dilution which corresponds to average stress, undercutting and blasting conditions for different slope wall surface geometries in the original database (Clark, 1998). The dilution prediction error (DPE) represents the differential dilution between actual measured dilution and the dilution factor. Since the current dilution design graph does not adequately or specifically consider factors such as stress, undercutting, blasting and exposure time, dilution prediction errors can be expected when using the graph. The DPE may be caused by the factors that the current dilution graph poorly accounts for or ignores. The following chapters look at the theoretical and actual influence of some of these parameters on the HBMS database.

CHAPTER 6

INFLUENCE OF STRESS ON STOPE HANGING WALL STABILITY AND DILUTION

6.1 Introduction

This chapter looks at methods of assessing the hanging wall geometry and pre-mining stress state to best estimate the zone of relaxation induced in the hanging wall of a stope. The goal is to determine if the hydraulic radius term does an adequate job of indirectly assessing the size of the relaxation zone around an open stope hanging wall. Methods for improving this approach based on the initial stress state are also included.

Empirical design and numerical modelling make up two broad general approaches for assessing underground stability in rock. Numerical modelling approaches usually start by determining the stress state around underground openings. A failure criterion is then applied to the rock mass to determine if the modelled stress state will induce failure. Empirical methods often assess the stress state around an opening in simple terms such as the ratio of induced stress to unconfined compressive strength to obtain a stress factor influencing stability. The stress factor is then combined with other variables such as rock mass classification and opening geometry and a stability assessment is estimated (Barton et al., 1974; Mathews, et al., 1981; Potvin, 1988).

Neither empirical nor stress-based failure criteria analyses are ideally suited for assessing stability in open stope hanging wall conditions (this will be discussed in the following sections). Open stope geometries are frequently long on strike and up dip and relatively narrow in width. This means hanging wall and footwall surfaces are usually

the largest surfaces of an open stope. Because of the geometry of stope hanging walls, these surfaces are usually in a state of relaxation or low stress, which often results in a modelled tensile zone around stope hanging walls. Section 6.4 discusses the relationship between opening geometry and stress in more detail. Neither stress based failure criteria nor empirical stress factors do an adequate job of assessing stability in zones of relaxation or induced tensile stress.

6.1.1 Stress Related Failure

The Mohr Coulomb failure criterion (Coulomb, 1776) and the Hoek and Brown failure criterion (Hoek and Brown, 1980) are the two most widely accepted failure criteria in rock engineering. The Mohr Coulomb failure criterion is primarily developed for evaluating intact rock failure. The Mohr Coulomb failure criterion is usually graphically shown as a straight line, with a tensile cut-off as shown in Figure 2.2. Hoek and Brown (1980) developed an empirical relationship for the peak failure stress for a range of confinements. The advantage of this failure criterion is that it attempts to account for the jointed nature of the rock mass. It relates the failure criterion to the rock mass classification value, RMR or Q, which takes rock mass properties into account rather than only intact rock properties.

The main problem with these failure approaches occurs when they are applied to a jointed rock mass in tension. Figure 6.1 shows a typical jointed rock mass that could exist underground. A jointed rock mass has a very low tensile strength and this tensile strength is scale dependent. If the excavation is very small relative to the joint spacing, the tensile strength of the rock mass, influenced by the excavation, approaches the strength of intact rock. As the excavation size gets much greater than the joint spacing, the tensile rock mass strength approaches zero. The stability of an excavation in a rock mass is strongly influenced by the size of the relaxation zone around the excavation related to the size of the rock mass block, or joint spacing (scale effect). Calculated tensile failure of the rock mass based on a Mohr Coulomb or Hoek Brown failure

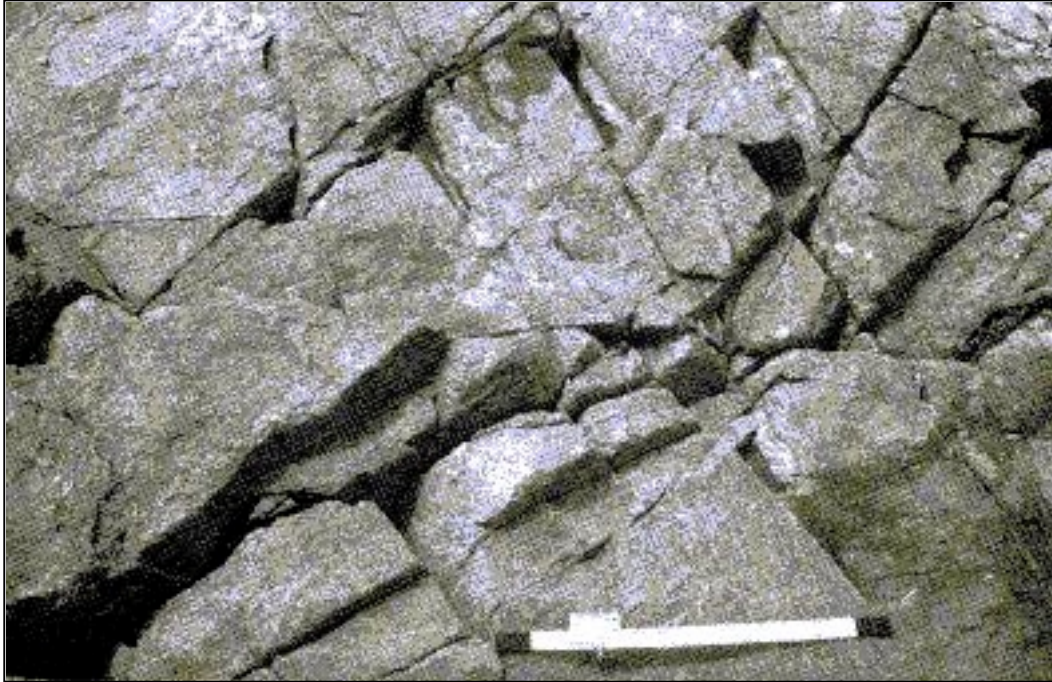


Figure 6.1. Rock fractures forming rock blocks within the rock mass with a 1 m long scale (from Hudson & Harrison, 1997)

criterion for the rock mass does not represent this scale dependent failure of interlocking blocks that make up a jointed rock mass.

6.1.2 Empirical Assessment of Hanging Wall Stress Conditions

An open stope hanging wall is commonly in a state of relaxation or modelled tensile stress. Empirical design methods such as the Barton's Q classification based Support Graph (Barton et al., 1974) and the Stability Graph (Mathews et al., 1981; Potvin, 1988) only consider induced compressive stresses, which may induce stability problems when they approach the unconfined compressive strength (UCS) of the rock. The Barton approach has a stress reduction factor (SRF) which reduces the overall assessed rock mass quality as the compressive stresses approach the rock strength. The Stability Graph design method has a stress factor term A, which reduces the overall stability number assessment N' for high compressive stresses. Both these approaches consider stress to be a factor influencing stability when the induced stress is greater than 10% of the UCS of the rock. The empirical assessment of the influence of stress on the stability

of a stope hanging wall is not directly influenced by the size of the modelled relaxation zone or by the magnitude of the modelled induced tensile stresses in the hanging wall.

Empirical methods do, however, consider the size of an opening when the overall stability is estimated. The Barton approach looks at tunnel span when assessing stability and the Stability Graph approach looks at the opening hydraulic radius to assess stability (Section 2.3). Previous work has suggested that the zone of relaxation around a stope hanging wall increases with the hydraulic radius of the hanging wall surface (Milne, 1997; Clark, 1998). Empirical design methods predict reduced stability with increasing hydraulic radius. The influence of the relaxation zone on the hanging wall may be indirectly accounted for in empirical design methods which use the HR term.

6.2 Stress Relaxation

When an underground excavation is made in a rock mass, the stresses that exist in the rock are disturbed and new stresses are induced around the opening. Hoek and Brown (1980) used a streamline analogy to represent this new stress field. The stress field is explained with the analogy of a cylindrical obstruction, such as the pier of a bridge, being introduced into a smoothly flowing stream; the water has to flow around this obstruction and the streamlines are deflected as shown in Figure 6.2. Immediately upstream and downstream of the obstruction, the water flow is slowed down and the streamlines are spread outwards. This separation is analogous to the reduction of stress that occurs in zones of tensile stress or relaxation around an opening. Since stress cannot flow through an opening, it must flow around it, in much the same way that water flows around an obstruction. In the zones on either side of the obstruction, the flow rate is increased and the streamlines are closer together. This is analogous to zones of increased compressive stress adjacent to an opening.

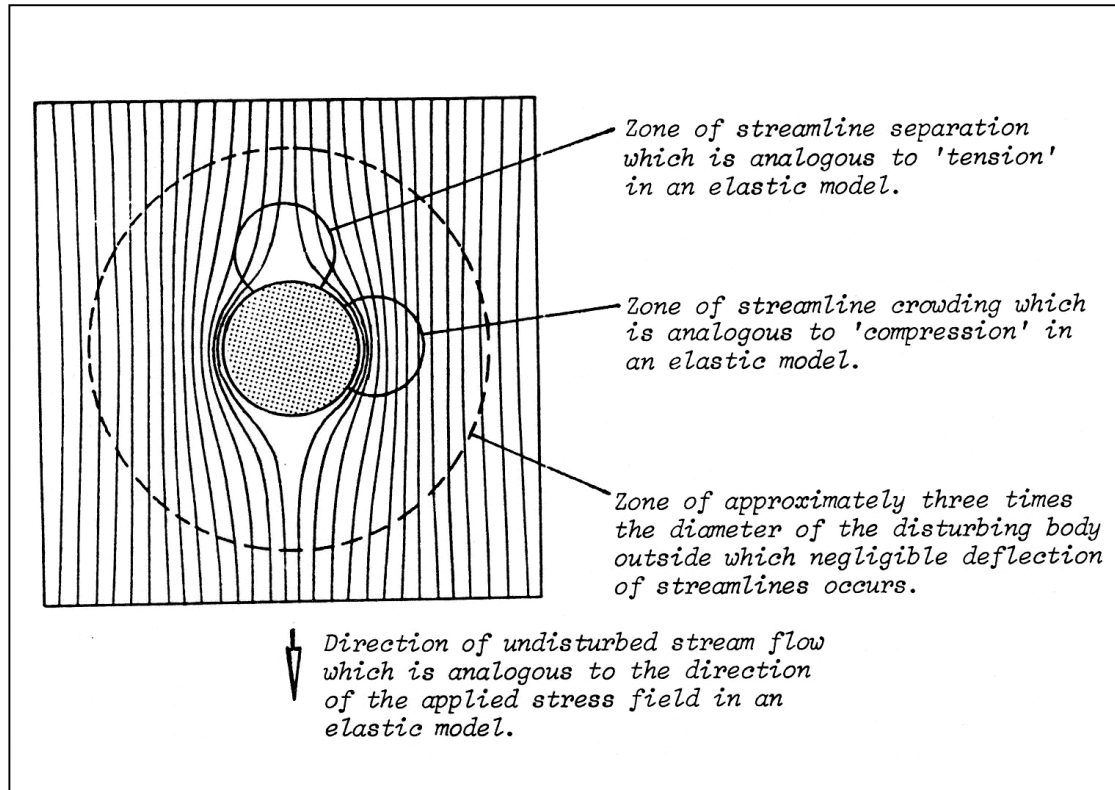


Figure 6.2. Deflection of streamlines around a cylindrical obstruction (from Hoek & Brown, 1980)

One of the first solutions for the two-dimensional distribution of stresses around an opening in an elastic body was published by Kirsch (1898) for a simple cross-sectional shape, a circular hole of an infinitely long tube within an infinite medium. The Kirsch equations are described in Section 2.2.1 a). Kirsch's equations show that the magnitude of stresses around the opening are related to the magnitude of the far field stress, the ratio of horizontal to vertical stress, the dimensions of the opening and the distance from the opening.

The Kirsch equation (Equation 2.1) shows that tensile stresses can be induced around a cylindrical opening in a compressive stress field. When the K value is three or greater, negative tangential stresses are induced at the opening boundary on the surface perpendicular to the maximum field stress, as shown by solving the Equation 2.1 for tangential stress.

$$\sigma_{\theta\theta} = \frac{\sigma_v}{2} \left[(1+K) \left(1 + \frac{a^2}{r^2}\right) + (1-K) \left(1 + \frac{3a^4}{r^4}\right) \cos 2\theta \right] \quad (2.1)$$

at the opening boundary, $a = r$ and,

$$\sigma_{\theta\theta} = \sigma_3 \{ (1+K) + 2(1-K) \} = \sigma_3 (3-K) \quad (6.1)$$

The Kirsch equations (Equation 2.1) also show that the zone of rock which will be in relaxation will increase in size as a direct function of the radius of the opening.

6.3 Assessment of Opening Geometry and Relaxation Extent

The geometry of underground openings is often very complicated and a simple and representative method of assessing the geometry of the walls of underground openings was adopted for this study. Simple and representative methods for quantifying the relaxation zone are also used.

6.3.1 Hydraulic Radius and Radius Factor

Hydraulic radius, HR, and radius factor, RF, are both terms used to quantify surface geometry for rock mechanics design, as briefly reviewed in Section 2.3.3. The hydraulic radius term was used in previous work on stope hanging wall dilation and the zone of relaxation (Clark, 1998). The radius factor is another term that has been used for assessing the geometry of more complex opening surfaces (Milne, 1997). Equations 2.31 and 2.32 show how HR and RF, respectively, are calculated. Both terms are used in this study.

For simple rectangular tunnels or drifts, the geometry of the tunnel roof or back can be adequately described by the tunnel width or span. The hydraulic radius of a rectangular tunnel converges to half the tunnel span as the tunnel length increases.

For a circular surface, the RF is equal to HR. For a square surface, the RF is about 1.1 times HR due to the increased distance to the abutment in the corners (Milne, 1997). For a rectangular shaped surface with a span of S and a length of L, the RF can be calculated by equation 6.2 (Milne, 1997):

$$RF = \frac{\pi}{8} \frac{L \times S}{\sqrt{L^2 + S^2}} \quad (6.2)$$

or

$$RF = \frac{\pi \times (L + S)}{4\sqrt{L^2 + S^2}} \times HR \quad (6.3)$$

The RF term more accurately represents complicated surface geometries and the HR term is used extensively in Rock Mechanics literature. Both terms are looked at in this study.

6.3.2 Quantifying the Relaxation Zone

Equivalent linear relaxation depth (ELRD) is a term introduced in this study. It is the average depth of relaxation on the excavation surface, and is expressed as:

$$ELRD = \frac{\text{Volume of Relaxation on a Stope Surface}}{\text{Stope Surface Area}} \quad (6.4)$$

The average depth of the relaxation zone, ELRD, was determined by calculating the volume of the relaxation zone and dividing by the area of the surface. The relaxation zone was bounded by the zero stress iso-surface and the surface investigated. The ELRD term was introduced because of its similarity to the Equivalent Linear Overbreak or Slough term (ELOS) developed by Clark (1998) which is the average over break depth on a stope surface and is defined in Section 2.3.5 of Chapter 2.

Expressing average relaxation depth and average depth of slough in the same format allows easy comparison of the two terms and assists in determining if there is a relationship between relaxation and dilution. The eventual goal of this research is to determine if the average depth of relaxation can be empirically related to some component of the average depth of slough or dilution on a slope hanging wall.

6.4 Previous Modelling Studies

The previous sections show the importance of the initial stress state and the opening size on determining the size of the relaxation zone around an opening. Numerical modelling simulations are required to estimate the influence of opening geometry and stress state on the relaxation zone. Detailed two and three dimensional modelling has been conducted. Previous modelling work on the zone of stress relaxation was conducted by Clark (1998) to determine the maximum relaxation depth around a rectangular shaped surface of an open slope. An elastic continuum approach was used to study the size and shape of the zone of relaxation using the indirect boundary element method program Map3D (Wiles, version 35). Eleven different rectangular vertical slope geometries were modelled. Slope heights were varied between 20 m and 100 m and strike lengths were varied between 10 m and 100 m (Figure 6.3). Models were run on isolated slopes only. It was assumed that all the slopes were located at a depth of 500 m. Two stress ratios were defined: $K_h = \sigma_1/\sigma_2$ (where σ_1 is the major principal stress oriented perpendicular to strike and σ_2 is the intermediate principal stress, aligned along the strike); and $K_v = \sigma_1/\sigma_3$ (where σ_3 is the vertical stress). Three in-situ stress regimes were examined: $K_h = K_v = 1.5$; $K_h = K_v = 2.0$; and $K_h = K_v = 2.5$. The modelled results (Figure 6.4) showed a linear relationship between ELOS and hydraulic radius. In this case, ELOS is defined as the average depth of relaxation.

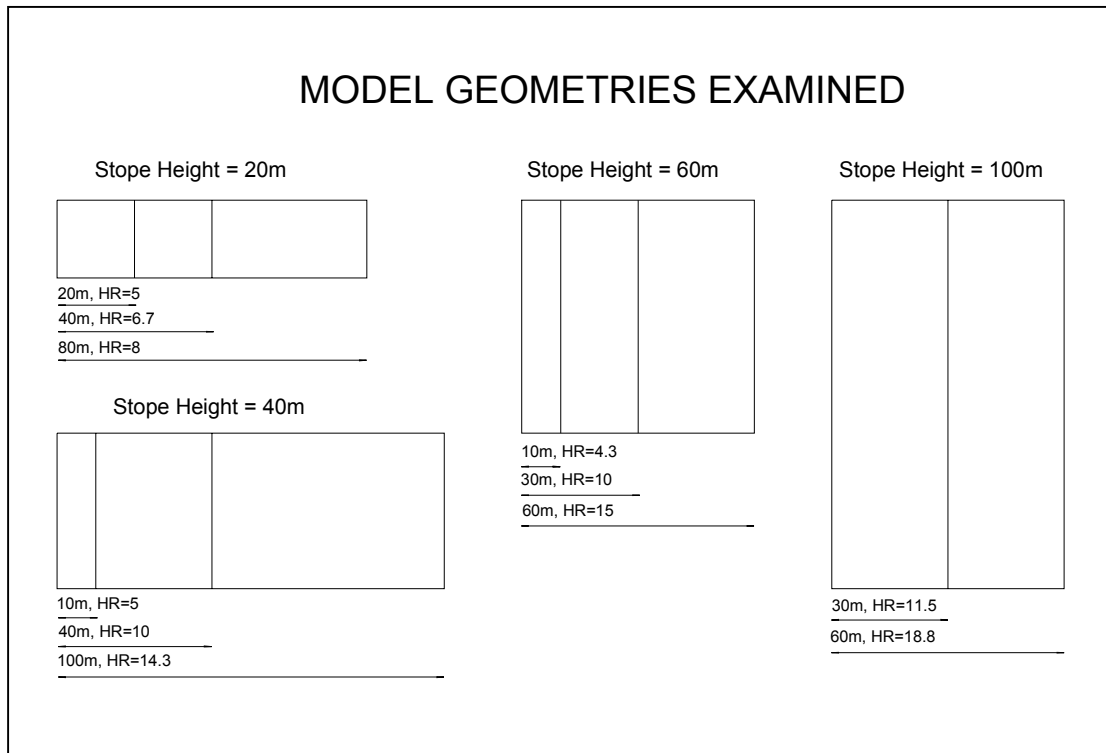


Figure 6.3. Schematic illustrating of model geometries modelled by Clark (1998)

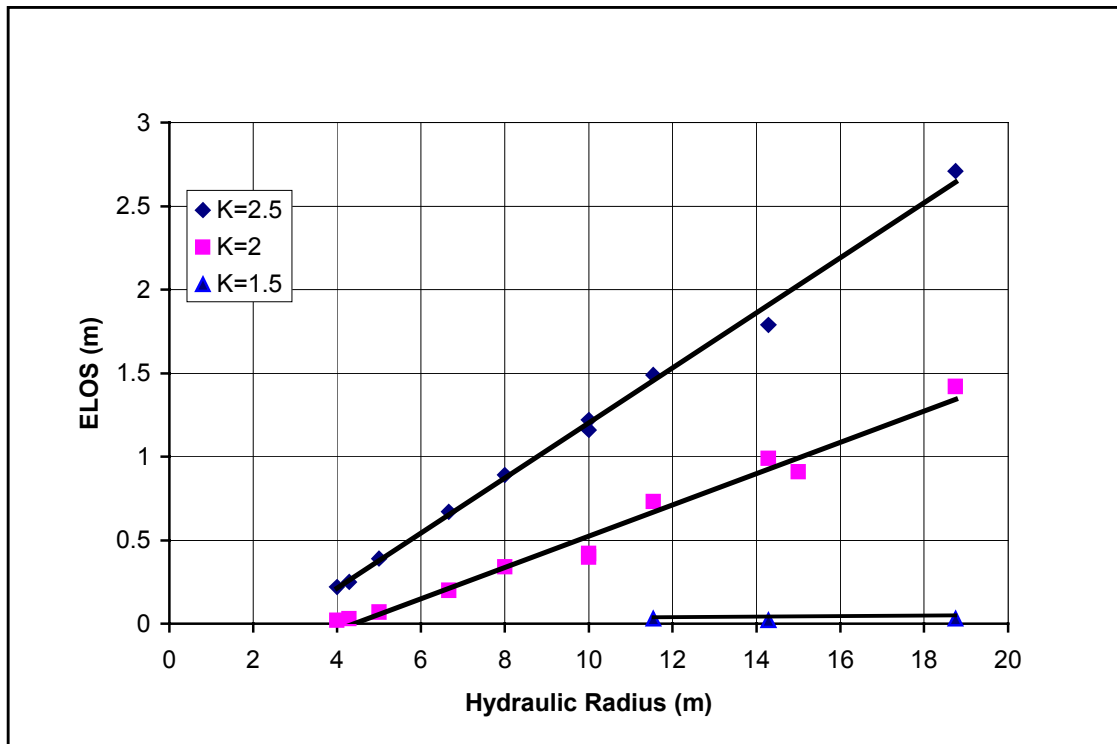


Figure 6.4. ELOS vs. HR (Clark, 1998)

This study indicated that the stress ratios were found to dramatically affect the size of the relaxation zone. Increased stress ratios resulted in significantly increased ELOS values. This work has been advanced through the use of more detailed analysis with a greater variety of opening geometries.

6.5 Current Modelling Studies

Additional modelling work was conducted to look at the relationships presented by Clark (1998). To expand and further investigate the relationship among stope shape, dimensions, stress condition and relaxation extent, the current study was conducted using two boundary element method programs (Examine 3D and Examine 2D, Curran and Corkum, 1993 & 1994). The tasks of the numerical modelling study include the following:

- Reproduce the Map3D modelling conducted by Clark (1998) using the Examine3D code
- Analyze the relationship between radius factor/hydraulic radius, stress ratio and depth of tension for 2D tunnel geometries using Examine2D
- Analyze the relationship between radius factor/hydraulic radius, stress ratio and depth of tension for disc shaped geometries using Examine3D

6.5.1 Modelling Geometries and Input Parameters

A series of simulations was performed on rectangular and circular shaped surfaces of excavations and tunnel geometry surfaces. Figure 6.5 shows the modelling geometry. All the stopes were modelled as isolated stopes and the dip of the hanging wall and footwall were held constant at 90° . All the rectangular and circular shaped stopes had a constant width of 10m. In the study, the stress relaxation zone was defined as the zone around the hanging wall where the minor principal stress was tensile ($\sigma_3 \leq 0$).

The same in-situ vertical stress was used for all the simulations. The major (σ_1), intermediate (σ_2) and minor (σ_3) principal stresses were orientated normal to the stope

hanging wall, parallel to the strike and along the hanging wall dip, respectively. The vertical gravitational overburden stress corresponded to 500 metres depth and was kept constant at approximately 13.5 MPa for the modelled zone. The horizontal stress parallel to the surfaces investigated (i.e. along the strike length) was set equal to the vertical stress (i.e. $\sigma_2 = \sigma_3$) and the horizontal stress perpendicular to the surface investigated was varied and expressed in terms of the stress ratio, K:

$$K = \frac{\sigma_1}{\sigma_3} = \frac{\sigma_1}{\sigma_2} \quad (6.5)$$

where,

σ_1 is the maximum principal stress and perpendicular to the surface investigated, σ_2 is the intermediate principal stress and parallel to the surface investigated, and σ_3 is the vertical and minimum principal stress; $\sigma_3 = \gamma z$ (γ is the overburden rock mass unit weight and z is the stope location depth; in this study $\gamma = 0.027 \text{ MN/m}^3$ and $z = 500 \text{ m}$).

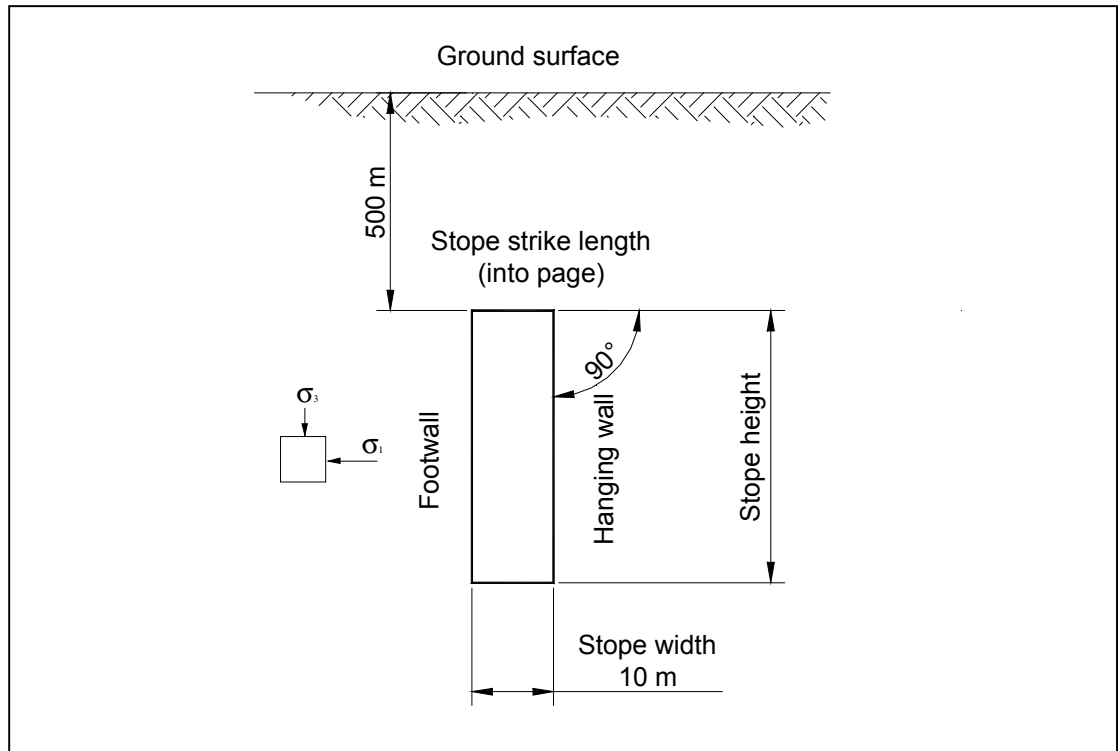


Figure 6.5. Schematic illustration of the numerical modelling geometry.

Three stress regimes ($K = 1.5$, $K = 2.0$ and $K = 2.5$) were examined and linear elastic, homogenous, isotropic rock material properties were assumed. Modelled deformations were not considered important for this analysis and rock mass properties have a negligible effect on the stresses for an elastic continuum. To fulfill the model input requirements, a rock modulus of elasticity of 50 GPa and a Poisson's ratio of 0.2 were assumed. The excavation boundary was divided into elements and the element size ranged between $1/20^{\text{th}}$ to $1/10^{\text{th}}$ of the slope height.

Various excavation geometries were modelled to determine if either the hydraulic radius or radius factor terms have a consistent effect on the relaxation zone adjacent to an underground opening. Models were run on rectangular, disc shaped and square tunnel geometries. In all cases the opening surface was quantified using both the HR and RF terms. Three stress regimes, as described in the previous section, were assessed for each opening geometry. Eleven different rectangular shaped stopes were examined for each of the three stress regimes, resulting in 33 simulations. Six different disc shaped geometries were modelled for 18 simulations and 7 tunnel geometries were modelled for an additional 21 simulations. For the tunnel geometries, the stress modelling was accurately performed by treating it as a 2-dimensional plane strain problem. The two dimensional boundary element program Examine 2D was used to examine the relaxation on the tunnel side walls for different side wall heights for each of the three stress regimes.

6.5.2 Modelling Study of Rectangular Hanging Wall Geometries

As described previously, Clark (1998) examined various rectangular shaped stope hanging wall geometries. This section attempts to reproduce the Map3D modelling by using another boundary elementary code, Examine3D.

The modelling geometry configurations are given in Figure 6.3 and Table 6.1.

Table 6.1. Modelling geometry (HW) configurations

Model No.	Stope Height (m)	Strike Length (m)	Surface Area (m ²)	Hydraulic Radius (m)	Radius Factor (m)
1	20	20	400	5.0	5.6
2	20	40	800	6.7	6.7
3	20	80	1600	8.0	7.6
4	40	10	400	4.0	3.8
5	40	40	1600	10.0	11.1
6	40	100	4000	14.3	14.6
7	60	10	600	4.3	3.9
8	60	30	1800	10.0	10.5
9	60	60	3600	15.0	16.7
10	100	30	3000	11.5	11.3
11	100	60	6000	18.8	20.2

Thirty-three simulations (11 geometries with 3 different stress regimes), were run. Figures 6.6, 6.7 and 6.8 illustrate example plots of σ_1 , σ_2 and σ_3 respectively for a 40 m x 40 m stope hanging wall with $K = 2.0$.

Both the relaxation depth at the centre of a stope HW and the average relaxation depth (ELRD) for the stope HW surface were obtained from modelling. The relaxation depth at the centre of the HW was defined as the distance from the excavation boundary surface centre, to the stress iso-surface where $\sigma_3 = 0$. It was noticed that the maximum depth of relaxation was not always at the centre of the HW. For a stress ratio less than 1.5, the maximum depth of relaxation is at the centre of the HW. As the K value increases, the maximum depth of relaxation lies somewhere between the abutment and the centre of the HW. The location of maximum relaxation depth is discussed in detail in Appendix III.

The depth of relaxation at the centre of the HW was measured from the modelling results. Table 6.2, Figure 6.9 and Figure 6.10 show the modelling results for varied surface HR and RF values and stress ratios for rectangular shaped stope hanging walls.

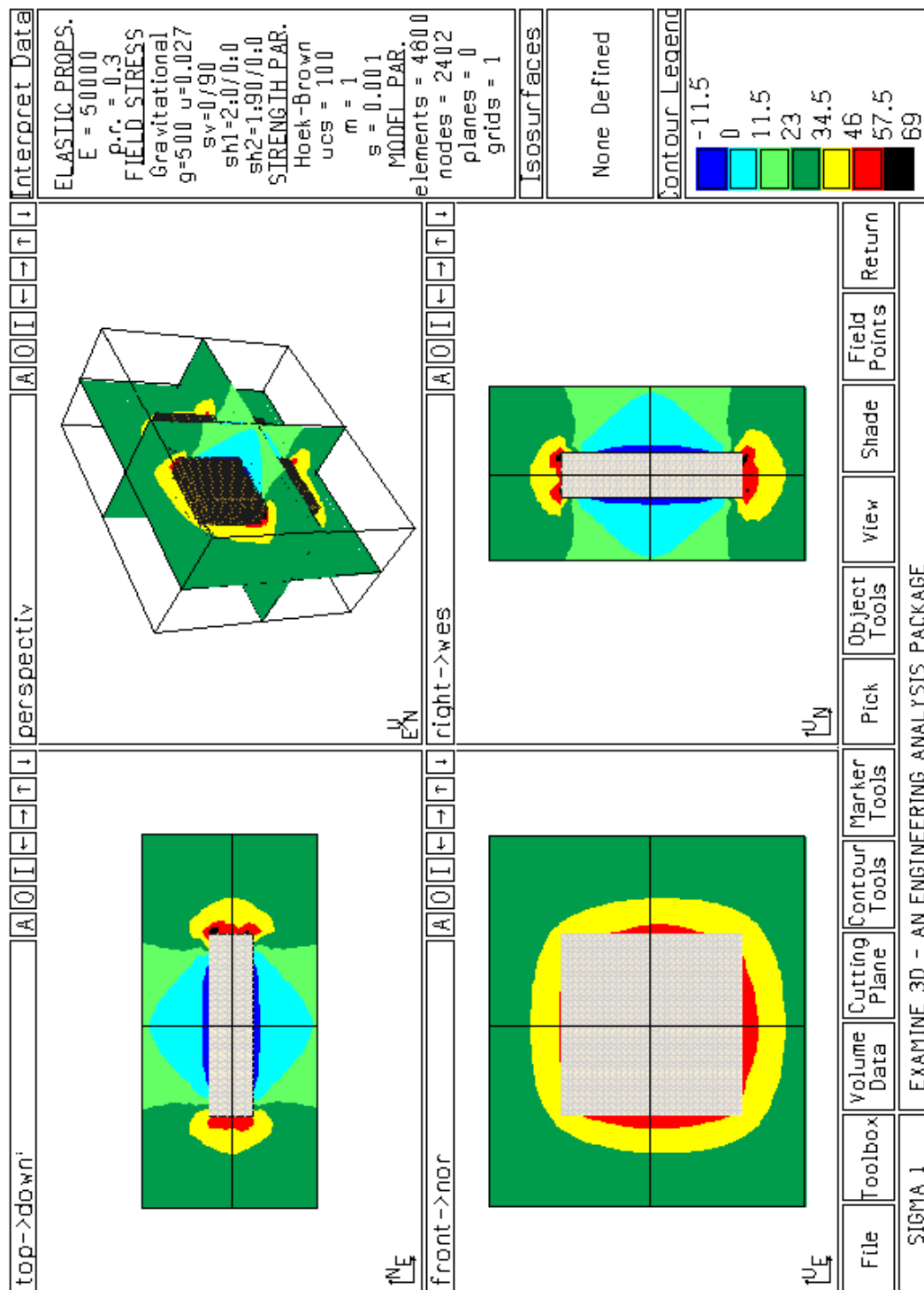


Figure 6.6. σ_1 predicted using Examine3D; example plot for a 40x40x10m slope with K=2.0

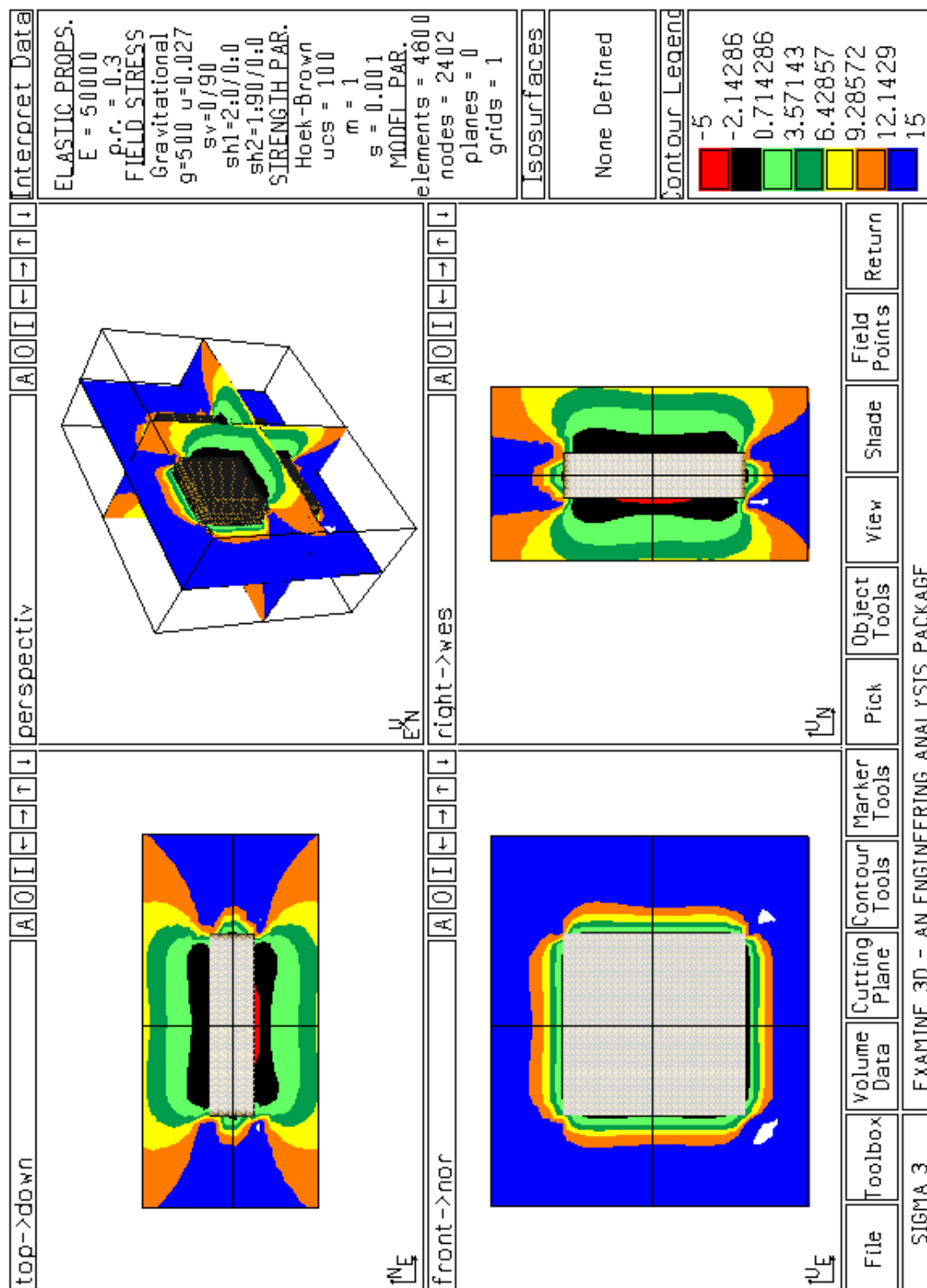


Figure 6.8. σ_3 predicted using Examine3D; example plot for a 40x40x10m slope with $K=2.0$

Table 6.2. Modelled results showing the depth of relaxation at the centre of a slope HW for rectangular shaped HWs

Dimension	HR	RF	Relaxation Depth at Centre of HW (m)		
			K=2.5	K=2.0	K=1.5
20 x 20	5	5.6	2.2	1.1	0.9
20 x 40	6.7	7	2.5	1.2	1
20 x 80	8	7.6	2.6	1.8	1.3
40 x 10	4	3.8	1	0.5	0.6
40 x 40	10	11.1	4.4	2.8	1.4
40 x 100	14.3	14.6	6.4	3.5	2
60 x 10	4.3	3.9	0.8	0.6	0.8
60 x 30	10	10.5	4.4	2	1.7
60 x 60	15	16.7	7.3	4.5	2
100 x 30	11.5	11.3	4.3	3.4	1.7
100 x 60	18.8	20.2	9.6	5.2	2.2

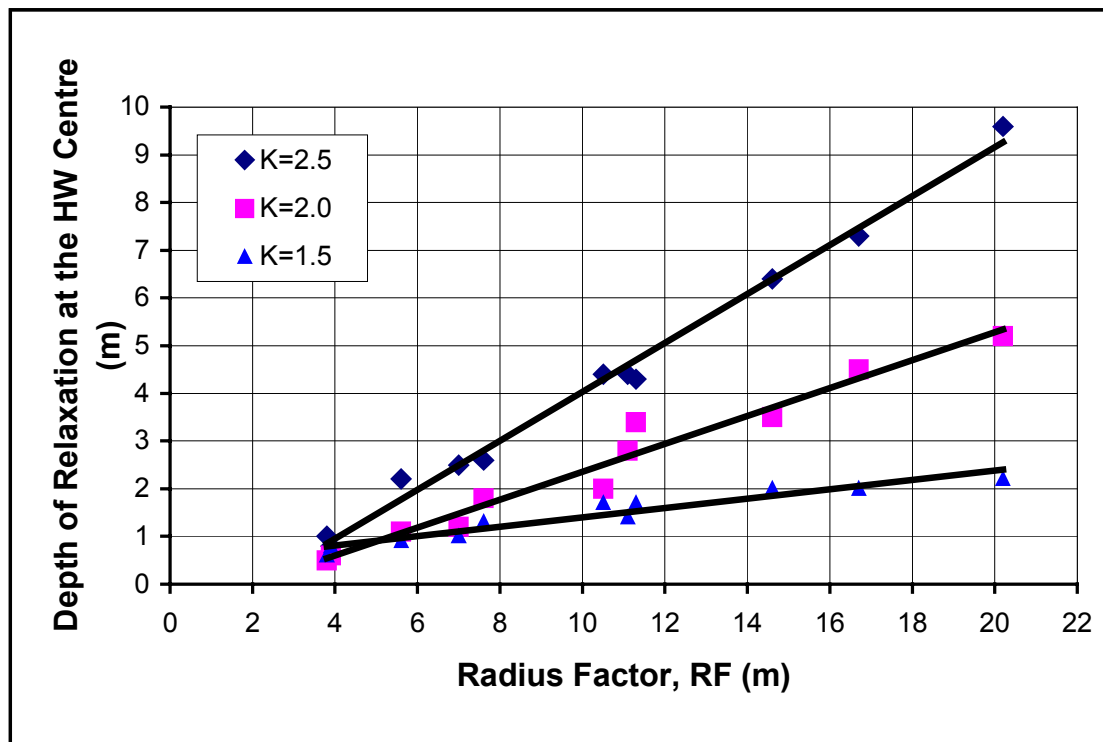


Figure 6.9. The depth of relaxation at the centre of the slope HW vs. radius factor for different stress ratios for rectangular shaped slope HWs

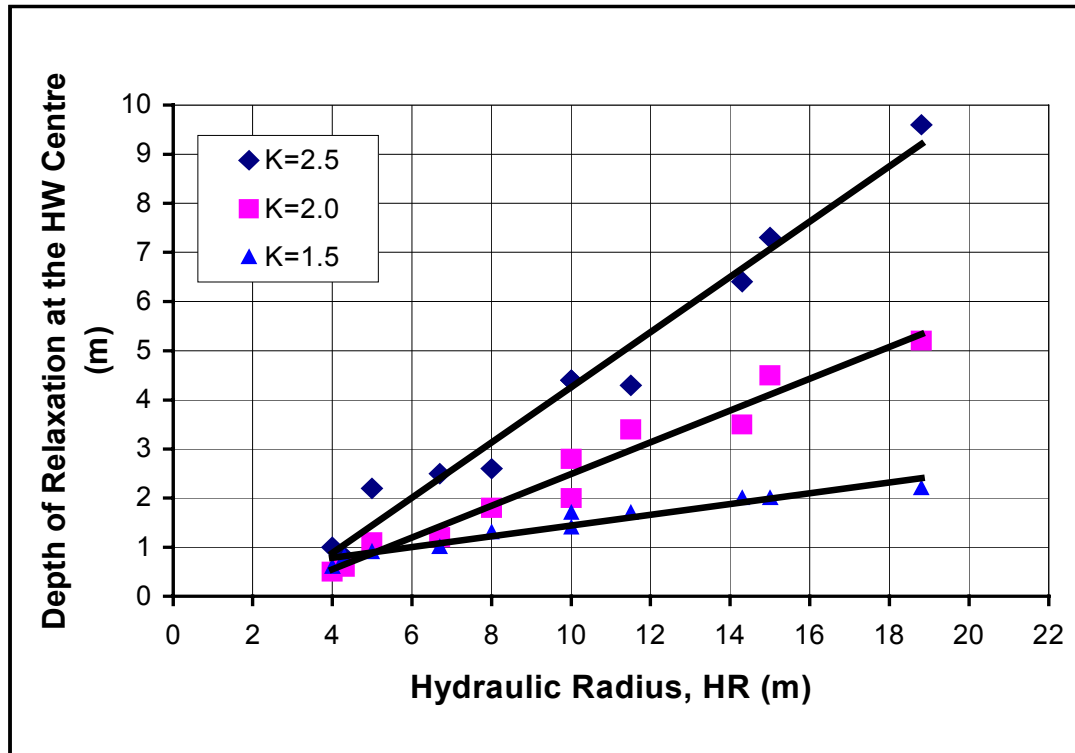


Figure 6.10. The depth of relaxation at the centre of the stope HW vs. hydraulic radius (HR) for different stress ratios for rectangular shaped stope HWs

ELRD, as described in section 6.3.2, is the average depth of relaxation on a stope HW. The ELRD value is obtained by measuring the modelled relaxation volume in the HW divided by the area of the HW. The modelled ELRDs for modelling rectangular shaped HW are listed in Table 6.3. The ELRD versus radius factor and hydraulic radius plots for different stress ratios are shown in Figures 6.11 and 6.12.

The modelling results showed that both the depth of relaxation at the centre of a stope HW and the ELRD are related to the radius factor or hydraulic radius and the stress ratio K . With an increase in relaxation depth, the relaxation volume will increase. The findings are listed as follows:

- With an increase in the radius factor or hydraulic radius, both the relaxation depth at the centre of the stope HW and the ELRD increases

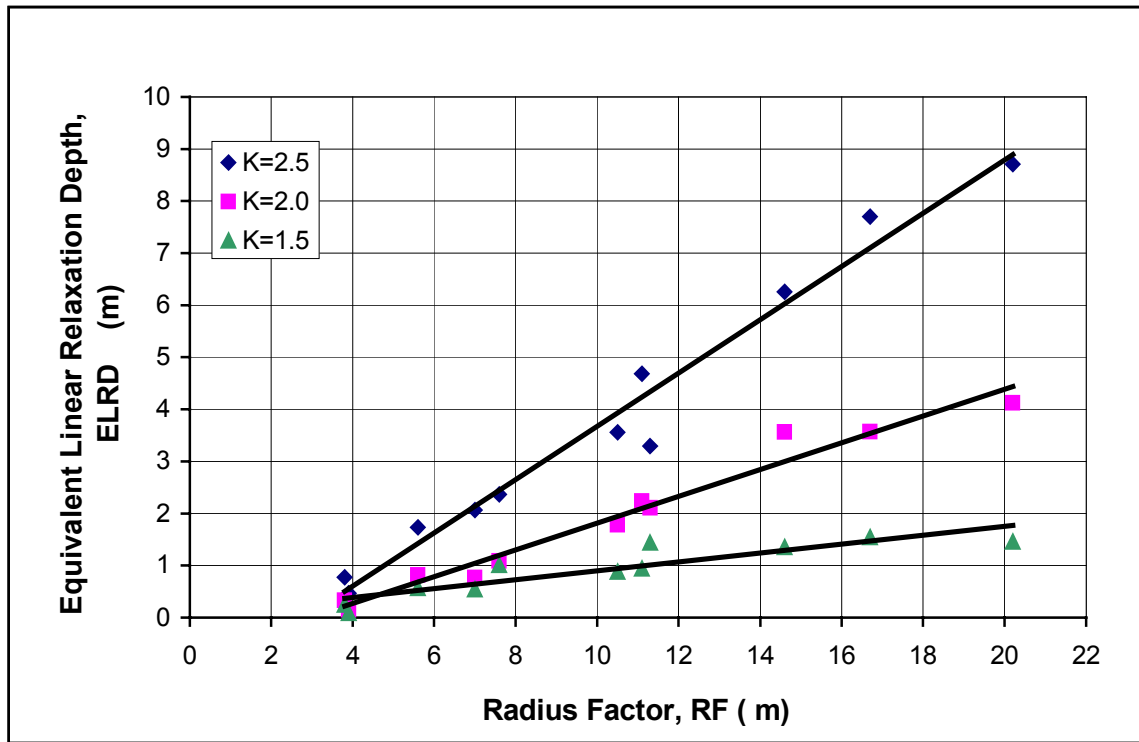


Figure 6.11. ELRD vs. radius factor for different stress ratios for rectangular shaped stope hanging walls

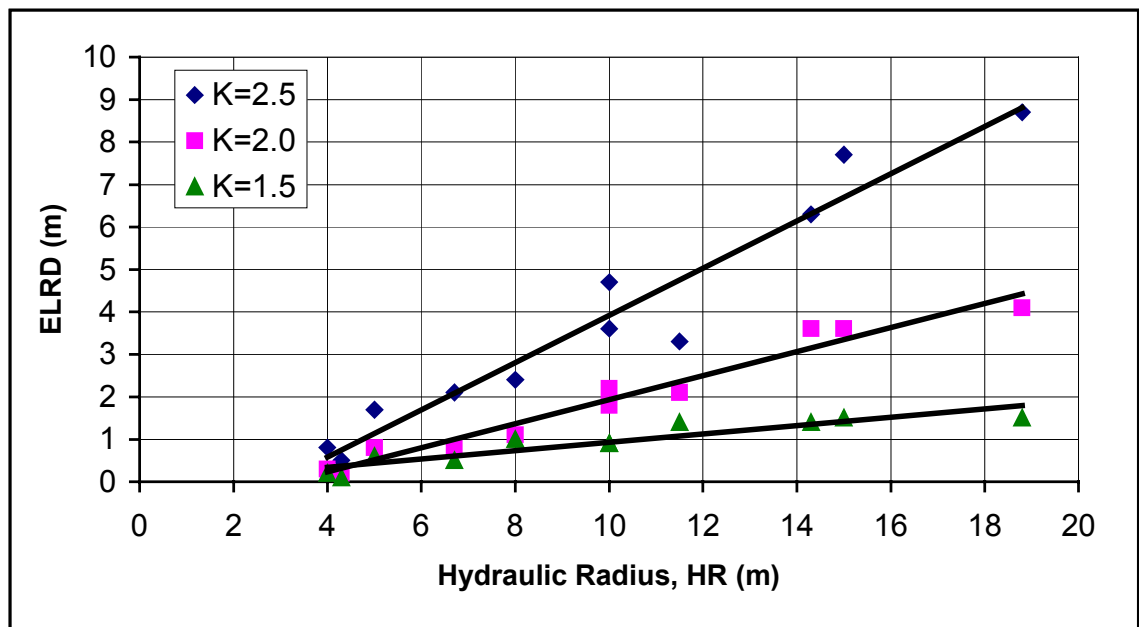


Figure 6.12. ELRD vs. HR for different stress ratios for rectangular shaped stope hanging walls

Table 6.3. Modelled results of ELRD for a rectangular shaped HW

Dimension	Area (m ²)	HR (m)	RF (m)	ELRD (m)		
				K=2.5	K=2.0	K=1.5
20 x 20	400	5.0	5.6	1.7	0.8	0.6
20 x 40	800	6.7	7.0	2.1	0.8	0.5
20 x 80	1600	8.0	7.6	2.4	1.1	1.0
40 x 10	400	4.0	3.8	0.8	0.3	0.2
40 x 40	1600	10.0	11.1	4.7	2.2	0.9
40 x 100	4000	14.3	14.6	6.3	3.6	1.4
60 x 10	600	4.3	3.9	0.5	0.2	0.1
60 x 30	1800	10.0	10.5	3.6	1.8	0.9
60 x 60	3600	15.0	16.7	7.7	3.6	1.5
100 x 30	3000	11.5	11.3	3.3	2.1	1.4
100 x 60	6000	18.8	20.2	8.7	4.1	1.5

- The stress ratio has a significant effect on depth of relaxation at the HW centre and the ELRD. The higher the stress ratio, the larger the maximum relaxation depth
- For the three stress regimes modelled, the relaxation depth at the centre of a surface has a linear relationship with radius factor and hydraulic radius
- Similar relationships exist between ELRD and RF and between ELRD and HR. With an increase in RF and HR, ELRD increases linearly
- The RF value appeared to show a slightly better trend than the HR value.

6.5.2.1 Comparison with Previous Modelling Studies

Previous work by Clark (1998), shown in Figure 6.4, also showed a linear relationship between ELOS and the hanging wall HR. However, the slope of the lines relating the average relaxation depth (ELRD) and hanging wall HR predicted in the current modelling study did not match the work by Clark (1998). For a 60 m × 60 m stope (HR = 18.8) and a stress ratio K = 2.5, work by Clark (1998) gives an estimated average depth of relaxation (ELRD) of about 2.7 meters whereas the current study suggest an ELRD of 7.3 meters. To verify the accuracy of the relationship between ELRD and HR,

additional modelling work has been done by looking at more varied hanging wall geometries and by using a second computer modelling code. The modelling results show that the current work gives consistent trends.

The following modelling studies assess the hanging wall geometry in terms of the radius factor. The radius factor is a better term for assessing varied geometries and the RF term appeared to show a more linear trend with the HW relaxation zone extent.

6.5.3 Relationship between Radius Factor, Stress Ratio K and the Depth of Relaxation for 2D Tunnel Geometries

The radius factor (RF) has been related to tunnel wall sizes (Milne, 1997). A tunnel geometry is defined as a rectangular shaped surface geometry with a width of S (span), a height of H and an infinite length L. For general rectangular geometries, the radius factor was defined in equation 6.2

The RF and HR for a tunnel side-wall can be determined from the following equation:

$$RF = \lim_{L \rightarrow \infty} \left(\frac{\pi}{8} \frac{L \times H}{\sqrt{L^2 + H^2}} \right) \approx \frac{\pi}{8} \left(\frac{\infty \times H}{\infty} \right) = \frac{\pi}{8} H \quad (6.6)$$

$$HR = \lim_{L \rightarrow \infty} \frac{H \times L}{2(H + L)} = \frac{H}{2} \quad (6.7)$$

Therefore, the radius factor can be estimated for tunnel walls. For a tunnel geometry, we can simplify the stress modelling into a 2D plane strain problem. The boundary element program Examine 2D was used to examine the maximum depth of relaxation with different equivalent tunnel wall size for three different stress regimes. For easy comparison, all tunnel cross sections are square. Seven tunnel wall size geometries were examined, as shown in Table 6.4.

The depth of relaxation at the middle height of the side-wall and the ELRDs were

obtained from each of the 7 model geometries and 3 stress regimes and are presented in Table 6.5. Figure 6.13 shows the depth of relaxation at the middle height of the side-wall versus RF for the three stress regimes. Figure 6.14 is the ELRD versus RF plot for tunnel geometries. With an increase in the surface dimension (expressed in terms of radius factor), the relaxation depth increases linearly. The stress ratio has a significant influence on the maximum depth of relaxation.

Table 6.4. Examine 2D geometries modelled

No.	Tunnel Cross Section Size (m ²)	Tunnel Height (m)	Side Wall HR (m)	Side Wall RF (m)
1	10 x 10	10	5	3.93
2	15 x 15	15	7.5	5.89
3	20 x 20	20	10	7.85
4	25 x 25	25	12.5	9.8
5	30 x 30	30	15	11.78
6	35 x 35	35	17.5	13.74
7	40 x 40	40	20	15.71

Table 6.5. Maximum relaxation depth and ELRD for tunnel geometries

No.	Tunnel Section Size (m ²)	Tunnel Height (m)	RF	Relaxation Depth at the middle Height of Side-walls (m)			ELRD (m)		
			HR (m)						
				K=1.5	K=2.0	K=2.5	K=1.5	K=2.0	K=2.5
1	10 x 10	10	3.93	1.0	1.1	1.5	0.4	0.5	1.0
			5						
2	15 x 15	15	5.89	1.2	1.3	2.3	0.7	0.9	1.6
			7.5						
3	20 x 20	20	7.85	1.3	1.7	3.2	0.8	1.4	2.4
			10						
4	25 x 25	25	9.8	1.0	1.8	4.3	1.0	1.6	3.1
			12.5						
5	30 x 30	30	11.8	1.5	2.8	4.9	1.2	2.0	4.1
			15						
6	35 x 35	35	13.7	1.9	3.9	6.1	1.4	2.4	5.0
			17.5						
7	40 x 40	40	15.7	2.0	4.1	7.0	1.6	3.0	6.0
			20						

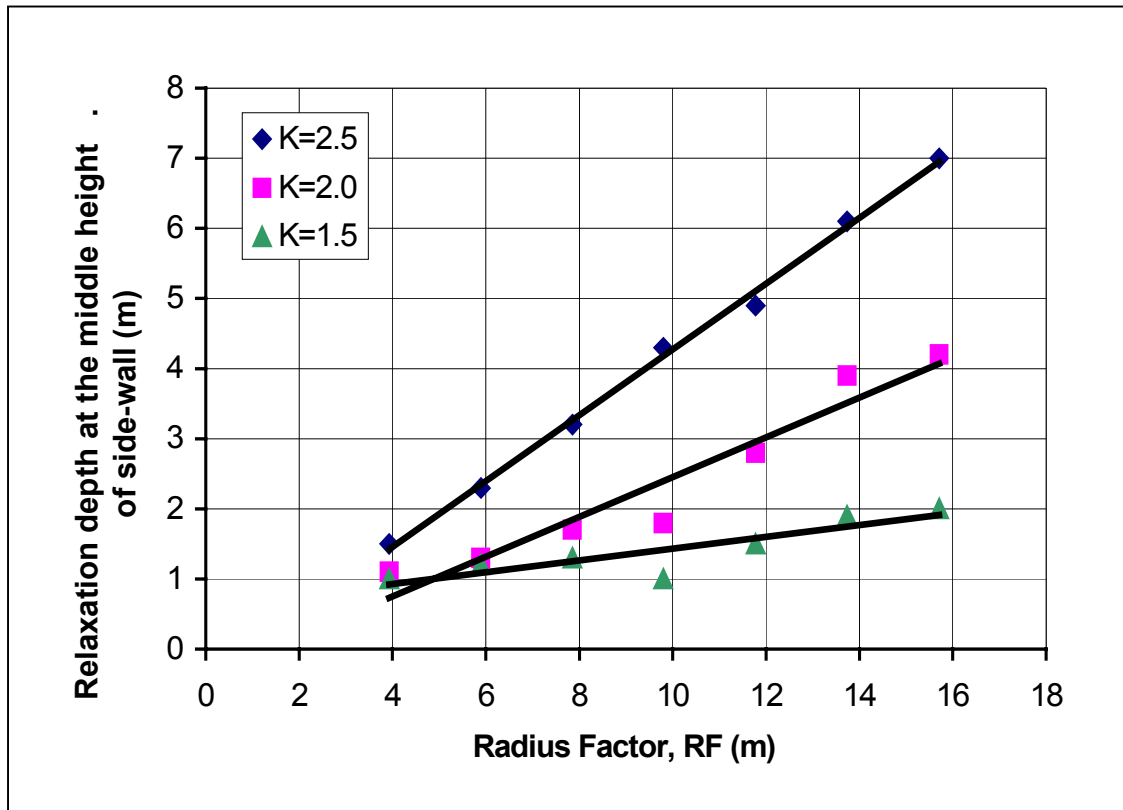


Figure 6.13. Relaxation depth at middle height of side-walls vs. RF for K=1.5, 2.0 and 2.5

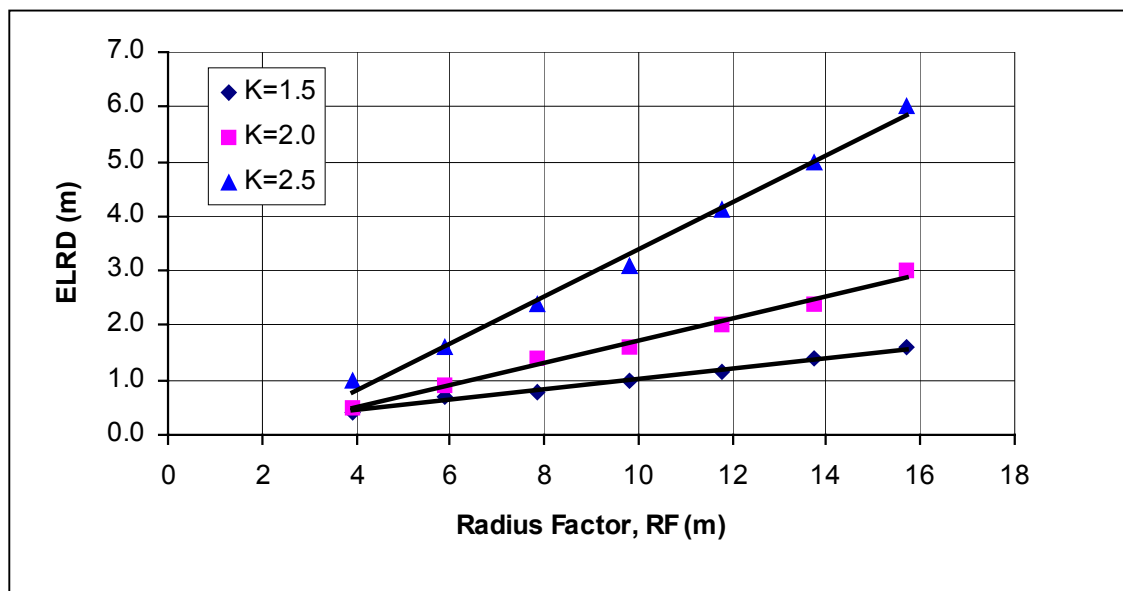


Figure 6.14. Variation of ELRD with radius factor for tunnel side walls

6.5.4 Modelling Study of Disc Shaped Geometries

To further determine the effect of surface geometry, six different disc shaped openings were modelled for each of the three stress regimes. The end wall surfaces of each disc were oriented vertically. Table 6.6 lists the geometries modelled.

Examine 3D was used for the modelling. The modelled results show that the stress distribution around a disc shaped excavation is similar to that for rectangular shaped excavations. The stresses are concentrated on the side of the excavation along the cylindrical wall and are relaxed around the centre of the disc end walls. Figure 6.15, 6.16 and 6.17 illustrate the example stress distributions for a disc shaped excavation. Table 6.7 and 6.8 present the modelled results of depth of relaxation at the centre of the disc end wall and the ELRD on the end wall, respectively. The variation of depth of relaxation at the centre of an end wall surface (Hanging wall) and the ELRD with the radius factor for disc shaped openings is shown in Figure 6.18 and 6.19 respectively. The results were similar to those for the rectangular shaped openings.

Table 6.6. Modelling geometries for disc shaped openings

No.	Disc Height (m)	Disc Radius (m)	End Wall Surface Area (m ²)	End Wall Surface HR (m)	End Wall Surface RF (m)
1	10	10	7.85	5	5
2	10	16	12.6	8	8
3	10	20	15.7	10	10
4	10	26	20.4	13	13
5	10	30	23.6	15	15
6	10	36	28.3	18	18

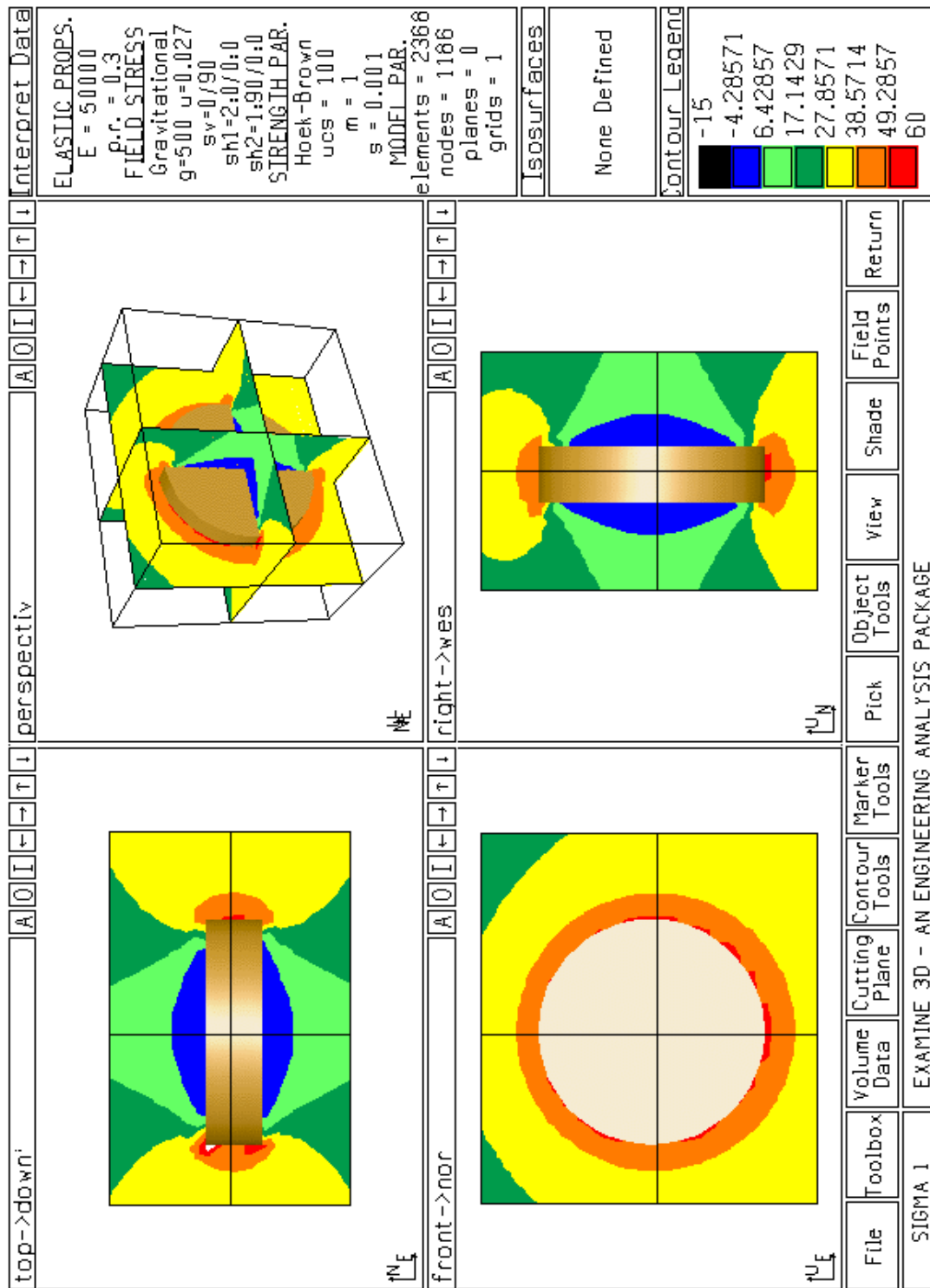


Figure 6.15. σ_1 predicted using Examine3D; example plot for a 20 m radius disc shaped opening with $K=2.0$

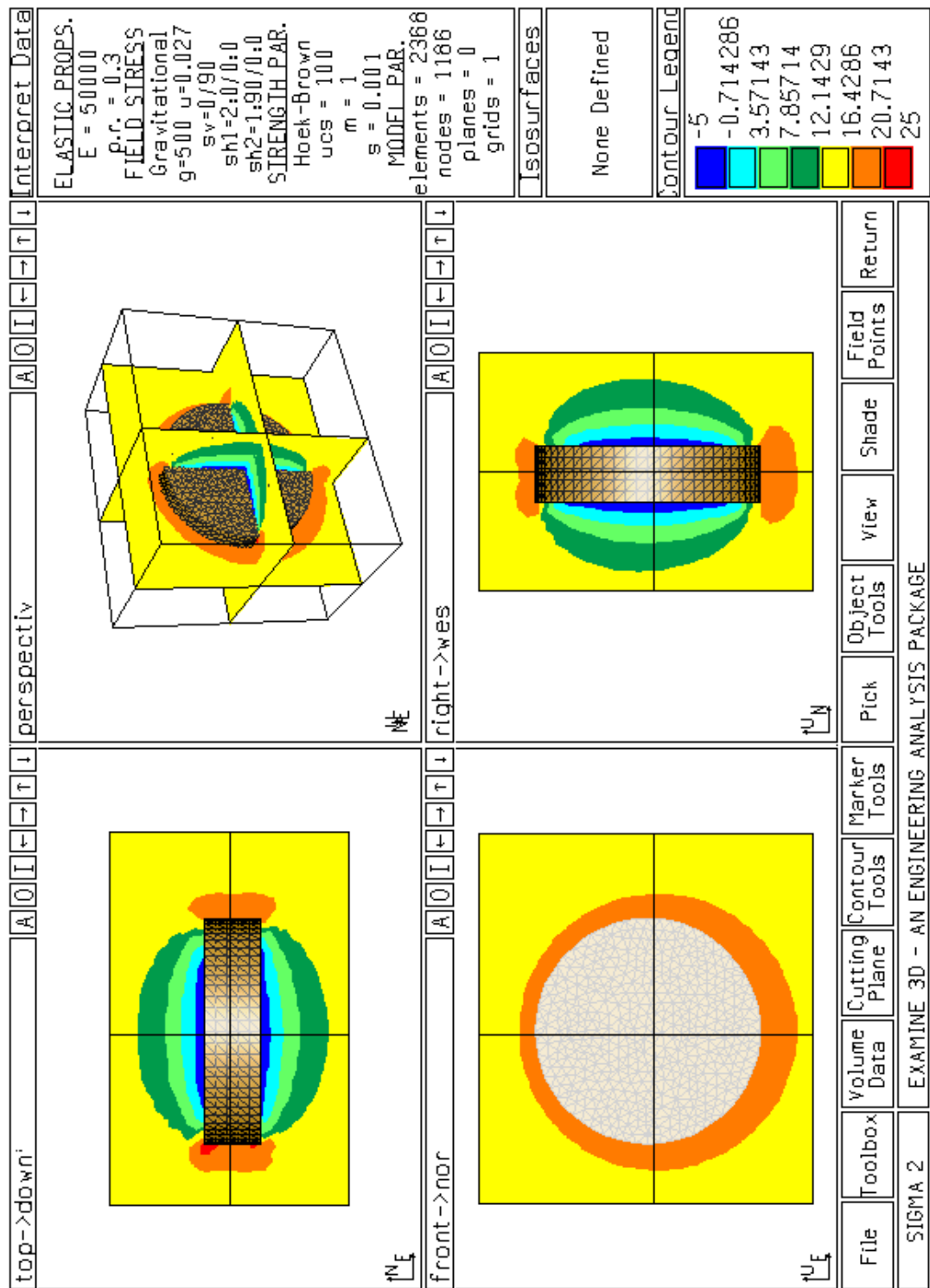


Figure 6.16. σ_2 predicted using Examine3D; example plot for a 20 m radius disc shaped opening $K=2.0$

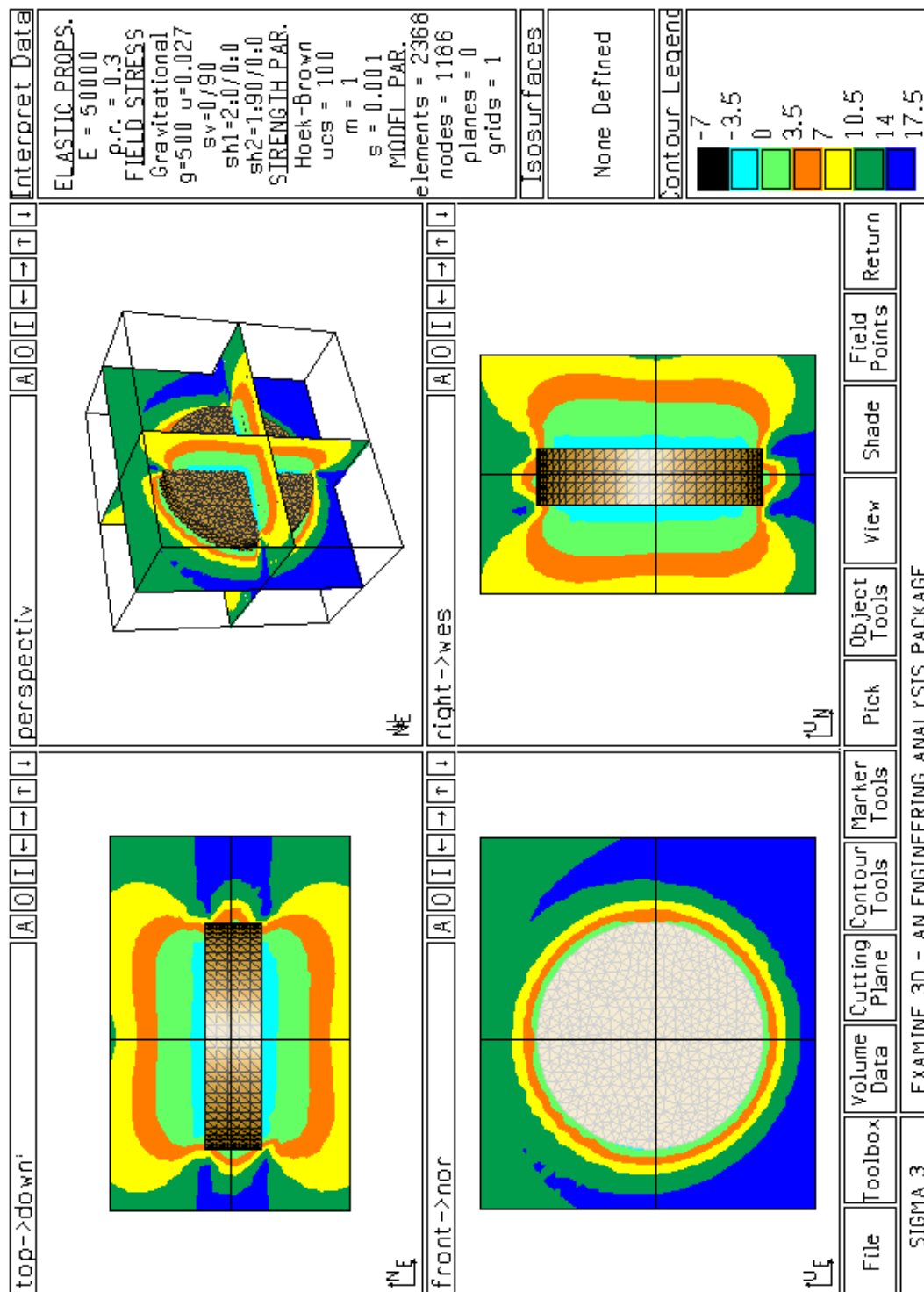


Figure 6.17. σ_3 predicted using Examine3D; example plot for a 20 m radius disc shaped opening with $K=2.0$

Table 6.7. Relaxation depth at the centre of HW

Radius (m)	HR	RF	Relaxation Depth at the Centre of HW (m)		
			K=2.5	K=2.0	K=1.5
10	5	5	1.3	0.7	0.3
16	8	8	3	1.7	1.2
20	10	10	4	2.6	1.5
26	13	13	5.1	3.4	1.7
30	15	15	6.7	4.1	2.5
36	18	18	8.1	5.1	2.8

Table 6.8. ELRD for disc shaped stope HW modelling results

No.	Radius (m)	Surface Area (m ²)	HR (m)	RF (m)	ELRD (m)		
					K=1.5	K=2.0	K=2.5
1	10	314	5	5	0.3	0.4	1.2
2	16	804	8	8	0.7	1.2	2.5
3	20	1257	10	10	1.0	1.6	3.4
4	26	2124	13	13	0.8	2.2	4.8
5	30	2827	15	15	1.2	2.8	6.6
6	36	4072	18	18	1.6	4.3	8.3

6.5.5 Discussion of the Modelling Results

The modelled results of the depth of relaxation at the centre of a HW surface and the average relaxation depth, ELRD, were compared for rectangular shapes, square tunnel geometries and disc shaped openings for three stress regimes. There was good agreement among different shapes modelled for both the depth of relaxation at the surface centre and the ELRD. Figures 6.20 and 6.21 show the overall comparison of depth of relaxation at the centre of stope HW in terms of the RF and HR values, respectively. Figures 6.22 and 6.23 show the overall ELRD comparison for different shaped models for three stress regimes in terms of RF and HR, respectively.

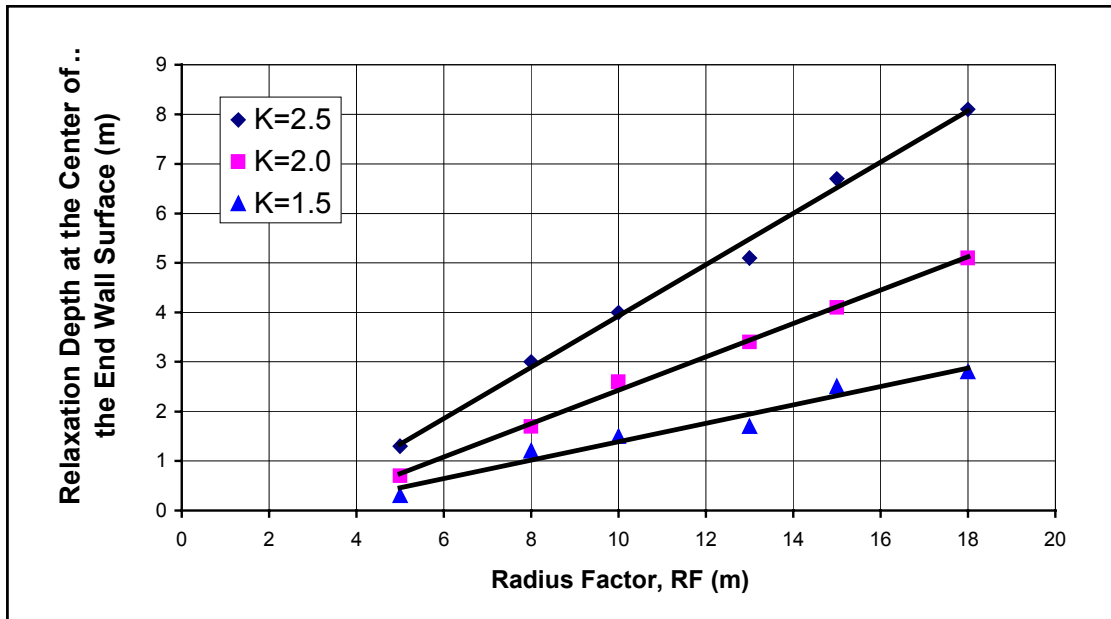


Figure 6.18. The depth of relaxation at the centre of the slope vs. radius factor for different stress ratios for disc shaped slope hanging walls

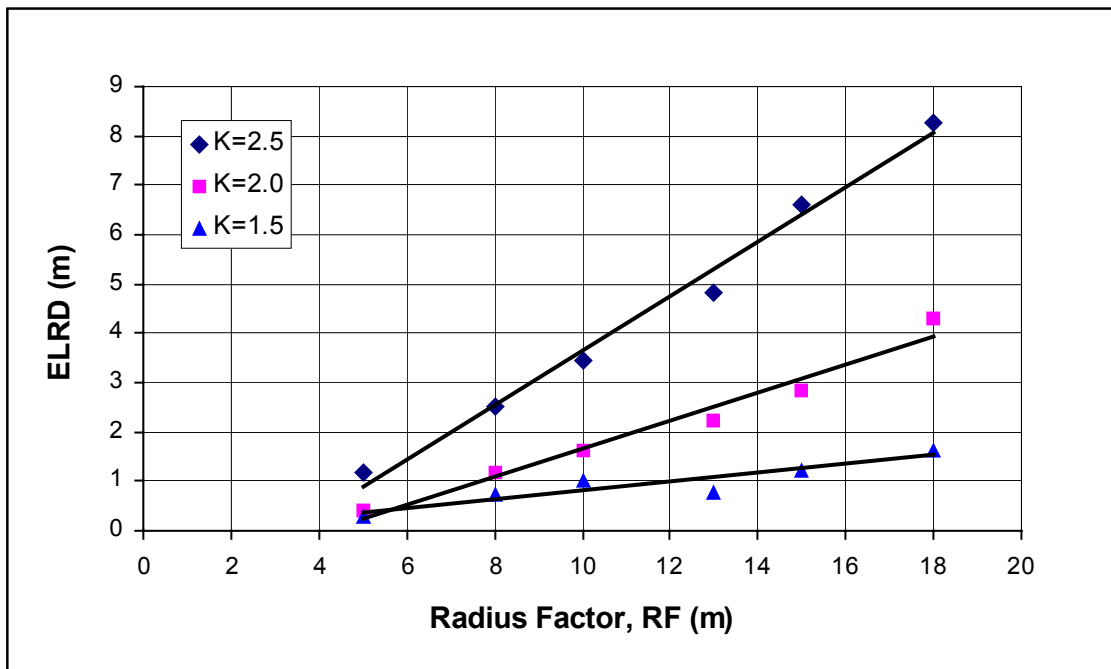


Figure 6.19. ELRD vs. radius factor plot with three stress regimes for disc shaped surfaces

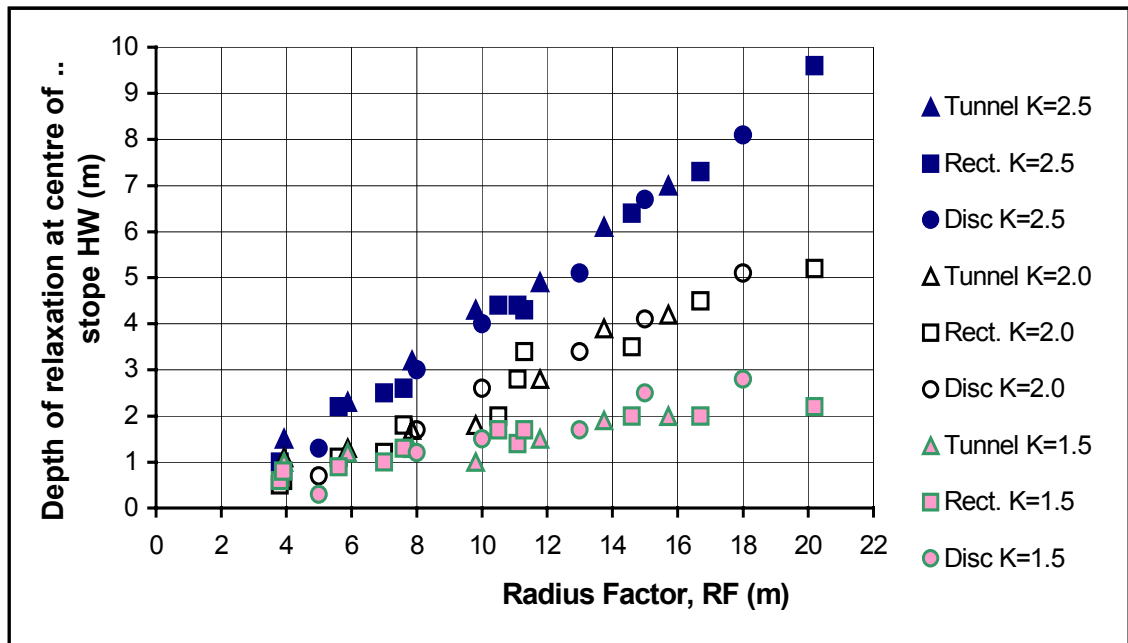


Figure 6.20. Overall comparison of depth of relaxation at the centre of stope HW versus RF for different shaped models for three stress regimes

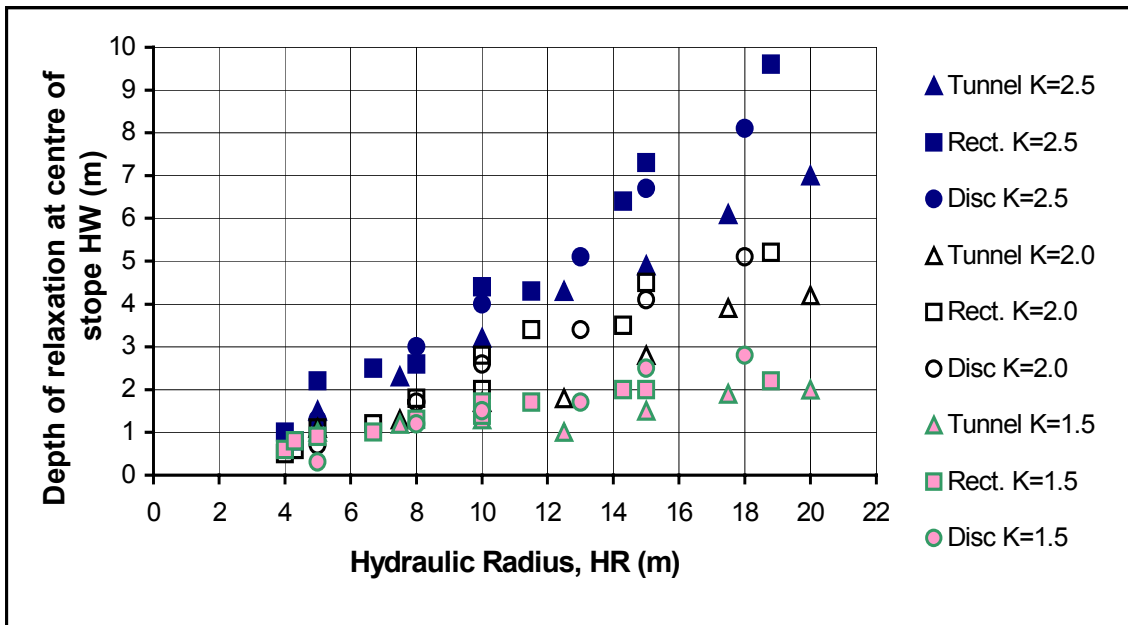


Figure 6.21. Overall comparison of depth of relaxation at the centre of stope HW versus HR for different shaped models for three stress regimes

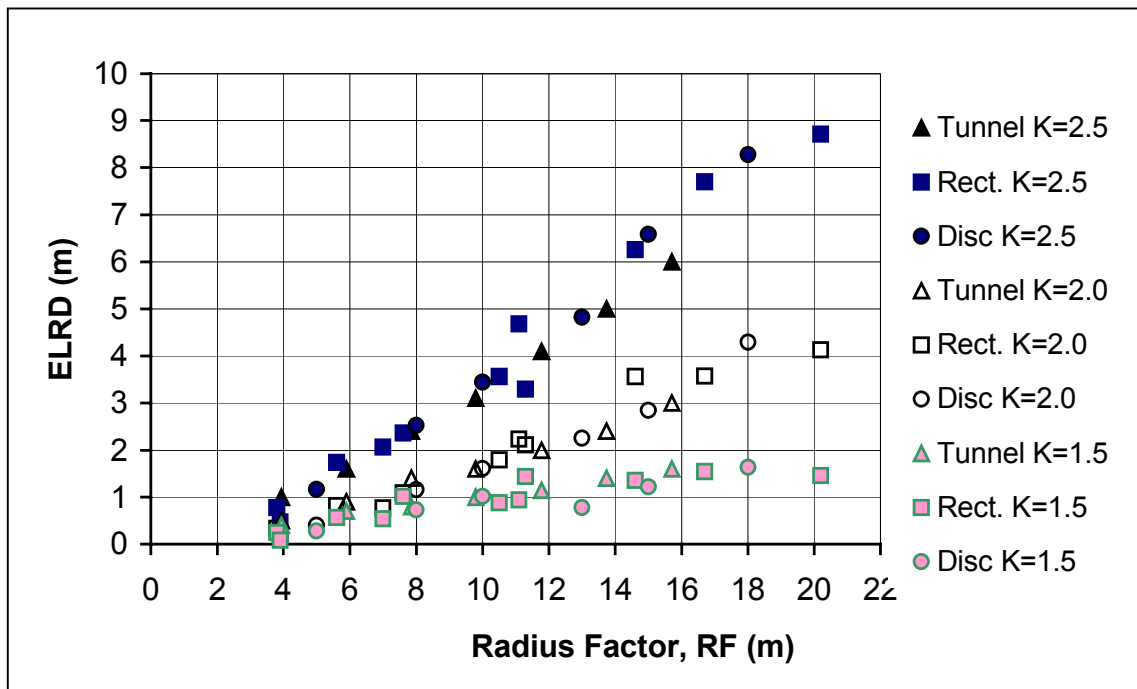


Figure 6.22. Overall comparison of ELRD vs. RF for different shaped models for three stress regimes

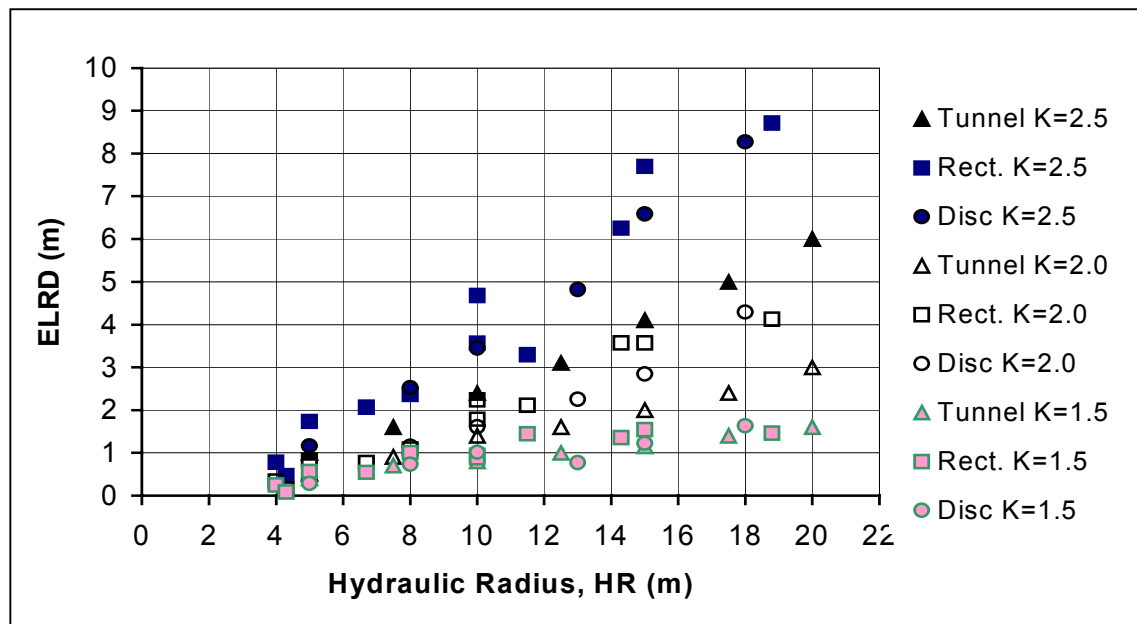


Figure 6.23. Overall comparison of ELRD vs. HR for different shaped models for three stress regimes

The results for different geometries show the same linear relationship between relaxation depth and the surface geometry shape factor, RF , as well as between ELRD and surface geometry shape factor, RF , for a given stress level. This is significant because it means that the depth of relaxation and ELRD can be estimated for a surface geometry, provided the stress ratio and geometry is known. The relationship between relaxation depth and the HR , as well as between ELRD and HR also showed a similar relationship. There is, however, a greater degree of scatter. It was noticed that this scatter was primarily due to the differences in tunnel geometry for the cases considered.

As described by Milne (1997), the HR has some shortcomings in accounting for surface geometries that are non-circular shapes. For a circular opening the HR and RF values give the same results. Figure 6.24 shows how the HR and RF factors assess the geometry of a 10 metre wide opening with an increasing length. The tunnel wall is a special case of a rectangular surface with an infinite length. Milne (1997) stated that “for a rectangular opening with a given span, the length is 9 times the span before the hydraulic radius is equal to 90% of its maximum. This implies the ends of a drift apply significant support to the centre”. The radius factor geometry assessment ceases to be significantly influenced by the ends of an opening when the opening length is about three times the width. Modelling results suggest the RF value does a better job of quantifying surface geometry for assessing the relaxation zone when the opening aspect ratio is greater than 3. The HR term over emphasises the influence of opening length on the stress redistribution when the opening length to width ratio exceeds 3 to 1. For the HBMS database, the majority of stopes (148 out of 150 stopes, 98%) have an aspect ratio (L/H or H/L ratio) of less than 3. This suggests the HR term will do an adequate job of assessing stope geometries for most cases and will be used for the majority of this study since it is easier to use and has a wider industry acceptance.

The modelled results showed that the depth of relaxation and ELRD are related to stope surface geometry (in terms of RF or HR) and stress situation (in terms of stress ratio).

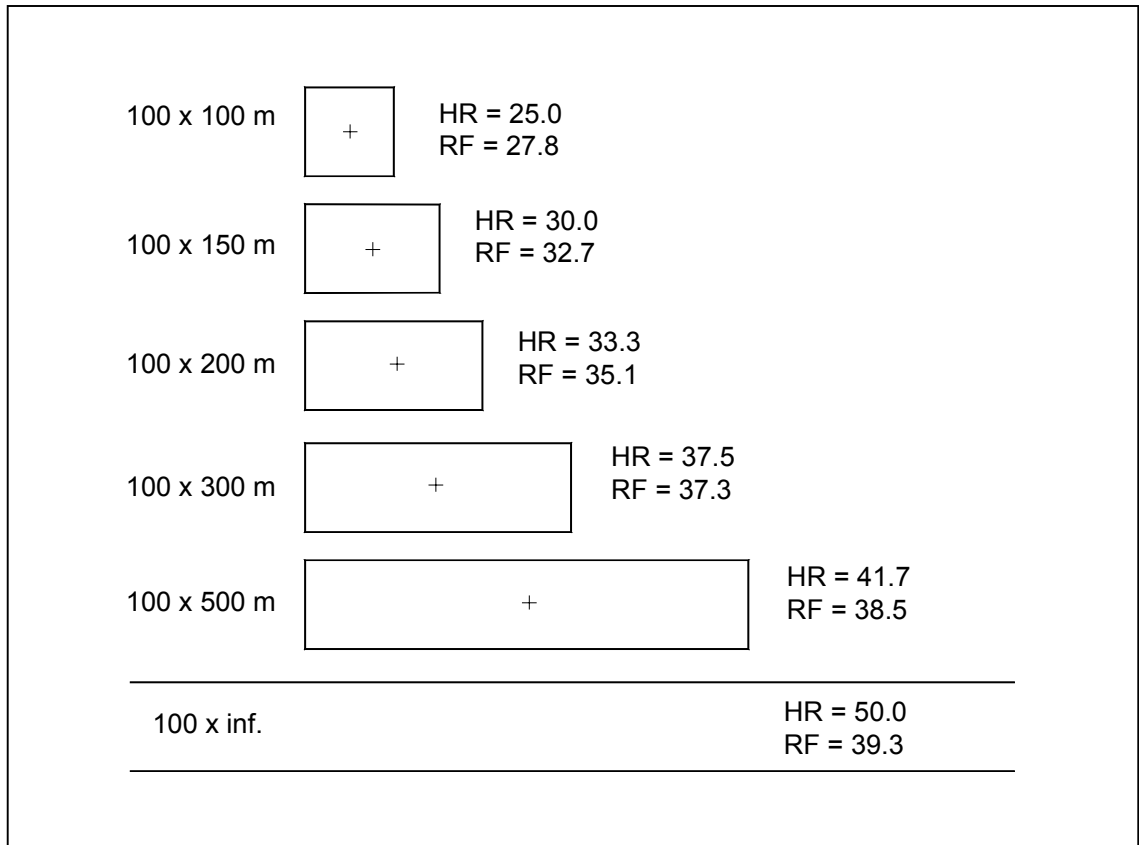


Figure 6.24. Variation in hydraulic radius and radius factor for a constant 100 metre span and increasing length (after Milne, 1997)

A fairly linear relationship can also be obtained for the radius factor or hydraulic radius and degree of hanging wall relaxation. The linear trend was obtained for 3 types of opening geometries using two different numerical packages.

The major findings are:

- With an increase in radius factor or hydraulic radius, the HW relaxation depth and ELRD increases linearly for a constant stress ratio
- Stress ratio has a significant effect on the depth of relaxation; the higher the stress ratio, the greater the relaxation depth and ELRD for a given RF or HR
- The slope of the depth of relaxation versus RF or HR lines and the ELRD versus RF or HR lines are controlled by the stress ratio K

6.5.6 Proposed Application of the ELRD to RF Relationships

Based on the new modelling results, relaxation graphs were developed for estimating the depth of relaxation at the centre of a stope HW surface and the ELRD for a known HW radius factor RF or HR and stress ratio K, as shown in Figures 6.25, 6.26, 6.27 and 6.28. These relaxation graphs were generated by linear regression analyses of the model results. The models were based on the assumptions of a homogeneous, isotropic and linear elastic rock properties. The in-homogeneity and fractured nature of a rock mass will undoubtedly alter the relaxation shape and dimensions, depending on the rock mass properties and the nature of fractures in the rock mass. However, the graphs show the relative influence of stope geometry and stress state. For example, if an open stope has a strike length of 40 m and a height of 40 m, then the stope hanging wall radius factor is 11.1 m. For an in-situ stress ratio of 2.0, the approximate size of the relaxation zone can be quickly obtained from the relaxation graphs. The stope hanging wall, depth of relaxation at the centre of the stope HW is about 2.8m and ELRD is approximately 2.1 m. The stope hanging wall is expected to have a 2.1m average depth of relaxation for this particular stress condition.

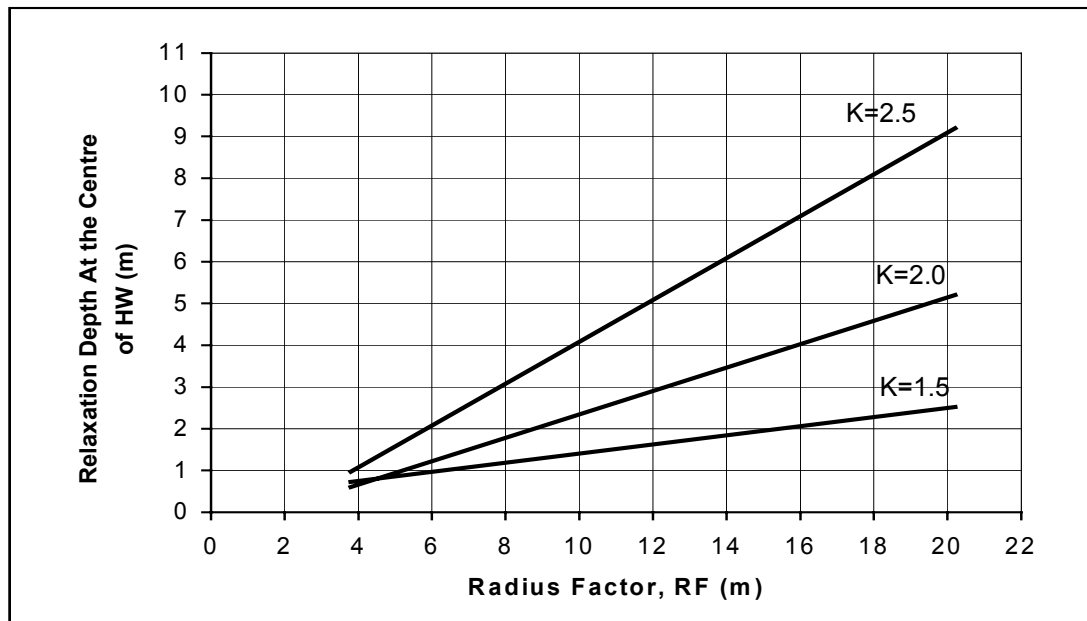


Figure 6.25. Design graph of depth of relaxation at the centre of stope HW surface based on RF.

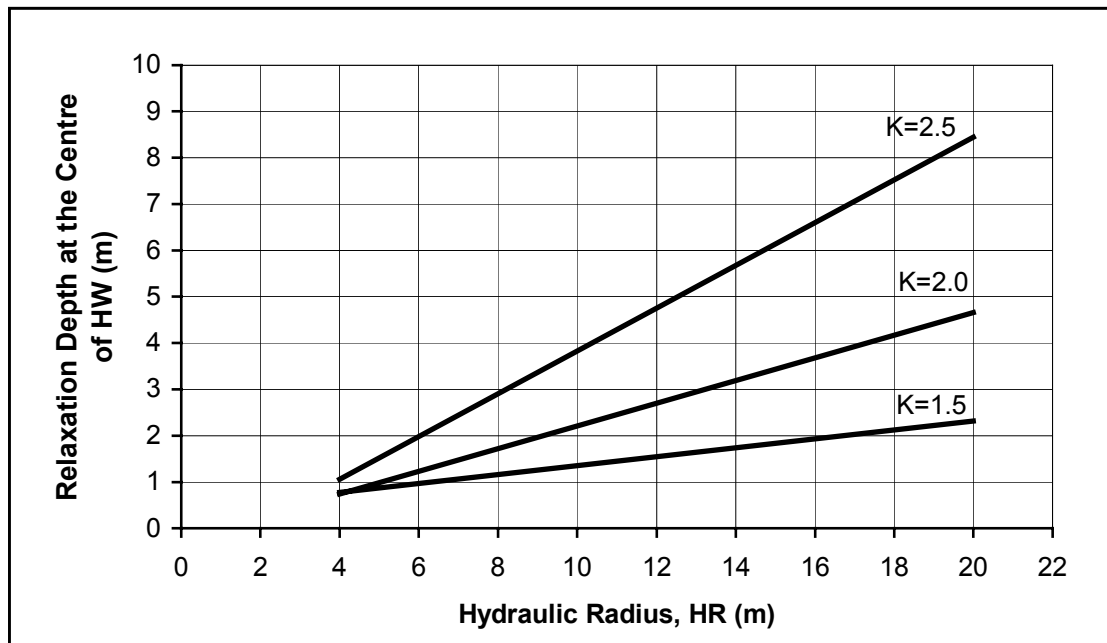


Figure 6.26. Design graph of depth of relaxation at the centre of stope HW surface based on HR

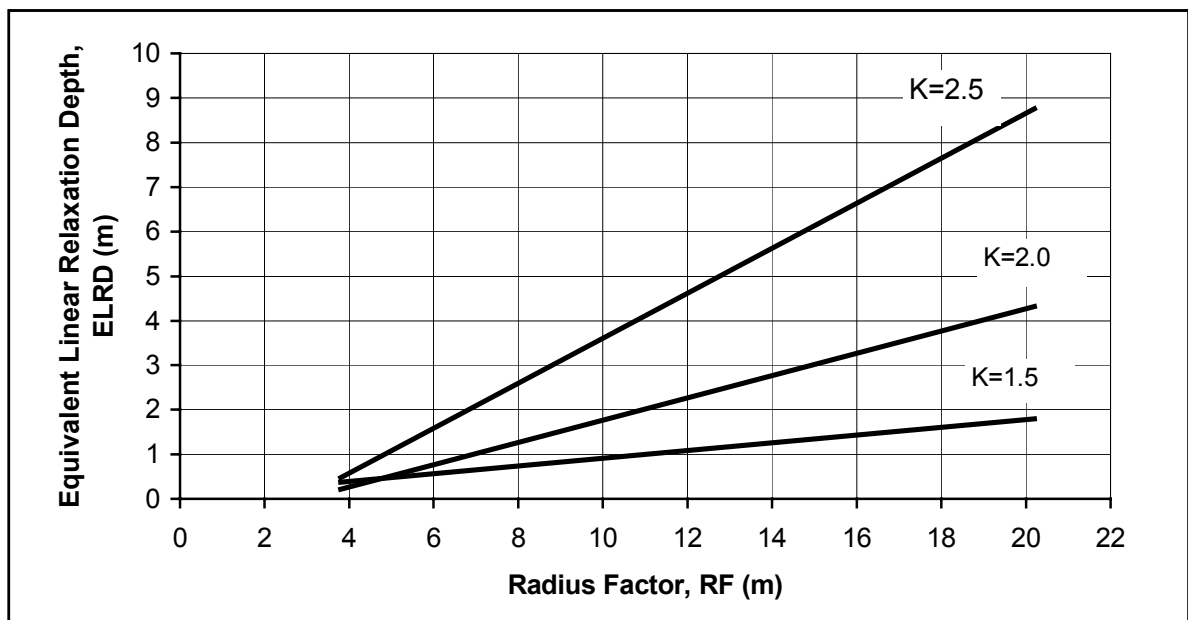


Figure 6.27. ELRD design graph based on RF

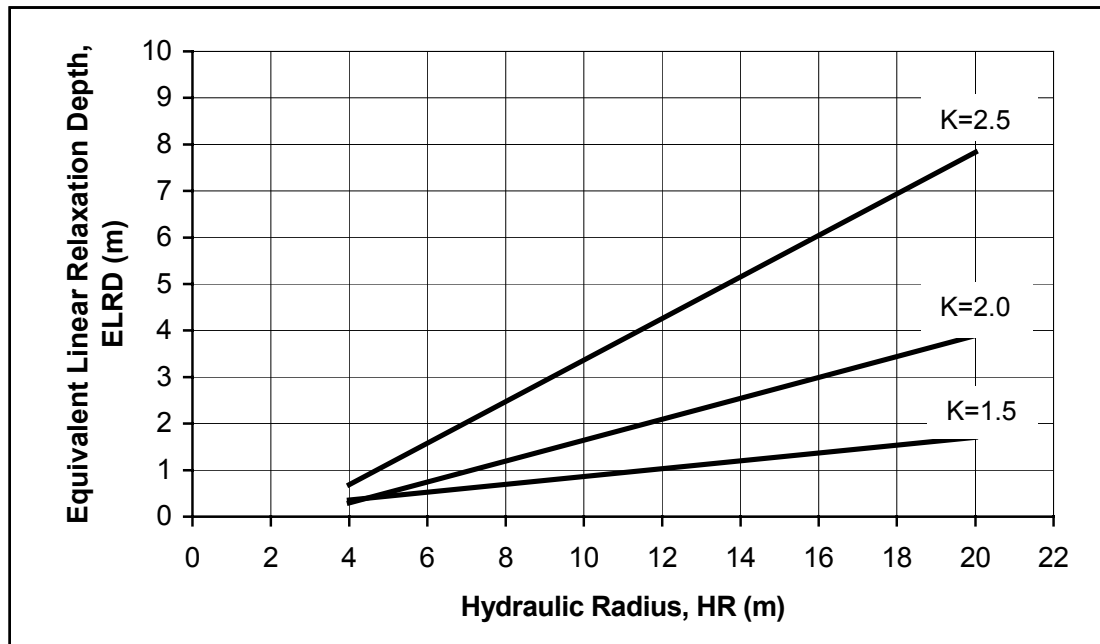


Figure 6.28. ELRD design graph based on HR

The Dilution Design Graph (Clark, 1998) is commonly used by many Canadian mines to estimate open stope dilution (Section 2.3.5). An attempt was made to compare the modelled ELRD values with ELOS values plotted on the dilution graph. The relaxation zone surrounding a stope hanging wall is related to the hanging wall stability, as discussed in Section 2.2.3. The dilution graph can estimate the influence of the hanging wall HR or RF value on dilution, expressed as ELOS. The relaxation graphs can estimate the average depth of relaxation ELRD, for a given stress condition, also as a function of HR or RF.

Theoretical conditions typical of an underground stope in the Canadian Shield have been assumed for the following hypothetical example:

For Modified Stability Number N' (Section 2.3.2)

Rock Classification Q'	= 2.5	(fair to weak rock)
Stress Condition A	= 1.0	(relaxation zone)
Joint Orientation Factor B	= 0.3	(Joints parallel to the HW)

Surface Orientation Factor $C = 8.0$ (Vertical hanging wall)

$$N' = Q' \times A \times B \times C = 6$$

A high horizontal to vertical stress ratio of $K = 2$ can be assumed as fairly typical of stress conditions in the Canadian Shield (Arjang, 1991). Four different stope sizes were considered to look at the relative influence of stope hanging wall size on predicted stope dilution and average depth of relaxation. The stope hanging wall sizes considered had RF values of 6, 8, 10 & 12 m, corresponding to equivalent HR values of 5.5, 7.3, 9.1 & 10.9 m, respectively. The estimated average depth of relaxation ELRD, can be estimated from Figures 6.27 and 6.28. Figure 6.29 shows the ELRD estimates plotted on the dilution graph. It shows that ELRD values for $K = 2$ correlated reasonably well with the dilution graph ELOS estimates when a stability number of 6 is used.

This example implies that the hydraulic radius term used in the dilution graph, adequately takes into account the influence of the relaxation zone around a stope hanging wall, when the stress ratio K is approximately 2.0. When the stress ratio K exceeds $K = 2.0$, it can be expected that the zone of relaxation will increase and the dilution graph may underestimate the component of dilution due to relaxation. Many mining conditions occur where the stress ratio K exceeds 2.0 due to nearby mining activity. The next section looks at assessing the influence of the pre-mining stress state on hanging wall dilution and stability.

6.6 Relating Mining Activity, Stress State and Dilution

Near-by mining activity has a significant influence on the state of stress prior to mining a stope. The initial stope in-situ stress state (in term of the stress ratio, K) is directly affected by mining sequence and the location of a stope relative to adjacent mined stopes. As mining progresses and more stopes are mined, stresses will be transferred to the remaining unmined stopes. The stress normal to the remaining stope hanging walls

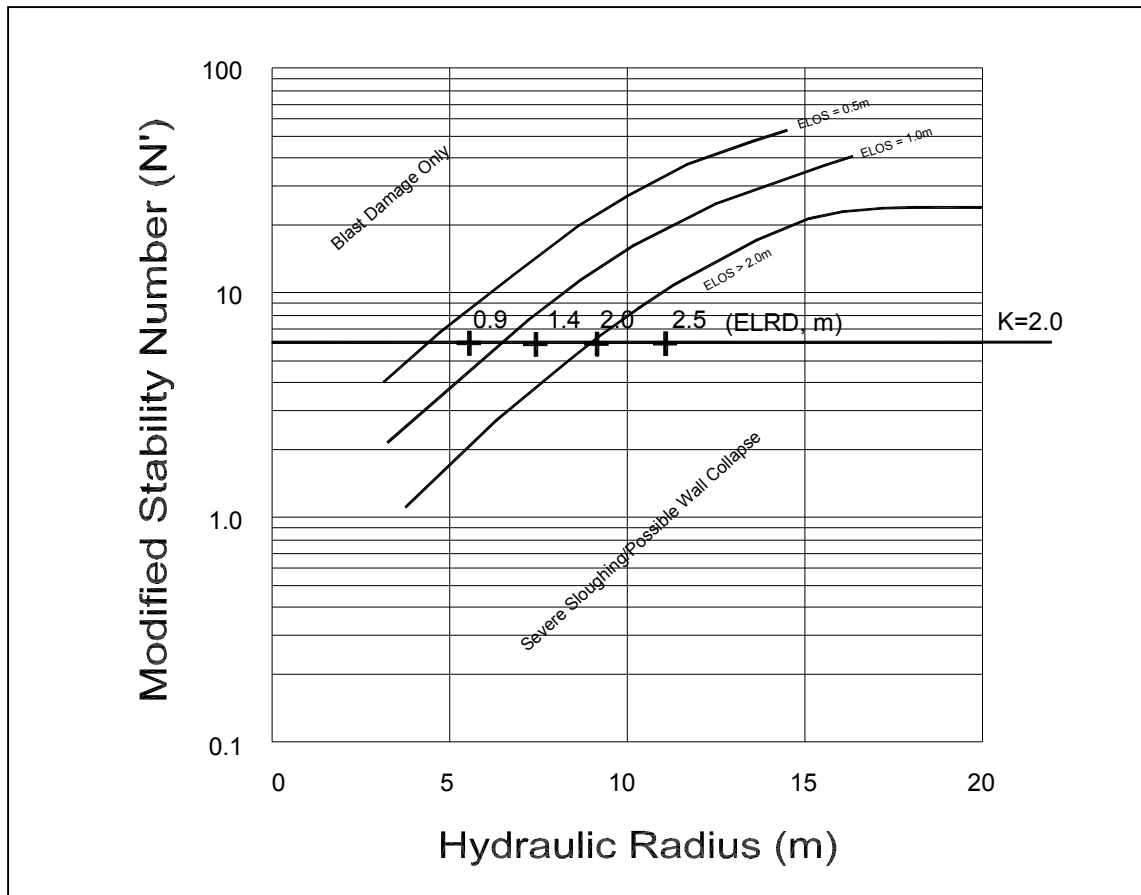


Figure 6.29. Comparison of modelled values of ELRD with ELOS on Clark's dilution graph for $K=2.0$

increases, resulting in a higher K ratio. An increased zone of relaxation, which may be related to stope dilution, can be expected in later excavated stope hanging walls as local mining progresses. To assess this, six stope configuration categories have been introduced as a preliminary assessment of pre-mining stress states. These categories are shown in Figure 6.30. The six categories represent increased local mining and a resulting increased stress ratio K . Category 1 corresponds to the first stope mined in an ore lens. The stope's initial in-situ stress ratio is the undisturbed or virgin stress state. For HBMS mines, $K = 1.3$, where the major principal stress perpendicular to the stope HW surface is 1.3 times the minor principal stress parallel to the surface (HBMS, 1996). Category 6 corresponds to a stope with mined and backfilled stopes above, below and to one side of the stope. Theoretically, stope category 1 has the lowest K ratio (original

stress condition before mining), and the K ratio generally increases with the stope category. This will result in an increase in the zone of relaxation for a given stope HW size, which will tend to reduce the stability of the hanging wall rock mass (Section 2.1.3).

A comparative 3D numerical analysis was conducted to determine the relative change in the stress ratio from stope categories 1 to 6.

The modelling input parameters were:

- surface elevation: $z = 500$ m
- Rock mass unit weight: $\gamma = 0.027$ MN/m³
- In-situ original stress: $\sigma_3 = \gamma z$, $\sigma_1 = K_0 \sigma_3$, $K_0 = \sigma_1 / \sigma_3 = 1.3$ and $\sigma_1 / \sigma_2 = 1.3$

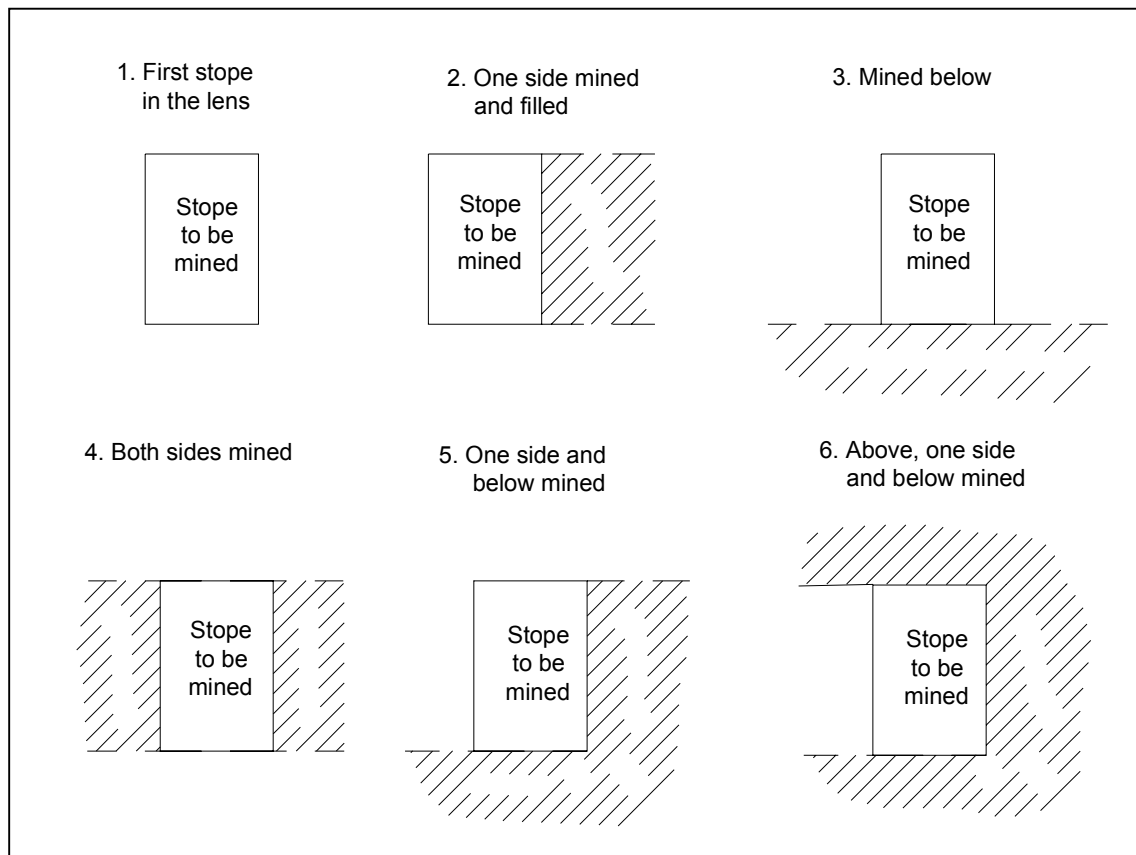


Figure 6.30. Stope categories showing adjacent mining configurations

The stope HW dips were set to 90° and a stope size of 30 x 40 x 5 m was used for all the models.

The stresses (σ_1 and σ_3) were measured at the centre of the stope HWs (this is about the average values within the stope). Table 6.9 and Figure 6.31 show the modelled results. The results show the stress ratio increasing with the stope categories from K=1.3 to K=2.0 for the categories 1 to 6. Figure 6.32 shows the modelled and inferred K ratios corresponding to the stope categories with the ELRD values plotted for the stope HR from 4 to 20 metres. The solid lines are directly from numerical modelling results and the dashed lines are interpolated from the modelling based on the assumption of equal spacing. Based on Figure 6.32, the average relaxation depth can be estimated based on the stope HR and the stope configuration.

The influence of stress based on the stope location configuration was compared to the ELOS values as measured in CMS surveys for single lens stopes (88 stopes) as shown in Figure 6.33. The average stope hydraulic radius for these stopes was 6.6 m. Based on the average HR value, the average depth of relaxation or ELRD for the 6 stope categories can be estimated from Figure 6.32. For the average HR of 6.6 m, the average relaxation depth (ELRD) increased from approximately 0.4m (K=1.3) to 0.9 m (K=2.0). There is only a small change in the ELRD because the initial K ratio of 1.3, measured for the HBMS mines, is low compared to other mines in the Canadian Shield (Arjang, 1991).

Table 6.9. Stress situation modelled results

Category #	σ_1	σ_3	K	Notes
1			1.3	Original stress ratio measured at HBMS Flin Flon
2	19	13.4	1.4	
3	19	13	1.5	
4	21	13.5	1.6	
5	25	15	1.7	
6	30	15	2.0	

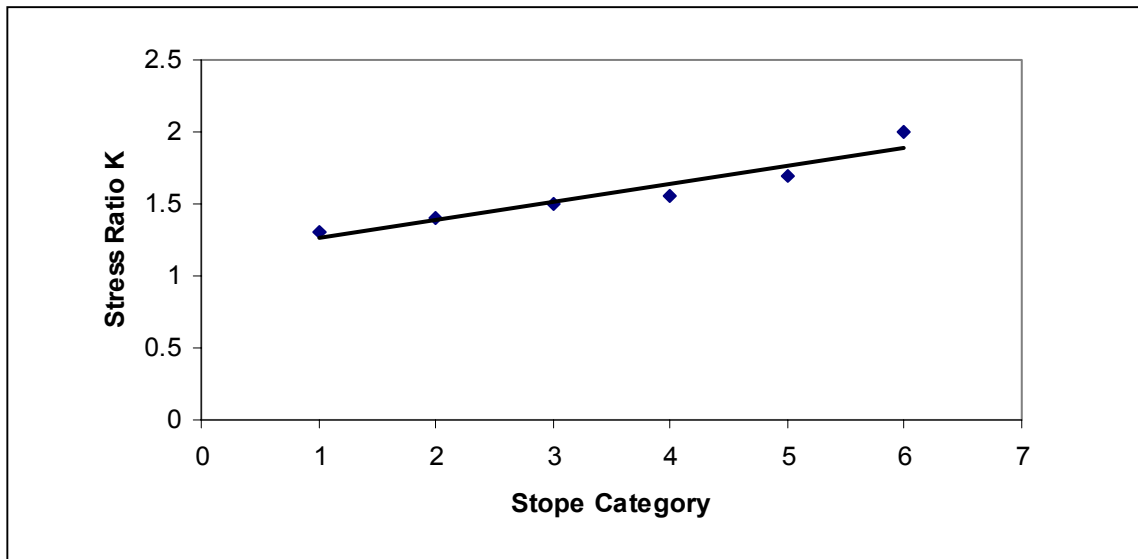


Figure 6.31. Modelled stress ratio change for the slope categories ($K_{\text{initial}} = 1.3$) for an $HR = 6.6$ m

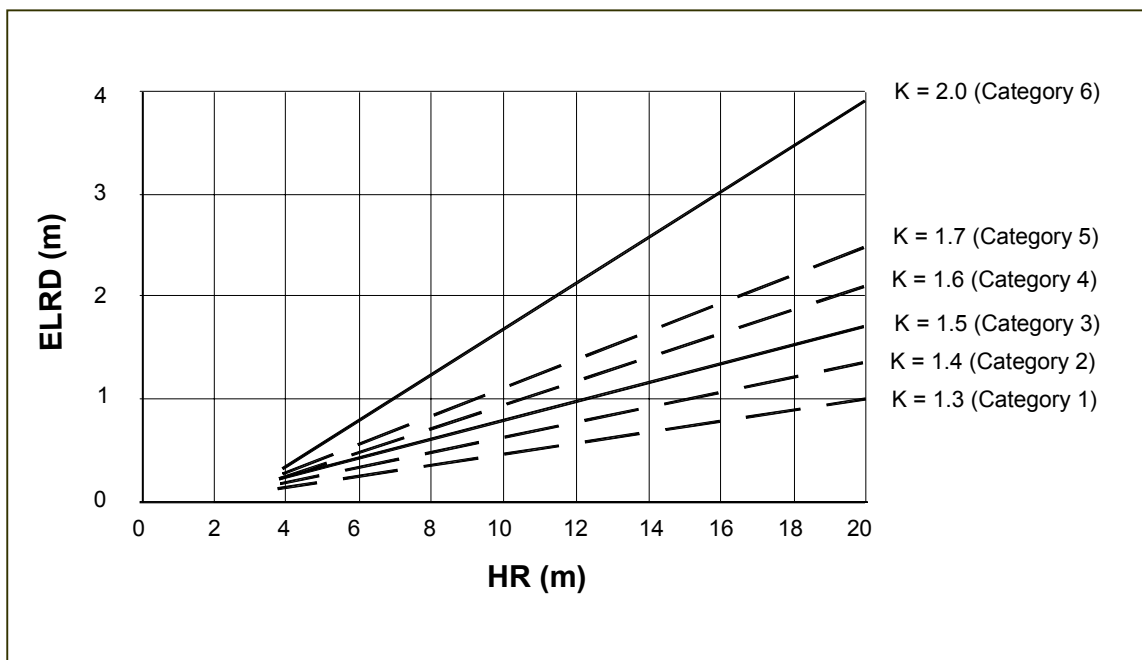


Figure 6.32. ELRD estimate for slope stress categories (solid lines are modelled and dashed lines are inferred from the modelled results)

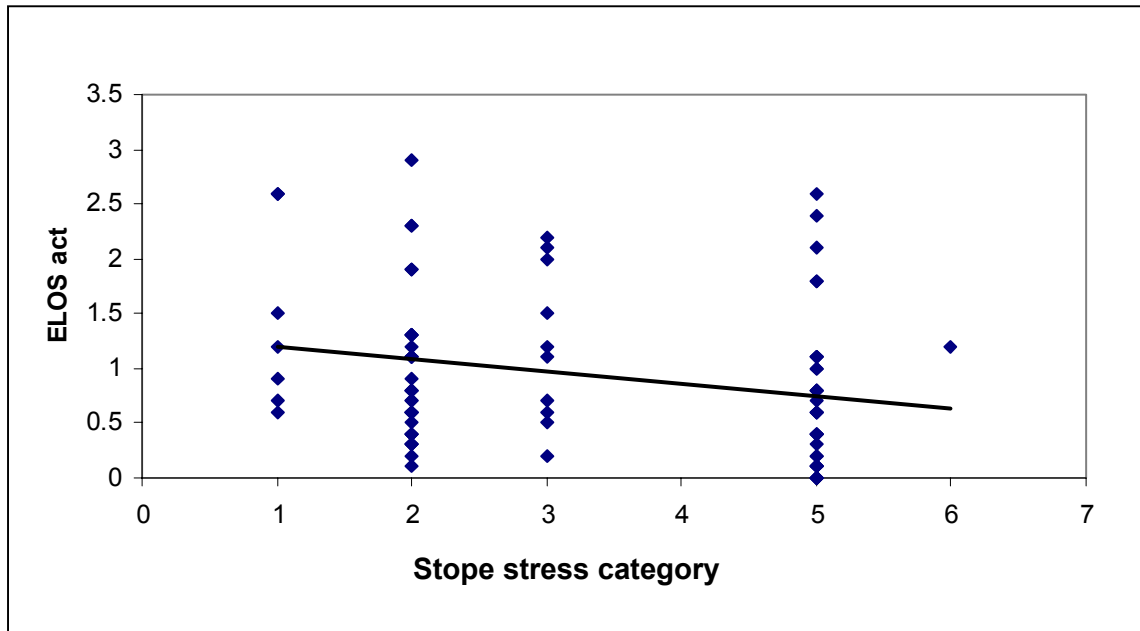


Figure 6.33. CMS measured ELOS versus stope categories plot

Figure 6.33 shows the actual ELOS versus the stope categories. There is no apparent trend in the data. The ELOS versus stope category plot ignores the influence of stope geometry and rock mass conditions. Figure 6.34 shows the actual dilution measured minus the Dilution Factor (DF) plotted against the stope category. Including the Dilution Factor in the graph accounts for the influence of changing ground conditions and HR values between the stope categories (Chapter 5). The average additional dilution, not accounted for by the dilution graph, is shown for each stope category.

The modelling results indicate a 0.5 metre increase in the average depth of relaxation from a category 1 to category 6 stope configuration. The assumed corresponding increase in actual dilution has not been observed with the HBMS data on single lens stopes. For competent, stable rock masses the lack of confining stress may not be sufficient to cause hanging wall slough or dilution. The data corresponding to a less

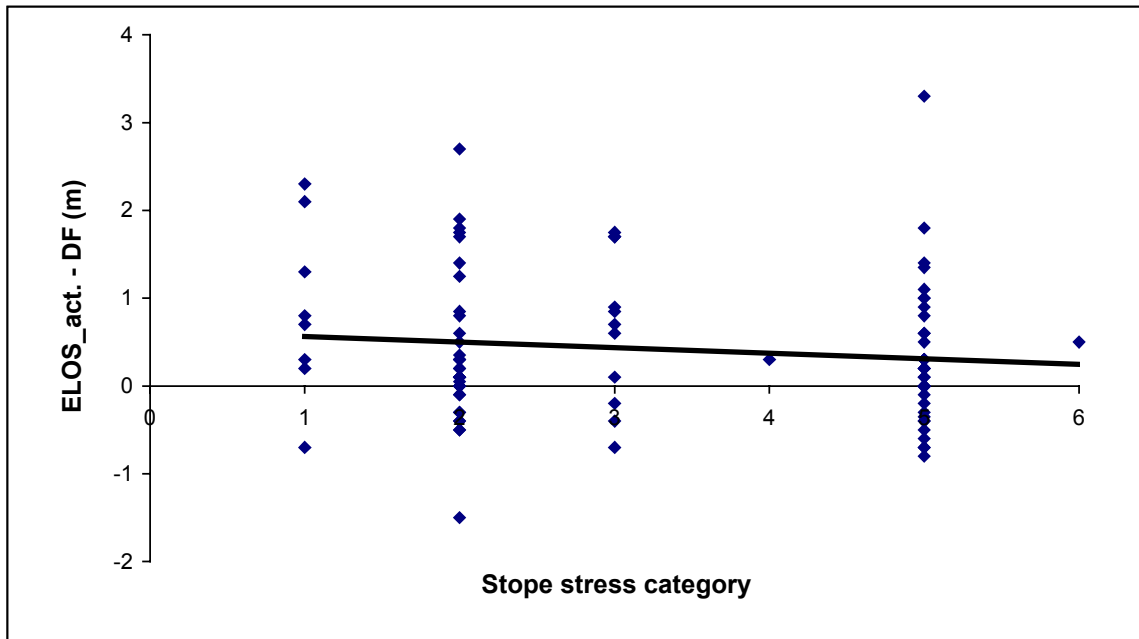


Figure 6.34. Actual ELOS minus dilution factor against stope stress category case history plot

competent rock mass (low N' values) and a lower stability (High DF values) has been plotted separately in Figures 6.35 and 6.36. Both graphs show a plot of the actual measured dilution minus the dilution predicted from the Dilution Graph. For Figure 6.35 only N' values less than 10 have been plotted to show the additional dilution versus stope categories. Only 31 case histories have been plotted and the average values have been indicated for each category. Figure 6.36 shows only the case histories where the DF value was greater than 1.0 metres. Only 37 case histories are shown on this graph with the average values indicated.

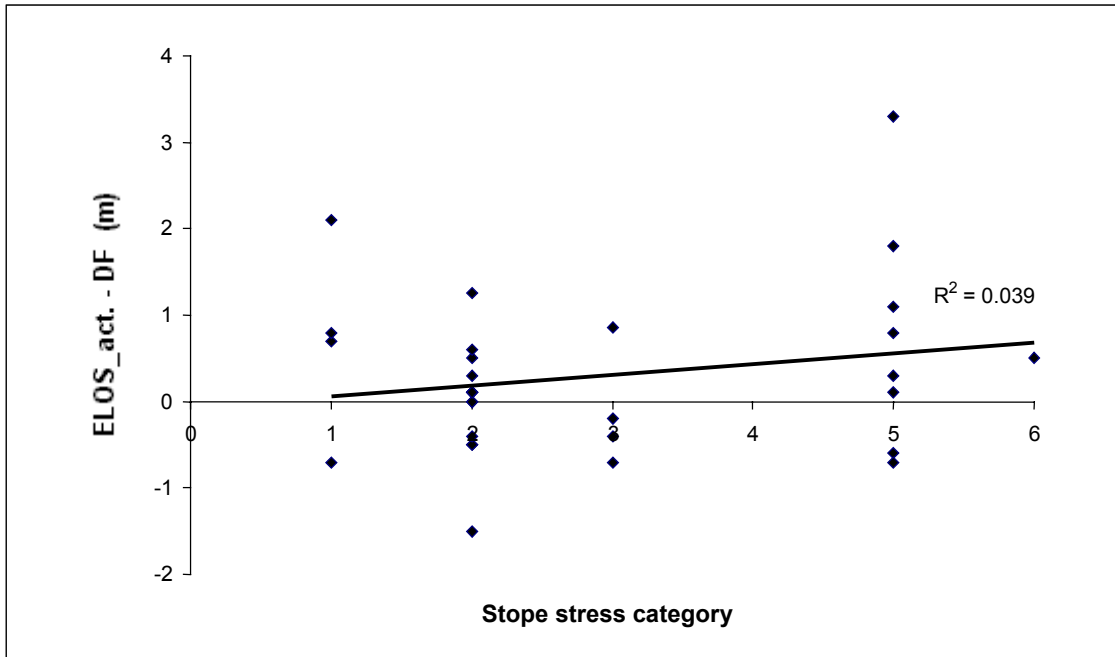


Figure 6.35. Actual ELOS minus dilution factor versus the stope stress category for the cases with $N' < 10$ (31 cases)

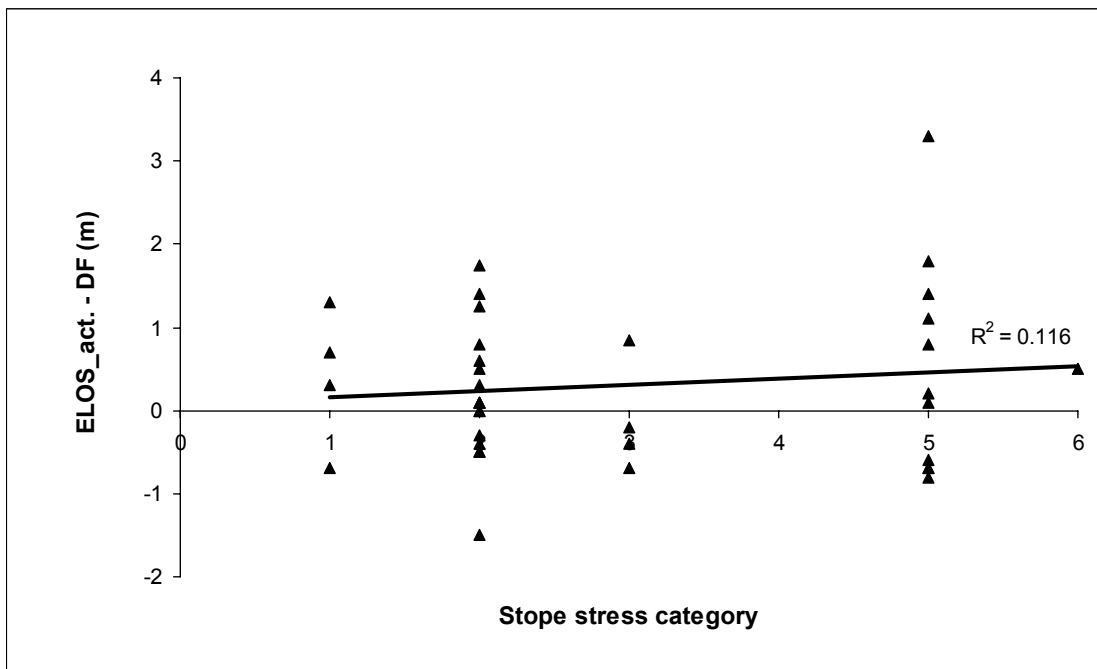


Figure 6.36. Actual ELOS minus the dilution factor versus the stope stress category for the cases with $DF > 1.0$ metres (37 cases)

The assessment of relaxation based on slope categories has not showed the expected trends, possibly due to a low initial stress estimate or due to excessive scatter in the data due to factors such as blasting. A more detailed assessment can be made on relaxation by estimating the actual zone of relaxation for each single lens slope based on the estimated stress ratio K from the slope configuration and the slope hydraulic radius. Figure 6.37 shows the dilution not accounted for with the dilution graph ($ELOS_{act.} - DF$) plotted against the estimated ELRD based on slope geometry and slope configuration (88 cases). The data does not show a trend. Figure 6.38 is the same graph showing only the case histories with an N' value less than 10 (29 cases).

The data indicate that the zone of relaxation may influence hanging wall stability and dilution for weaker rock masses and less stable slope walls. The theoretical influence of the stress categories on the ELRD is small (up to about 0.5 m) and there is too much scatter in the ELOS data to verify the influence of stress relaxation on measured dilution.

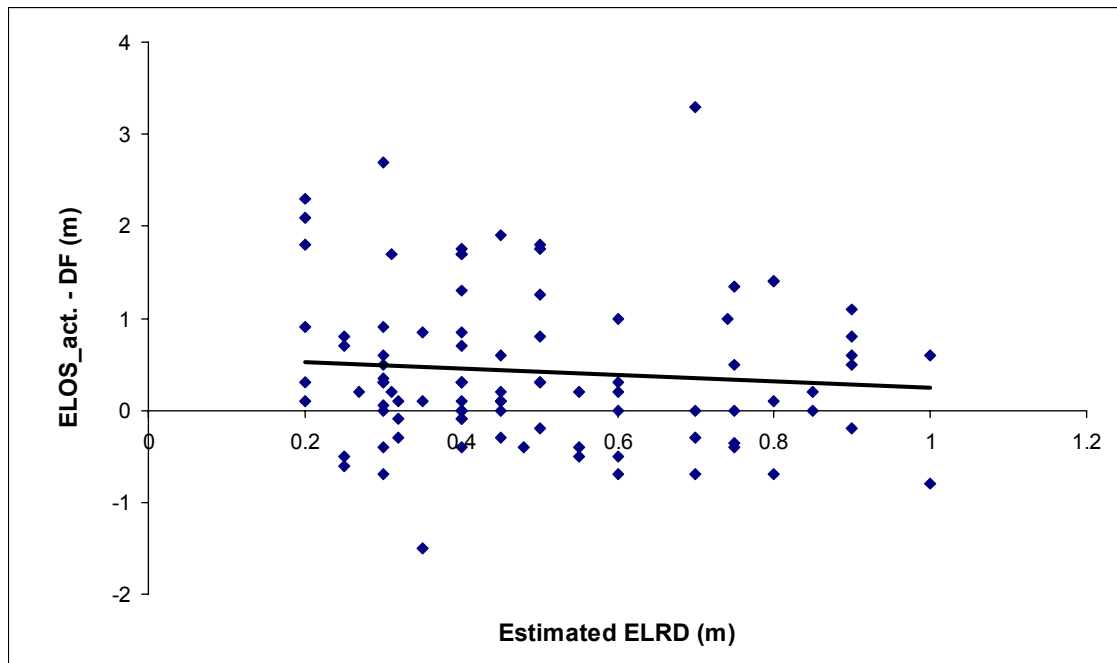


Figure 6.37. Dilution prediction error ($ELOS_{act.} - DF$) against the estimated ELRD cases history plots (88 cases)

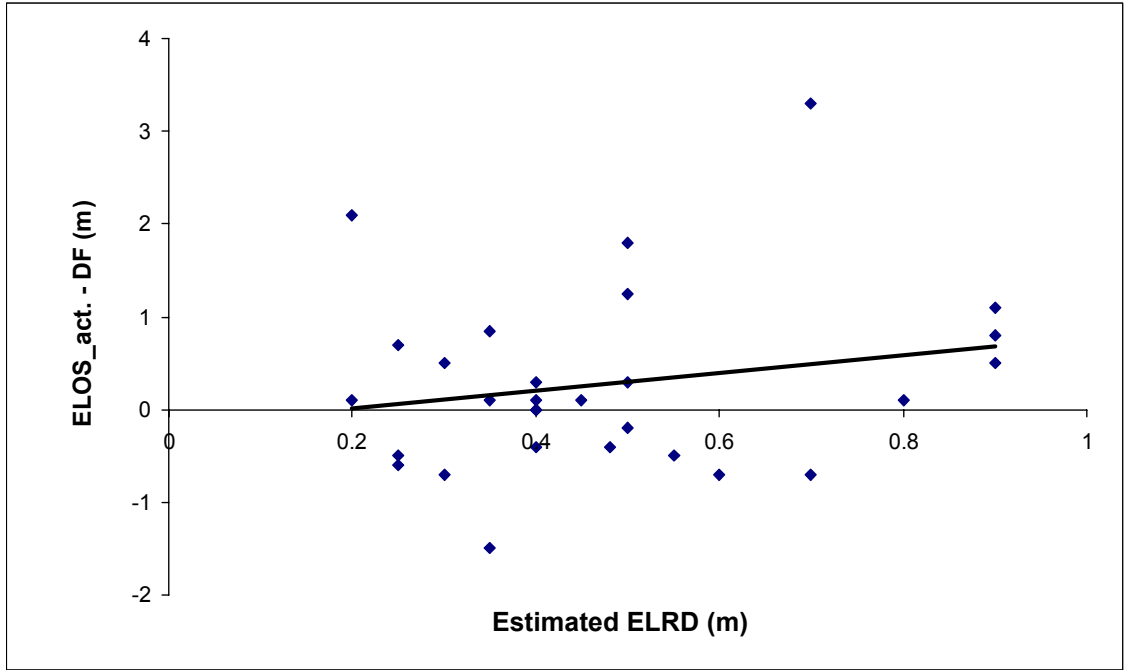


Figure 6.38. Dilution prediction error ($ELOS_{act.} - DF$) against the estimated ELRD cases history plots for the cases with the $N' < 10$ (29 cases)

6.7 Summary

In this chapter, the open slope HW instability and dilution were linked to the zone of HW stress relaxation. The relaxation zone around an open slope HW corresponding to the in-situ stress and the HW surface geometry (in terms of RF and HR) was evaluated using 2D and 3D numerical modelling. The relationships between the size of the relaxation zone, the in-situ stress state and the size and shape of the HW surface were established. The size of the relaxation zone is directly related to the in-situ stress ratio (σ_1/σ_3) rather than the magnitudes of stresses. HW geometry also has an influence. The depth of relaxation and the equivalent linear relaxation depth (ELRD) corresponding to the stress state and HW size were studied. ELRD varies linearly with hanging wall RF and HR. With an increase in the hanging wall HR or RF value, the ELRD increased proportionately. With an increase in the stress ratio, the size of the relaxation zone also increases significantly. Two relaxation graphs were developed to estimate the ELRD and depth of relaxation at the centre of a HW surface.

A direct link between the modelled hanging wall relaxation zone, the stope HR (or RF) and the pre-mining stress ratio K has been made and verified using two computer modelling programs and a wide variety of opening geometries. Six stope categories have been introduced which have been linked to the induced stress regime and the average depth of relaxation for a given initial stress state. Attempts were made to link the stress state (in terms of the stress ratio) to mining case histories based on the six stope configuration categories. The expected trend was not found between the estimated stress state and the degree of measured hanging wall dilution. Due to the relatively small initial stress ratio K at HBMS operations, the influence of increased stress only increased the K ratio to about 2.0. This increase in K from 1.3 to 2.0 with mining makes a small difference on the average relaxation depth. For the average HBMS stope HR of 6.6 m, the ELRD increased from 0.4 to 0.9 metres (Figure 6.32). The other factors which contribute to dilution, such as blasting, undercutting and geological structures may over-shadow the stress influence on stope HW dilution. An assessment of the HBMS stopes with weaker rock mass conditions and higher predicted dilution values (DF based on the Dilution Graph) was also made. The data are not conclusive and there are not enough case histories to make a realistic assessment of the influence of stope categories on dilution. Additional case histories from operations with higher stress ratios and weaker rock masses are required to verify or discount the stress relaxation influence on dilution.

CHAPTER 7

INFLUENCE OF UNDERCUTTING ON STOPE STABILITY AND DILUTION

7.1 Introduction

Undercutting the stope hanging wall (HW) on both the overcut and undercut development drifts are well recognized factors which contribute to hanging wall instability and dilution (Wang et al., 2002; Yao et al., 1999; Suorineni et al., 1999; Suorineni, 1998). Undercutting occurs when the drifts that are driven for stope development extend past the desired mining limit. Development drifts are commonly located at stope sub-levels or on the overcut and undercut levels of a stope. The HBMS database does not include stopes developed with sub-levels so only undercutting of the hanging wall on the overcut and undercut drifts are considered. Undercutting may or may not occur along the total stope strike length. Where it does occur, the degree of undercutting may vary.

Observations and case history studies show that undercutting on both overcut and undercut drifts has a similar influence on overall dilution. Yao et al. (1999) state “Cutting into the hanging wall with production development can be a major cause of instability. Undercutting can occur during development of the overcuts/undercuts and/or by upward caving of previously mined stopes that have had hanging wall slough.”

Many factors can cause an open stope hanging wall to be undercut. These factors include: drift location design errors caused by incorrect geological ore definition, changes in ore contact orientation or ore width, drift development errors, drill equipment

space requirements, and undercutting by underlying stope caving. The HBMS database shows that approximately 74% of stopes (111 cases out of 150) have a degree of undercutting. Of these cases, approximately half of them have an average undercutting depth of 1 to 2 metres. Figure 7.1 shows undercutting information for the HBMS database. Undercutting depth is defined by the distance the drifts cut into the stope hanging wall past the ore contact, as shown in Figure 7.2. The database shows that undercutting of the stope hanging wall is a very common problem for open stope mining.

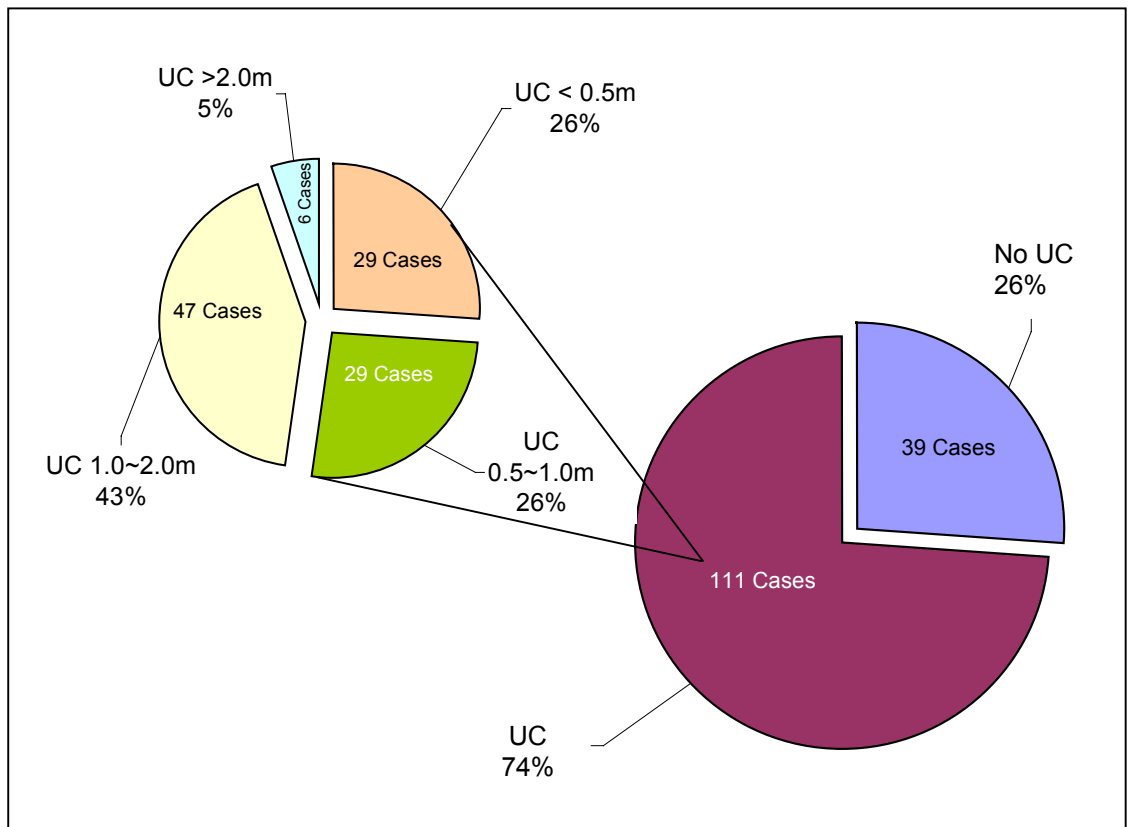


Figure 7.1. Percentage of undercutting (UC) and the undercutting depth from the HBMS database

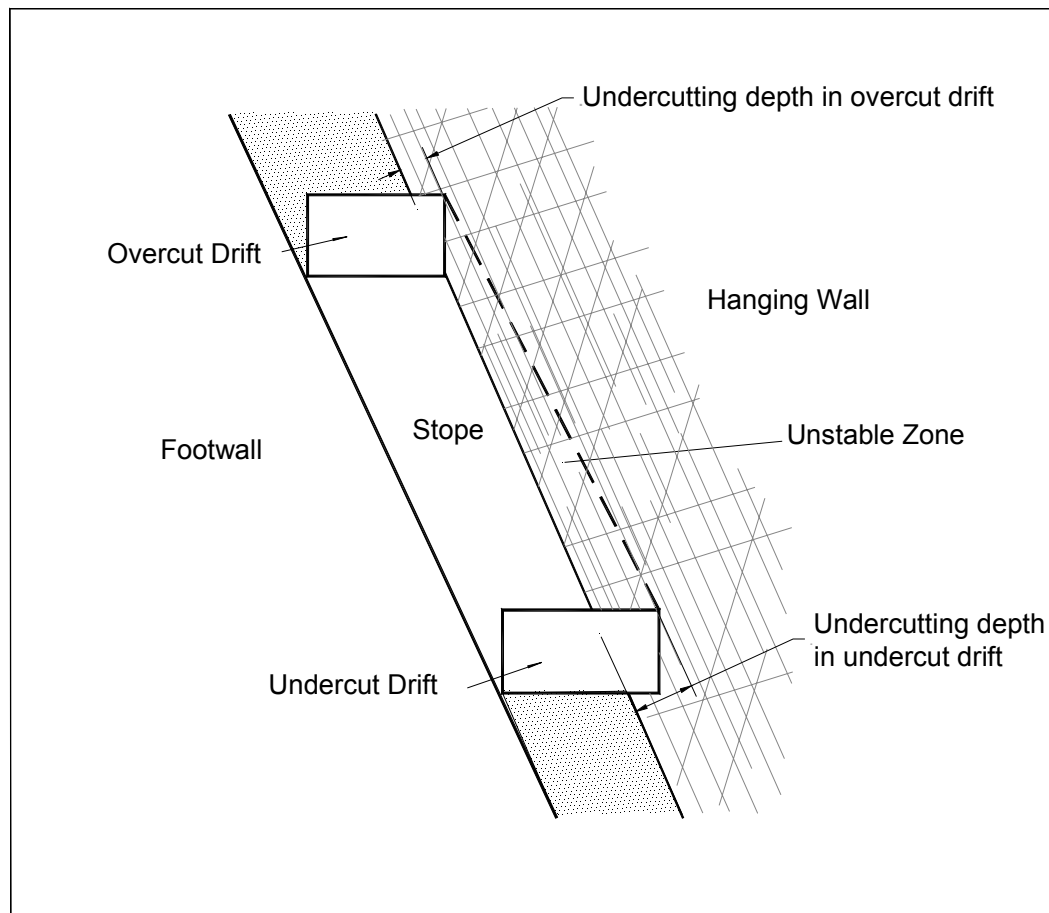


Figure 7.2. Schematic illustration of instability caused by undercutting

Undercutting the stope hanging wall has the following effect on a hanging wall rock mass:

- An additional free face is developed with the creation of the undercut
- Confinement of the immediate hanging wall is reduced which allows a jointed rock mass to “loosen up”
- The beam created by the immediate hanging wall is broken
- There is an increased zone of relaxation associated with hanging wall undercutting

These factors can be summarized into two main categories.

1. Reduction of immediate hanging wall confinement and support due to removal of the hanging wall abutment and
2. Increasing the zone of stress relaxation in the hanging wall by changing the stope geometry.

In many mines, the major discontinuities in the HW rock mass consist of foliation or bedding planes orientated parallel to the HW contact. This is true for the HBMS database. Undercutting the hanging wall breaks the integrity of the “beam” that may form along continuous foliation or bedding planes parallel to the stope HW contact. This reduces the stope HW stability. Undercutting the stope HW removes the support and “hangs” the jointed rock mass for the portion of HW being undercut. The dead weight of wedges and blocks formed by joints and foliation may fall due to gravity in the undercut area (Figure 7.2). Undercutting also influences the zone of relaxation in the HW and this is discussed in Section 7.3.

7.2 Quantifying Hanging Wall Undercutting

In order to try and account for the undercutting influence on stope HW stability and dilution, an undercutting influence factor (UF) has been developed as part of this research. The first step is to quantify the contributing geometry factors.

Undercutting of the hanging wall can occur on both the overcut and undercut drifts and has a similar influence on the overall dilution. Undercutting may not occur along the total stope strike length and where it does occur, the degree of undercutting may vary. As the total stope up dip height (H) increases, the overall influence of undercutting in the drifts decreases. An equation has been proposed to account for the influence of these contributing geometry factors. The term quantifying the degree of undercutting is called the undercut factor (UF). It is proposed that an undercutting factor should be dependent on the following terms

1. The average depth of undercutting

$$\frac{(d_o + d_u)}{2} \quad (7.1)$$

where, d_o = Average depth of undercutting along the overcut drift length l_o (m)

d_u = Average depth of undercutting along the undercut drift length l_u (m)

2. The fraction of the stope strike length where undercutting occurs and the distance between the undercut and overcut drifts. This can be expressed as the length where undercutting occurs divided by the stope perimeter or total abutment length.

$$\frac{l_o + l_u}{2(L + H)} \quad (7.2)$$

where, l_o = Drift length where undercutting occurs on the overcut drift (m)

l_u = Drift length where undercutting occurs on the undercut drift (m)

L = Stope strike length (m)

H = Stope height (up dip height, this reflects the true stope dimension) (m)

These factors which contribute to the influence of hanging wall undercutting are shown in Figure 7.3. The UF is expressed as:

$$UF = \left(\frac{l_o + l_u}{2(L + H)} \right) \times \frac{(d_o + d_u)}{2} \quad (7.3)$$

where, UF = Undercutting Factor (m), note: $2(L+H)$ = Stope perimeter

Figure 7.3 shows the geometric parameters that contribute to the undercutting factor. This simplification was used for ease of application. It assesses a similar length of undercutting on both the overcut and undercut drifts. If a significant difference exist, the overcut and undercut should be assessed independently.

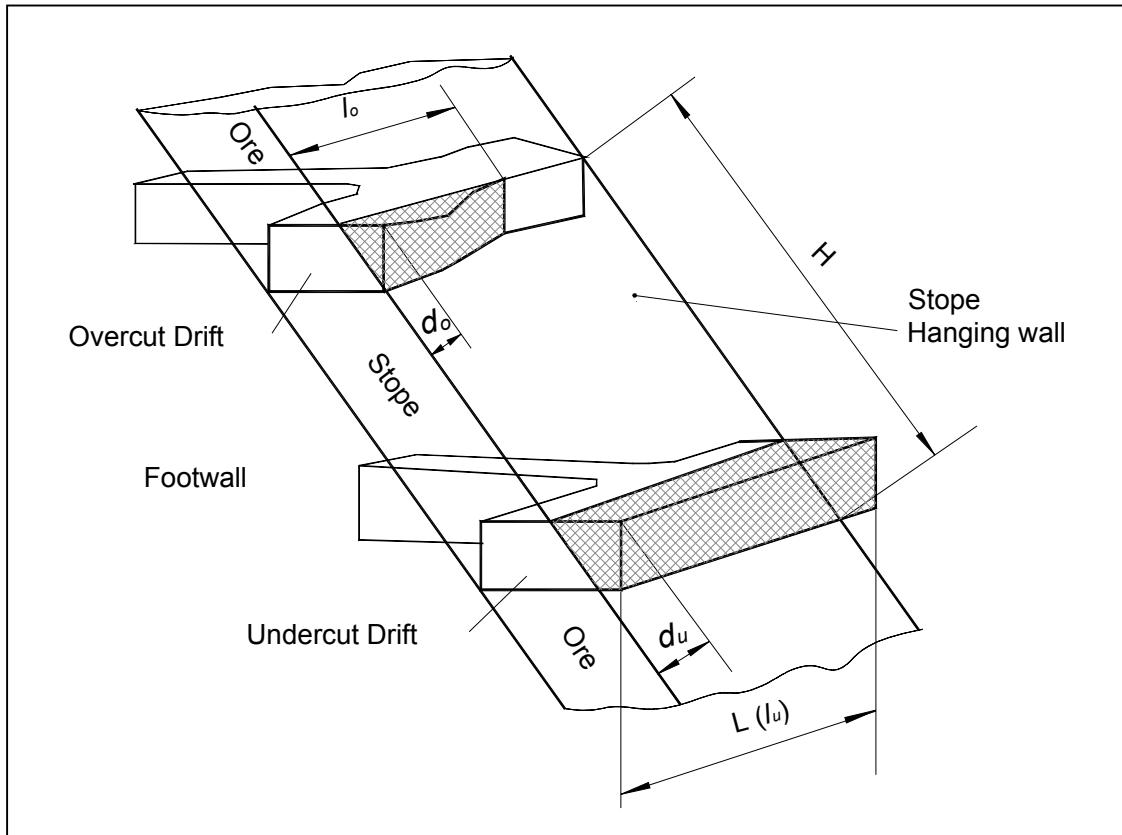


Figure 7.3. Stope isometric showing the undercutting parameters

Figure 7.4 shows the distribution of the calculated UF values for the HBMS database. The majority of the stopes are in the range of UF values between 0 and 0.4.

7.3 Interaction of Undercutting and Stress

Chapter 6 discussed the influence of stress on the volume of stope HW rock in relaxation. The relaxation zone is dependent on the stress state prior to mining as well as the shape of the stope. Undercutting a stope HW will also increase the volume of the tensile or relaxation zone (Diederichs and Kaiser, 1999).

When drifts cut into a HW, the stope HW abutment location will be pushed back into the HW. The total HW zone of relaxation, which is a zone of decreased stability, may contribute to increased dilution (Figure 7.5).

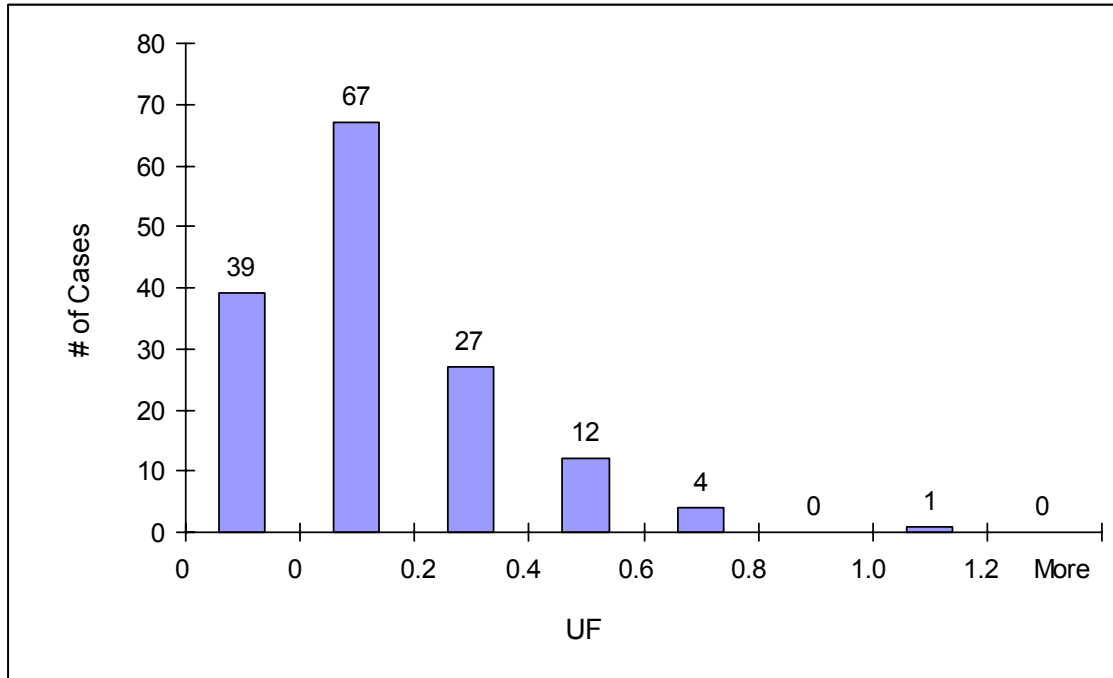


Figure 7.4. Distribution of the calculated UF values for the HBMS database (150 cases)

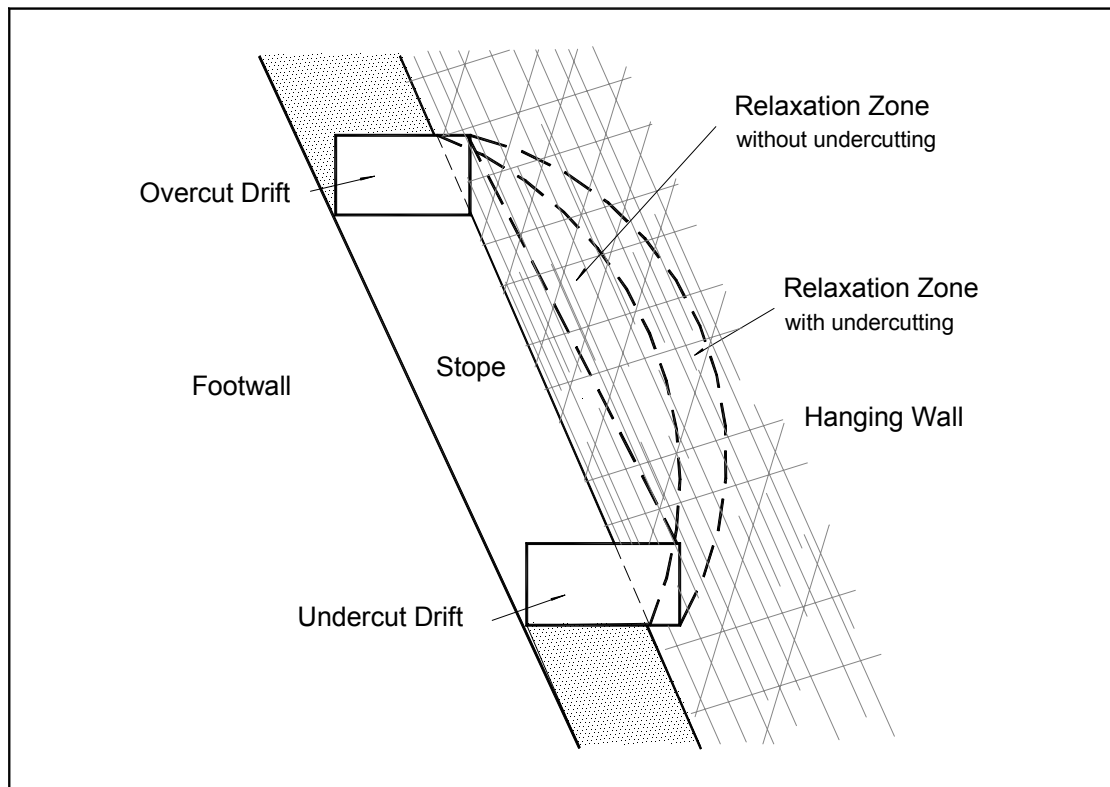


Figure 7.5. Schematic showing influence of undercutting on stope relaxation

Numerical modelling, using Examine 2D (Curran and Corkum, 1994) on a 40 metre exposure height with a width of 5 metres, shows the difference between the case without undercutting (Figure 7.6) and the case with 5 metres of undercutting on both of the stope top and bottom (Figure 7.7). Comparison of the stress distributions in the two figures shows an increase in the relaxation zone with undercutting (Figure 7.7), resulting in a larger zone of potential instability or dilution.

3D numerical modelling was conducted to quantify the effect of undercutting on the extent of the stope HW relaxation zone. The modelling was conducted on a 40 x 30 x 5m vertical stope as shown in Figure 7.8. The 3D boundary element program, Examine 3D, was used (Curran and Corkum, 1993).

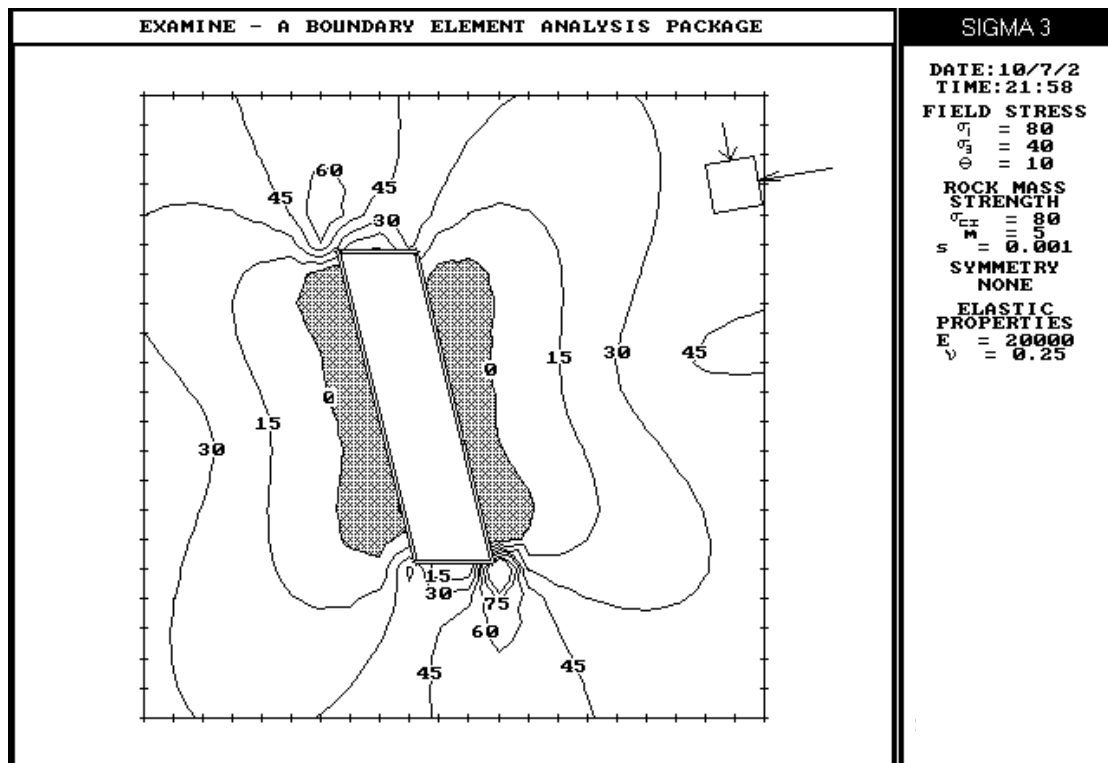


Figure 7.6. Stress relaxation zone (shaded) around a stope with no undercutting

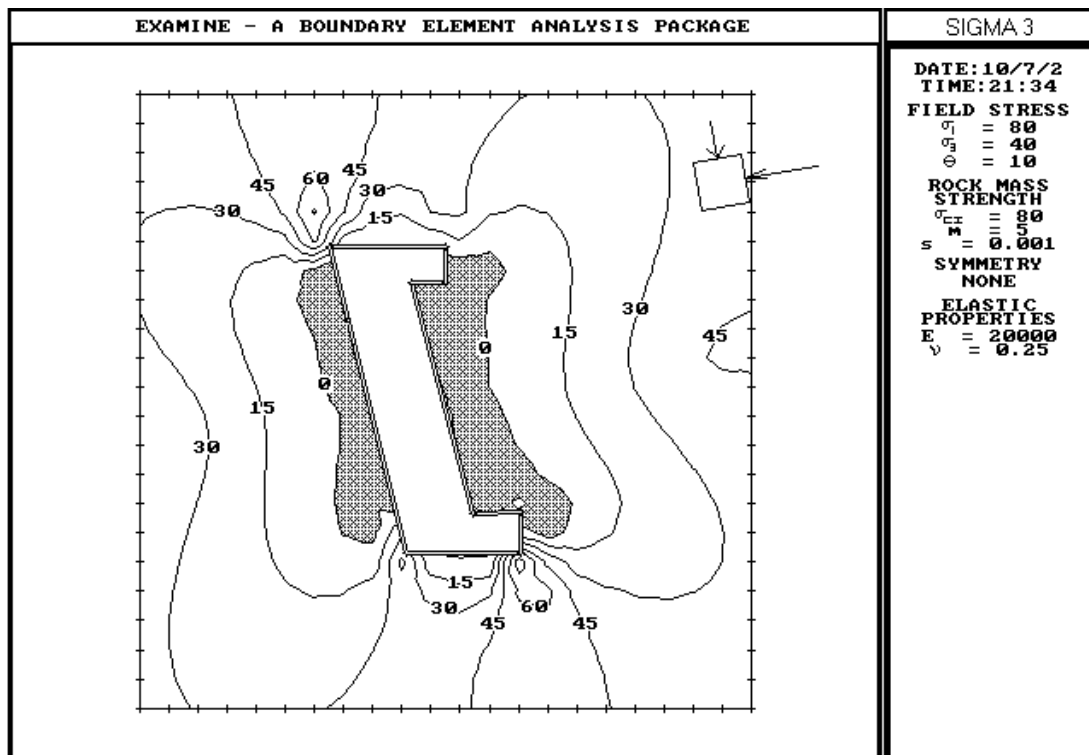


Figure 7.7. Stress relaxation zone (shaded) around a stope with 5 metres of undercutting

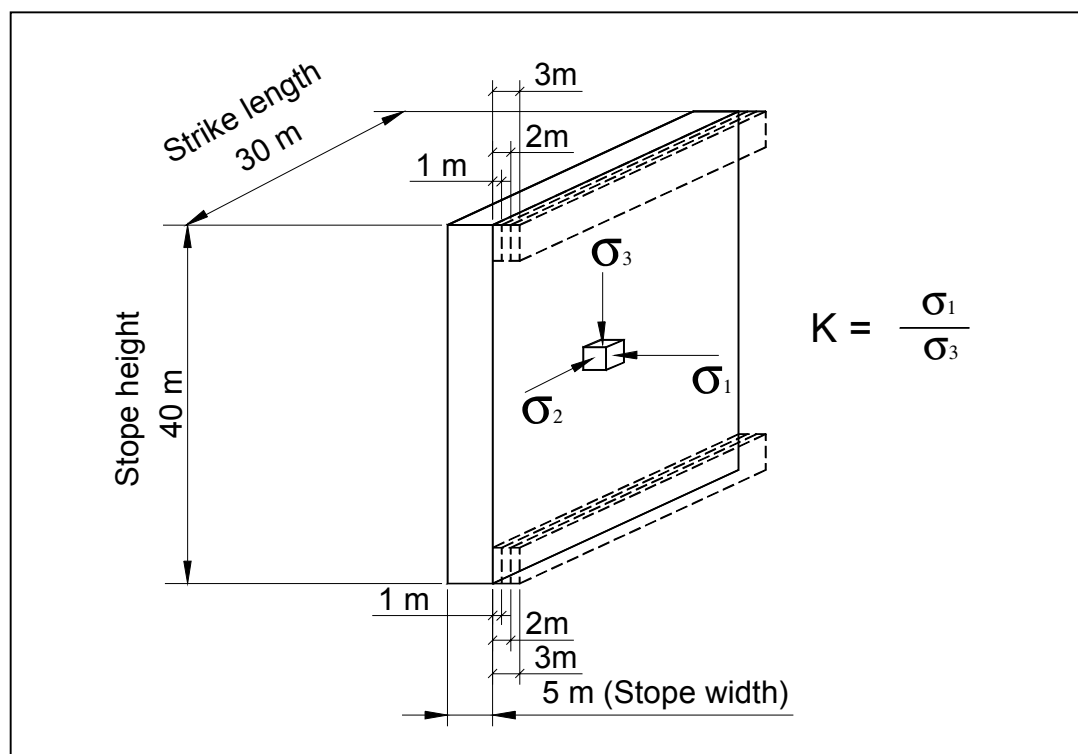


Figure 7.8. Effect of undercutting on stress relaxation modelling model

The undercutting geometry factor, UF, was calculated by substituting the stope HW and undercutting geometries, $l_o = l_u = L = 30$ m, $H = 40$ m, and $\frac{(d_o + d_u)}{2} = 1, 1.5, 2, 3$ m respectively, into equation 7.3. The calculated UF values are shown in Table 7.1.

Table 7.1. Calculated UF for test case Examine 3D model stope

d_o (m)	d_u (m)	$(d_o + d_u)/2$	UF
1.0	1.0	1.0	0.4
1.0	2.0	1.5	0.6
2.0	2.0	2.0	0.9
3.0	3.0	3.0	1.3

Computer models were run showing combinations of 0, 1, 2 and 3 metres of undercutting on both the overcut and undercut drifts (Figure 7.8). The undercutting into the hanging wall was set at a constant depth for the total stope strike length. However, the degree of undercutting was varied between the undercut and overcut drifts. The zone of relaxation was quantified as the zone of rock with a modelled confining stress, σ_3 , of zero or less. The relaxation zone was expressed as a depth of relaxation averaged over the hanging wall surface or ELRD (Equivalent Linear Relaxation Depth). Three initial or original stress regimes were modelled: $K=1.5, 2.0$ and 2.5 . The maximum stress direction was set perpendicular to the stope HW. The ELRDs due to undercutting ($ELRD_{uc}$) were calculated by subtracting the ELRD with undercutting from the ELRD without undercutting for each case modelled.

Figures 7.9, 7.10 and 7.11 show the modelled σ_3 stress distribution plots for a stress ratio of $K = 2$. Figure 7.9 shows the model without undercutting. The average depth of stress relaxation (ELRD) in the stope HW is approximately 1.8 m. Figure 7.10 shows the σ_3 stress distribution for 1m and 2m of undercutting in the overcut and undercut drifts, respectively (with an average undercutting depth of 1.5m). For this geometry, the ELRD is approximately 2.5m. There is about a 0.7m ELRD increase due to undercutting

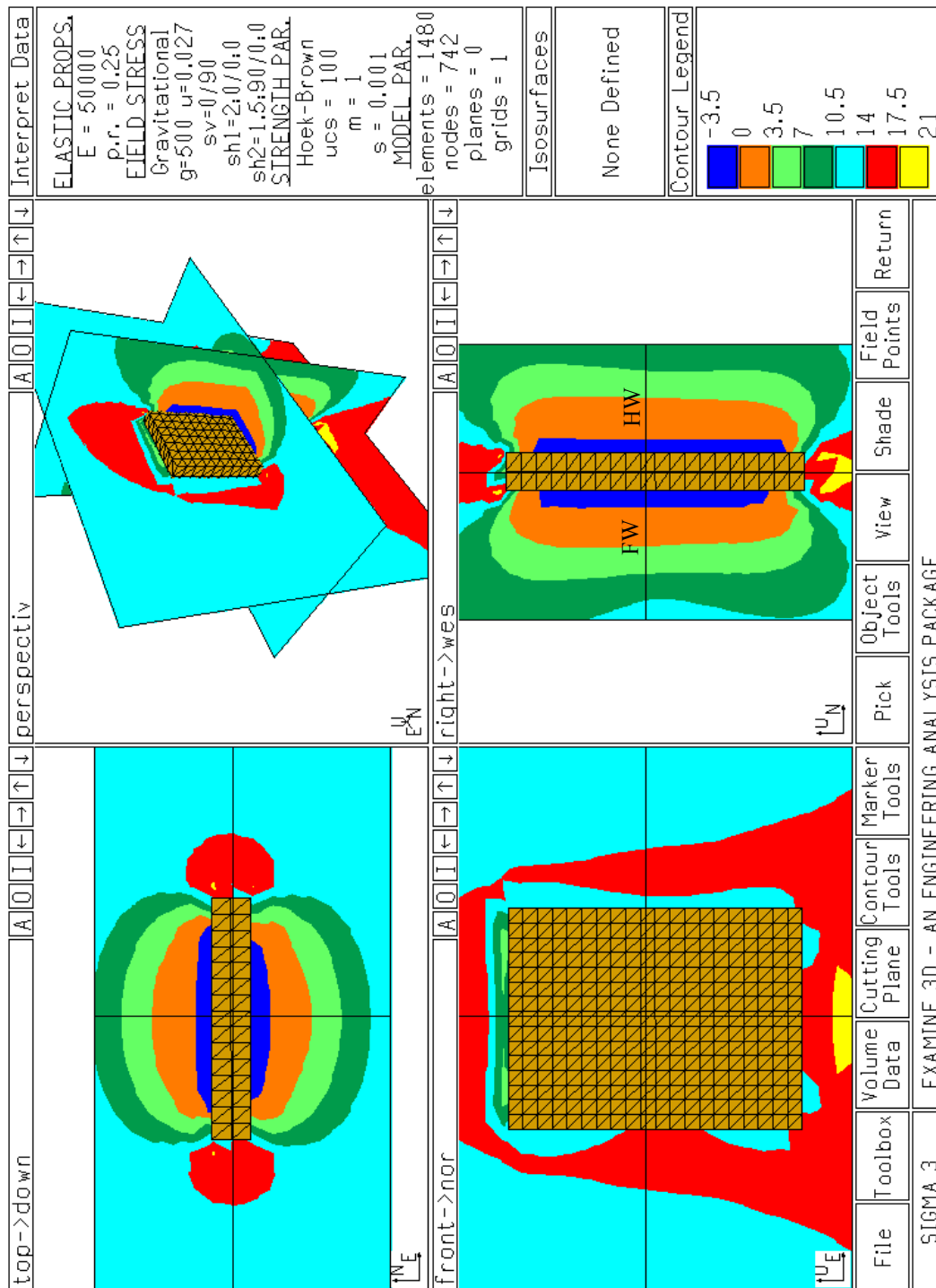


Figure 7.9. Examine 3D σ_3 plot for the slope geometry without undercutting with K = 2

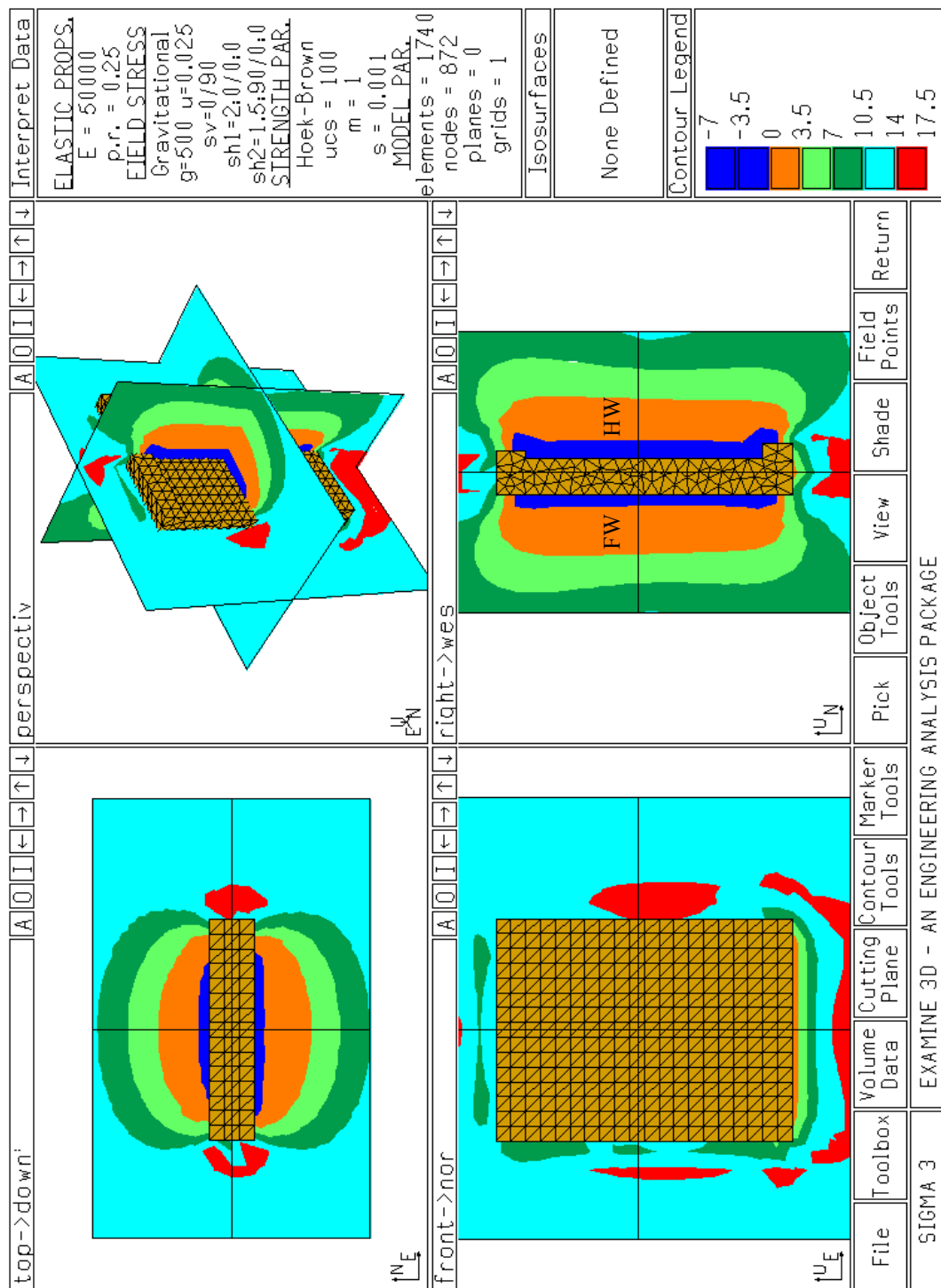


Figure 7.10. Examine 3D σ_3 plot for the slope geometry with 1.5m average undercutting with $K = 2$

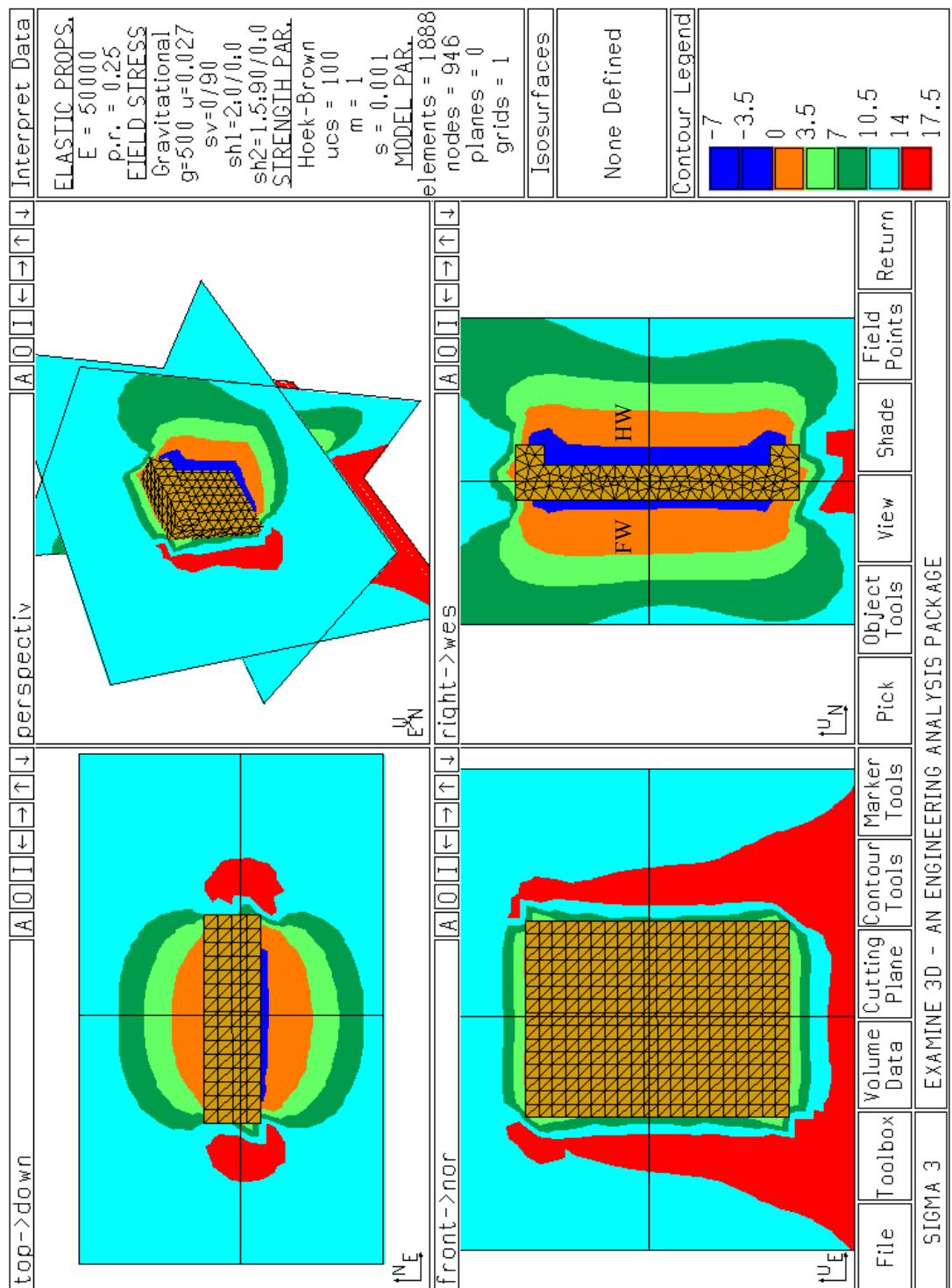


Figure 7.11. Examine 3D σ_3 plot for the slope geometry with 3m average undercutting with $K = 2$

of the slope HW. Figure 7.11 shows the model with a depth of 3m of undercutting in both overcut and undercut drifts. This geometry shows 2.9m of ELRD, which presents a 1.1m of ELRD increase compared to the case with no undercutting.

Table 7.2 summarizes the results of this modelling. Figure 7.12 shows the ELRD for undercutting factors (UF) from 0.0 to 1.3 metres, for various stress ratios. Figure 7.13 shows the component of relaxation due to the undercutting ($ELRD_{uc}$) for the same geometries and stress conditions.

The modelling results showed that the ELRD due to undercutting the slope HW ($ELRD_{uc}$) has a linear relationship with the average depth of undercutting in the overcut and undercut drifts for a constant slope height. With an increase in the average depth of undercutting, the $ELRD_{uc}$ increases. The stress state (in terms of the stress ratio) has a significant influence on this linear relationship. A higher stress ratio results in a higher $ELRD_{uc}$ for a given average depth of undercutting.

This modelling test case shows the importance of undercutting on the hanging wall zone of relaxation. As well as increasing the hanging wall zone of relaxation, undercutting the hanging wall removes the abutment support and increased the probability of failure due to gravity loading. The next section discusses these combined undercutting influences on hanging wall dilation.

Table 7.2. $ELRD_{uc}$ results for test case Examine 3D model slope

u/c* depth in oc* drift (m)	u/c* depth in uc* drift (m)	Avg. depth of u/c* (m)	ELRD					
			K=1.5		K=2.0		K=2.5	
			Total ELRD (m)	$ELRD_{uc}$ (m)	Total ELRD (m)	$ELRD_{uc}$ (m)	Total ELRD (m)	$ELRD_{uc}$ (m)
0.0	0.0	0.0	0.8	0.0	1.8	0.0	3.2	0.0
1.0	1.0	1.0	0.9	0.1	2.3	0.5	4.0	0.8
1.0	2.0	1.5	1.0	0.2	2.5	0.7	4.3	1.1
2.0	2.0	2.0	1.1	0.3	2.7	0.9	4.8	1.6
3.0	3.0	3.0	1.2	0.4	2.9	1.1	5.2	2.0

* oc =overcut, uc = undercut, u/c =undercutting

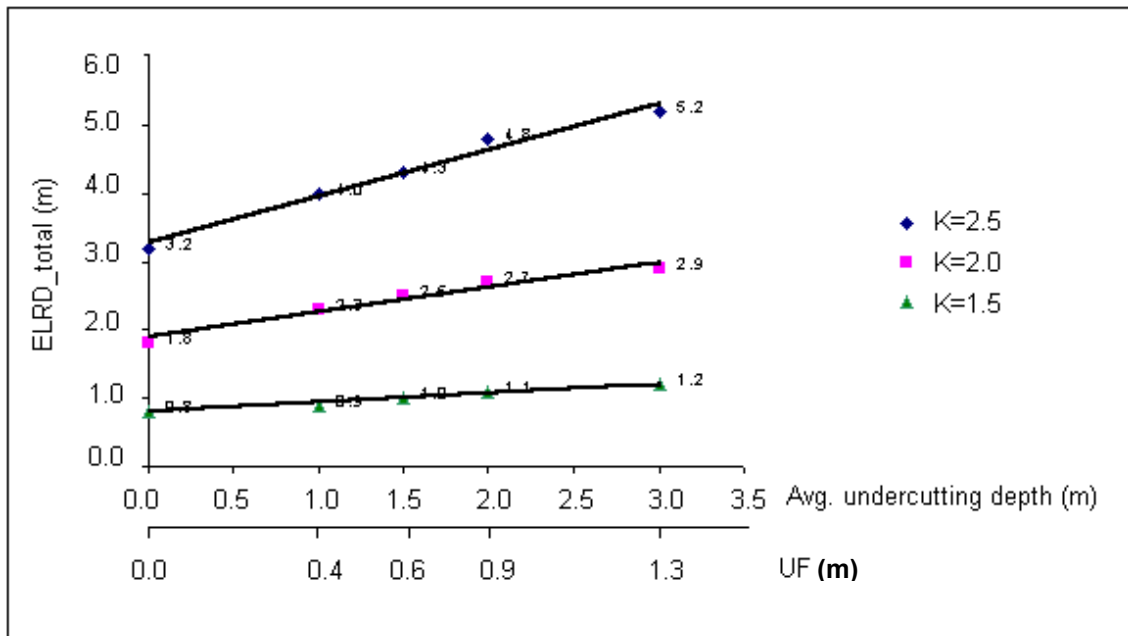


Figure 7.12. Example plots of ELRD versus average depth of undercutting (for a 40x30x5 m slope)

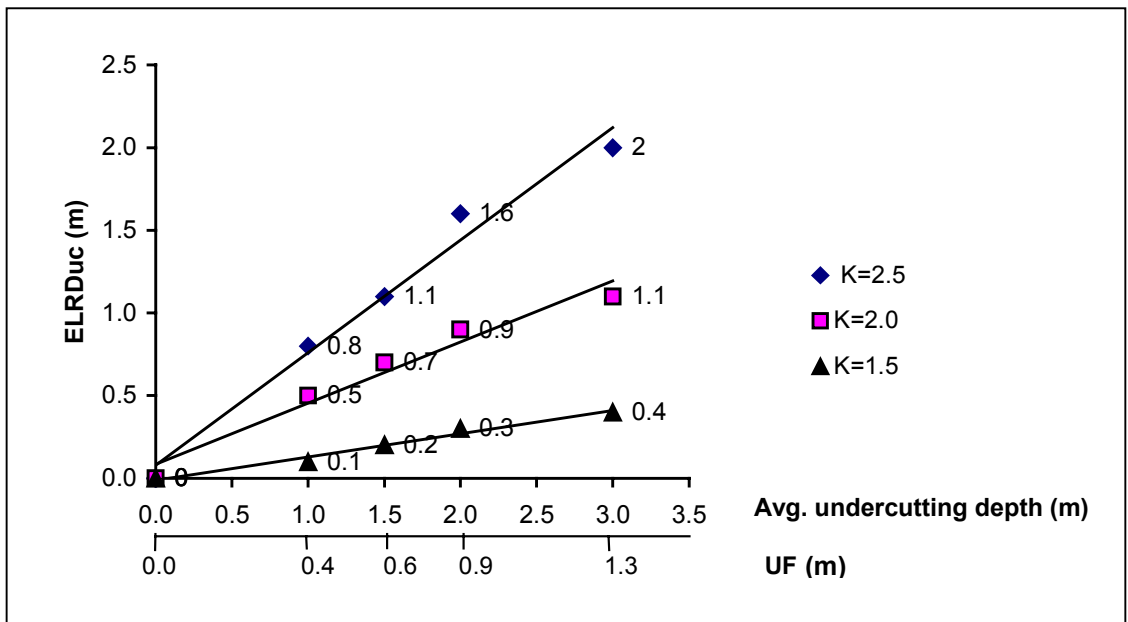


Figure 7.13. Example plots of additional ELRD due to undercutting versus average depth of undercutting (for a 40x30x5m slope)

7.4 General Interaction of Undercutting on Stability and Dilution

Undercutting the hanging wall decreases stability by increasing the zone of relaxation as well as by reducing abutment support. The loss of abutment support will not extend past the depth of undercutting, as shown in Figure 7.14. The additional relaxation due to undercutting may extend well past the area of lost abutment support for high K ratios. For low values of the K stress ratio, the additional zone of relaxation caused by the undercut may be entirely within the zone of lost abutment support (Figure 7.14). For this reason, the influence of undercutting will be considered as two factors with the $ELRD_{UC}$ representing the influence of the increased zone of relaxation. The UF term, which is based on the average depth of undercutting and the total distance along which undercutting occurs, should be related to the increased dilution due to the loss of abutment support.

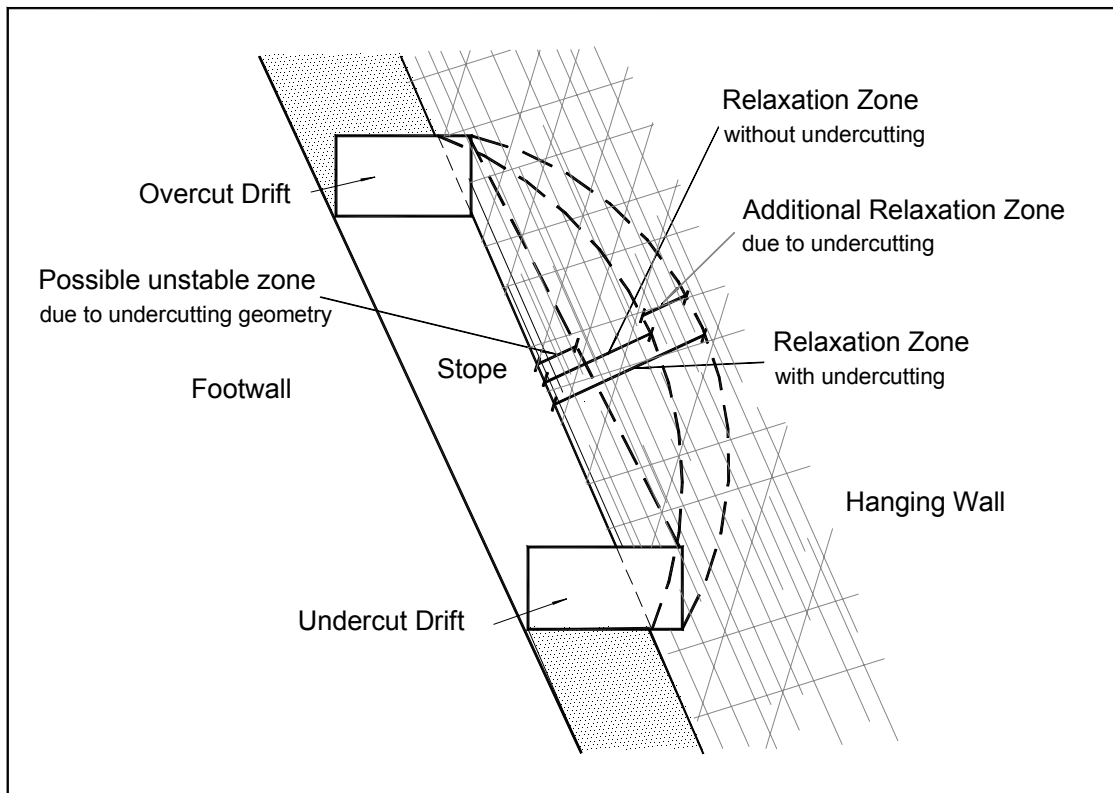


Figure 7.14. Schematic cross section showing the zones of undercutting influence

The overall competence of the HW rock mass also plays an important role on the influence of undercutting on stope HW stability. With increasing rock mass quality, the influence of undercutting on the stope HW stability decreases. The stability of a stope HW is closely related to the HW rock mass strength, joint frequency and joint condition as well as the dip of the stope HW. The modified stability number N' accounts for both rock mass quality and stope HW dip. Therefore N' should be included in the influence of the undercutting factor.

7.5 Case History Assessment

It is not easy to accurately determine the influence of undercutting on hanging wall stability and a purely empirical approach is taken. The database for Trout Lake and Callinan Mines has been analyzed and the dilution factor has been determined for each stope. The equation developed (Eq. 7.3) was used to calculate the undercutting factor UF for these two mines' case histories. The two components of undercutting, relaxation and abutment loss, are assessed separately.

7.5.1 Stress Influence

Figure 7.13 shows the additional ELRD that can be expected due to undercutting for a typical HBMS stope geometry with a HR about 8.6 m. Figure 7.15 shows the additional ELRD due to undercutting that can be expected for the 6 stope stress categories. The fact that UF values less than 0.4 metres (Figure 7.4) were calculated for the majority of stopes for the HBMS database indicates that the majority of $ELRD_{uc}$ values will be well under 0.5 metres (Figure 7.15). An estimate can be made for the total average depth of relaxation by adding the $ELRD_{uc}$ from Figure 7.15 and the ELRD from Figure 6.32. The $ELRD_{uc}$ is only an estimate based on a typical HBMS stope geometry. However, since 75% of the HBMS case histories have HR values between 6.0 to 9.0 metres, the $ELRD_{uc}$ correction should be reasonable. Figure 7.16 shows a graph of the combined $ELRD_{total}$ versus the actual dilution minus the dilution factor. There is no apparent trend relating the total depth of relaxation to additional dilution (prediction error). This is perhaps due

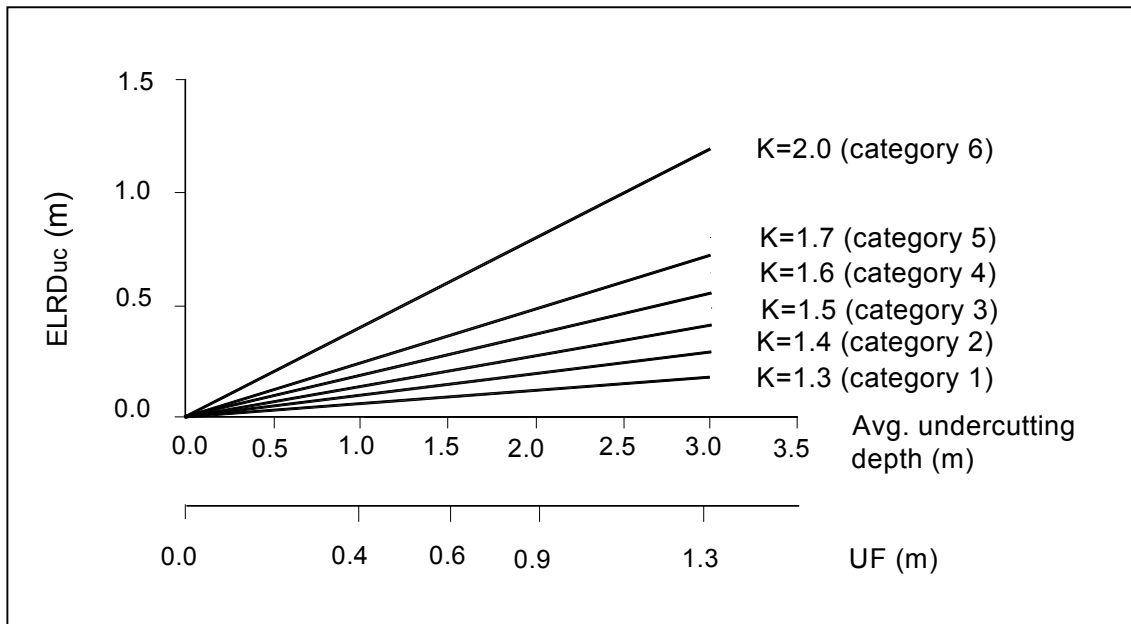


Figure 7.15. Additional ELRD due to undercutting that can be expected for the 6 stope stress categories (for a typical HBMS stope geometry with a HR of 8.6m)

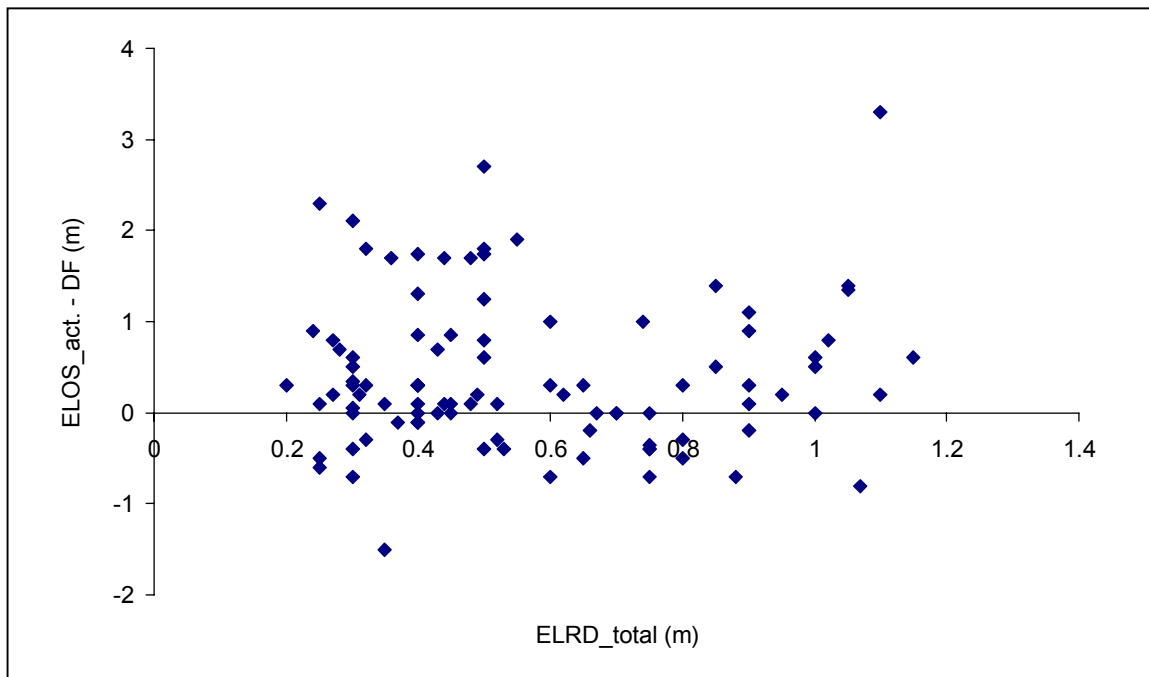


Figure 7.16. ELRD_{total} versus the actual dilution minus the dilution factor case history plots (88 cases)

to the low initial stress state and relatively competent nature of the hanging wall rocks. Figure 7.17 shows the same data for the case histories where N' is less than 10 (29 cases). No significant trend was found. Other contributing factors may overshadow the stress influence.

7.5.2 Abutment Loss Influence

The actual recorded stope dilution ($ELOS_{act.}$) minus the dilution factor (DF) has been plotted versus the calculated undercutting factor (UF) and is shown in Figure 7.18. There is a wide variation in the individual stope cases. However, Figure 7.18 does show a general trend of increasing average unpredicted dilution with an increasing undercutting factor. As discussed in Section 7.4, the influence of undercutting increases as rock mass quality decrease and the UF/N' can be used to quantify this combined

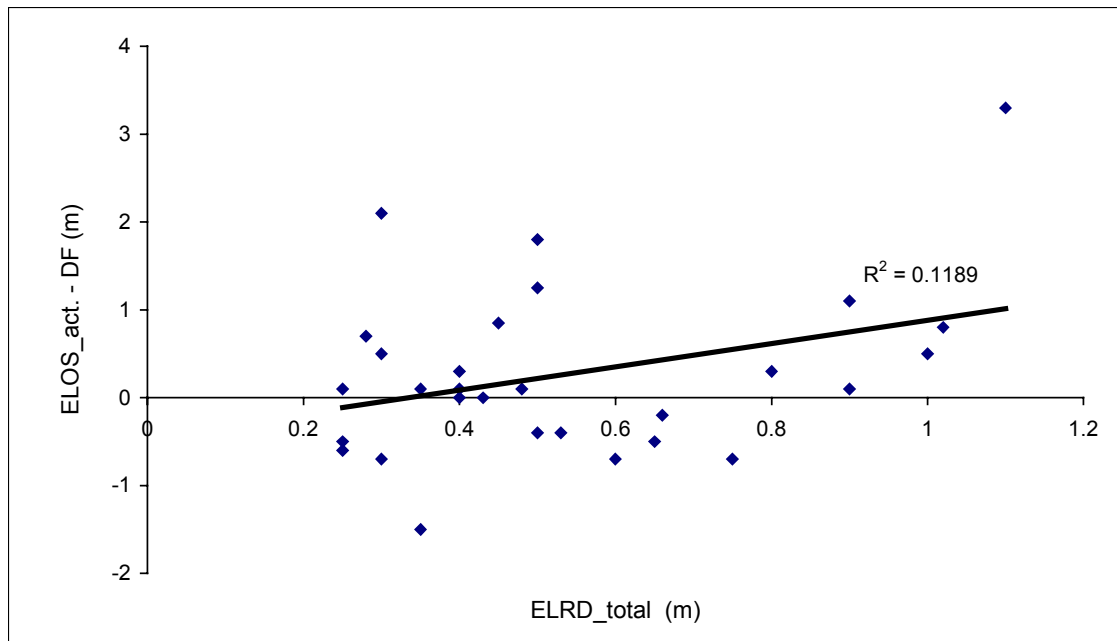


Figure 7.17. $ELRD_{total}$ versus the actual dilution minus the dilution factor case history plots for the cases with $N' < 10$ (29 cases)

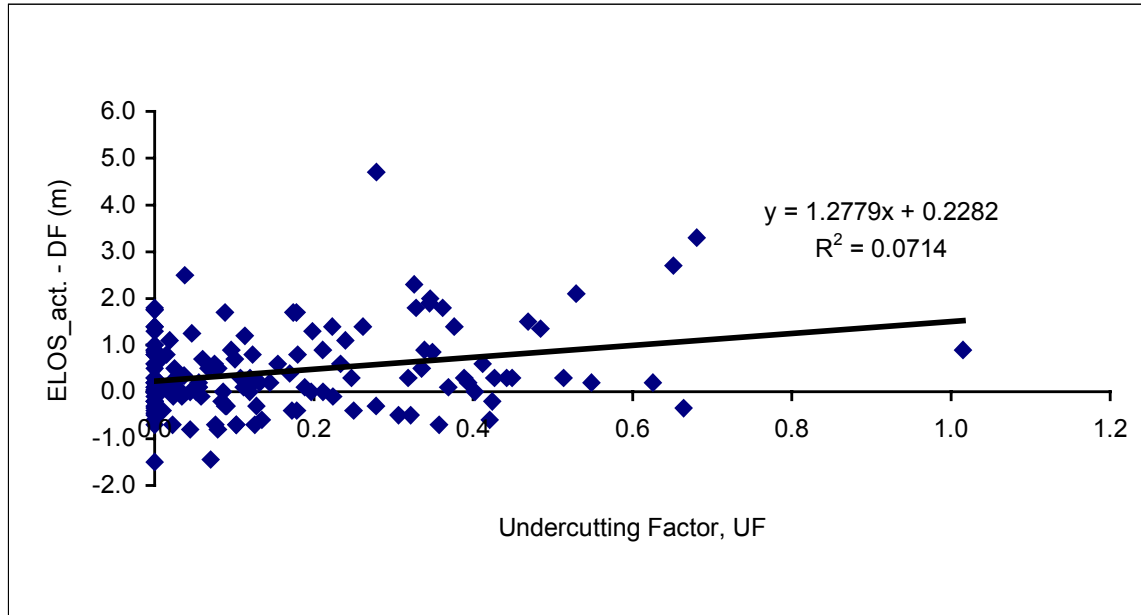


Figure 7.18. Comparison between UF and dilution in excess of predicted values

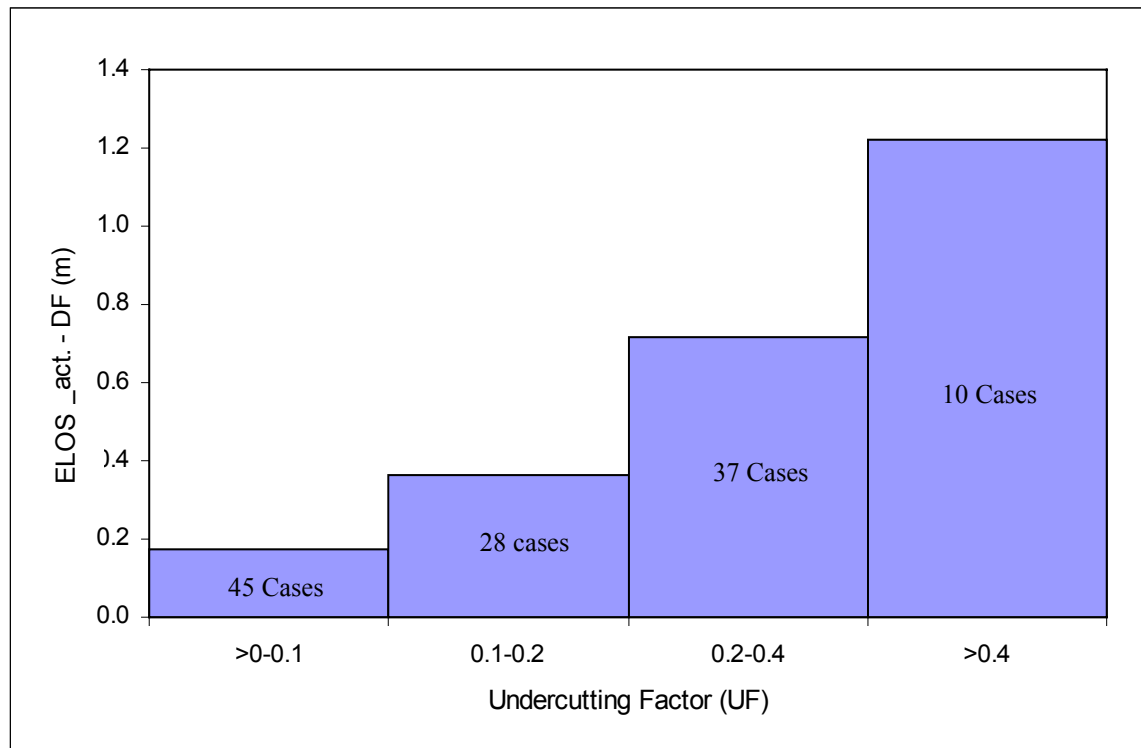


Figure 7.19. UF versus average dilution in excess of predicted values

influence. The UF/N' versus ELOS prediction error plot (Figure 7.20) also shows a similar weak trend. The absence of trends suggests that other factors may overshadow much of the influence of undercutting on dilution.

7.5.3 Case History Example

The 900 M3-3 stope of Trout Lake Mine case history gives some evidence of the effect of undercutting on stope HW slough. The 900 M3-3 stope is located in the Middle Zone orebody of Trout Lake Mine. The stope has a strike length of 23m, exposed height of 34m, and ore width of 5.2m. The stope HW contact dips at 67°. Both overcut and undercut drifts partially undercut the HW. Figure 7.21 is the plan view of the stope drift layouts. The shaded areas are the undercut areas outside the ore contact. The blastholes within the orebody were drilled from the overcut drift down to the undercut drift.

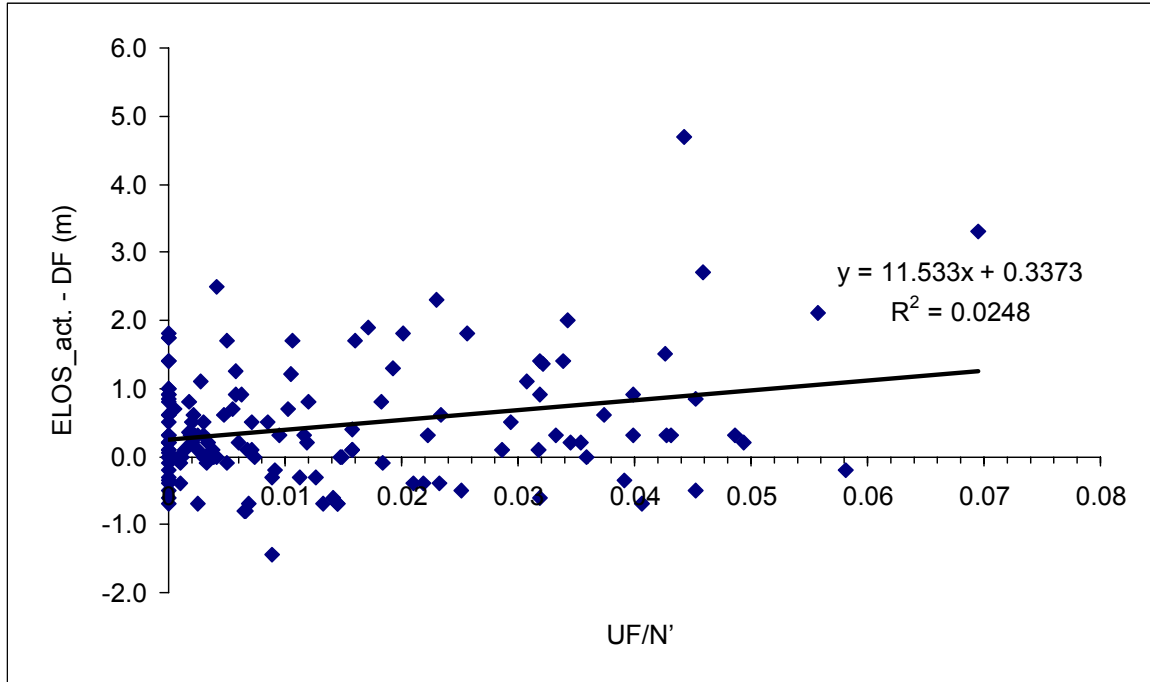


Figure 7.20. UF/N' versus ELOS prediction error case history plot

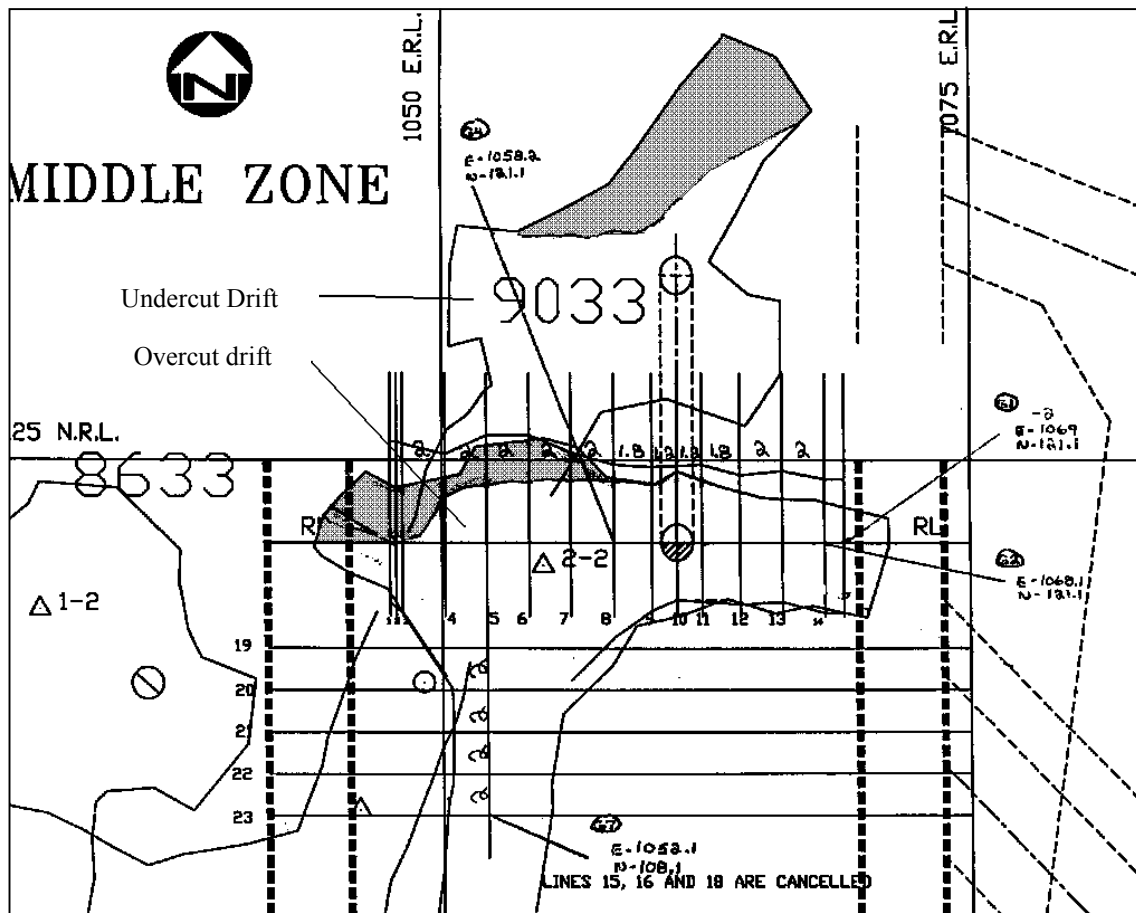


Figure 7.21. Plan view of stope drift layout and undercutting (shaded areas)

The plan view shows a gradual increase in undercut depth, on the undercut drift, from line 6 to line 14. Figure 7.22 shows the cross sections of drill lines 7, 8 and 9. These three typical sections show that the stope HW overbreak tends to extend to the outer limits of the undercut drifts, to form an arched failure showing the importance of the HW abutment support in the undercutting area.

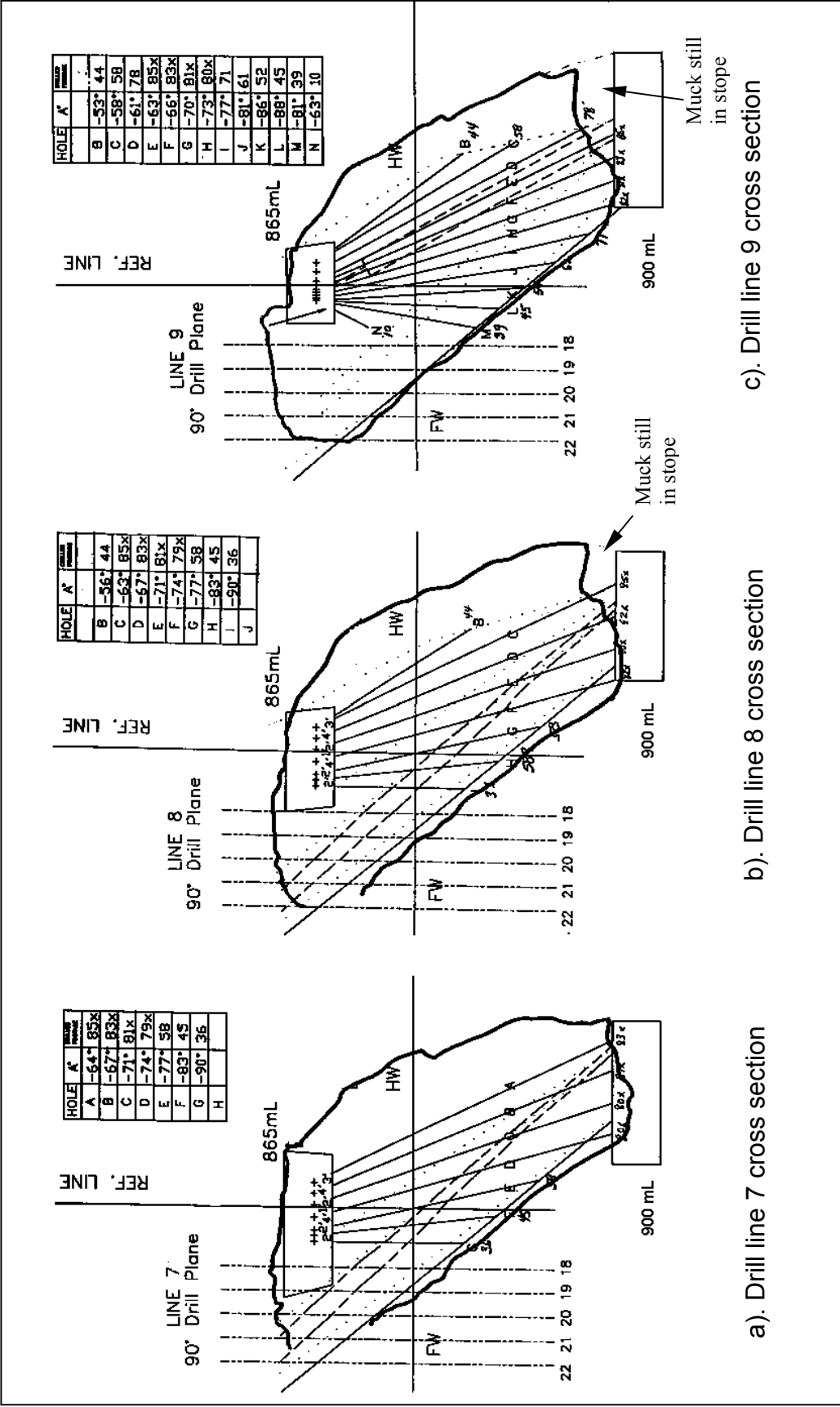


Figure 7.22. Drilling cross section showing CMS surveyed overbreak profiles and undercutting

7.6 Summary

The influence of undercutting on the stope HW stability and dilution was quantified by analytical and numerical methods. Instability caused by undercutting on the stope HW consists of two parts in general:

- a). Jointed rock mass rock failure caused by removal of support due to undercutting (abutment loss);
- b). Increased zone of distressed or relaxed rock failure due to undercutting.

An equation has been developed to account for the undercutting geometry influence on the stope HW stability and dilution (called undercutting factor, UF). The UF is proportional to the portion of stope HW being undercut and the average depth of undercutting. Attempts have been made to account for the rock mass condition and stress on the undercutting influence. The UF term has an influence on the zone of relaxation. Increased HW ELRD due to undercutting occurs for highly deviatoric stress conditions with σ_1 perpendicular to the HW. The influence of undercutting on stope HW ELOS $ELRD_{UC}$ can be added to the ELRD estimated based on the overall hanging wall geometry (HR or RF) and stress state (Figure 7.5 and 7.14)

The proposed relationships were examined with the existing database and comparisons were conducted with the prediction error ($ELOS_{Act} - DF$). No obvious trend of increasing unpredicted dilution (average) with an increasing undercutting factor or with UF/N' can be discovered. The influence of the ELRD & $ELRD_{uc}$ was not apparent with the HBMS database, perhaps due to the low initial K ratio.

CHAPTER 8

INFLUENCE OF BLASTING ON STOPE HANGING WALL STABILITY AND DILUTION

8.1 Introduction

The drilling, blasting and mucking cycle is the most commonly used method for obtaining ore in open stope mining. Blasting of the ore is conducted to sufficiently destroy the structural integrity of the rock mass to allow mechanical mucking and transport. A good blast design results in the ore breaking into easily handled fragments with a uniform block size distribution. Unbroken ore left in the stope results in lost revenue and the creation of large blocks create handling problems which may require secondary blasting and create costly delays. These goals for a good blast lead the blast engineer to design a blast which can sufficiently fragment the ore within the design line, but minimises the blast damage to adjacent waste rock to reduce ore dilution. These conflicting general goals for good blasting create much of the driving force for blasting research.

An ideal blast creates easily handled fragments of ore, leaves no unbroken ore behind in the stope and does no damage to the waste rock past the ore contact. All these goals cannot be met and some degree of hanging wall damage results after a blast. Hanging wall blast damage acts to loosen the rock mass and induce new fractures. Blast damage can degrade the rock mass quality and this can result in hanging wall instability in the form of increased hanging wall slough and dilution.

This chapter reviews some blasting theory, describes the parameters which have been collected in the data base and looks at their theoretical and actual influence on hanging wall dilution.

8.2 Blasting Background

The technique of rock breakage using explosives involves drilling blastholes, loading the blastholes with explosive and then sequentially detonating the explosive in each hole. Before discussing the influence of blasting damage on the stope HW, it is necessary to have a general understanding of the mechanism of rock blasting.

In a rock blast, there are at least eight rock breakage mechanisms that have been identified (Hagan, 1967 & 1973; Mercer, 1980; Carlos et al., 1995). They are:

- Crushing of rock
- Relative radial motion
- Release of load
- Reflection breakage or spalling
- Gas extension of strain wave-generated and /or natural cracks
- Flexural rupture
- Shear fracturing along natural and strain wave generated cracks
- In-flight collisions.

The following descriptions of rock blast mechanisms are based on Mercer (1980). When an explosive detonates, the ingredients of the explosive are rapidly converted into gaseous products at very high temperatures and pressures. The gases, usually exceeding about 18,000 atmospheres, impact the blast hole wall and transmit a shock wave or shock strain, which travels at a speed of 2000 - 6000 metres per second, into the surrounding rock as shown in Figure 8.1 (Hagan, 1967). Crushing occurs around a blasthole wall when the pressure of the detonation front exceeds the dynamic compressive strength of the rock (Hagan, 1967; Bauer, 1978). The out-going strain wave (strain pulse) generated by the high-pressure detonation front disperses and loses

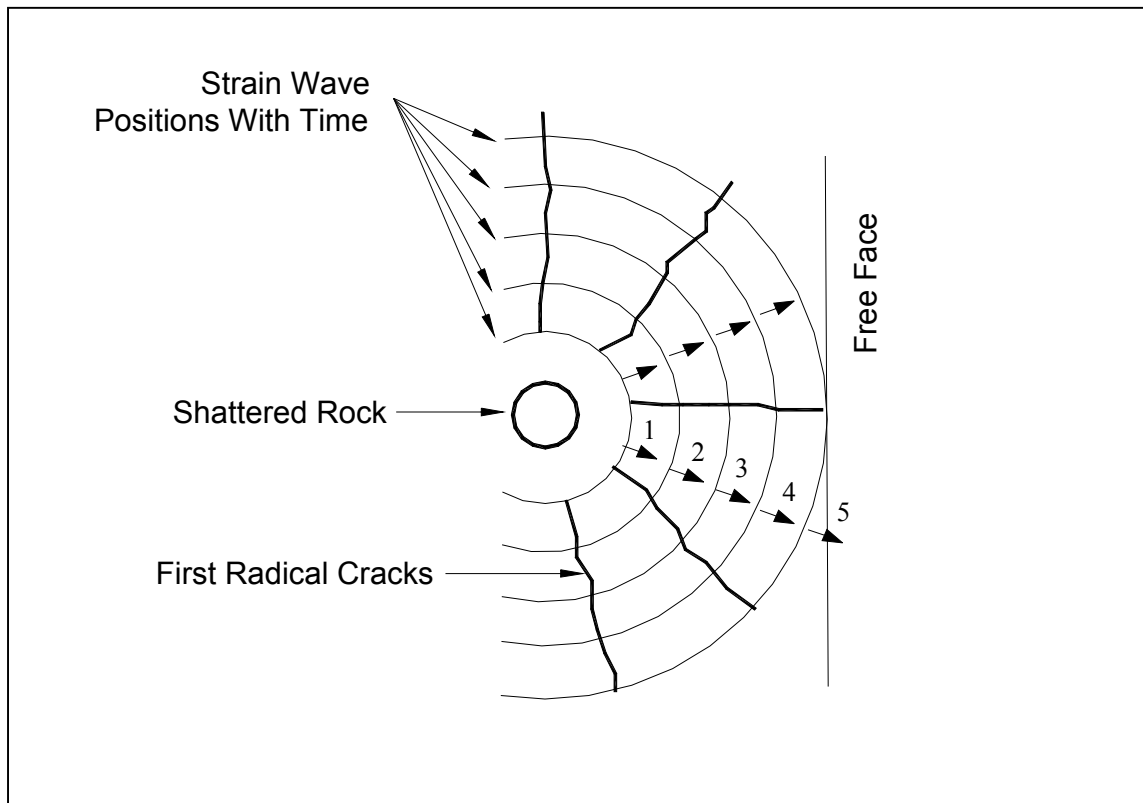


Figure 8.1. First stage of explosive /rock interaction (after Mercer, 1980)

energy rapidly. Crushing ceases when the strain level in the pulse drops below the elastic limit of the rock. The rock directly outside the crushing zone is subject to very sudden compression due to the dispersing strain pulse. This radial compression results in tangential tensile stresses, which can cause cracks to develop radially from the blasthole. Fractures occur immediately after the strain or compression pulse passes due to the release of compressive loading.

During and after the stress wave propagation, high-pressure explosion gases penetrate the available fractures, which include natural fractures and the fractures developed by shock waves, and wedge them open as shown in Figure 8.2 (Mercer, 1980). This leads to an increase in the volume and permeability of the rock mass and a subsequent reduction in the pressure of the explosion gases. The opening of fractures and the creation of new fractures effectively reduce the rock mass strength.

When the stress/strain waves reach a free face, an imbalance of forces occurs. This will cause the burden rock to move. Burden rock is defined as the rock between the blast hole and the open excavation, or free face, as shown in Figure 8.1.

Eventually the gases dissipate through the fracture network or are released to the atmosphere. The confining pressure then rapidly drops and rock movement reduces until the driving force is consumed.

Stope blast layout and design is generally conducted by mine engineers and technicians and is strongly based on past experience. Blast design can vary significantly between mines based on the individual experience and preferences of the operators. Many factors influence the performance of a blast and the degree of blast damage that can result. Not all of these factors are measured at mines. These contributing factors include rock mass quality, blast design, blasthole diameter and length, drillhole layout,

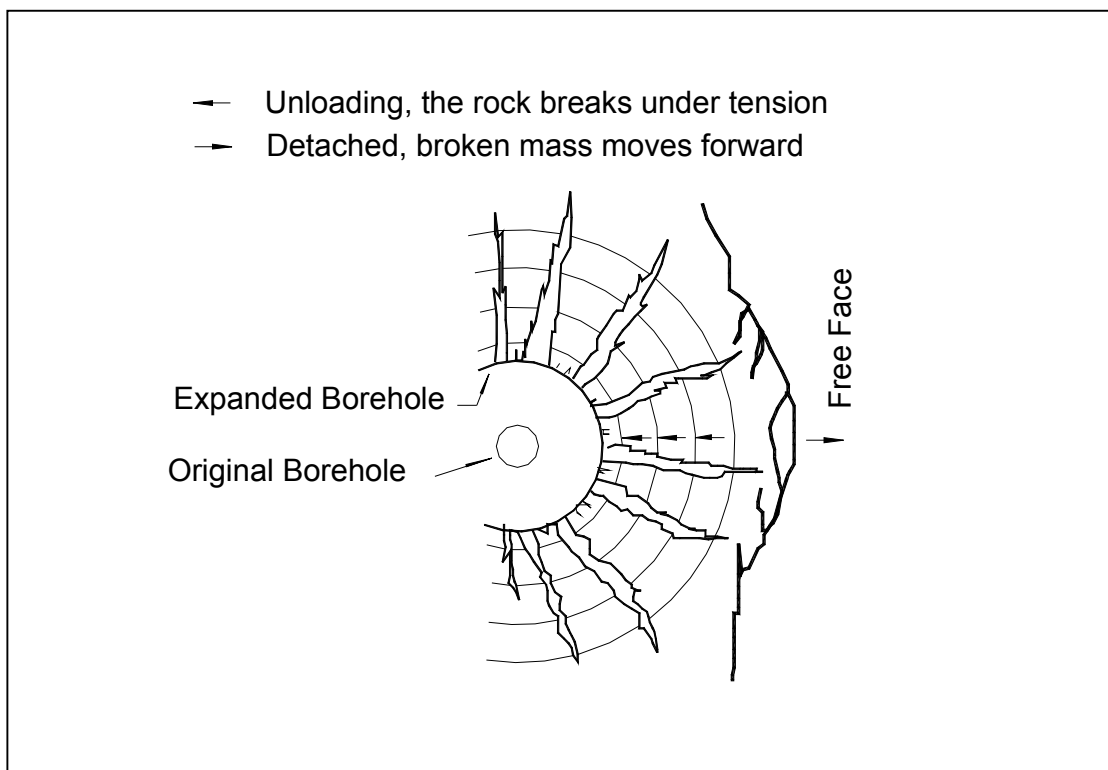


Figure 8.2. Later stages of explosive/rock interaction (after Mercer, 1980)

drilling accuracy, explosive distribution, initiation sequence and wall control technique etc.. The next section discusses methods of assessing blast damage, which is difficult to both quantify and determine a cause for.

8.3 Methods of Assessing Blast Damage

There are no consistent methods to measure and quantify blast induced damage (Yang et al., 1993). Joint mapping before and after blasting can sometimes highlight damage to the rock mass induced by blasting. This approach is highly subjective and cannot be used in this study because of the lack of access after blasting. The measurement of peak particle velocity (PPV) induced by blasting has been used as a measurement of blast damage. This approach is discussed in this chapter. It cannot be used in this study because these measurements have not been consistently recorded at the mine. The Hoek and Brown failure criterion, discussed in Section 2.2.1, has been used to assess the failure criteria for undisturbed and disturbed rock masses. The disturbed and undisturbed description can be applied to blast damaged and undamaged rock masses. This approach does not give an indication of the degree of blast damage, but does give a suggested limit to the influence of blast damage. After the blast, an indication of the degree of blast damage can be obtained from CMS surveys or visual inspection of the walls of the excavation created. Instability may be an indication of blast damage. The problem is determining if the failure is caused by blasting or other factors such as a weak rock mass.

8.3.1 Peak Particle Velocity Method

Peak particle velocity has been used for the measurement of blast damage to structures and to rock masses. The fragmentation of rock by detonation of an explosive charge depends on the effects of both strain induced in the rock and upon the gas pressure generation of the explosive. The particle velocity is a measure of the velocity during the passage of the vibration wave, not the velocity of the wave itself. Many empirical relationships between blast geometries and vibration velocities have been developed.

Most of them relate the PPV to the explosive charge and the distance from the charge. Holmberg and Persson (1980) suggested the following empirical equation for estimation of PPV:

$$PPV = k \frac{w^\alpha}{R^\beta} \quad (8.1)$$

where PPV is the Peak Particle Velocity in mm/sec.,
 w is the charge weight per single blast in kg.,
 R is the radial distance from the point of detonation in metres,
 k , α and β are constants which depend upon the structure and elastic properties of the rock mass, which vary from site to site.

The constants k , α and β are site specific. The constants k , α and β must be determined for each site in order to apply equation 8.1 to estimate the PPV. This can be done by carrying out a series of trial blasts and monitoring the induced particle velocities at different distances from these blasts. Once the PPV has been estimated, the blast damage thresholds of PPV can be applied to estimate the blast damage. Hagan (1996) reported a list of Peak Particle Velocity threshold damage levels as shown in Table 8.1.

Table 8.1. Peak Particle Velocity threshold damage levels (from Hagan, 1996)

PPV (mm/sec.)	Damage Level
50	Limit below which risk of damage to structure is very slight
230	Cracks in concrete blocks
300	Rock falls in unlined tunnel
635	Onset of cracking in rock
2500	Breakage of rock

Two problems exist for trying to use this approach. The site specific constants k , α and β are not available for the HBMS rock mass. Also, there is no way to link the damage level shown in Table 8.1 with the expected hanging wall damage or an increase in

dilution. This may be a valid approach for trying to link blast damage and hanging wall dilution. An extensive test program would be required which is beyond the scope of this study.

8.3.2 Blast Damage Consideration in the Hoek and Brown Failure Criterion

Hoek and Brown (1980) developed a rock mass failure criterion to assess the stability of a rock mass, as discussed in Section 2.2.1. The Hoek and Brown failure criterion is expressed as:

$$\sigma_1 = \sigma_3 + \sqrt{m\sigma_c\sigma_3 + s\sigma_c^2} \quad (8.2)$$

where σ_1 is the major principal stress at failure,

σ_3 is the minor applied principal stress,

σ_c is the uniaxial compressive strength of the intact rock,

m and s are constants which depend upon the properties of the rock

The constants m and s have been linked to the rock type and the rock mass classification values. Two sets of values for m and s were introduced to account for blast damage and the two sets of values refer to an undisturbed rock mass and a disturbed rock mass (Hoek and Brown, 1988) as shown in Table 8.2. The drop in the m and s value for a given rock mass condition can be equated to a drop in the rock classification value caused by blasting as shown in the following equation (Milne et al., 1998).

$$RMR_{Undisturbed} = RMR_{Disturbed} + (50 - 0.5RMR_{Disturbed}) \quad (8.3)$$

The equation can be solved for $RMR_{Disturbed}$ with $RMR_{Undisturbed}$ as the initial rock mass classification assessment. An approximated correlation between RMR and Q is (Bieniawski, 1979 and 1993):

$$\text{RMR} = 9\ln Q + 44 \quad (8.4)$$

For the average rock classification values for Trout Lake Mine of $Q' = 6$ (disturbed), the undisturbed Q' of 55 before blast damage can be calculated by using equations 8.3 and 8.4. This indicates a Q' reduction of 49 can be caused by blast damage. This reduction in Q' would correspond to an increase in the average dilution prediction (based on the dilution graph, Figure 2.16) from about 0.1 metres to 1 metre for the HBMS mines' average stope HW dip and HR values. This is an interesting approach for looking at the effect of blasting on dilution. The approach is not substantiated by empirical data and cannot consider the degree of blast damage or the effect of changing blasting practice and only gives an indication of a possible role of blast damage on increasing hanging wall dilution.

8.3.3 Visual Inspection and CMS Survey Methods

Visual inspections or CMS survey data can provide useful information on the blast damage on opening walls by observing or measuring the wall profile. Slough or failure off the stope walls is readily measured with a CMS and the degree of slough may be an indication of blast damage. The problem with this approach is the difficulty in distinguishing between stress or structurally controlled instability and the instability caused by blast damage. This research attempts to estimate blast induced damage to the hanging wall by assessing the large number of case histories in the HBMS database.

8.4 Factors Influencing HW Blast Damage and Dilution

The previous section discussed possible methods of measuring blast damage after it has occurred. From an operational point of view, a method of predicting blast damage based on the method of blasting and current ground conditions is needed. There are many blasting procedures that the operator can vary. Their influence on blast damage is hard to quantify. Some of the main factors include:

Table 8.2. Hoek and Brown failure criterion m and s constants values (Hoek & Brown, 1988)

Approximate relationship between rock mass quality and material constants						
Disturbed rock mass m & s values		<i>Undisturbed rock mass m & s values</i>				
Empirical Failure Criterion $\sigma_1 = \sigma_3 + \sqrt{m\sigma_c\sigma_3 + s\sigma_c^2}$ $\sigma_1 = \text{major principal stress}$ $\sigma_3 = \text{minor principal stress}$ $\sigma_c = \text{uniaxial compressive strength of intact rock, and}$ $m \text{ \& } s \text{ are empirical constants}$		Carbonate Rocks With Well Developed Crystal Cleavage dolomite, limestone and marble	Lithifels Argillaceous Rocks mudstone, siltstone, shale and slate (normal to cleavage)	Arenaceous Rocks With Strong Crystals and Poorly Developed Crystal cleavage Sandstone and quartzite	Fine Grained Polyminerallc Igneous Crystalline Rocks Andesite, dolerite and rhyllite	Coarse Grained Plyminerallic Igneous and Metamorphic Crystalline Rocks Amphibolite, gabbro, gneiss, granite, norite and quartz-diorite
Intact Rock Samples Lab .size specimens free from discontinuities CSIR rating: RMR = 100 NGI rating = 500		m 7.00 s 1.00 <u>m</u> <u>7.00</u> <u>s</u> <u>1.00</u>	10.00 1.00 <u>10.00</u> <u>1.00</u>	15.00 1.00 <u>15.00</u> <u>1.00</u>	17.00 1.00 <u>17.00</u> <u>1.00</u>	25.00 1.00 <u>25.00</u> <u>1.00</u>
Very Good Quality Rock Mass Tightly interlocking undisturbed rock with unweathered joints at 1 to 3 m CSIR rating : RMR = 85 NGI rating = 100		m 2.4 s 0.082 <u>m</u> <u>4.1</u> <u>s</u> <u>0.189</u>	3.43 0.083 <u>5.85</u> <u>0.189</u>	5.14 0.082 <u>8.78</u> <u>0.189</u>	5.82 0.082 <u>9.95</u> <u>0.189</u>	8.56 0.082 <u>14.63</u> <u>0.189</u>
Good Quality Rock Mass Fresh to slightly weathered rock. Slightly disturbed with joints at 1 to 3 m CSIR rating: RMR = 65 NGI rating = 10		m 0.575 s 0.00293 <u>m</u> <u>2.006</u> <u>s</u> <u>0.0205</u>	0.821 0.00293 <u>2.865</u> <u>0.0205</u>	1.231 0.00293 <u>4.298</u> <u>0.0205</u>	1.395 0.00293 <u>4.871</u> <u>0.0205</u>	2.052 0.00293 <u>7.163</u> <u>0.0205</u>
Fair Quality Rock Mass Several sets of moderately weathered joints spaced at 0.3 to 1 m CISR rating: RMR = 44 NGI rating = 1		m 0.128 s 0.00009 <u>m</u> <u>0.947</u> <u>s</u> <u>0.00198</u>	0.183 0.00009 <u>1.353</u> <u>0.00198</u>	0.275 0.0009 <u>2.03</u> <u>0.00198</u>	0.311 0.00009 <u>2.301</u> <u>0.00198</u>	0.458 0.00009 <u>3.383</u> <u>0.00198</u>
Poor Quality Rock Mass Numerous weathered joints at 30 -500mm, some gouge; clean compacted waste rock CSIR rating: RMR = 23 NGI rating = 0.1		m 0.029 s 0.000003 <u>m</u> <u>0.447</u> <u>s</u> <u>0.00019</u>	0.041 0.000003 <u>0.639</u> <u>0.00019</u>	0.061 0.000003 <u>0.959</u> <u>0.00019</u>	0.069 0.000003 <u>1.087</u> <u>0.00019</u>	0.102 0.000003 <u>1.598</u> <u>0.00019</u>
Very Poor Quality Rock Mass Numerous heavily weathered joints spaced <50mm with gouge. Waste rock with fines CSIR rating: RMR = 3 NGI rating = 0.01		m 0.007 s 0.0000001 <u>m</u> <u>0.219</u> <u>s</u> <u>0.00002</u>	0.01 0.0000001 <u>0.313</u> <u>0.00002</u>	0.015 0.0000001 <u>0.469</u> <u>0.00002</u>	0.017 0.0000001 <u>0.532</u> <u>0.00002</u>	0.025 0.0000001 <u>0.782</u> <u>0.00002</u>

- Rock mass properties
- Drillhole design (drillhole size, length, spacing, burden, and orientation)
- Drillhole accuracy (drillhole deviation)
- Explosive type
- Wall control methods
- Explosive distribution
- Explosive per delay
- Initiation sequence
- Availability of a free face

The influence of these factors is briefly discussed in the following sections.

8.4.1 Rock Mass Properties

The rock mass properties are of fundamental importance to the design of blasts. Rock mass properties in a stope hanging wall will influence the effect of blasting practice on dilution. A poorly designed blast may result in significant dilution and hanging wall damage in a poor quality rock mass (low N or Q' values). The same blasting practice may not show up as dilution or instability in a good quality hanging wall. This influence of rock mass condition is shown in equation 8.3, where the reduction in the rock mass classification value due to blasting is less for good quality rock (high RMR values). Initial rock mass properties need to be considered to assess the influence of blasting practices on hanging wall dilution. The dynamic strength of the rock and the rock joint characteristics are two important rock mass properties for blasting. The strength of rocks is normally quite well correlated with their density (Carlos et al., 1995). In general, low-density rocks are deformed and broken quite easily, requiring relatively low energy factors, whereas dense rocks need a higher energy to achieve a satisfactory fragmentation. Rocks generally have discontinuities (such as bedding planes, planes of lamination or foliation, fractures and joints), which influence the physical and mechanical properties of the rocks and, consequently, the blasting results. Neglecting the rock mass properties when blasting will lead to either over blasting in

some areas or under blasting in other areas. Over blasting can cause damage to the adjacent rock mass (e.g., stope walls in open stope mining), and under blasting can result in the loss of economic ore. The expense of these deviations from expected performance can be costly. In open stope mining, overbreak-caused wall damage is a significant problem. Blast damage cannot only increase dilution, but also can cause mine opening instability problems. Blasting performance is determined by the interaction of the detonation of an explosive and the surrounding confining rock mass. Rock mass properties strongly influence this process.

8.4.2 Drillhole Design

Drillhole design is also a major factor in blast design. The drillhole design governs the distribution of explosive in the rock mass. In general, blast performance improves with better explosive distribution. In theory, smaller more frequent holes improve the explosive distribution. However, drilling more holes increases expense and the smaller holes will increase the chance of drillhole deviation.

Drillhole design is related to the drill machine's capabilities and the desired explosive distribution. Drillhole design includes drillhole length, hole diameter, drillhole spacing and burden. Drillhole length and diameter are closely related since long holes need to be drilled with a larger diameter hole size to reduce hole wander or deviation. Spacing is the distance between drillholes in the direction parallel to the available free surface, and burden is the distance between drillholes in the direction perpendicular to the available free surface (Figure 8.3). These parameters depend upon the drillhole diameter, the properties of the rock and the explosives used, as well as the desired degree of fragmentation. A larger hole diameter results in more explosive being loaded per hole. To maintain a certain explosive consumption per tonne of rock being blasted, larger hole diameters will require a larger spacing and burden. Too large a burden or too large a hole spacing will cause underbreak of the ore leading to handling and mucking problems. On the other hand, too small a burden will create fly rock and waste explosive energy. Figure 8.3 illustrates the effect of burden change on the blast

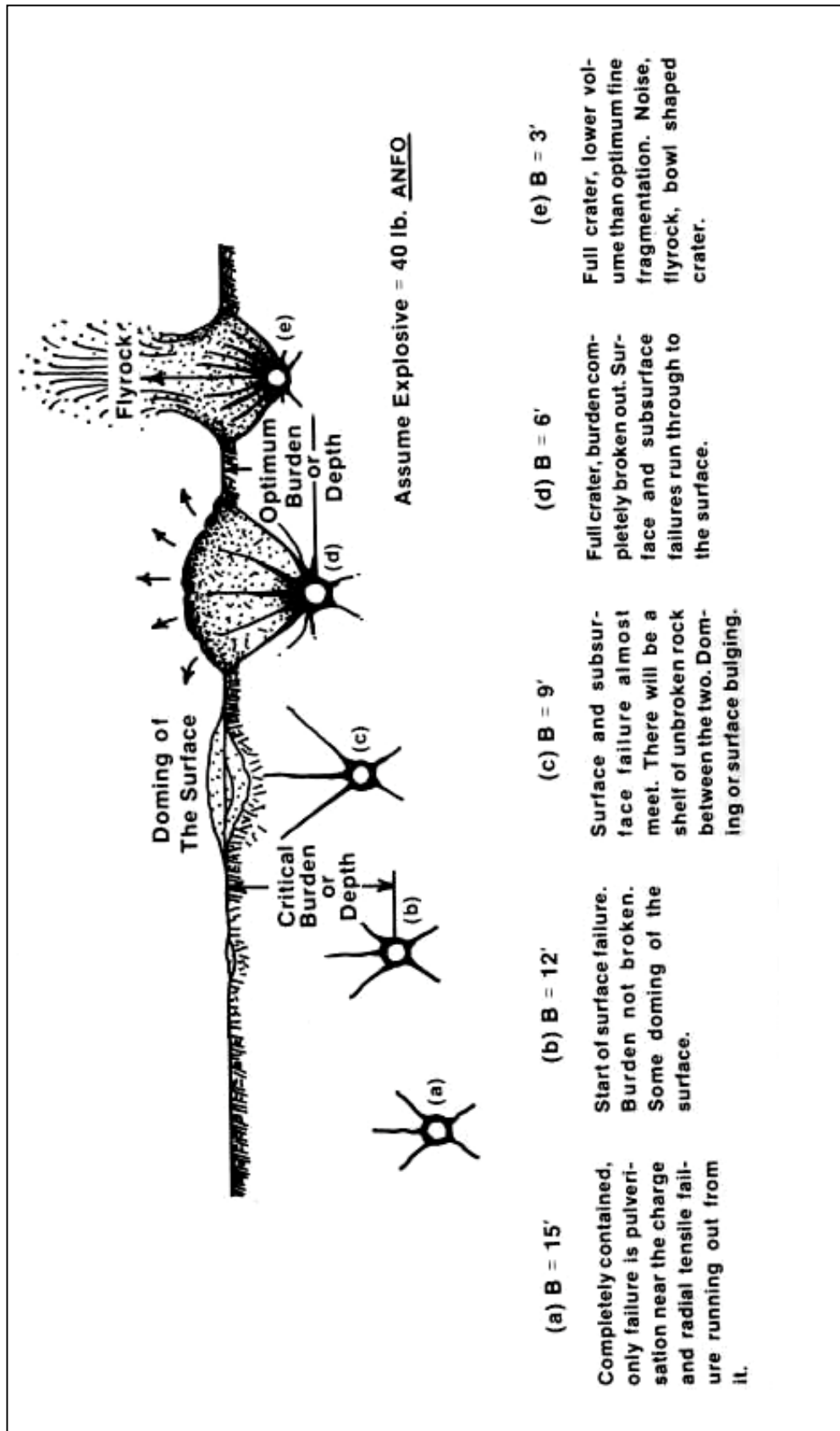


Figure 8.3. Schematic illustration of the effect of burden on explosives fired in rock (from Atlas Powder Company, 1987)

behaviour. The drillhole diameter, length, spacing and burden reflect the explosive distribution. For the same hole length, a smaller drillhole size has a better explosive distribution and less explosive concentration than larger drillholes. Smaller diameter drillholes usually have more hole deviation compared to larger diameter drillholes. The drillhole deviation will be discussed in detail in section 8.4.7.

8.4.3 Explosive Type

The type of explosive used forms an important part of blast design. The selection of explosive type is usually based on the analysis of factors that include rock mass characteristics, volume of rock to be blasted, presence of water, safety conditions, supply problems as well as the cost of rock breakage. For underground open stope mining, including HBMS mines, the most commonly used explosive is ANFO (Ammonium Nitrate and Fuel Oil) due to its low cost and safety. ANFO has some shortcomings which include poor water resistance and low density. Other explosives also are used for special purposes, such as Dyno Split and low ANFO for wall control and emulsion for wet conditions. Explosive type also effects HW stability and dilution. High energy explosives (e.g., emulsion, Dyno Split) produce good fragmentation but may cause damage to the stope HW. Low energy explosives (e.g., low ANFO) cause less damage to the HW but more drilling metres are required to get satisfactory fragmentation.

8.4.4 Wall Control Methods

Many wall control methods exist to avoid damage to the stope HW. A reasonable wall control technique can create better blasting results and protect the adjacent structure from damage. This is especially important for weak, heavily jointed or foliated stope walls. The methods for wall control blasting can vary depending on the rock mass condition and the operation's preference. The general approach for wall control blasting is to reduce the detonated explosive energy in the areas close to structures which need to be protected from damage. There are many ways to reduce the

detonating explosive energy to the hanging wall. Using low energy explosives (e.g., low ANFO), traced small diameter explosive cartridges (e.g., Dyno split cartridge or cartridge ANFO) or drilling smaller diameter drillholes with a closer spacing along the HW contact are some of the options. Optimizing initiation sequence and reducing the explosive per delay are other alternatives for reducing blast damage.

The cartridge or traced small diameter explosive cartridge (e.g., Dyno cartridge or Dyno split traced cartridge) was the most frequently used methods for wall control blasting in HBMS open stopes.

8.4.5 Explosive Distribution

The distribution of explosives within a blast influences both the rock fragmentation and the degree of damage to the adjacent rock mass. The explosive distribution is controlled by several drilling and blasting parameters. These parameters include drillhole size, drillhole spacing and burden, charging geometry (e.g., charge length and location in a drillhole and stemming parameters), and the drillhole accuracy (drillhole deviation). Stemming is the portion of a blasthole which has been packed with inert material (usually drill cuttings), above the explosive charge. Stemming is used to confine and retain the gases produced by the explosion. A good explosive distribution tends to create better ore fragmentation and often results in less hanging wall damage. A high concentration of explosive energy can result in increased blast damage. Usually when designing a blast, the drillhole burden and drillhole spacing are determined based on the drillhole size. A larger hole size will result in a larger burden and spacing. As described in section 8.4.2, for the same hole length, a smaller drillhole size has better explosive distribution and less explosive concentration than larger drillholes. The overall explosive distribution for a blast is usually expressed in terms of powder factor. The powder factor (PF) is the average weight of explosive (in kilograms or pounds) used to break each cubic metre of solid rock. The powder factor is not necessarily related to overbreak or blast damage, it only indicates an average consumption of explosive used to break a cubic metre of ore. The explosive contribution is controlled

by the drillhole size, drillhole spacing and burden as well as the explosive charging geometry in holes. Drillhole deviation also can affect the explosive distribution. Evenly distributing the available explosive within the whole planned stope is expected. However, hole deviation can significantly alter the expected explosive distribution.

8.4.6 Initiation Sequence, Explosive Per Delay and Availability of Free Surface

Initiation sequence, explosive per delay and available free surface are other important blasting aspects, which can significantly affect blasting results. The outcome of a multi-hole production blast is very dependent on interactions between blastholes (Hagan, 1996). The sequence in which blastholes are initiated and the time interval between successive detonations has a major influence on overall blast performance. The performance of a production blast can only be optimised when charges detonate in a controlled sequence at suitable discrete but closely spaced time intervals. The initiation sequence should make use of the available free surface to maximize the use of explosive energy and minimize the damage to stope walls. Explosive per delay shows the weight of explosive being initiated at the same time. The explosive per delay is the single most important factor which indicates the shock and heave energy from a single delay blast. The bigger the explosive per delay the greater the damage. An optimized initiation sequence can fully use the available free surface and detonating explosive energy to create desired fragmentation with minimal surrounding damage.

8.4.7 Drillhole Deviation

Drillhole deviation is normally defined as the distance between the actual and planned toe location of blast holes, divided by the hole length:

$$\text{Hole deviation (\%)} = \frac{\text{Distance between the actual and planned hole toe}}{\text{True length of the planned hole}} \times 100 \quad (8.5)$$

Drillhole deviation can be a result of many factors. These include the inaccurate placement of drill reference marks, incorrect drill set-up (collaring and alignment errors, which can be due to human error or equipment limitations), inconsistent drill operation, and geological structure. Both the trend and plunge of boreholes can deviate. There are two ways the drillholes can deviate along stope height (dip). The drillholes can deviate toward the stope HW or away from the stope HW (Figure 8.4). Drillhole deviation can also cause the loading of explosives away from designed locations (Figure 8.5) causing undesired explosive concentrations in some areas and a lack of explosive in other areas. An explosive concentration will cause excessive energy in some areas which can result in damage to adjacent structures, and lack of explosive in other area will cause larger fragmentation or underbreak. In general, drillhole deviation often results in poor blasts and can result in blast damage and increased dilution. When explosives are loaded into holes which deviate into the stope hanging walls, significant damage is done to the hanging walls (Figure 8.4).

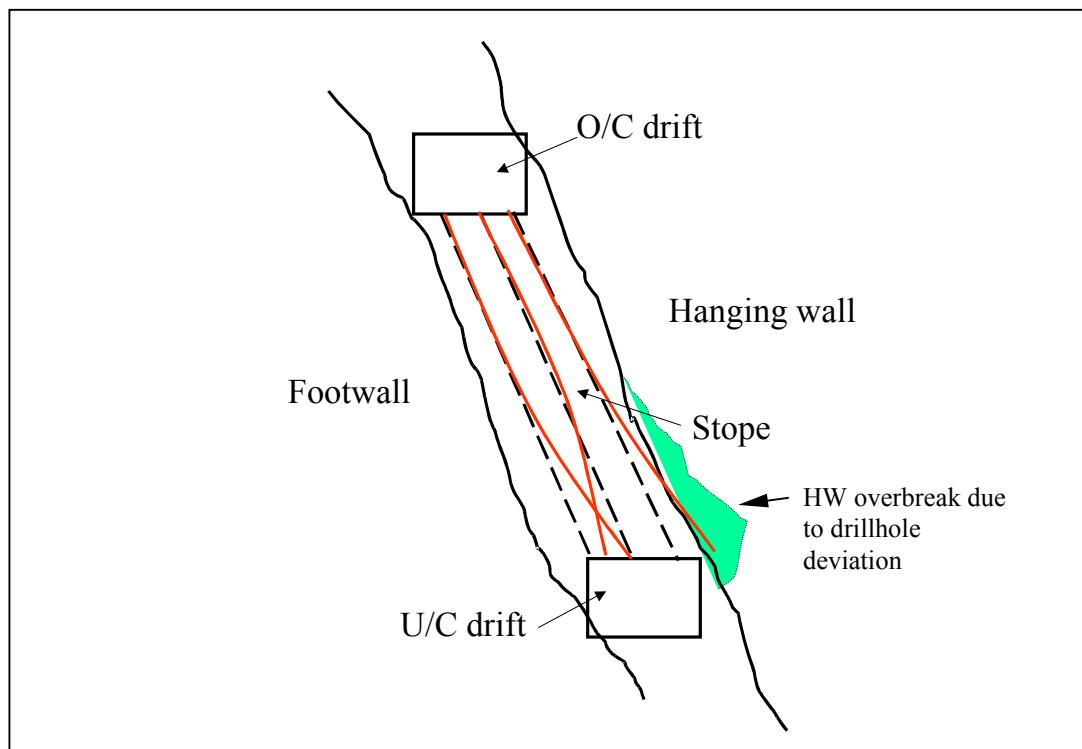


Figure 8.4. Cross section showing the drillhole deviation orientations

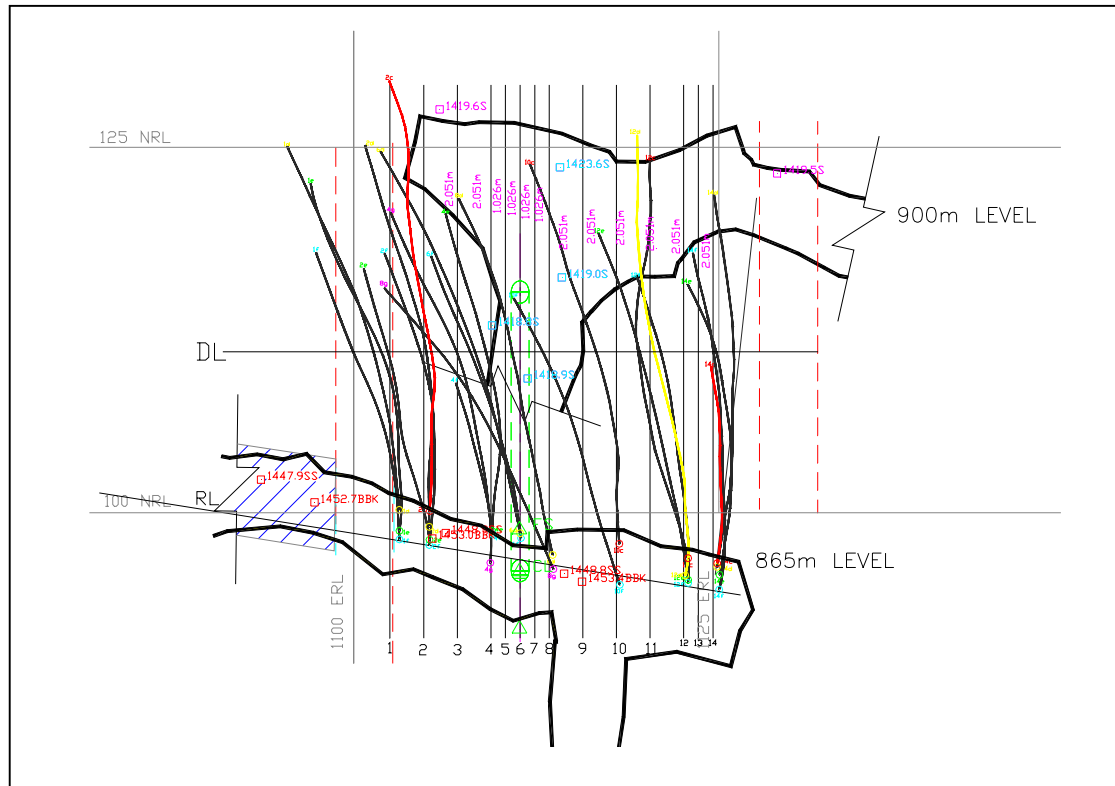


Figure 8.5. Plan view showing surveyed drillhole deviation along strike (Trout Lake Mine, HBMS, 2000)

Magnetometer drillhole deviation survey data shows that hole deviation at HBMS mines is an average of 7% of the drillhole length at the toe of surveyed holes, giving an average toe deviation of 2.1metres (30m stope average height). A study from the Noranda Technology Centre also shows that most of their surveyed holes have a deviation range from 0% to an occasional 20% of the hole length at the toe (Piché et al., 2000). Borehole deviation has not been measured frequently at HBMS operations and cannot be used in the database as a direct measure of possible causes of dilution.

8.5 Database Assessment of Blasting Parameters and Dilution

The HBMS database includes several parameters important to blast performance which were introduced in Section 4.2.5. These parameters include drillhole size, drillhole

pattern and powder factor. The drillhole size and powder factor were found to show no correlation with observed dilution or with the predicted minus observed dilution (Figures 8.6 to 8.9).

8.5.1 Drillhole Pattern versus Stope HW Dilution

Different drillhole patterns are used at HBMS operations. The drillhole patterns in this study are defined as:

- a). Parallel drillhole pattern - hole patterns where the holes close to the stope HW on cross section, are parallel or near parallel to the HW;
- b). Fanned drillhole patterns – hole patterns where the holes close to the stope HW on cross section are angled toward the HW contact.

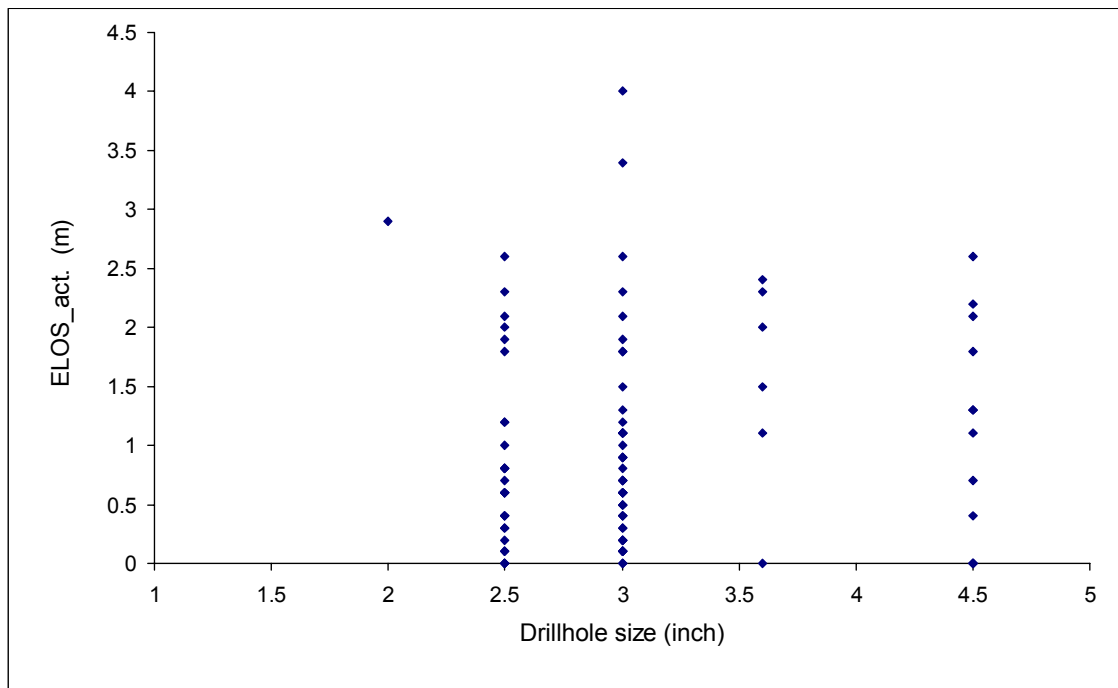


Figure 8.6. Drillhole size versus actual ELOS case history plots

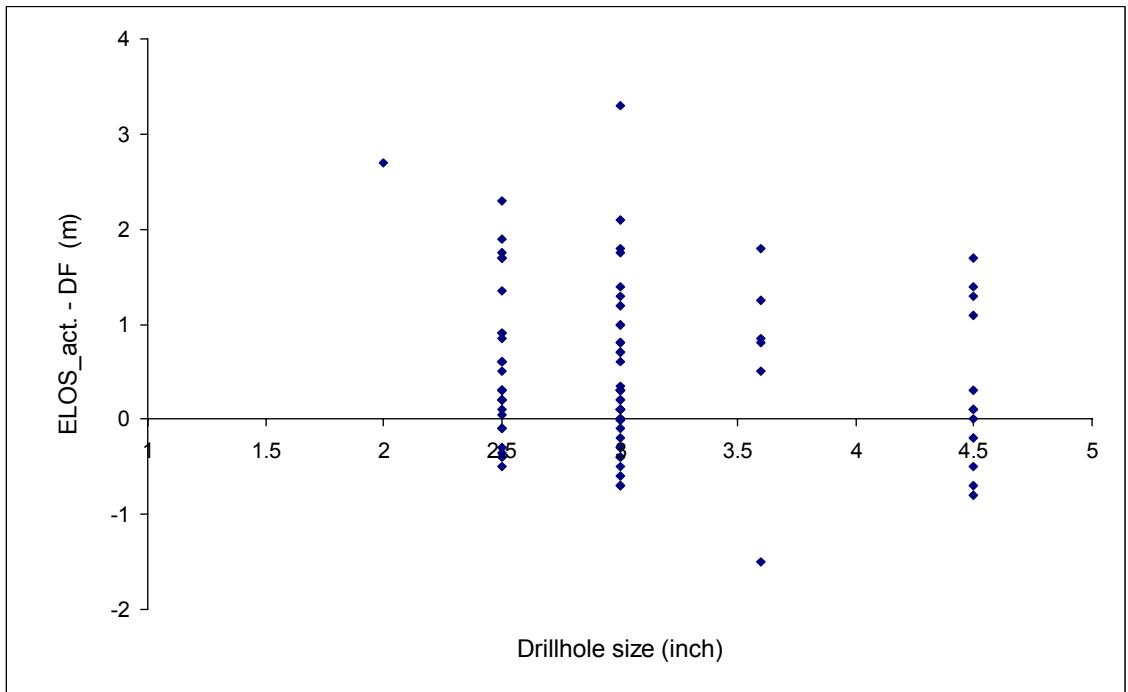


Figure 8.7. Drillhole size versus actual ELOS minus DF case history plots

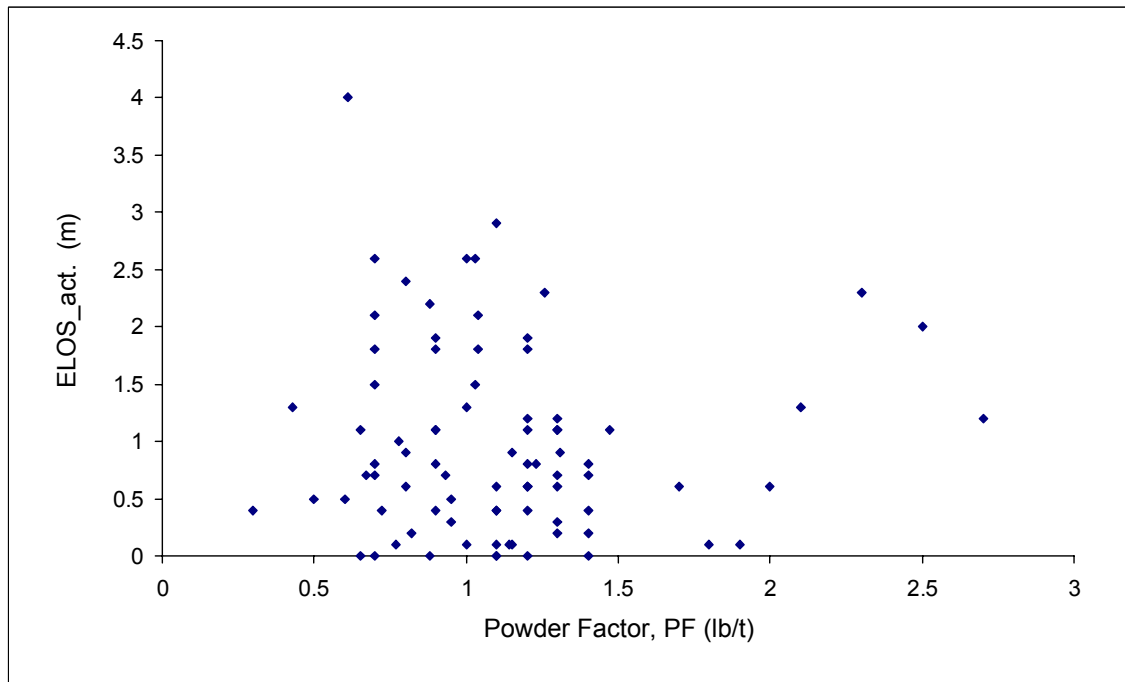


Figure 8.8. Powder factor versus actual ELOS case history plots

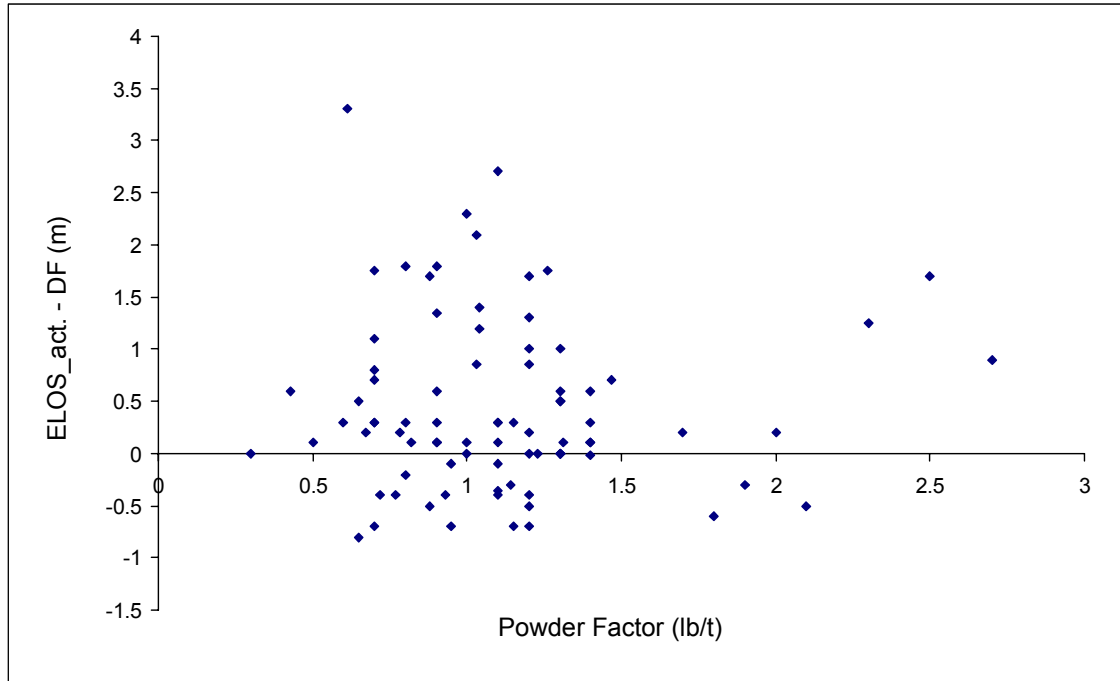


Figure 8.9. Powder factor versus actual ELOS minus DF case history plots

Figure 8.10 (a and b) illustrates parallel drillhole patterns. Figure 8.10 (b) is an example where most of the holes (other than the holes close to stope HW) are fanned out from the overcut drift. The drillhole pattern is classified as a parallel drillhole pattern in this study, because the holes closest to the hanging wall are parallel or nearly parallel to the stope HW. Figure 8.11 shows a fanned drillhole pattern. The influence of parallel drilled versus fan drilled blast patterns was compared in this study.

From a rock mechanics perspective, blast damage can be reduced by drilling holes parallel to the planned opening wall. Parallel drilling gives a better explosive distribution and allows for the application of wall control blasting techniques. Fan drilling results in blast holes butting into the stope hanging wall and this can locally concentrate the blast energy and cut into the hanging wall. From a mining perspective, however, stope hanging wall stability is very sensitive to drillhole deviation for the blast holes drilled parallel to the hanging wall. A 30 metre hole that deviates 5 degrees from the planned orientation towards the hanging wall can result in a blast hole toe located

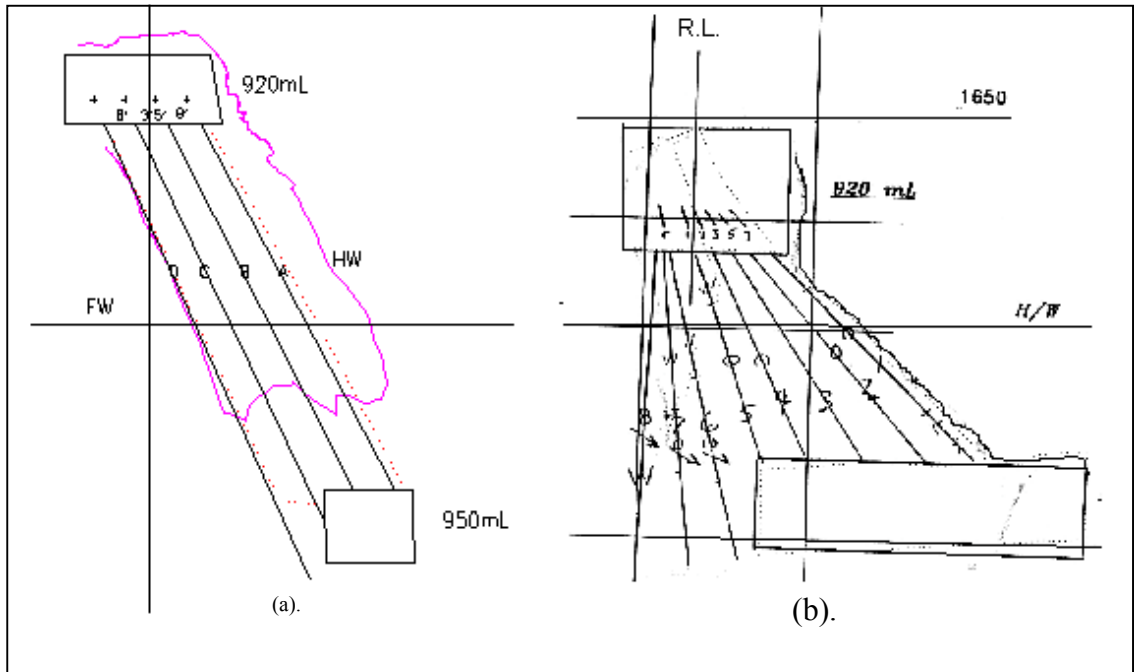


Figure 8.10. Definition of parallel drillhole pattern

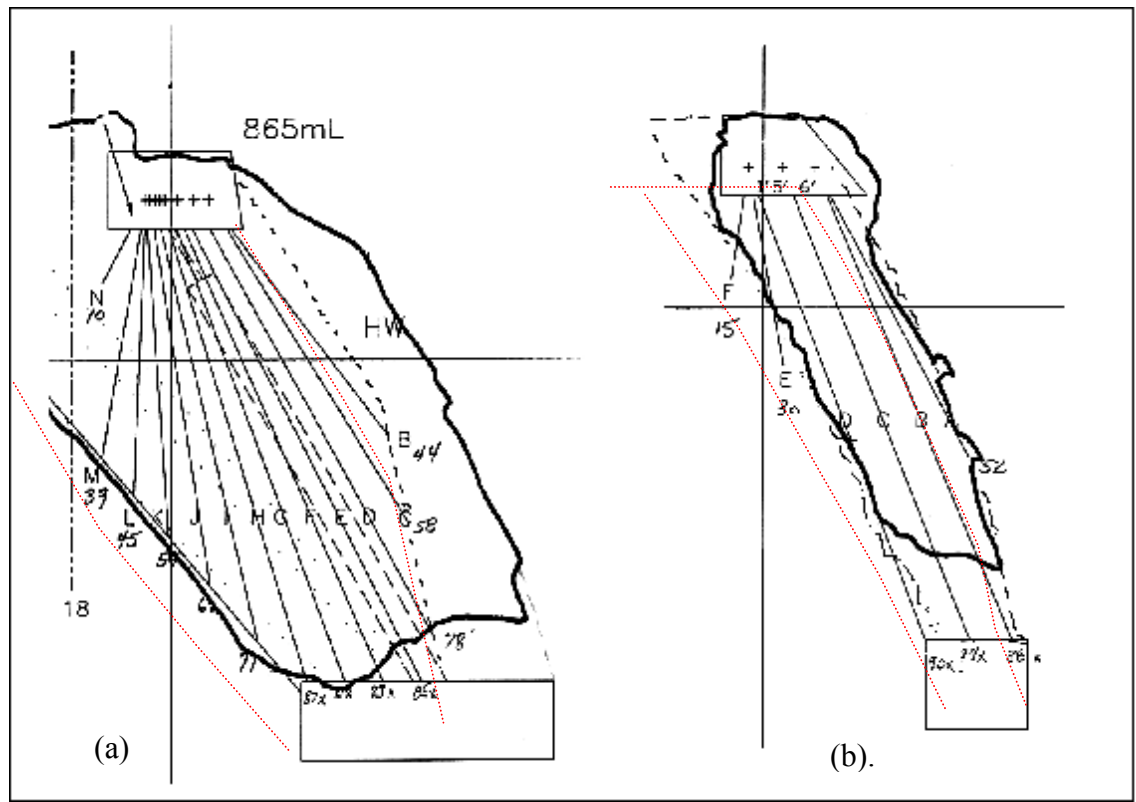


Figure 8.11. Definition of fanned drillhole pattern

over 2.5 metres into the hanging wall (Figure 8.12). This can result in significant overall stope hanging wall slough. For fan drilled holes, the steeper the angle between the drillhole and the contact, the less influence drillhole deviation will have on the toe location of the hole relative to the hanging wall.

Drillhole deviation is a well recognized factor contributing to stope dilution at HBMS operations (Yao et al., 2002). A case history study was conducted on the established database of 131 cases with drilling information. Figure 8.13 looks at stopes with blast holes drilled parallel to the hanging wall contact and those that had fanned drill patterns. The two types of stopes are compared to the average metres of slough from the hanging wall (Figure 8.13). On average there is about 40% (0.4m) more slough for parallel drilled stopes versus fan drilled stopes. When the average actual slough minus predicted metres of slough is compared for the two drill patterns, the difference is much more striking. The discrepancy between the actual and predicted average metres of

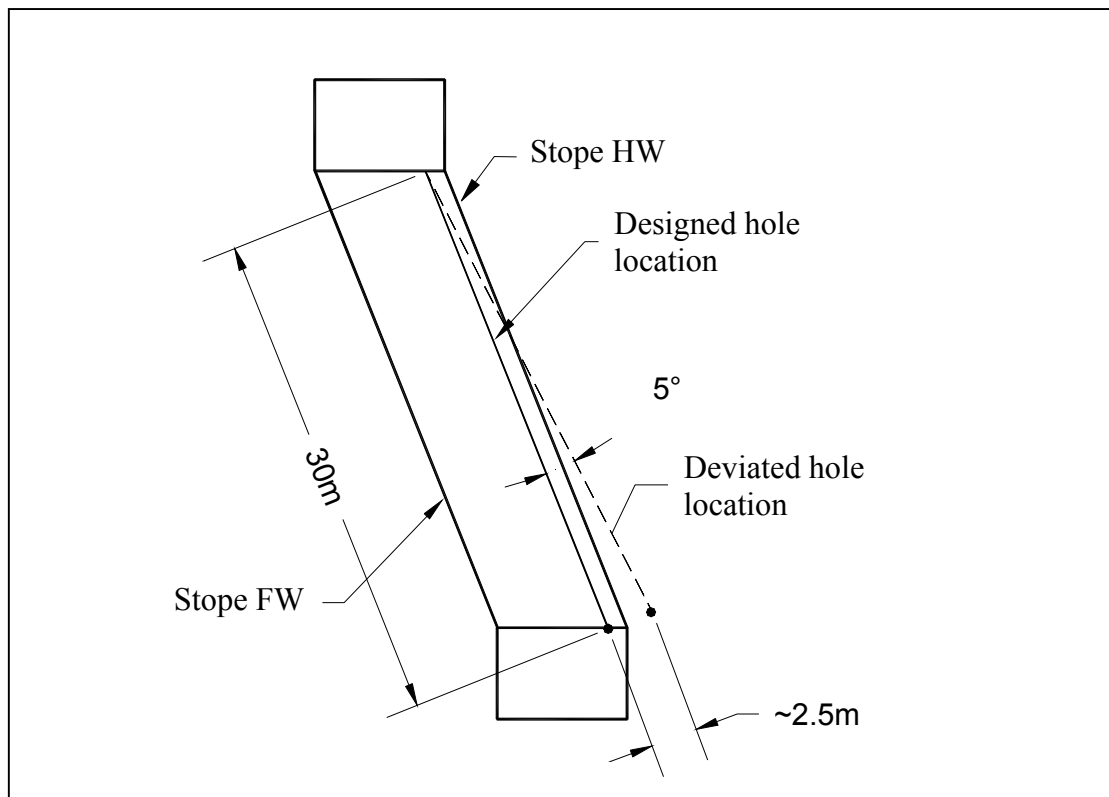


Figure 8.12. Schematic Illustration of drillhole deviation

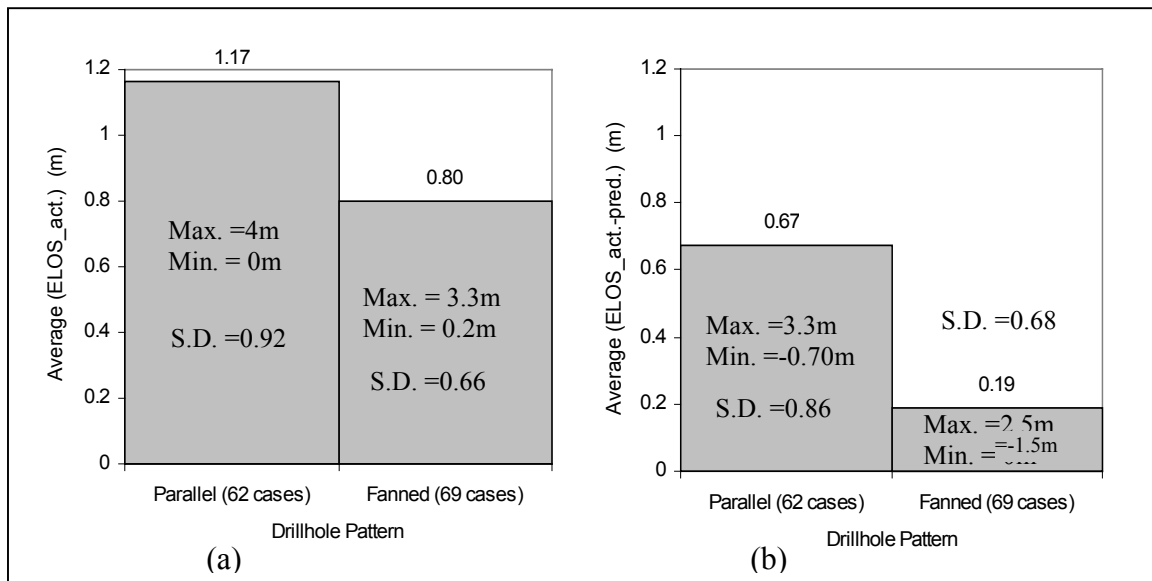


Figure 8.13. Histograms showing the influence of parallel and fanned drillhole pattern on stope dilution (Wang et al., 2002)

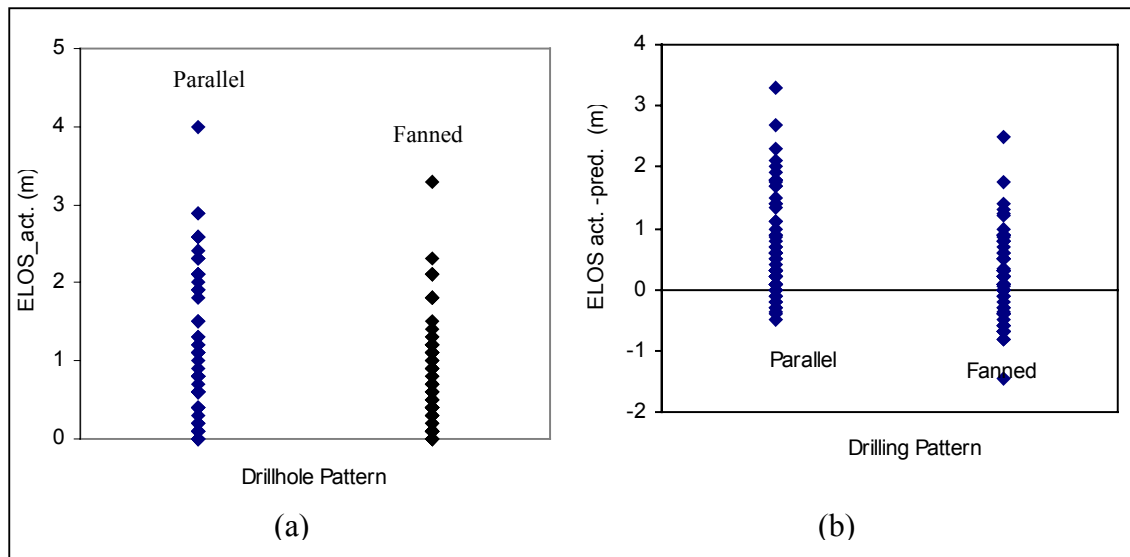


Figure 8.14. Individual cases showing the influence of parallel and fanned drillhole patterns on stope dilution. (Wang et al., 2002)

slough is 3.5 times as much for parallel drilled stopes for an additional half metre of slough, compared to fanned drillhole pattern. The plot of actual minus predicted dilution accounts for factors ignored by the dilution graph method. The 0.5 metre difference between the fanned and parallel drilled stopes can be related to increased slough associated with the influence of drillhole deviation on parallel drilled stopes. Only the average values of slough were plotted in Figure 8.13. There is a wide range in the actual metres of slough measured (Figure 8.14) (Wang et al., 2002).

To verify the observed relationship for individual mines, similar studies were carried out on Callinan and Trout Lake mines, respectively. The analyses showed an identical pattern: parallel drillhole patterns have more average dilution than fanned drillhole patterns. Figure 8.15 and Figure 8.16 show the comparison between two drillhole patterns on HW dilution for Callinan Mine and Trout Lake Mine, respectively. The influence of the drillhole pattern in the HBMS database was examined in more detail and the drillhole pattern was compared to undercutting. The database showed that stopes drilled with a parallel drillhole pattern had, on average, more undercutting than fanned holes (Figure 8.17). Based on conversations with mine engineers, it was suggested that the occurrence of more undercutting with a parallel drillhole pattern was purely a coincidence. No undercutting was made to provide space for a parallel drillhole pattern. The drillhole design is decided based on the actual surveyed drift locations and geological ore definition. The drillhole pattern was mainly decided by the stope orebody shape, the developed overcut drift location and width relative to the ore width. Parallel drillhole patterns were generally used when the overcut drift wall on the stope hanging wall side was aligned or undercut into stope hanging wall, so there was enough space to enable drilling equipment to drill holes close to and parallel to the stope HW. On the other hand, stopes with the drill drift located on the footwall side of the orebody were more likely designed with a fanned drillhole pattern to get a maximum ore recovery.

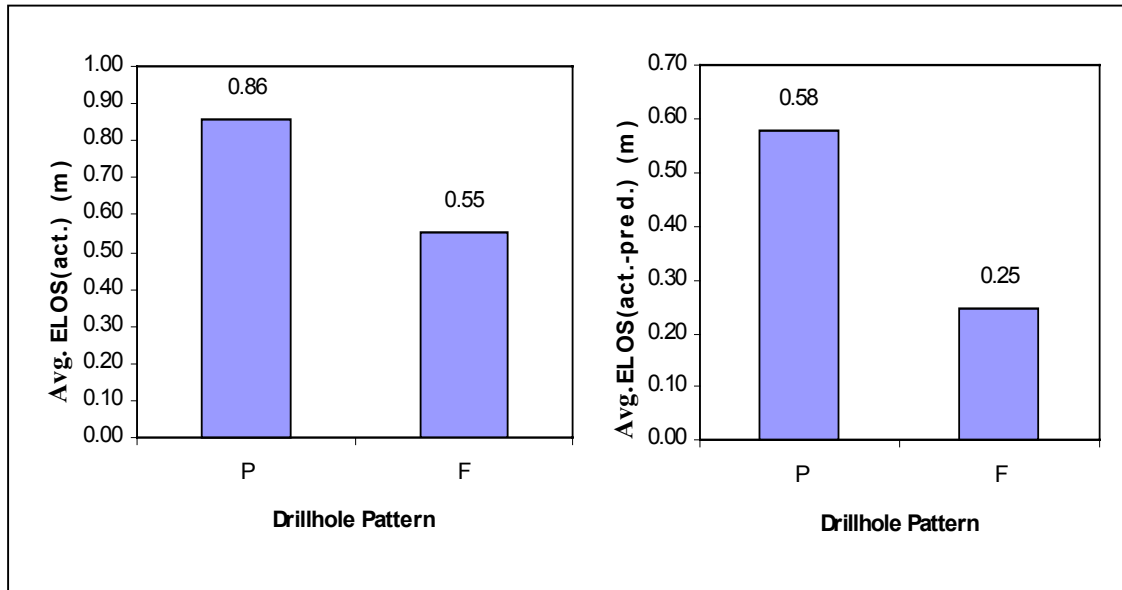


Figure 8.15. Comparison between two drillhole patterns on HW dilution at Callinan Mine

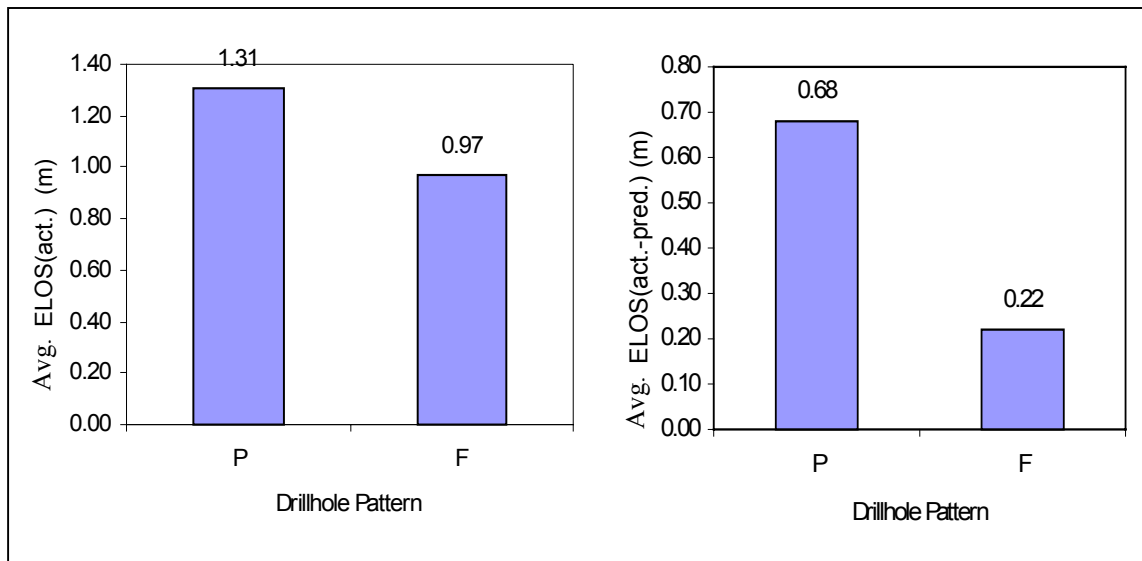


Figure 8.16. Comparison between two drillhole patterns on HW dilution at Trout Lake Mine

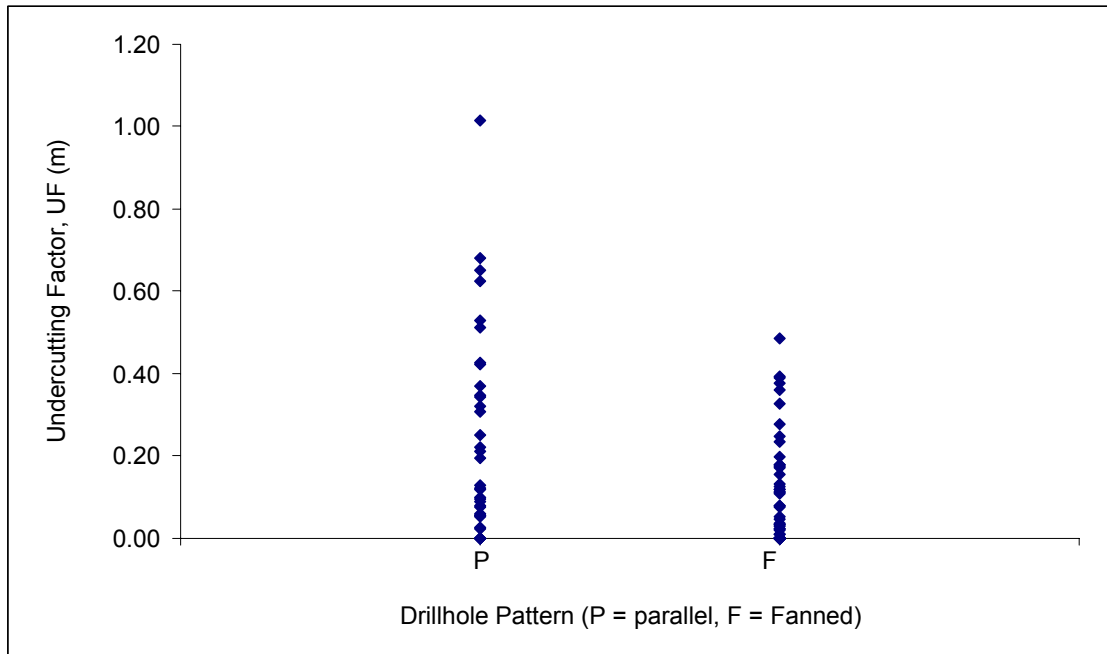


Figure 8.17. Drillhole pattern versus undercutting factor

The average undercutting influence on the drillhole pattern on the dilution was compared between the two drillhole patterns. The average UF value difference between parallel and fanned patterns is about 0.1 m on average (Figure 8.17). The average ELOS prediction error between the parallel and fanned drilled stopes differed by approximately 0.48 m (Figure 8.13). This indicates that the drillhole pattern and not the associated difference in undercutting is influencing the recorded ELOS.

8.6 Summary

Numerous factors can cause blasting damage to a stope hanging wall. Based on current blasting design techniques and operational practice, it was found that drillhole deviation is a factor that significantly influences blast damage to stope hanging walls. Analysis of the HBMS database showed that parallel drillholes cause more damage to hanging walls than fanned drillholes due to a combination of drillhole deviation and undercutting. The overall HW average metres of overbreak difference between parallel drillhole and

fanned drillhole is about 0.37m (Figure 8.13(a)). If considering a HBMS average stope HW size of 30x30m, then the 0.37m of additional overbreak will present about 900 t of dilution. Using a direct cost of \$20 per tonne, (Yao et al., 1999), this gives an additional cost to the mine of over \$18,000 per stope, ignoring any milling and processing costs. At a yearly production of 1 million tonnes, the additional overbreak represents a significant cost.

CHAPTER 9

INFLUENCE OF STOPE EXPOSURE TIME ON HANGING WALL STABILITY AND DILUTION

9.1 Introduction

The open time or the length of time a surface is left exposed is a contributing factor influencing the stability of underground openings. Lauffer (1958) and Bieniawski (1976) noticed time-dependent instability in tunnel excavations. They introduced the term “stand-up time” for an unsupported tunnel. The stand-up time was defined as “the length of time which an underground opening will stand unsupported after excavation” (Hoek and Brown, 1980). Better ground conditions were found to have longer stand-up times for a given span. After the stand-up time was exceeded, instability was likely to occur. With increasing time, the stability of an opening decreases.

Time is an important factor influencing mine opening stability as well as tunnel stability. Ran (2002) presented a case history from Ruttan Mine showing the influence of time on stope stability. Three subsequent CMS surveys were conducted over a period of one year as shown in Figure 9.1. The CMS profiles show the progressive sloughing of the stope, highlighting the importance of exposure time on stability.

Both the Q and RMR classification systems can be used for estimating tunnel stability and in both systems there is an approach that can be used to incorporate the influence of time (Barton et al., 1974; Bieniawski, 1989). With the RMR system, a graph has been developed to relate tunnel span, RMR and unsupported stand-up time (Figure 9.2).

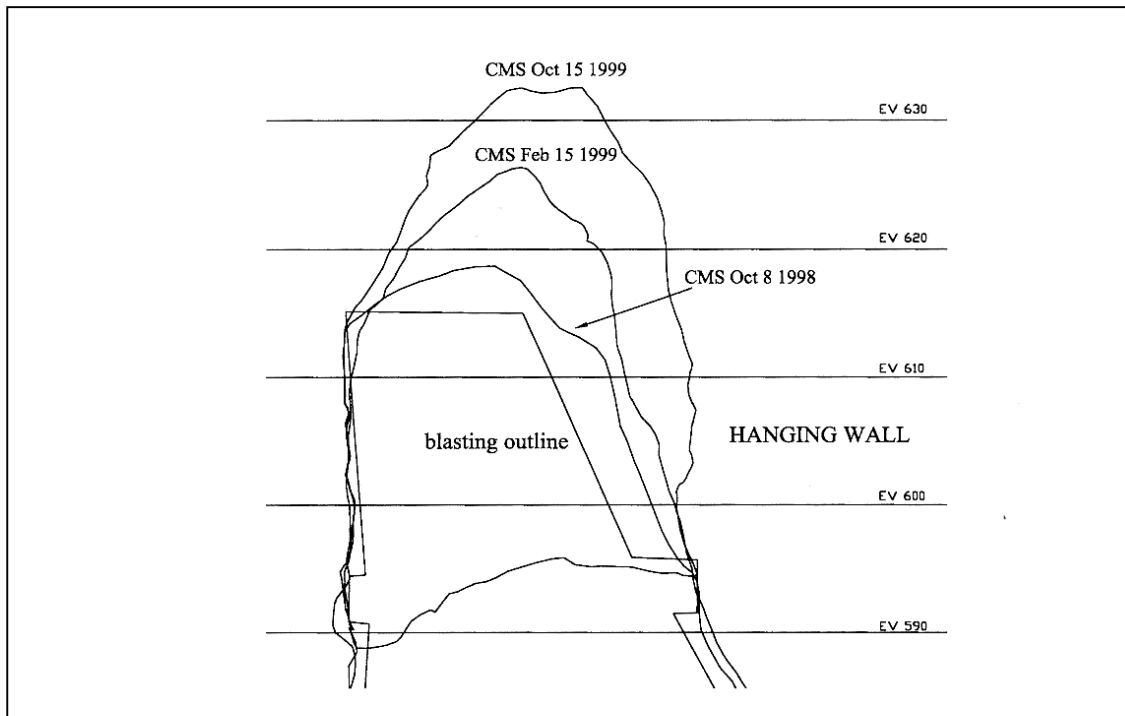


Figure 9.1. CMS surveyed progressive caving with time (from Ran, 2002)

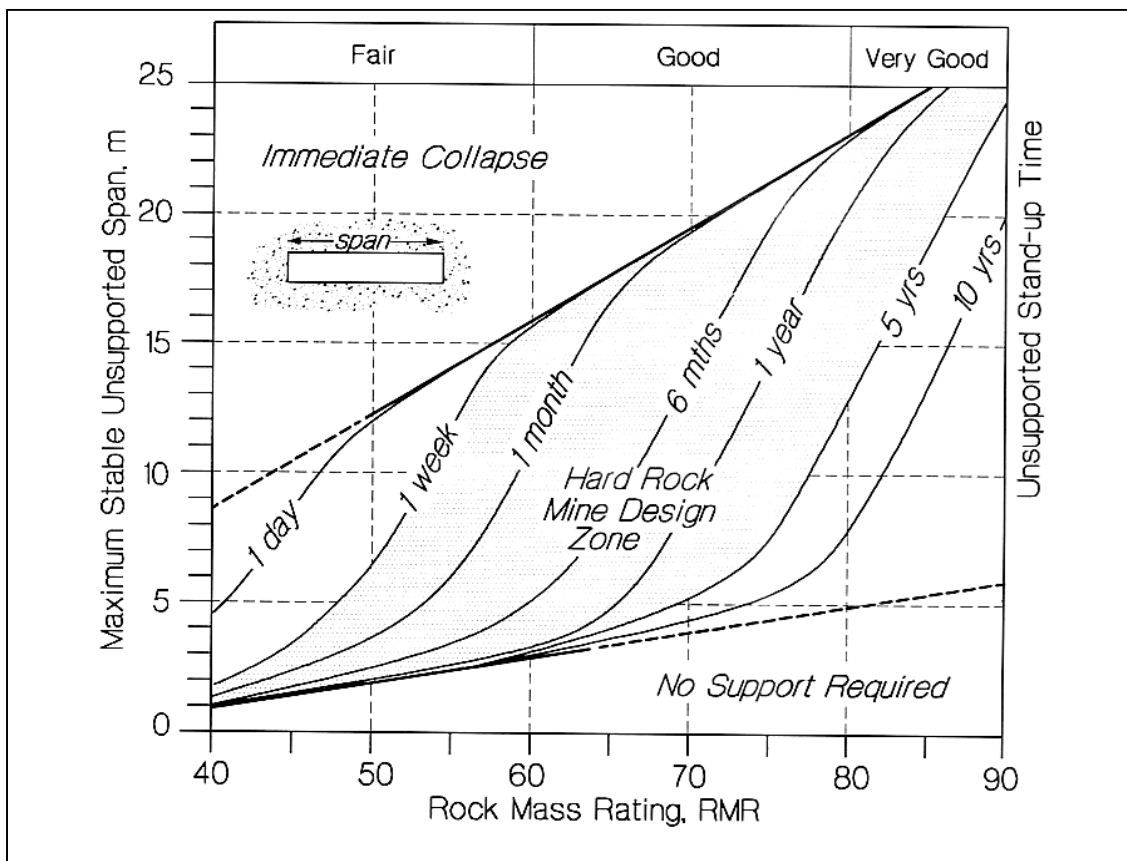


Figure 9.2. Stand-up time guidelines (from Hutchinson and Diederichs, 1996)

With the Q system, the Excavation Support Ratio (ESR) is used with a graphical design technique for estimating support requirements. The ESR value is used to reduce the effective drift span for tunnels that require shorter stand-up times. The Q classification approach with the ESR term infers rather than quantifies the influence of time on stability. The HBMS database has been assessed to determine the influence of exposure time on the magnitude of slough. Additional case histories have been assessed from Geco Mine in northern Ontario. These different methods of assessing the influence of time on stability have been compared with trends obtained from the HBMS database.

9.2 Mechanism of the Influence of Time on Stability and Dilution

The time influence on slope stability and dilution is related to the redistribution of stress caused by the creation of nearby openings, as well as a time dependent crushing/buckling mechanism along existing structures. This general crushing/buckling mechanism is illustrated in Photo 9.1. The hanging wall and footwall surfaces of a large slope are de-stressed (relaxed) and more prone to the effects of gravity loading. Stress redistribution around a slope may also have a time dependent component. In the highly stressed slope abutments, the rock may fail under compression. This leads to an increased zone of stress shedding around the slope hanging wall which in turn increases the stress levels in the abutment, as well as increasing the zone of relaxation. Figure 9.3 is a schematic illustration of this time influence mechanism on slope stability and dilution. The figure shows that before the creation of an excavation, the virgin stress is in a state of equilibrium (Figure 9.3.a). When an excavation is made in a pre-stressed rock, the stress field is disturbed. The magnitude and orientation of stresses in the vicinity of the excavation will be changed to form a new state of equilibrium. Following the creation of the excavation, the stresses previously existing in the hanging wall and footwall cannot go through the void created and will be transferred to the abutments. At the hanging wall and footwall abutments, high stress concentrations are created. The surfaces of the hanging wall and footwall will be de-stressed (Figure 9.3.b). At the highly stressed hanging wall and footwall abutments the rock mass may

undergo deformation and shed the induced stresses. This will cause the stress concentration to occur farther away from the opening (Figure 9.3.c). This process in turn will increase the hanging wall and footwall zone of relaxation. This stress shedding and redistribution can be time dependent.

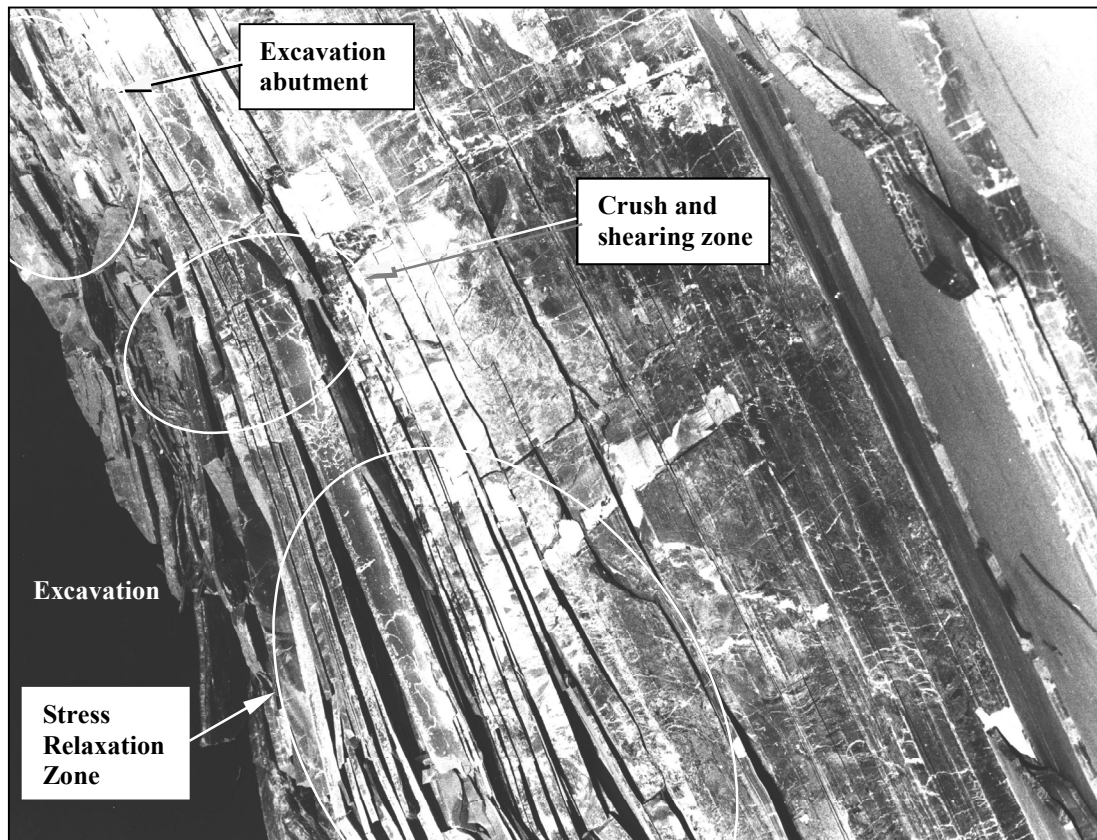


Photo 9.1. Illustration of instability caused by stress redistribution process (Mount Isa, lead mine)

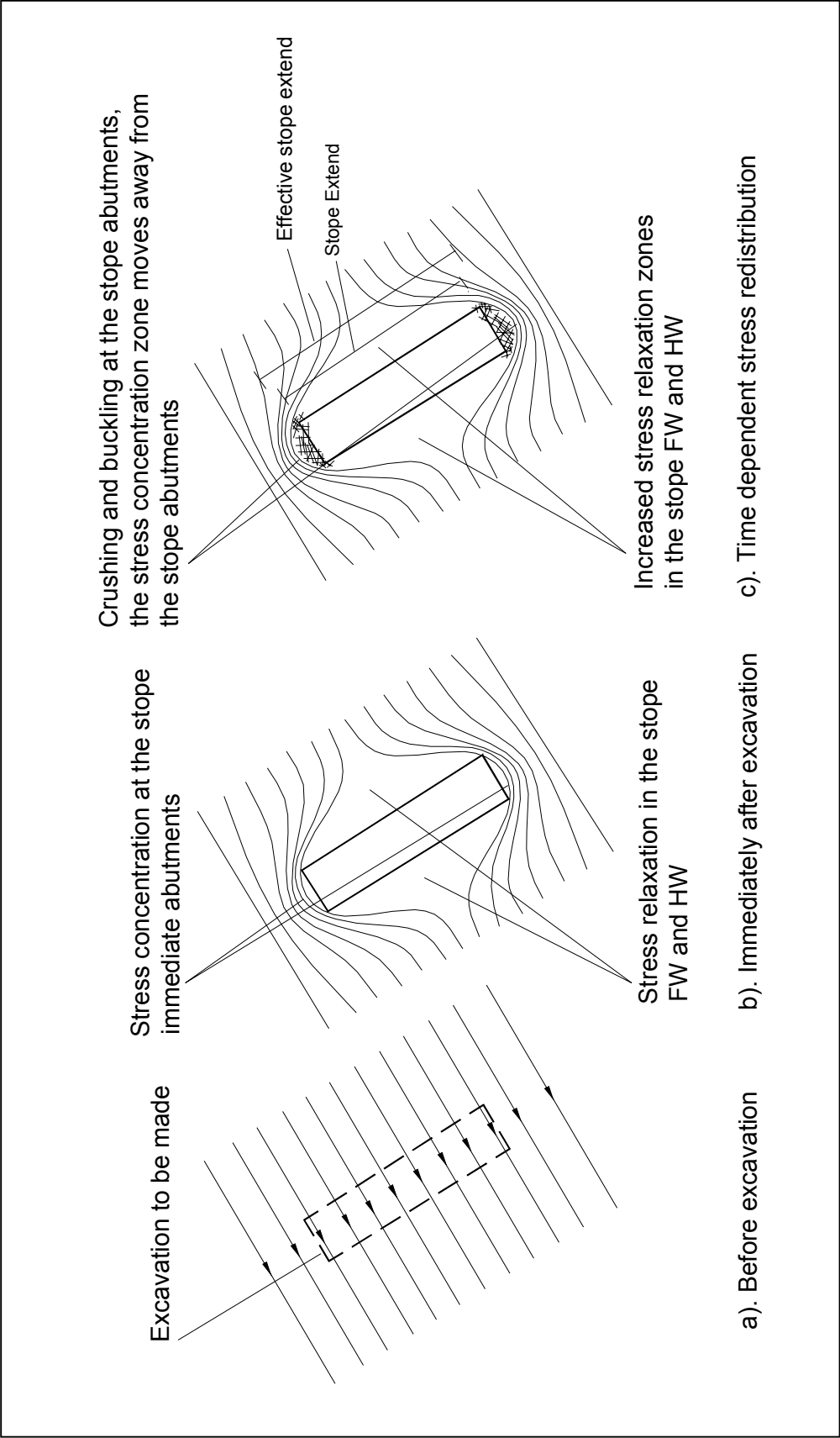


Figure 9.3. Schematic illustration of time dependent stress redistribution

9.3 Influence of Exposure Time on the HBMS Database

As shown in Figure 9.1, exposure time can have a significant influence on the measured open stope dilution. An open stope is usually blasted in stages so the initial time when the stope is open is not a definite date. The creation of an open stope hanging wall starts with a slot which is a small void created with closely spaced blast holes or with a boring machine. Little ground is opened with a slot, which is typically approximately 2 metres by 2 metres (by blasting) or 1.2 metres in diameter (by boring machine), open for the height of the stope. The slot creates the necessary free surfaces for the rest of the stope blasting. After the slot is created, the rest of the stope is typically blasted in a series of rings or rows of blast holes, over a period of several days to several months. In this study, the opening exposure time is measured as the time between the first blast after the creation of the slot and the time of the CMS survey. The CMS survey is usually conducted near the end of the stope mucking.

For most of stopes included in the database from HBMS, the stope exposure time ranges from 4 days to 300 days. Eighty four percent (84%) of case histories have stope exposure time less than 60 days. Figure 9.4 shows a stope exposure time pie chart.

Figure 9.5 shows the CMS surveyed actual ELOS versus stope exposure time. It shows a general trend of increasing ELOS with increased exposure time. Although there is no statistically significant relationship, the general trend indicates that ELOS increases at a rate of 0.008 m/day or 0.24 metres per month. The large amount of scatter shown in Figure 9.5 is due to the many factors which influence open stope dilution. Some, but not all the factors influencing dilution have been examined in this study. As discussed in Chapter 1, factors such as discrete geological structure (e.g., shears and faults) as well as data on blasthole deviation, have not been well-recorded at the mine site and are therefore not included in this study.

A further analysis was conducted trying to minimise the scatter due to other factors influencing dilution. Figure 9.2 suggests that the influence of time on the rock mass

rating or classification is more significant for weaker rock masses. The influence of rock mass quality (in terms of modified stability number N') and the slope hanging wall geometry (in terms of HR) were corrected from the measured ELOS. The dilution factor (DF) (dilution graph prediction) is used to represent the combined influence of N' and HR. The N' value represents the overall rock mass strength. Figure 9.6 shows the average actual measured ELOS minus the dilution factor (DF) against grouped time plotted as a histogram. It shows a trend of increasing dilution with time. Figure 9.7 shows the individual case histories actual ELOS minus dilution factor plotted against slope exposure time. Subtracting the dilution factor from actual ELOS will eliminate the influence of rock mass condition and the slope surface geometry factors on dilution. No trend of increasing dilution with time can be discovered.

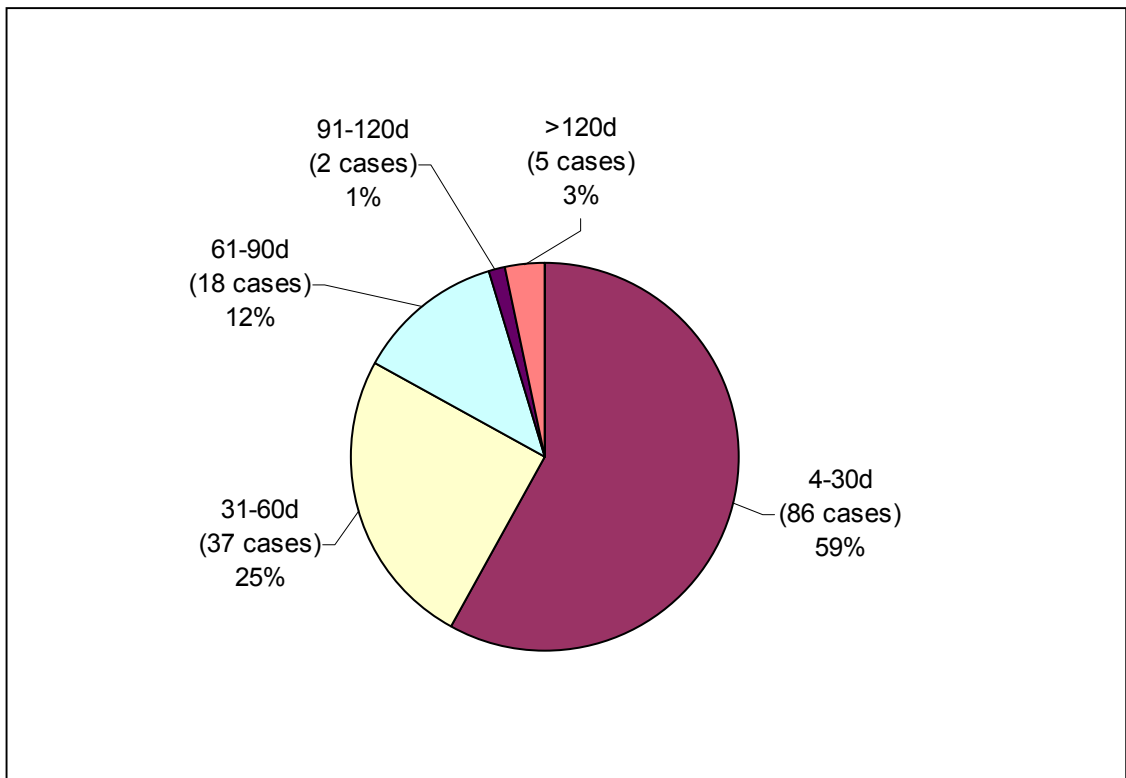


Figure 9.4. Stope exposure time case histories

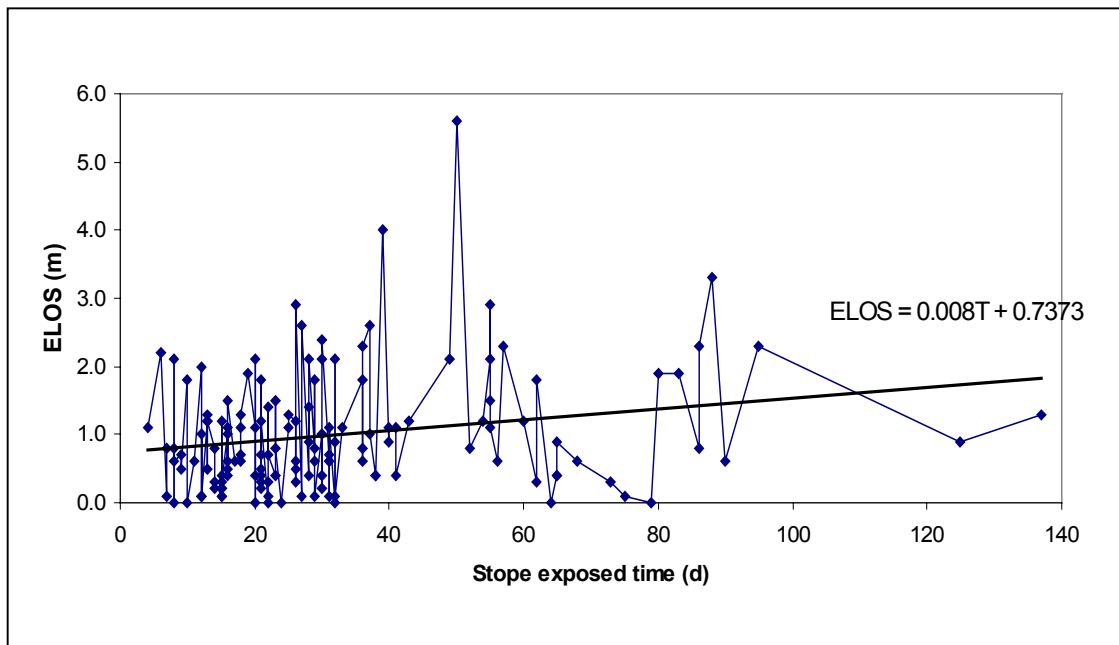


Figure 9.5. CMS measured ELOS versus exposure time case history plots

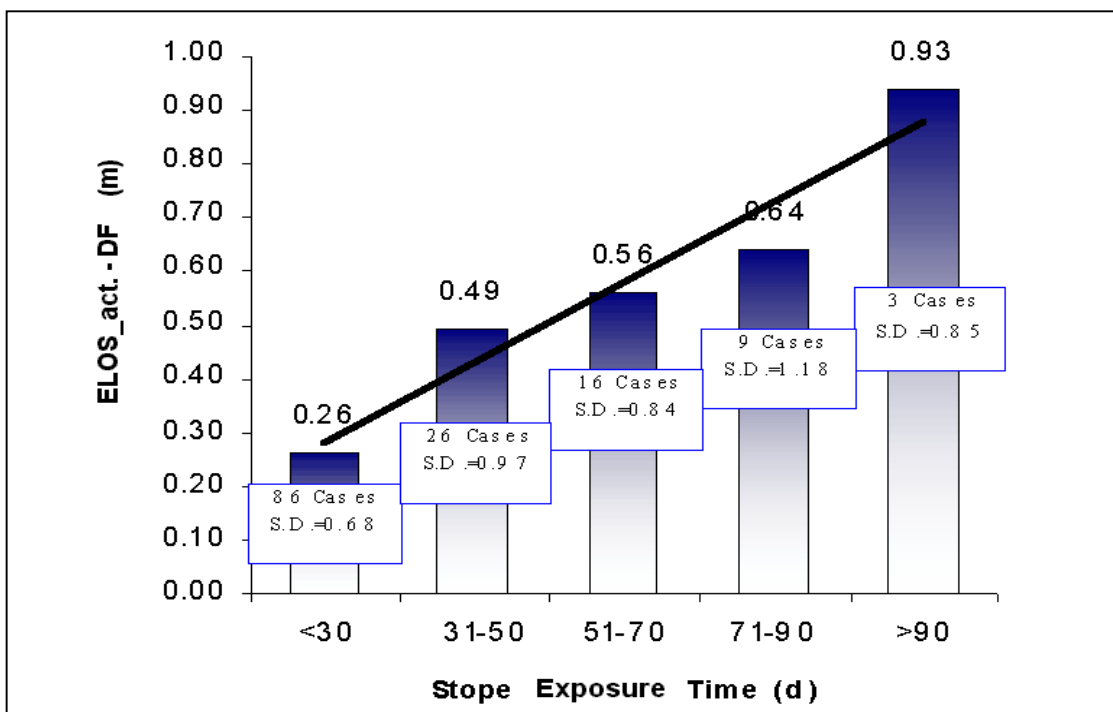


Figure 9.6. Histogram plot of average ELOS prediction error versus slope exposure time (Wang, et al., 2003)

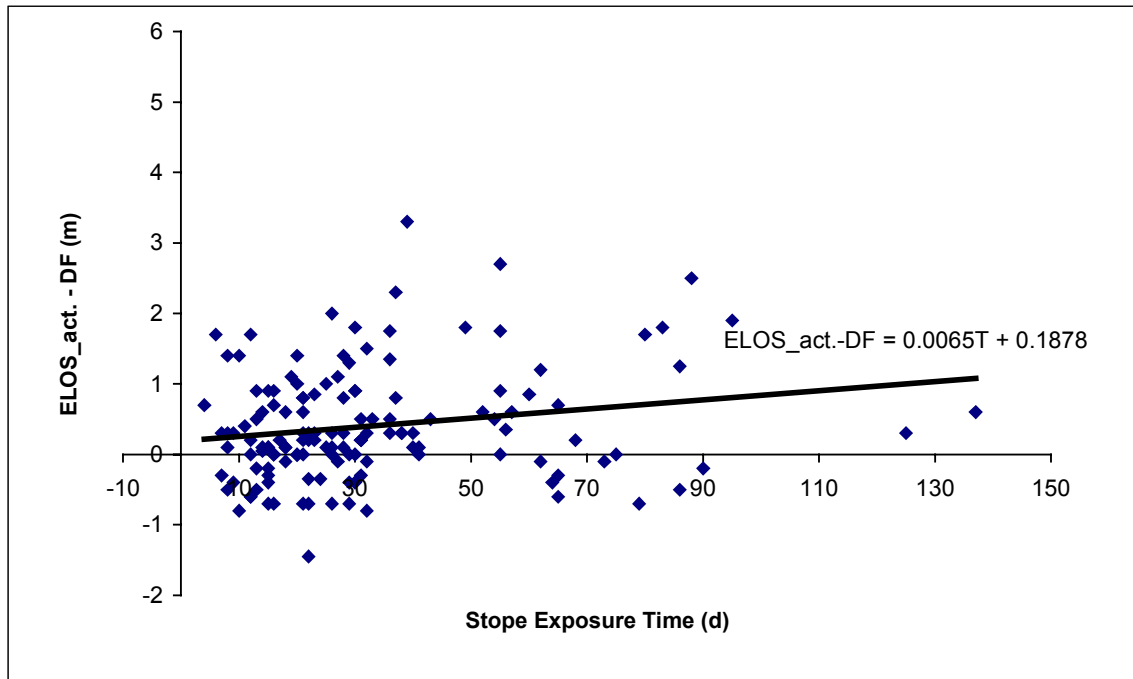


Figure 9.7. Stope exposure time versus ELOS prediction error case history plots

It is also noticed that the exposure time is related to the stope size. A longer exposure time is usually corresponds to a larger stope size, since a bigger stope takes more time to muck out.

Figure 9.2 suggests that the influence of time on an excavation stability is more significant for weaker rock masses. To account for this, an additional analysis was considered where actual ELOS – DF was plotted against exposure time in days divided by the N' value for each case history (Figure 9.8). The N' value represents the overall rock mass strength. However, the analysis did not show a trend.

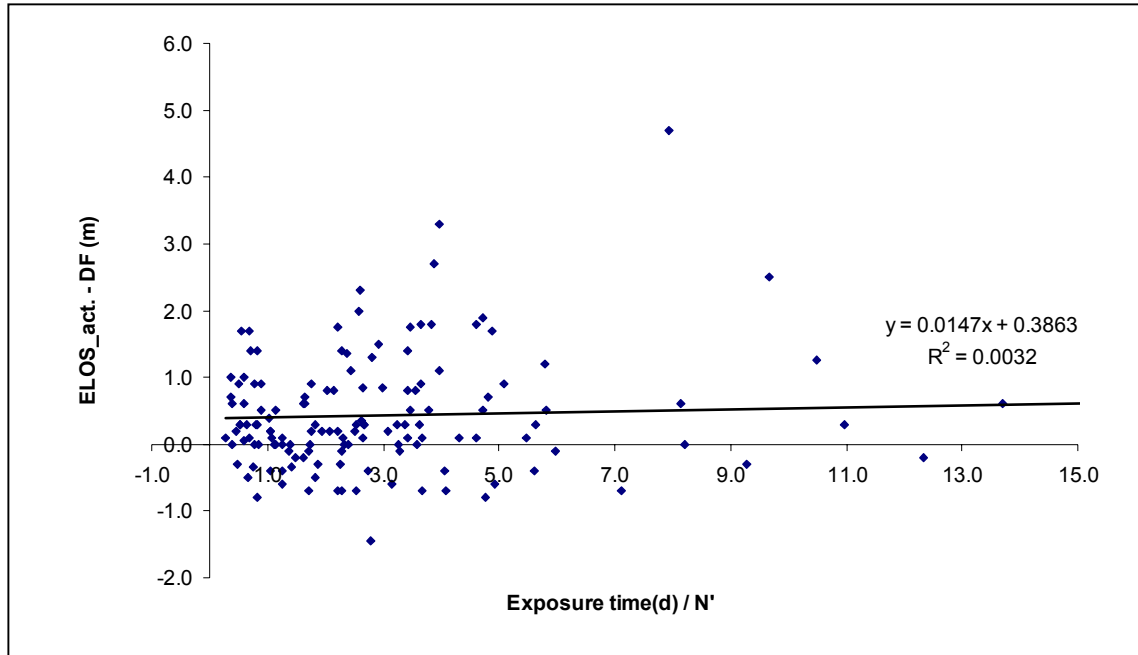


Figure 9.8. Slope exposure time divided by N' versus ELOS prediction error case history plots

9.4 Complementary Data on the Influence of Exposure Time

9.4.1 Stand-up Time Graph Analysis

Lauffer (1958) and Bieniawski (1976) both noticed the influence of time on drift stability. Figure 9.2 shows the RMR Stand-up time graph as presented by Hutchinson and Diederichs (1996). Figure 9.2 shows that the influence of time on the stability of a rock mass is much more pronounced for a weaker rock mass (lower RMR value).

The stand-up time graph (Figure 9.2) predicts immediate collapse for a 10 metre tunnel span with an RMR of 44. An RMR of 50 will remain stable for about 3 days and an RMR of 65 will have a stand-up time of approximately 150 days. The stand-up time relationship can also be expressed as a reduction in RMR. An RMR of 50 will have the stability of an RMR of 44 after 3 days of exposure while an RMR of 65 will take 150 days to have stability of an RMR of 44. This can be expressed as a reduction of RMR

with time. The reduction in RMR with time can also be expressed as a reduction in Q with time based on an empirical equation relating RMR and Q (equation 8.4).

Table 9.1 shows the influence of exposure time on stability and classification values as indicated by the stand-up time graph (Figure 9.2). Table 9.1 also shows the influence of the initial rock mass condition on the sensitivity of the rock mass behaviour on exposure or stand-up time. The reduction in RMR or Q with time can be equated to an increase in dilution. For this comparison, a rock mass condition similar to that found in the HBMS database is used. The Q' values for the HBMS database averaged about 6.3 for Trout Lake Mine and 18.8 for Callinan Mine for an average value of approximately 13. For a 10 metre span, a Q of 13 would have a stand-up time of approximately 180 days. Since immediate collapse on the stand-up time graph corresponds to a Q of 1.0 for a 10 metre span, the reduction in Q with exposure time can be expressed as a rate of Q reduction of approximately 0.067 per day.

On the Dilution Graph, the HBMS case histories plot (Figure 9.9) showed a cluster of data corresponding to a Modified Stability Number (N') of 11 and a hydraulic radius of 7.0. In this region of the graph, an increase in dilution from 0.5 metres ELOS to 1.0 metres ELOS can be obtained from a decrease in the Q' classification value built into the N' term. In the HBMS database, the average Q' value of 13 corresponds to an N' value of 11. A decrease in Q' from 13 to 5.9 reduces the N' value from 11 to 7, increasing the estimated ELOS from 0.5 metres to 1.0 metres. Based on average conditions in the HBMS database, a 0.5 metre increase in ELOS would correspond to an exposure time of 106 days, based on Q' being reduced at a rate of 0.067 per day. Considered over a 30-day period, this can be expressed as an ELOS rate of 0.14 metres of slough per month of exposure.

Table 9.1. Influence of stand-up time on stability and effective classification values (10m span) based on the RMR Stand-up Time Graph (Wang et al., 2003)

Initial RMR	Initial Q	Time to Immediate Collapse (days)	Reduction in Effective RMR	Reduction in Effective Q
44	1.0	0	0	0
50	2.0	3	6	1.0
55	3.4	8	11	2.4
60	5.9	45	16	4.9
65	10.3	150	21	9.3
70	18	300	26	17
75	31.5	730	31	30

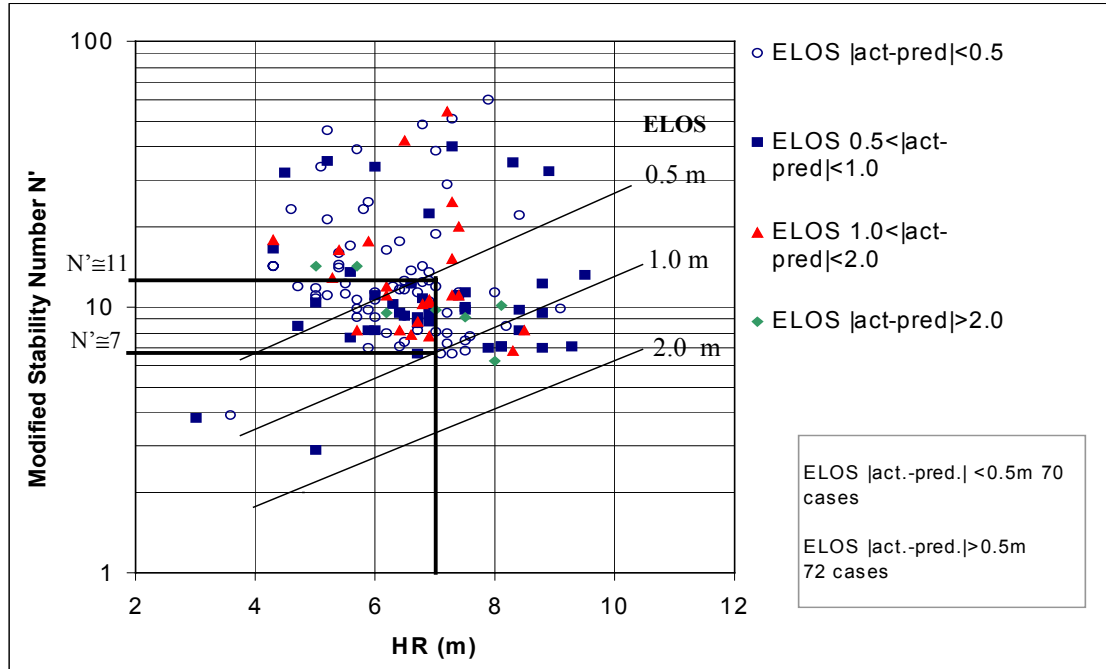


Figure 9.9. Manipulating the N' change for the ELOS increase on Clark's (1998) dilution graph (HBMS Database)

9.4.2 Geco Mine Case History Study

A brief dilution study was conducted at Noranda's Geco Mine in 1986 (Milne, 1996; Wang et al., 2003). Hanging wall conditions at Geco mine were worse than average conditions found at the HBMS mines. The average Q' value for the Geco hanging wall was 4. This study looked at dilution from 8 open stopes where dilution values were estimated from records of tonnes mucked from the stopes. A very tentative relationship was proposed which suggested dilution was dependent on the hydraulic radius of the stope hanging wall and the exposure time expressed in months. The case histories of 8 stopes had exposure time between 8 to 65 months and had hydraulic radius values that ranged between 15.3 metres to 30.5 metres. The recorded dilution ranged between approximately 1.7 metres to 4.6 metres ELOS. A relationship between exposure time and dilution was estimated at approximately 0.16 metres of slough per month. This is comparable to the 0.14m/month from the RMR stand-up time graph.

9.5 Summary

This study revealed that stope exposure time is an important factor that can significantly influence open stope stability and dilution. Although the HBMS database did not show any clear trend, work conducted by Bieniawski (1989) suggests that the influence of exposure time on rock mass behaviour increases as the rock quality decreases. For a rock mass similar to conditions encountered at HBMS, the Stand-up time graph (Figure 9.2) would indicate approximately 0.14 metres of ELOS per month of exposure. A database of 8 stopes from Geco Mines reported a similar influence of exposure time on ELOS with a rate of 0.16 metres additional ELOS per month. Data from these analyses suggest that hanging wall slough increases between 0.14 to 0.16 metres per month for a rock mass Q' value between 4 to 31 (N' between 3 to 60). This slough rate can produce a significant amount of dilution from an open stope hanging wall with a long exposure time.

Minimizing stope exposure time by promptly mucking after blasting and minimizing the mucking time has been recognized as an effective way of significantly reducing stope dilution.

CHAPTER 10

STATISTICAL ANALYSIS OF EMPIRICAL DATA

10.1 Introduction

The database described in Chapter 4 and the analyses conducted in Chapters 6 through 9 showed that there are many variables that contribute to open stope hanging wall dilution. A statistical analysis was conducted to evaluate the approaches in previous chapters, to further investigate the relationship between these variables and to verify their influence on dilution or ELOS. There were two objectives for this analysis. The first objective involved using multiple parameter regression analysis to build a probabilistic model that related the dependent variable, ELOS, to the available hanging wall dilution contribution factors (parameters). The significance of the contributing factors was also determined. The second objective was to establish a simplified stope hanging wall ELOS model using the most significant contributing factors. The SPSS (Statistics Package for Social Sciences) for Windows (SPSS Inc., 1989-1999) software package was used for the statistics analysis. The statistical analysis results were compared to results drawn from the previous studies.

10.2 Parameters in the Statistical Analysis

The parameters involved in the analysis included stope geometry parameters, rock mass stability number N' , undercutting parameters, drilling and blasting parameters, stope exposed time and CMS surveyed ELOS in the established HBMS database, which was presented in Chapter 4. Table 10.1 lists the parameters included in the statistical analysis. Although there are 150 cases in the database, some of the cases have missing

parameters and cannot be used in the statistical analysis. Only 115 cases, without missing data, were included in the statistical analysis.

Table 10.1. Parameters included in the analysis and descriptive statistics

Parameter	Max. Value	Min. Value	Mean	Std. Deviation	Number of Case
ELOS (m)	4.00	0	0.97	0.81	115
Hydraulic Radius, HR (m)	9.50	3.0	6.58	1.24	115
Ore Width, OW (m)	52.00	1.9	7.02	5.31	115
Modified Stability Number, N'	60.00	2.9	14.40	10.80	115
Hole Size, HS (m)	0.14	0.05	0.08	0.02	115
Drill Pattern, DP*	2	1	1.43	0.49	115
Powder Factor, PF (lb./ton)	2.70	0.30	1.10	0.42	115
Stope Exposed Time, T (day)	137	4	32.44	24.24	115
Undercutting Factor, UF* (m)	0.7	0	0.15	0.18	115
<p>* The drillhole pattern is defined as the drillhole pattern in stope cross section. Two patterns were defined: fanned and parallel patterns. For fanned patterns, DP = 1 and for parallel pattern, DP = 2. More details on drillhole pattern definition were given in Chapter 9.</p> <p>** The undercutting factor UF is derived from quantifying the influence of undercutting parameters on hanging wall overbreak. UF is defined as:</p> $UF = \frac{l_o + l_u}{4(L + H)} \times (d_o + d_u)$ <p>The terms are described in detail in Chapter 7.</p>					

10.3 Multiple Parameter Statistical Analysis

Multiple parameter regression analysis was conducted on the parameters listed in Table 10.1. The stress factor was not included in the statistical analysis as there was not sufficient quantitative information available. The analysis starts with the assumption that the parameters (except ELOS) listed in Table 10.1 are the contributing factor to ELOS. The ELOS is defined as a “dependent” variable and the remaining parameters are referred to as “independent” variables in the study.

In a multiple parameter regression, the objective is to build a statistical model that relates a dependent variable to multiple “independent” variables (Devore, 1995). In this analysis, the objective is to build a statistical model that relates the dependent variable ELOS, to the multiple independent variables (listed in Table 10.1) which contribute to ELOS.

The general additive multiple parameter regression model takes the form of (Devore, 1995):

$$Y = \beta_0 + \beta_1 x_1 + \beta_2 x_2 + \dots \beta_i x_i \dots + \beta_k x_k + \epsilon \quad (10.1)$$

where,

Y is the dependent variable

β_i are coefficients

k represent the number of independent variables

x_i denotes the independent variables

ϵ is a random variable and usually is referred to as the random deviation or random error term. When ϵ is normally distributed, the ϵ term vanishes.

By Replacing the dependent variable Y in equation 10.1 by ELOS and the independent variables x_i by HR, OW, N', HS, DP, PF, T and UF, (defined in Table 10.1), we have the multiple parameter regression model given as equation 10.2:

$$\begin{aligned} ELOS = & \beta_0 + \beta_1 * HR + \beta_2 * OW + \beta_3 * N' + \beta_4 * HS + \beta_5 * DP + \beta_6 * PF \\ & + \beta_7 * T + \beta_8 * UF + \epsilon \end{aligned} \quad (10.2)$$

The objective of the multiple parameter regression is to obtain the quantitative coefficients β_0 to β_8 and the random deviation ϵ .

The case history data were imported into the statistical analysis package SPSS and a multiple parameter regression was conducted. The correlations between parameters and

the multiple parameter regression quantitative coefficients were obtained. Table 10.2 presents the correlation matrix for the parameters involved in the analysis. Table 10.3 shows the calculated coefficients.

The correlations shown in Table 10.2 display Pearson correlation coefficients and significance values for the cases with non-missing values. Pearson correlation coefficients assume the data are normally distributed. The Pearson correlation coefficient is a measure of linear association between two normally distributed variables.

The values of the correlation coefficients in the Table 10.2 can range from -1 to 1. The sign of the correlation coefficient indicates the direction of the relationship (positive or negative). The absolute value of the correlation coefficient indicates the strength, with larger absolute values indicating stronger relationships. The correlation coefficients on the main diagonal are always 1.0, because each variable has a perfect positive linear relationship with itself. Correlations above the main diagonal are a mirror image of those below. Table 10.2 shows that the exposure time T has the strongest correlation with ELOS (with a correlation coefficient of 0.233) and the powder factor has the weakest correlation with ELOS (with a correlation coefficient of 0.01) among the independent variables. Table 10.2 also shows that stronger correlations exist between some of the independent variables, such as blasting hole size with modified stability number N' , blasting hole size with HW hydraulic radius HR , and undercutting factor with drillhole pattern.

The significance of each correlation coefficient is also displayed in the correlation table (Table 10.2). The significance level is the probability (likelihood) that a particular correlation could occur by chance. The significance (or p value) represents the degree of rarity of a certain result. A significance less than 0.05 ($p < 0.05$) means that there is less than a 5% chance that this relationship occurred by chance. If the significance level is very small (less than 0.05) then the correlation is significant and the two variables are

Table 10.2. Correlations between parameters

		ELOS	HR	OW	N	HS	DP	PF	TIME	UF
Pearson Correlation	ELOS	1.000	.215	.087	-.197	.085	.012	.010	.233	.160
	HR	.215	1.000	-.051	.028	.292	-.073	-.084	.104	-.020
	OW	.087	-.051	1.000	.000	-.055	-.140	-.234	.145	-.081
	N'	-.197	.028	.000	1.000	-.331	.059	.141	-.013	-.052
	HS	.085	.292	-.055	-.331	1.000	.024	-.008	-.068	.042
	DP	.012	-.073	-.140	.059	.024	1.000	.242	-.249	.246
	PF	.010	-.084	-.234	.141	-.008	.242	1.000	-.146	-.100
	T	.233	.104	.145	-.013	-.068	-.249	-.146	1.000	-.018
	UF	.160	-.020	-.081	-.052	.042	.246	-.100	-.018	1.000
Significance (p value)	ELOS	.	.011	.178	.018	.184	.451	.456	.006	.044
	HR	.011	.	.294	.384	.001	.218	.187	.134	.414
	OW	.178	.294	.	.499	.279	.068	.006	.061	.194
	N'	.018	.384	.499	.	.000	.264	.067	.444	.292
	HS	.184	.001	.279	.000	.	.401	.467	.234	.327
	DP	.451	.218	.068	.264	.401	.	.005	.004	.004
	PF	.456	.187	.006	.067	.467	.005	.	.060	.145
	T	.006	.134	.061	.444	.234	.004	.060	.	.424
	UF	.044	.414	.194	.292	.327	.004	.145	.424	.

linearly related. If the significance level is relatively large (for example, 0.50) then the correlation is not significant and the two variables are not linearly related.

The strength of the correlations for the analyzed “independent” variables (parameters) to the dependent variable (ELOS) are sequenced from strongest to the weakest as: T → HR → N' → UF → OW → HS → DP → PF.

The Unstandardized Coefficients in Table 10.3 are the coefficients β_i for equation 10.2. The “independent” variables in Table 10.3 are often measured in different units. It is difficult to compare the Unstandardized Coefficients (B's) to each other. The standardized coefficients or betas are an attempt to make the regression coefficients more comparable. The t-statistic helps determine the relative importance of each variable in the model. The bigger the values, the more important the parameters in the model. The t-statistics in Table 10.3 show that stope HW shape factor HR, modified stability number N' and stope exposure time T are the most important influence factors for ELOS, compared to the other contributing factors. The drillhole pattern DP has the smallest t value compared to the other factors listed. This means that the drillhole pattern is the least important influence factor among the independent variables. The t-statistic and its significance value are used to test the null hypothesis that the regression coefficient is zero (or that there is no linear relationship between the dependent and independent variables). If the significance value is small (less than 0.05) then the coefficient is considered significant. The significance values in Table 10.3 indicate that the coefficients for HR, N' and T have values smaller than 0.05 and these coefficients can be considered significant. This agrees with the t-statistic indications.

From the multiple parameter regression results, the relationship between “independent” variables and the dependent variable ELOS can be established as:

$$\begin{aligned} \text{ELOS} = & -0.477 + 0.125 \cdot \text{HR} + 1.746\text{E-}02 \cdot \text{OW} - 1.705\text{E-}02 \cdot \text{N}' \\ & - 4.761\text{E-}02 \cdot \text{HS} + 6.645\text{E-}02 \cdot \text{DP} + 0.25 \cdot \text{PF} + 7.299\text{E-}03 \cdot \text{T} \\ & + 0.79 \cdot \text{UF} + \epsilon \end{aligned} \quad (10.3)$$

Table 10.3. Multiple parameter regression coefficients

Model Variables	Unstandardized Coefficients		Standardized Coefficients	t	Sig.
	B	Std. Error	Beta		
(Constant)	-.4770	.586	.000	-.814	.418
HR	.1520	.062	.234	2.476	.015
OW	.0175	.014	.114	1.240	.218
N'	-.0171	.007	-.227	-2.371	.020
HS	-.0476	.106	-.045	-.449	.654
DP	.0665	.159	.041	.419	.676
PF	.2500	.188	.127	1.328	.187
T	.0073	.003	.218	2.351	.021
UF	.7900	.430	.170	1.840	.069

As defined in equation 10.1, ϵ is a random variable and usually is referred to as the random deviation or random error term. When ϵ is normally distributed, the ϵ term vanishes. This can be tested by plotting a histogram of the data with a normal curve superimposed to see if the data appear to be normally distributed. Figure 10.1 shows the histogram of regression standardized residual. It shows a reasonable fit to a normal distribution, so equation 10.3 becomes:

$$\begin{aligned}
 \text{ELOS} = & -0.477 + 0.125 \cdot \text{HR} + 1.746\text{E-}02 \cdot \text{OW} - 1.705\text{E-}02 \cdot \text{N}' \\
 & - 4.761\text{E-}02 \cdot \text{HS} + 6.645\text{E-}02 \cdot \text{DP} + 0.25 \cdot \text{PF} + 7.299\text{E-}03 \cdot \text{T} \\
 & + 0.79 \cdot \text{UF}
 \end{aligned} \tag{10.4}$$

Figure 10.2 shows the comparison between CMS measured ELOS and the multiple parameter regression model calculated ELOS on case histories. The average error between CMS measured ELOS and the multiple parameter regression derived model calculated ELOS is about 0.1 m.

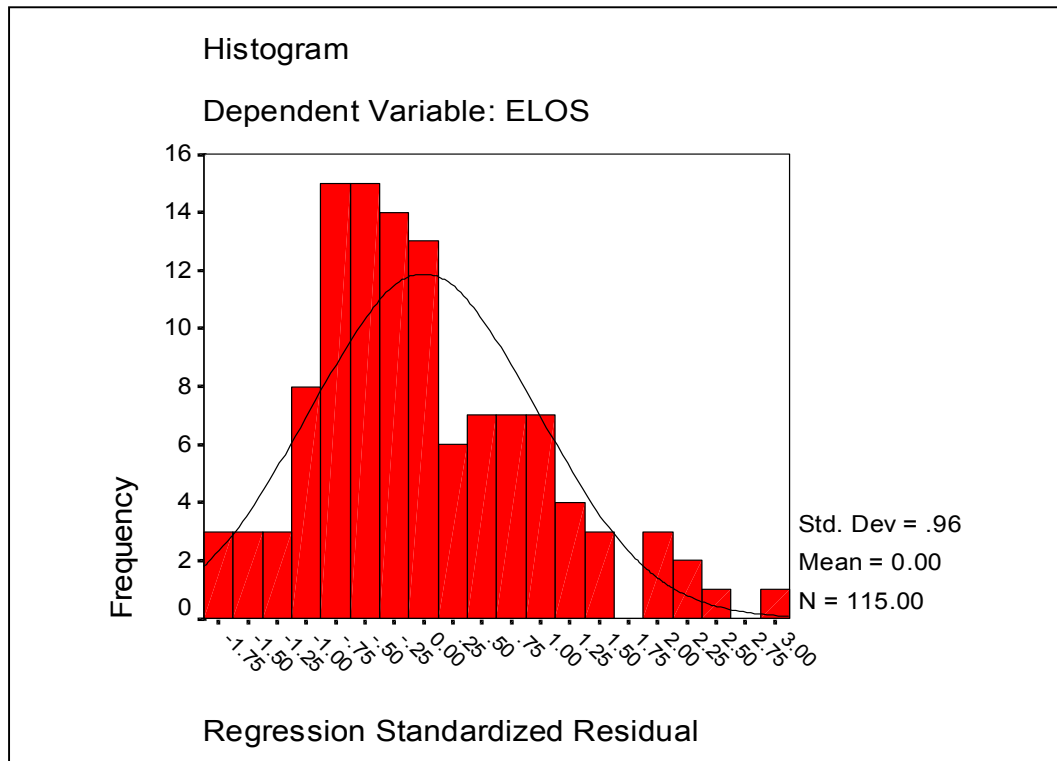


Figure 10.1. Histogram of regression standardized residual

It was noticed that some of the parameters have low input values and very small coefficients, which tends to result in negligible influence on ELOS. In the next section, another method of statistical analysis was used to eliminate some of the least influential parameters and to simplify the model.

10.4 Stepwise Multiple Parameter Regression Analysis

To simplify the model and to verify the major factors influencing ELOS, a further analysis was carried out by using a stepwise multiple parameter regression method.

The stepwise multiple parameter regression procedure first analyses all the parameters entered, and then removes variables one at a time based on a preset significance value (probability of value) for removal. The default value from the program is $p \geq 0.05$.

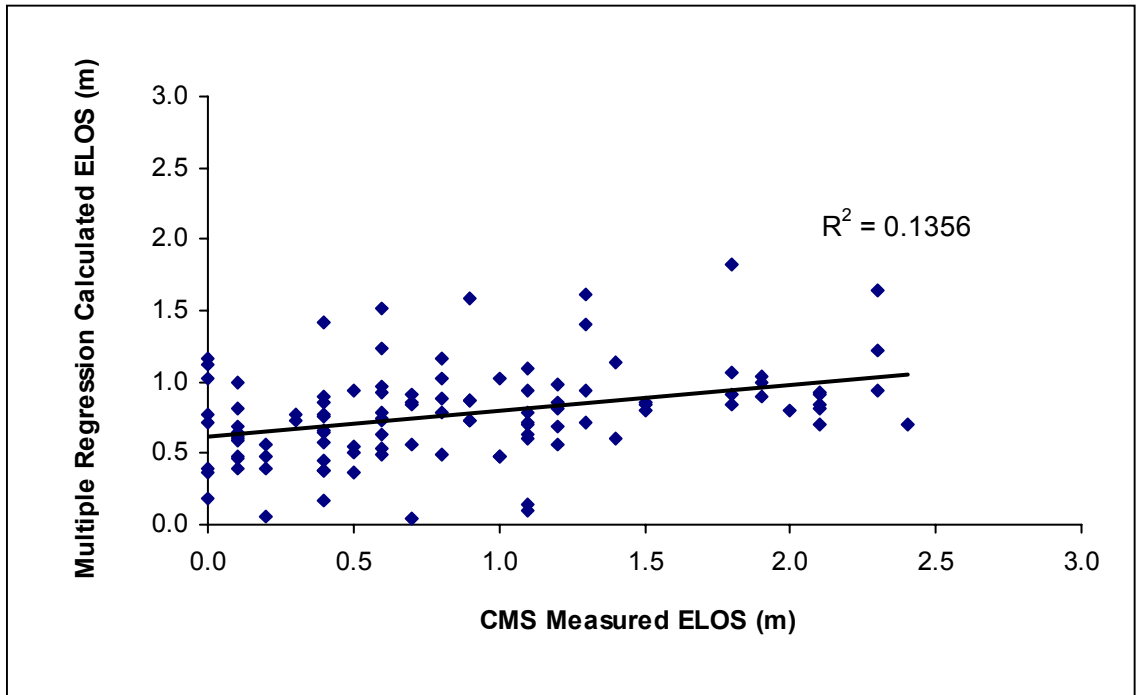


Figure 10.2. Comparison between CMS measured ELOS and multiple parameter regression model calculated ELOS

However, due to the high variability of the input factors, a $p \geq 0.075$ was chosen as the cut-off. This means that the parameters with a probability of obtaining a result by chance larger than 7.5% will be removed. It initially removes the least significant variable from the variables entered. The remaining variables are reanalyzed and the excluding criterion is applied again to eliminate the second least significant variable. This is continued in a step by step procedure to eliminate the least significant variable one at a time, until none of the variables meet the requirement for removal.

Initially, all the parameters listed in Table 10.1 were entered. Table 10.4 is a list of the parameters removed at each step. The least significant parameters that were removed at each step were: drillhole pattern (DP) → drillhole size (HS) → ore width (OW) → powder factor (PF).

There is no further progress at step four for the applied removal criteria. The parameters having significant influence on ELOS were determined to be hydraulic radius (HR), modified stability number (N'), undercutting factor (UF) and stope

exposure time (T) as shown in Table 10.5. The terms used in Table 10.5 are the same as the ones used in Table 10.3 and were described in Section 10.3. The t-test and significance values in Table 10.5 indicate the four parameters that have significant influence on ELOS from strongest to weakest are: $T \rightarrow HR \rightarrow N' \rightarrow UF$. The modified stability number and hydraulic radius are well recognized parameters influencing stope hanging wall stability. This study indicates that, for a certain range of rock mass conditions, the stope exposure time and undercutting of the stope hanging wall have a significant influence on stope hanging wall stability and dilution based on the database compiled from HBMS Mines.

Table 10.4. Variables Entered/Removed

Model (step)	Variables Entered	Variables Removed	Removal Criteria
1	UF, T, N', HR, OW, PF, DP, HS	.	All Entered
2	UF, T, N', HR, OW, PF, HS.	DP	Significance value to remove $p \geq 0.075$).
3	UF, T, N', HR, OW, PF	HS	Significance value to remove $p \geq 0.075$).
4	. UF, T, N', HR, PF	OW	Significance value to remove $p \geq 0.075$).
5	. UF, T, N', HR	PF	Significance value to remove $p \geq 0.075$).

* Dependent Variable: ELOS

Figure 10.3 shows the histogram of regression standardized residual. It shows a normal distribution and the random variable ϵ therefore vanishes.

The simplified model for the parameters that have significant influence on ELOS can be written as follows, based on the stepwise analysis calculated coefficients (Bs) in Table 10.5:

$$\text{ELOS} = -0.0213 + 0.131*HR - 0.0144*N' + 0.0071*T + 0.731*UF \quad (10.5)$$

Table 10.5. Stepwise multiple parameter regression coefficients

Model		Unstandardized Coefficients		Standardized Coefficients	t	Sig.
		B	Std. Error	Beta		
1	(Constant)	-.4770	.586	.000	-.814	.418
	HR	.1520	.062	.234	2.476	.015
	OW	.0175	.014	.114	1.240	.218
	N'	-.0171	.007	-.227	-2.371	.020
	HS	-.0476	.106	-.045	-.449	.654
	DP	.0665	.159	.041	.419	.676
	PF	.2500	.188	.127	1.328	.187
	T	.0073	.003	.218	2.351	.021
	UF	.7900	.430	.170	1.840	.069
2	(Constant)	-.3960	.552	.000	-.719	.474
	HR	.1510	.061	.232	2.471	.015
	OW	.0172	.014	.113	1.229	.222
	N'	-.0169	.007	-.225	-2.362	.020
	HS	-.0465	.106	-.044	-.440	.661
	PF	.2670	.182	.136	1.464	.146
	T	.0070	.003	.209	2.324	.022
	UF	.8400	.411	.181	2.041	.044
3	(Constant)	-.5040	.492	.000	-1.025	.308
	HR	.1420	.058	.219	2.474	.015
	OW	.0173	.014	.113	1.238	.218
	N'	-.0158	.007	-.209	-2.371	.020
	PF	.2620	.181	.134	1.446	.151
	T	.0072	.003	.214	2.392	.018
	UF	.8330	.410	.180	2.033	.044
4	(Constant)	-.2930	.463	.000	-.634	.527
	HR	.1360	.057	.209	2.367	.020
	N'	-.0155	.007	-.206	-2.326	.022
	PF	.2090	.177	.107	1.185	.239
	T	.0076	.003	.227	2.554	.012
	UF	.7790	.408	.168	1.908	.059
5	(Constant)	-.0213	.402	.000	-.053	.958
	HR	.1310	.057	.201	2.279	.025
	N'	-.0144	.007	-.191	-2.179	.031
	T	.0071	.003	.212	2.408	.018
	UF	.7310	.407	.158	1.796	.075

- Dependent Variable: ELOS

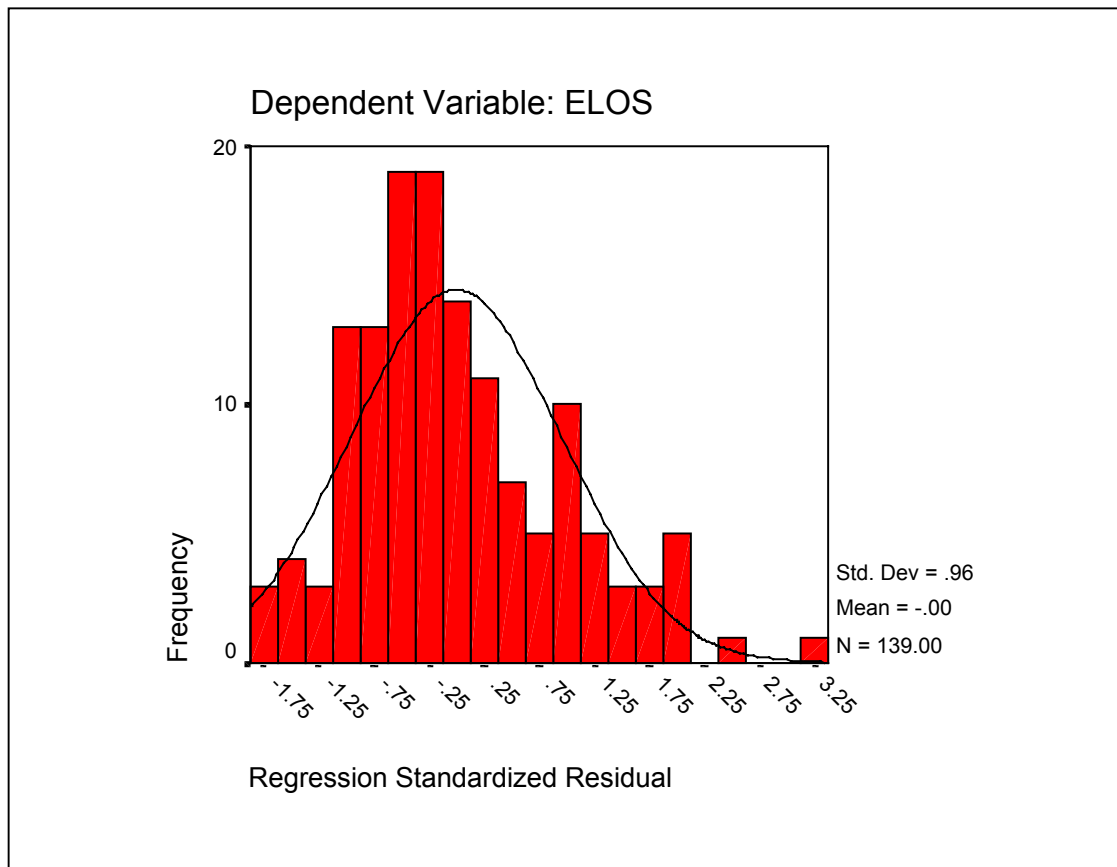


Figure 10.3. Histogram of standardized residual for stepwise analysis

Figure 10.4 shows the comparison between actual CMS surveyed ELOS and the most influential parameter regression model (Equation 10.5) calculated ELOS from case histories. It shows a reasonable fit. Figure 10.5 shows the comparison between Figure 10.2 and Figure 10.4. Though the model expressed in equation 10.5 has four parameters, compared to eight parameters in equation 10.4, it gives a correlation similar to the multiple parameter regression model (Equation 10.3), and is much easier to use.

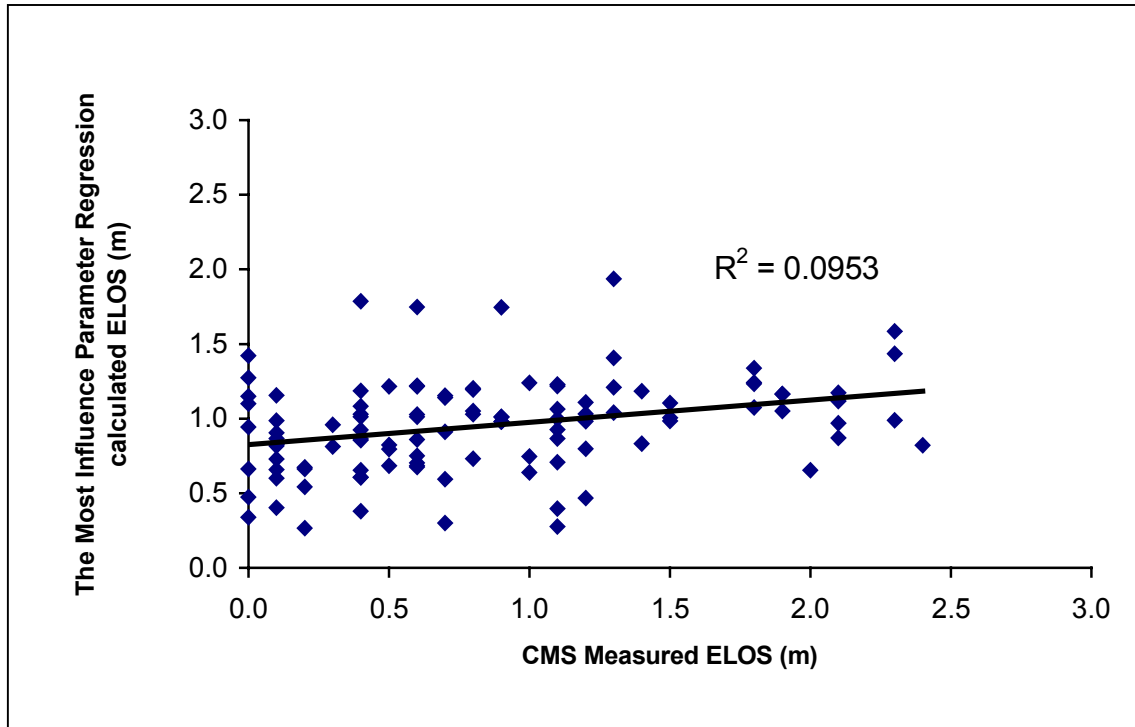


Figure 10.4. Comparison between CMS measured ELOS and the most influence parameter regression model calculated ELOS

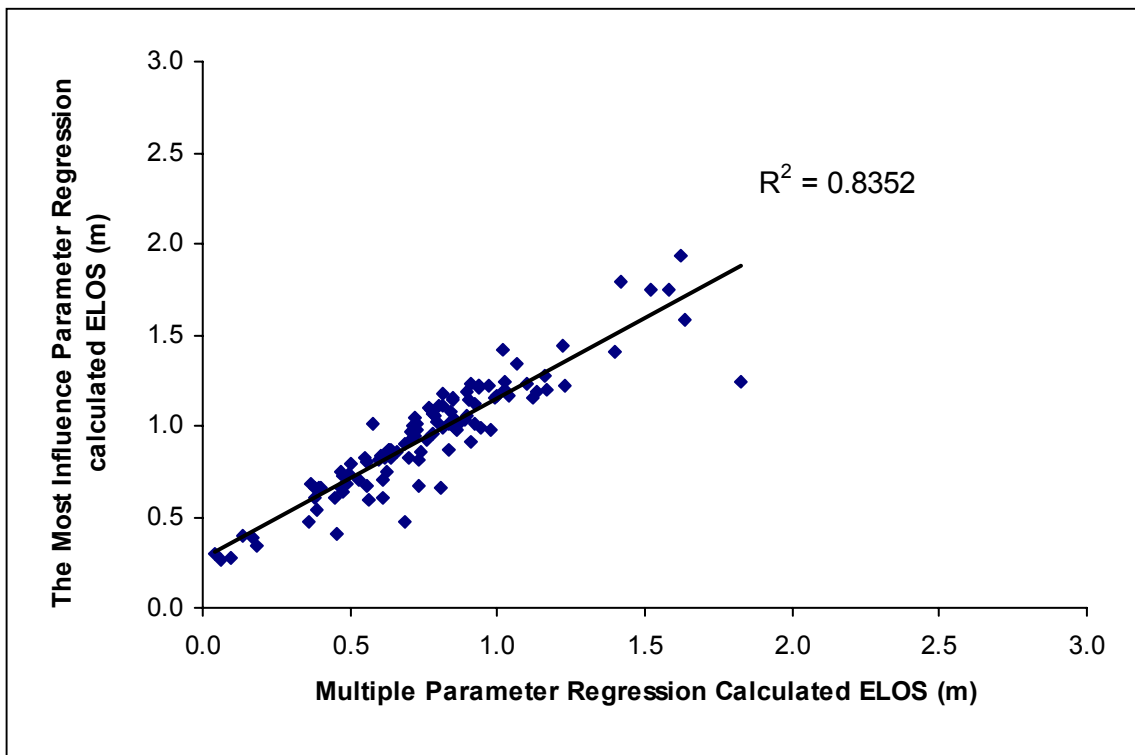


Figure 10.5. Comparison between the models shown in Figure 10.2 and Figure 10.4

10.5 Graphical Presentation of the Statistical Analysis Results

The model derived from the stepwise multiple regression analysis (Equation 10.4) showed that the stope hanging wall geometry, modified stability number N' , exposure time and undercutting factor (HR, N' , T and UF, respectively) are the most important parameters for assessing ELOS. The model showed that the stope hanging wall ELOS is directly proportional to stope hanging wall HR, degree of undercutting in terms of UF and exposure time T, and inversely proportional to the hanging wall modified stability number N' . This means that with the increase of stope hanging wall size, extent of undercutting and exposure time, the stope hanging wall ELOS increases, and with the increase of modified stability number N' , the ELOS decreases.

Figure 10.6 shows the ELOS model lines for the ELOS of 0.5 m, 1.0 m and 2.0 m respectively based on N' and HR, with case histories superimposed. The plots are based on setting UF and T to the average values from the HMBS database. The average values of UF and T are 0.15 m and 33 days respectively. The case histories poorly fit the model design lines. This is because the stope exposure time and undercutting values have a significant influence on stope hanging wall ELOS and the average values of T and UF do not account for this. To use the design lines in Figure 10.6, the additional influence from T and UF should be considered by using Equation 10.4 to add or subtract the additional contributions of T and UF from the average values used for the design lines.

To illustrate the influence of T on ELOS, the variable UF was fixed and set to zero. The ELOS was calculated by changing the T value for different HR and N' combinations. Figure 10.7 illustrates the influence of T on stope hanging wall ELOS. The example ELOS design lines for 1 metre of ELOS were plotted on the N' versus HR graph for 30, 60 and 90 days. Figure 10.7 shows that with an increase in stope exposure time, the stope HW ELOS increases. For example, for an N' of 10, HW dilution of 1 metre would be expected for an HR of 4.0 metres, if the stope remained open for 90 days. With more rapid mining the same amount of dilution would be

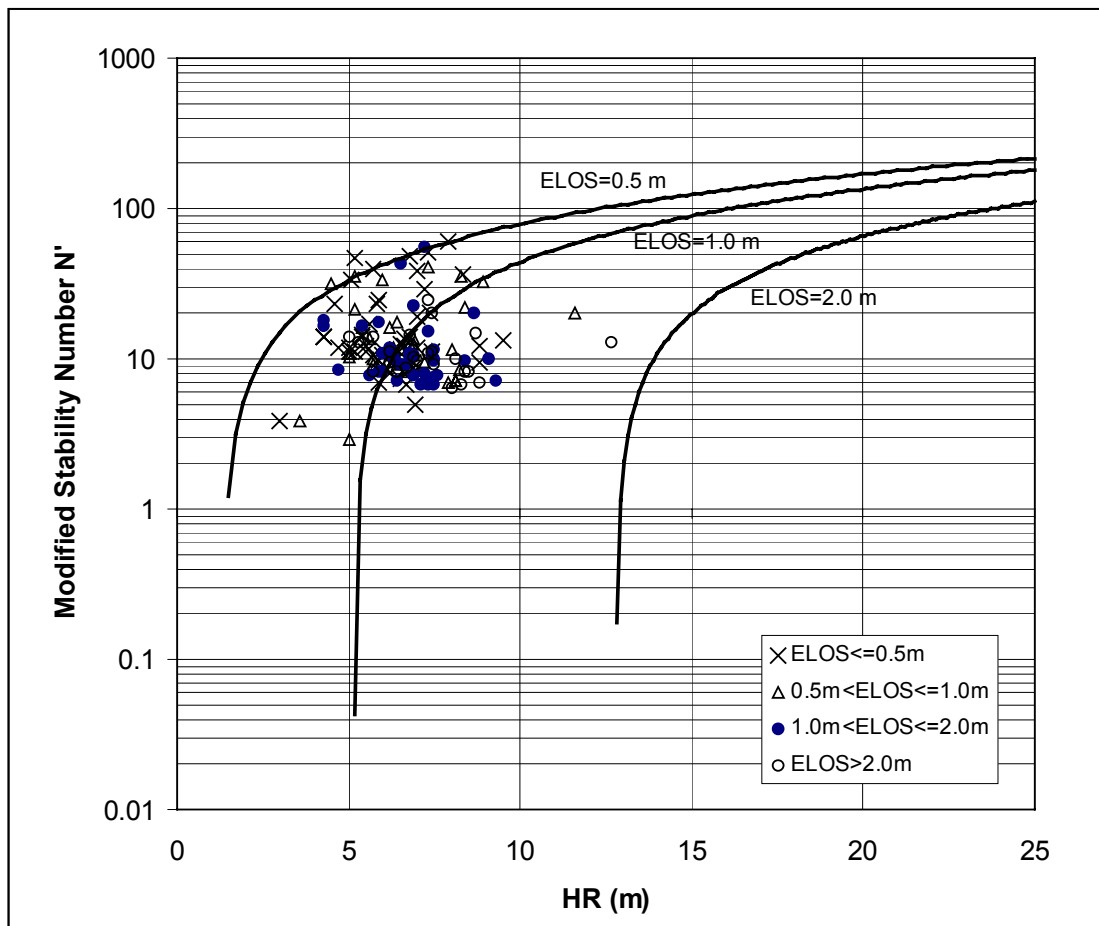


Figure 10.6. The model design lines for the average T and UF values with case histories plots

expected if the stope HW was opened to a HR of 7.0 metre, if the stope was only open 30 days. This shows that rapid mining makes a significant difference on HW dilution and will help mine operators put a dilution cost to mining delays. A similar procedure was used to demonstrate the influence of UF by fixing the T to 30 days and changing the UF value. Figure 10.8 illustrates the influence of UF on hanging wall ELOS for the UF values of 0, 0.5 and 1.0m for the ELOS =1.0 m design lines. The UF value can also have a significant effect on dilution. For example, for an N' of 10, an HR of only about 1.0 metre could be opened to give 1.0 metres of dilution for a UF of 1.0 metres, whereas, the same dilution would be expected for an HR of 7.0 metres if there was no undercutting. Both Figures 10.7 and 10.8 showed that T and UF have a significant influence on ELOS with increasing stope exposure time T and/or undercutting.

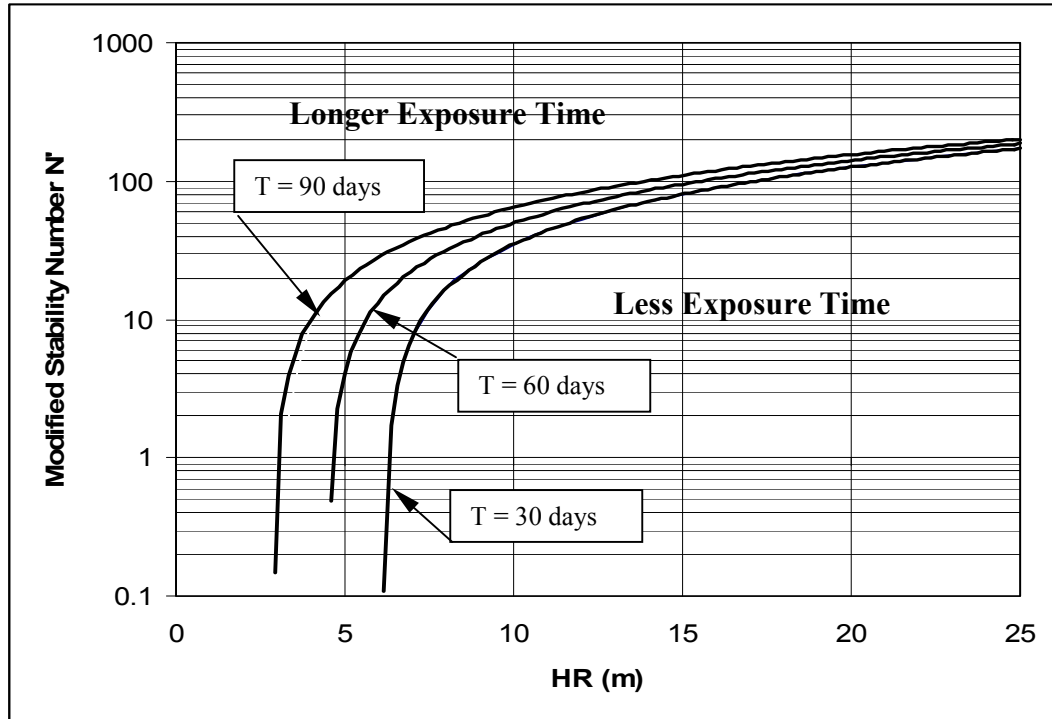


Figure 10.7. Illustration of the influence of stope exposed time (T) on hanging wall ELOS (ELOS = 1.0 m)

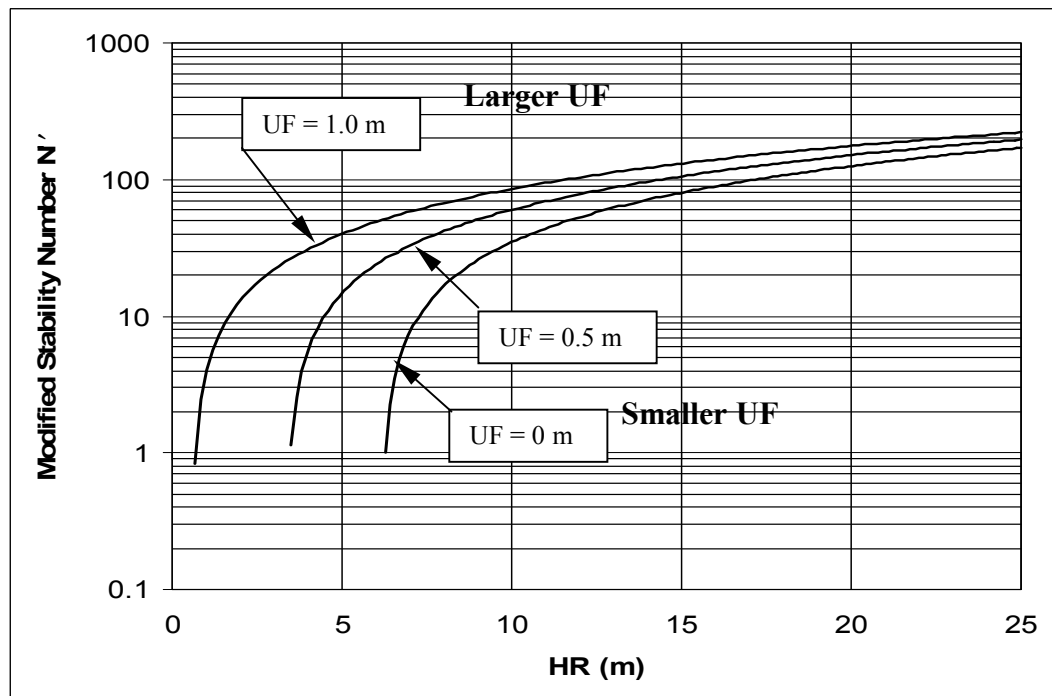


Figure 10.8. Illustration of the influence of undercutting factor (UF) on stope hanging wall ELOS (ELOS = 1.0 m)

10.6 Comparison of the Empirical and Statistical Analysis of the HBMS Database

Chapters 6 to 9 assessed the individual parameters of stress, undercutting, drillhole pattern and exposure time, to determine influence factors for the measured ELOS. The approach in these chapters was a simplified analysis that did not look at the possible interaction between variables. In this initial analysis the influence of HR and N' was accounted for with the Dilution Graph (Clark, 1998). The statistical analysis discussed in this chapter has looked at all these variables, as well as additional variables, to determine their combined influence on ELOS. These two approaches are compared in this section.

In the empirical assessment the HR and N' terms were assessed with the Dilution Graph. Figure 10.9 shows the Dilution Graph with the HBMS data plotted. The HR and N' values do not vary linearly with ELOS on the Dilution Graph. However, in the area where the HBMS data is concentrated, a rough estimate of a linear relationship can be made on this semi-log plot.

Figure 10.9 shows that if the N' increases from 4 to 8 for an HR of 5 m, the predicted ELOS decreases from 1.0 m to 0.5 m or with an increase of HR from 5 m to about 8 m for a N' of 8, the predicted ELOS increases from 0.5 to about 1.0 m. Also, if N' increases from 4 to 18 for an HR of 8, ELOS decreases from 2.0 m to 0.5 m. In this design region, the Dilution Graph shows that the correlations between ELOS and N' and between ELOS and HR are:

$$\text{ELOS} = -0.11 \text{ to } -0.13 \text{ N}', \text{ and} \quad (10.6)$$

$$\text{ELOS} = 0.17 \text{ HR} \quad (10.7)$$

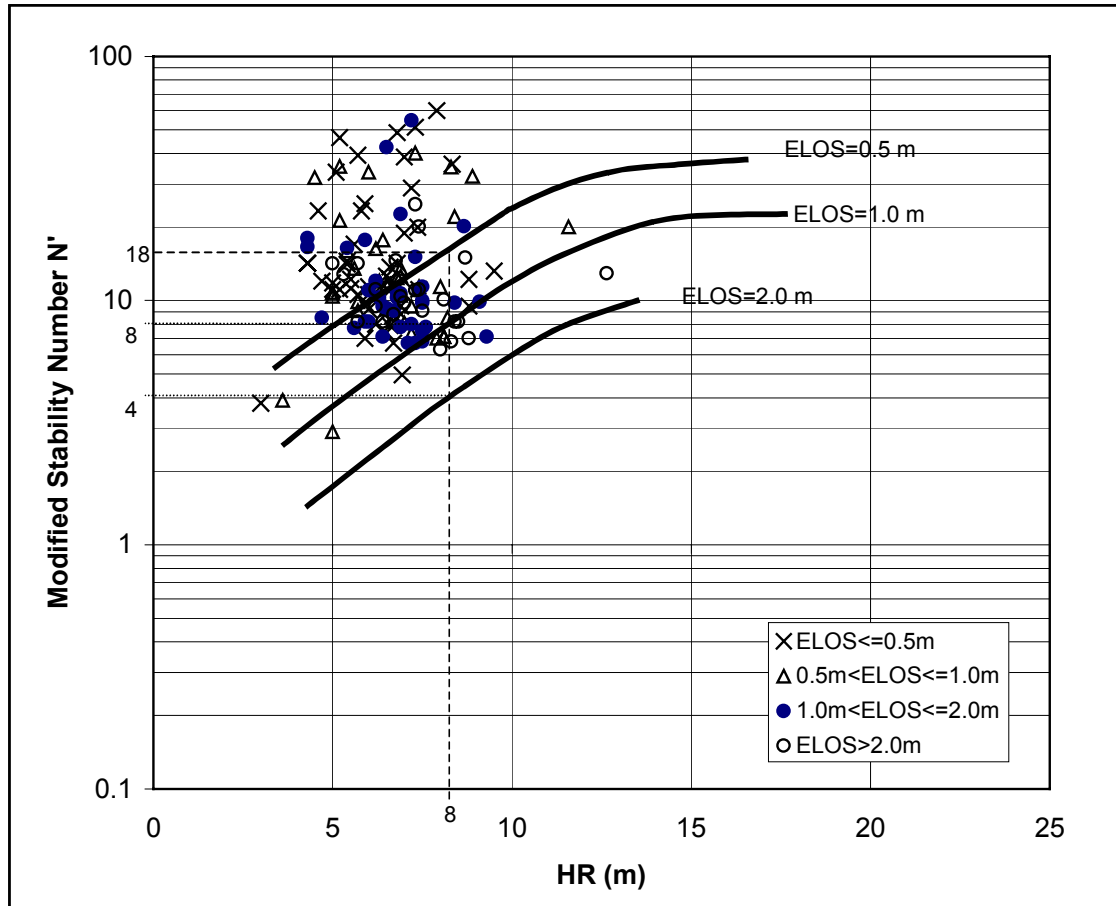


Figure 10.9. Example interpretation of dilution graph (dilution graph with the HBMS data plotted)(after Clark, 1998)

Table 10.6 shows the comparison between empirically analysed results and statistically analysed results for the HBMS database. Overall, the statistically analysed results generally agreed well with the empirically analysed results, except for the N' value and the drill pattern factors, which shows a significant difference. The difference between the empirically and statistically assessed influence of N' on ELOS is because the empirical approach, with the Dilution Graph, has assumed a logarithmic relationship between ELOS and N' , whereas the statistical approach assumes a linear relationship. Figure 10.10 shows the empirically and statistically derived approaches for assessing N' and the HR value plotted on the Dilution Graph.

Table 10.6. Comparison between empirical and statistical analyses (stepwise results)

Factor	Rate of contribution to ELOS		Comparison
	Empirically analysed results	Statistical analysed results	
Modified Stability Number, N'	$(-0.11 \text{ to } -0.13)N'$	$-0.0144 N'$	Poor fit
Hydraulic Radius HR (m)	0.17 HR	0.13 HR	Good fit
Exposure Time, T (days)	0.0065 T	0.0071 T	Good fit
Undercutting Factor (UF) (m)	(1.278 UF)	0.731 UF	Reasonable fit
Drill Hole Pattern	0.19m for Fanned 0.67m for Parallel	No relationship	Poor fit

The drill pattern factor appears to have a significant influence on dilution when it is empirically assessed on its own. The statistical assessment did not indicate any significant relationship between the drill pattern and ELOS, possibly because the undercutting factor tends to account for the cases with parallel drilling (Section 8.5.1). (Case histories with parallel drilled blast holes tend to have a significant amount of undercutting.)

10.7 Summary

The statistical approach is a valuable tool for the empirical database analysis. Based on available data, a relationship between ELOS and contributing factors was derived from the statistical analysis. The statistical analysis results showed that each parameter included in the analysis has a contribution to ELOS. Two models were obtained from the analysis. One is the multiple parameter regression derived model. The other is the stepwise multiple parameter regression model, which applied certain criteria to eliminate the least important ELOS contribution parameters, and considers the parameters that have significant influence on ELOS.

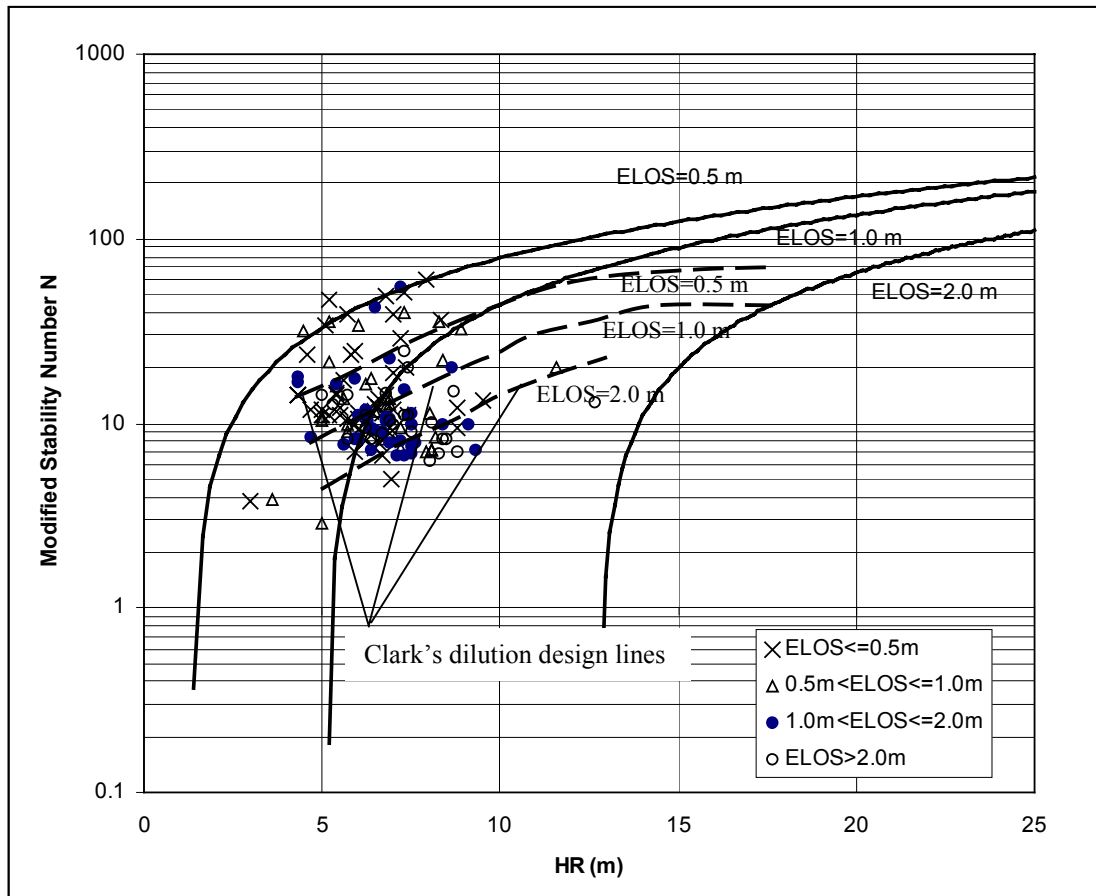


Figure 10.10. The model design lines for the average T and UF values with case history data and Clark's dilution design lines

The multiple parameter regression derived model (Equation 10.3), which included all the available parameters, showed a reasonable fit with the case history data (Figure 10.2) but would benefit from simplification. The stepwise multiple regression derived model (Equation 10.4) only included the four most significant parameters which contribute to ELOS. It showed a reasonable fit to case histories (Figure 10.4) and is easier to apply.

The statistical analysis results indicated that the parameters which have significant influence on stope hanging wall ELOS from strongest to weakest are: stope hanging wall exposure time T, hanging wall shape factor HR, modified stability number N' , and stope HW undercutting factor UF.

The statistical analysis further confirmed the trends relating ELOS to the contributing factors of undercutting (UF), exposure time (T), rock mass condition (N') and stope geometry (HR). The statistical analysis did not confirm the initially assessed importance of the drill hole pattern, possibly due to the fact that the undercutting factor and drill pattern do not appear to be independent factors or normally distributed.

CHAPTER 11

CONCLUSIONS AND RECOMMENDATIONS

Unplanned open stope dilution is a major cost factor for many mining operations. The objective of this thesis was to quantify the influence of the factors of stress, undercutting, blasting and stope exposure time, on dilution (ELOS). These factors were poorly accounted for or ignored by existing open stope stability and dilution design methods. These four factors were evaluated and quantified based on the established empirical database as well as 2D and 3D computer numerical modelling. The major achievements for this research include the following:

- Established a comprehensive geomechanics database
- Developed a simple approach to relate mining geometry to an induced stress state for assessing stress relaxation related dilution.
- Evaluated the undercutting influence on open stope HW stability and dilution
- Analysed the influence of blasting on open stope stability and dilution
- Quantified the influence of exposure time on open stope stability and dilution
- Statistically evaluated the factors influencing open stope stability and dilution

11.1 Establishment of a Comprehensive Database

Two full summers of field work were conducted to collect data for this research at the mines of Hudson Bay Mining and Smelting Co. Ltd.. Site geomechanics rock mass mapping and classification were conducted and case histories were collected from Cavity Monitoring System (CMS) surveyed stopes. Based on stope mining information, rock mass mapping and classification, as well as CMS survey data, a comprehensive

empirical database was established for the study. The database includes most of the CMS surveyed stopes from Callinan Mine, Ruttan Mine and Trout Lake Mine consisting of 150 case histories. The following information was included in the database:

- General stope information
- Stope geometry
- Rock mass properties and classification
- Undercutting information
- Adjacent mining information
- Drilling parameters
- Blasting information
- Time between blasting and CMS survey, and
- CMS survey data and calculations.

The database is an importance resource for the dilution study. The comprehensive database is presented in the Appendix II.

11.2 Quantifying Stress Relaxation as a Factor Influencing HW Dilution

Open stope hanging walls are usually in a state of low confining stress or relaxation. Numerical stress modelling of open stopes will often result in zones of tensile stress being predicted in the stope hanging wall with the tensile stresses oriented parallel to the hanging wall. Instability in the HW of an underground excavation has been closely related to the zone of relaxation (Potvin, 1988; Clark and Pakalnis, 1997; Kaiser et al., 1997; Diederichs and Kaiser, 1999; Martin et al., 2000). Much of the dilution or slough adjacent to open stopes occurs in the HW zone of relaxation where there is a lack of confining stresses locking the jointed rock mass together.

The extent of the zone of relaxation in the stope HW increases with the HW extent, expressed as the HW hydraulic radius, and is also related to the stress ratio (K) existing prior to mining the stope. Initial work by Clark (1998) showed a preliminary

relationship between hanging wall extent and the stress state. In this study, extensive 2D and 3D numerical modelling was conducted and it was found that the zone of hanging wall relaxation was much larger than initially predicted by Clark (1998).

A new term, the equivalent linear relaxation depth (ELRD), was introduced in this study. It is the average depth of relaxation on the excavation surface, and is expressed as:

$$ELRD = \frac{\text{Volume of Relaxation on a Stope Surface}}{\text{Stope Surface Area}} \quad (11.1)$$

A relationship between the size of the relaxation zone, the pre-mining stress state and the size and shape of the opening surface has been established. The size of the relaxation zone is directly related to the pre-mining stress ratio K ($K=\sigma_1/\sigma_3$). Various excavation geometries were modelled to determine if either the hydraulic radius or radius factor terms have a consistent effect on the relaxation zone adjacent to an underground opening. Models were run on rectangular, disc shaped and tunnel geometries. In all cases the opening surface was quantified using both the HR and RF terms. Three stress regimes, $K=1.5$, 2.0 and 2.5 , were assessed for each opening geometry. The average depth of the relaxation zone, ELRD, was determined by calculating the volume of the relaxation zone and dividing by the area of the surface. The relaxation zone was bounded by the zero stress iso-surface and the surface investigated.

The stope location relative to adjacent mined stopes will affect the stress condition, and the shape factor (Radius factor (RF) or hydraulic radius (HR)) of the stope hanging wall has been found to correlate linearly with the size of the relaxation zone. Two design graphs have been developed to relate stope geometry, pre-mining stress state and the zone of hanging wall relaxation in terms of the depth of the relaxation at the centre of a stope HW (Figure 6.25 and Figure 6.26) and the ELRD on stope HW surface (Figure 6.27 and Figure 6.28) respectively. Both the depth of relaxation at the centre of a stope

HW and the average relaxation depth (ELRD) vary linearly with radius factor for all modelled geometries. The slope of the ELRD versus RF and HR lines was controlled by the stress ratio K .

The stope hanging wall geometry is easily determined. However, estimating the stress state for a stope prior to mining can involve time consuming numerical modelling work that is difficult for a mine to do on a production schedule. A series of 6 stope categories were introduced as part of this research. The approximate stress ratio K has been estimated for each stope category, based on 3 dimensional boundary element modelling. This relationship is only valid for the HBMS database, since it is dependent on the initial mine stress state prior to all mining activity.

A relationship between the stress condition, hanging wall geometry (HR or RF) and zone of relaxation (ELRD) has been coupled with a simple approach for estimating the stress state for open stope hanging walls based on adjacent stope mining activity. The HBMS dilution database was analysed to determine if increased dilution was observed in stopes mined in a higher stress ratio. No trend was found, possibly due to the influence of other dilution contributing factors. Other factors such as the rock mass condition, blasting, undercutting, geological structures may over-shadow the stress influence on stope HW dilution. It is also believed that the relatively low stress ratio, even for category 6 situation at the HBMS operations ($K=2.0$), may be the reason for a lack of correlation between the observed dilution and the stoping categories.

11.3 Influence of Undercutting, Blasting and Exposure Time on Open Stope HW Dilution

The three factors of hanging wall undercutting, blasting and exposure time influence hanging wall dilution. These factors are currently ignored with the established methods of estimating dilution. In the case of undercutting, a factor has been introduced to quantify the degree of hanging wall undercutting. The influence of these factors on dilution has been assessed with the HBMS database. To assess these factors, an

estimate of expected dilution was made for each case history in the database, based on the dilution graph (Clark, 1998). The difference between the measured and predicted dilution was then compared to the three factors.

11.3.1 Influence of Undercutting on Open Stope HW Dilution

The influence of undercutting on stope HW dilution was quantified by analytical and numerical methods. The mechanism of the undercutting effect and the influence on case histories were investigated. Instability and dilution caused by undercutting on the stope HW has two main causes:

- a). Jointed rock mass rock failure caused by removal of the HW abutment support due to undercutting;
- b). Increased zone of distressed or relaxed rock failure due to undercutting.

An equation has been developed to quantify the undercutting geometry with a new term called the undercutting factor, UF. The UF is proportional to the portion of stope HW being undercut, and the average depth of undercutting. The UF is expressed as:

$$UF = \frac{l_o + l_u}{2(L + H)} \times \frac{(d_o + d_u)}{2} \quad (11.2)$$

where, UF = Undercutting Factor (m)

l_o = Drift length where undercutting occurs on the overcut drift (m)

l_u = Drift length where undercutting occurs on the undercut drift (m)

L = Stope strike length (m)

H = Stope height (up dip) (m)

d_o = Average depth of undercutting along the overcut drift length l_o (m)

d_u = Average depth of undercutting along the undercut drift length l_u (m)

Note: $2(L+H)$ = Stope perimeter

The parameters contributing to the UF are shown in Figure 7.3. This equation can be applied when undercutting is similar on both the overcut and undercut drifts.

The influence of the undercut factor (UF) on the zone of relaxation was quantified and compared to the HBMS database. No trends were observed. The UF term was then directly compared to the actual dilution minus predicted with the dilution graph design method ($ELOS_{act} - ELOS_{pred}$). It shows a weak general trend of increasing unpredicted dilution with an increasing undercutting factor UF, with a wide variation in the individual stope cases.

11.3.2 Influence of Blasting on Open Stope HW Stability and Dilution

The influence of blasting on open stope stability and dilution is a complex factor to assess. Numerous factors can cause blasting damage to a stope hanging wall, some of which are listed below:

- Rock mass properties
- Drillhole design (drillhole size, length, spacing, burden, and orientation)
- Drillhole accuracy (drillhole deviation)
- Explosive type
- Wall control methods
- Explosive distribution
- Explosive per delay
- Initiation sequence
- Availability of free face (e.g. slot)

Wherever possible, these factors were assessed with the HBMS database to determine if they influenced the dilution obtained for the open stope hanging walls. In some cases, factors such as drillhole deviation, could not be measured directly. Blast hole or drillhole deviation is occasionally measured at the mine and it is recognized as a problem. Unfortunately, it is not recorded for most stopes. An indirect measure of

drillhole deviation was assessed based on the drilling pattern used closest to the hanging wall.

At the HBMS mines the blast engineer endeavours to drill blast holes parallel to the hanging wall surface. This provides a better explosive distribution to reduce hanging wall blast damage. In some cases the mining geometry requires that the blast holes are fanned into the hanging wall resulting in blast holes butting into the stope hanging wall. This can locally concentrate the blast energy and cut into the hanging wall resulting in more blast damage. The two sets of case histories with parallel and fanned drilling on the hanging wall contact were analysed with the HBMS database. It was found that parallel drilled hanging wall holes had more hanging wall dilution. This was not the expected result. However, parallel drilled holes are more sensitive to the HW stability due to borehole deviation and this was felt to be the cause of the increased dilution.

The overall HW average meters of overbreak difference between parallel drillhole and fanned drillhole is about 0.37m. For an HBMS average stope HW size of 30x30m, this 0.37m of additional overbreak will represent about 900t of dilution. This significantly increases the mining costs. It was also found that stopes with parallel drilling on the hanging wall also had more hanging wall undercut on the drill drifts. This increased undercutting may have a greater influence on hanging wall dilution than the probable increase in drillhole deviation associated with parallel drilling.

11.3.3 Influence of Stope Exposure Time on Open Stope HW Stability and Dilution

Stope exposure time is a recognized factor contributing to stope dilution. Little work has been done to try and quantify the influence of exposure time on hanging wall dilution for open stope mining. This study quantifies the influence of exposure time on the HBMS database and compares the result to an assessment of the stand-up time graph (Bieniawski, 1989) and a complementary case history database from Geco Mine in Northern Ontario. Work conducted by Bieniawski (1989) suggests that the influence

of exposure time on rock mass behaviour increases as the rock quality decreases. For a rock mass similar to conditions encountered at HBMS, the Stand-up time graph (Figure 9.2) would indicate approximately 0.14 metres of ELOS per month of exposure. A database of 8 stopes from Geco Mines indicated a similar influence of exposure time on ELOS with a rate of 0.16 metres additional ELOS per month. The analyses of the Stand-up time graph and the Geco Mines data suggest that hanging wall slough increases between 0.14 to 0.16 meters per month for a rock mass Q' value between 4 to 31 (N' between 3 to 60). The HBMS database was also assessed to see if the hanging wall was more sensitive to exposure time for weaker rock masses. No apparent trends were observed on HBMS database.

Minimizing stope exposure time by promptly mucking after blasting and minimizing the mucking time has been recognized as an effective way of significantly reducing stope dilution.

11.4 Statistical Evaluation of the Factors Influencing Open Stope Stability and Dilution

A statistical analysis was conducted to assess the relationships obtained from the empirical and numerical analyses of the HBMS database. Based on available data, a relationship between ELOS and contributing factors was derived from the statistical analysis. The statistical analysis results showed that each parameter included in the analysis had a certain contribution to ELOS. Two models were obtained from the analysis. One is a multiple parameter regression derived model, and the other one is a stepwise multiple parameter regression model which determined the 4 parameters with the most significant influence on hanging wall dilution.

The multiple parameter regression derived model (Equation 10.4), which included the available parameters, showed a reasonable fit with case history data (Figure 10.2) but is too complicated for application. The stepwise multiple regression derived model

(Equation 10.5) only included the four most significant parameters which contribute to ELOS. It showed a reasonable fit to case histories (Figure 10.4) and is easy to apply.

The statistical analysis results indicated that the parameters which have significant influence on stope hanging wall ELOS from strongest to weakest are: stope hanging wall exposure time T , hanging wall shape factor HR , modified stability number N' , and stope HW undercutting factor UF . Due to the limited available data on stress, stress was not included in the statistical analysis.

The statistical analysis, and the individual assessment of factors in the HBMS database coupled with the Dilution Graph analysis, showed the same factors strongly influence dilution, except for the drill pattern factor. The statistical analysis indicated that parallel or fanned drilling had no significant influence on hanging wall dilution, whereas, assessed individually, the drilling pattern appeared significant. The database shows that parallel drilling was conducted more frequently when hanging wall undercutting was present. The hanging wall undercutting made the stope geometry more conducive to parallel drilling and it is likely that the undercutting was the larger contributing factor to dilution, highlighting the value of the statistical analysis. More work is needed to determine if fanned or parallel drilling does significantly influence hanging wall dilution.

The influence of the hanging wall hydraulic radius (HR), the undercutting factor (UF) and exposure time are generally similar for the empirically analysed approach with the Dilution Graph and for the statistically analysed approach (Table 10.6). The two approaches, however, give a significantly different assessment of the influence of the stability number N' . This is because the dilution graph is based on a $\log N'$ relationship with dilution whereas the statistical analysis has been done based on a linear relationship.

11.5 Summary and Assessment of Findings

Factors influencing hanging wall dilution have been assessed in this research. The approach taken for assessing the stope stress state based on the mining configuration is a quick, simple approach that can be used in the mine planning process. This mine configuration, based on adjacent mining coupled with the initial stress state, can be combined with the stope geometry to estimate the zone of hanging wall relaxation (ELRD). This zone of ELRD may be related to the zone of stope dilution (ELOS). The HBMS database did not show a relationship, possibly due to the low initial stress ratio K at the HBMS mines.

The Dilution Graph assessment of hanging wall dilution accounts for the factors of rock mass strength (Q'), joint orientation and surface geometry (hanging wall dip and hydraulic radius (HR)). The simplified statistical analysis looks at all these factors as well as undercutting and exposure time, with the following result:

$$ELOS = -0.0213 + 0.131HR - 0.0144N' + 0.0071T + 0.731UF \quad (10.5)$$

Figure 10.9 shows a comparison of the actual measured ELOS versus the ELOS predicted from the Dilution Graph. Only 115 cases (with no missing data) statistically analysed are shown. Figure 10.10 shows the actual measured ELOS versus the ELOS predicted from the statistical analysis shown by Equation 10.5. The statistical analysis shows a slight improvement in dilution prediction. With the Dilution Graph analysis 12 of the case histories had a discrepancy of more than 1.5 metres between the actual and predicted dilution. With the statistical assessment only 6 of the case histories differed by more than 1.5 metres between the actual and predicted dilution.

The improvement in dilution prediction is not overly significant. Of more importance is the assessment of the influence of exposure time and undercutting. The relationship

between exposure time and undercutting, shown in equation 10.5, allows the mining engineer to assign a probable magnitude of dilution due to hanging wall undercutting and mining delays. This enables a cost to be associated with these activities and will greatly assist in mine planning decisions.

11.6 Recommendations for Future Research

This study has investigated and quantified a stress factor, undercutting factor, blasting factor and a time factor for assessing open stope stability and dilution. Further work should be conducted in the following areas:

- Additional studies are needed to try and link the size of the hanging wall relaxation zone with stope HW dilution
- Additional data need to be collected to study the influence of the blasting drill pattern (parallel versus fanned patterns). It is unclear whether parallel drilling does influence dilution, or if it only appears to be a factor because parallel drilling tends to be used in areas where the hanging wall has been undercut.
- Case histories with more diverse ground conditions need to be analysed to determine if the factors influencing dilution, such as exposure time and undercutting, are influenced by ground conditions. Studies at other mine sites are required to do this.

REFERENCES

- Ame, D.A. and Taylor, C., 1996. Geology of the West Anomaly orebody, Ruttan volcanic-hosted massive sulphide deposit, Proterozoic Rusty Lake Belt. Geological Survey of Canada, Bulletin 426.
- Anderson, B and Grebence, B., 1995. Controlling dilution at the Golden Giant Mine, 1995 CIM Operators Conference.
- Andrieux, P., 2003. Personal communication.
- Anon, 1990. The geology of Callinan Mine. Internal Report, HBMS.
- Arjang, B., 1991. Pre-mining stresses at some hard rock mines in the Canadian Shield, CIM Bulletin, January 1991.
- Atlas Powder Company, 1987.
- Autodesk Inc. AutoCAD – Automatic Computer Aid Design program, 1982-1997.
- Barton, N., Grimstad, E., Aas, G., Opsahl, O.A., Bakken, A., Pedersen, L., and Johanson, E.D., 1992. Norwegian method of tunnelling. World Tunnelling and Subsurface Excavation, August, pp.324-331.
- Barton, N., Lien, R. and Lunde, J., 1974. Engineering classification of rock masses for the design of tunnel support. Rock Mech. Vol. 6, pp. 189-236.
- Bauer, A., 1978. Trends in drilling and blasting, CIM Bulletin, September.
- Beer, G. and Meek, J.L., 1982. Design curves for roofs and hangingwalls in bedded rock based on voussoir beam and plate solutions. Trans. Instn. Min. Metall. Vol. 91, pp. A18-22.
- Bieniawski, Z.T., 1974. Estimating the strength of rock materials. J.S. Afr. Inst. Min. Metall., 74, pp. 312-320.
- Bienawski, Z.T., 1976. Rock mass classification in rock engineering, Proceedings Symposium on Exploration for Rock Engineering, Johannesburg, Volume 1, pp. 97-106.
- Bienawski, Z.T., 1979. The geomechanics classification in rock engineering classifications. Proc. 4th Int. Congress on Rock Mechanics, ISRM, Montreux, Rotterdam: A.A. Balkema, 2,41 –48.

- Bienawski, Z.T., 1989. Engineering rock mass classifications. New York: Wiley.
- Bienawski, Z.T., 1993. Classification of rock masses for engineering: The RMR system and future trends. Comprehensive Rock Engineering, (ed. Hudson), Oxford: Pergamon, 3, 553-573.
- Brady, B.H.G., and Brown, E.T., 1993. Rock mechanics for underground mining, 2nd edition. Chapman & Hall.
- Brady, B.H.G., and Brown, E.T., 1985. Rock mechanics for underground mining. London: Allen and Unwin.
- Brady, B.H.G., and Brown, E.T., 1993. Rock mechanics for underground mining. 2nd edition, Chapman & Hall. ISBN 041247550 2.
- Carlos, L.J., Emilio, L.J., Carcedo, A., Javier. F., 1995. Drilling and blasting of rocks. Rotterdam, Netherlands, Brookfield, VT : A.A. Balkema.
- Carvalho, J.L., Hoek, E., Li, B., 1992-95. Unwedge program. Department of Civil Engineering, University of Toronto.
- Carvalho, J.L., Hoek, E. and Corkum, B.T., 1991. Phases program, Department of Civil Engineering, University of Toronto.
- Clark, L. and Pakalnis, R., 1997. An empirical design approach for estimating unplanned dilution from open stope hangingwalls and footwalls. CIM AGM, Vancouver.
- Clark, L., 1998. Minimizing dilution in open stope mining with a focus on stope design and narrow vein longhole blasting, Msc. Thesis, University of British Columbia, Canada, 316p.
- Coulomb, C.A., 1776. Essai sur une application des règles de maximis et minimis à quelque problèmes de statique, relatifs à l'architecture. Mémoires de Mathématique et de Physique, L'Académie Royale des Scences, 7, pp. 343-82.
- Crouch, S.L. and Starfield, A.M., 1983. Boundary element methods in solid mechanics. George Allen & Unwin Ltd. London. ISBN 0-04-620010-X.
- Curran, J.H. & Corkum, B.T., 1994. Examine 2D boundary element method code User's Manual. Version 5.11.
- Curran, J.H. & Corkum, B.T., 1993. Examine 3D Code, three-dimensional excavation analysis for mines. User's Manual, Version 3.0.

- Devore, J. L., 1995. Probability and statistics for engineering and the sciences. 4th edition. Duxbury Press.
- Diederichs, M.S., and Kaiser, P.K., 1999. Tensile strength and abutment relaxation as failure control mechanisms in underground excavations. *Int. Journal of Rock Mech. And Mining Sci.* 36(1999) pp. 69-96.
- Dunne, K., Pakalnis, R., Vongpaisal, S., 1996. Design analysis of an open stope at the Detour Lake Mine, 98th CIM AGM, Edmonton, Alberta.
- Evans, W.H., 1941. The strength of underground strata. *Trans. Instn. Min. Metall.*, 50, pp. 475-532.
- Gipson, G.S., 1987. Boundary element fundamental-basic concepts and recent developments in the Poisson Equation. *Topics in Engineering, Vol. 2. Computational Mechanics Publication.* 110p.
- Goodman, R. E., 1989. Introduction to rock mechanics. 2nd edition, John Wiley & Sons. pp.257-280.
- Graaf, De, P.J.H., Hyett, A.J. and Bawden, W.F., 1998. Optimisation of cable bolt reinforcement for underground mining – geology and rock mass characterisation at Callinan Mine, Flin Flon, Manitoba. Report to HBMS, 81p.
- Griffith, A.A., 1921. The phenomena of rupture and flow in solids. *Phil. Trans Roy. Soc.*, A221, pp. 163-97.
- Griffith, A.A., 1924. Theory of rupture, in *Proc. 1st Congr. Appl. Mech.*, Delft, pp.55-63.
- Hagan, T.N., 1967. Performance characteristics of ammonium nitrate/fuel explosives, Ph.D. Thesis, University of Queensland.
- Hagan, T.N., 1973. Rock breakage by explosives, *National Symp. On Rock Fragmentation*, Australian Geomechanics Society.
- Hagan, T., 1996. Safe and cost effective blasting for surface mines and quarries, short courses by Golder Associates Ltd. and ICI Australia Operations Pty. Ltd.
- Hendricks, C., Scoble, M. and Boudreault, F., 1994. A study of blasthole drilling accuracy: monitoring instrumentation and practice. *CIM Bulletin Vol. 87. No. 977*, February.
- Hoek, E., & Brown, E.T., 1980. *Underground excavation in rock.* The Institution of Mining and Metallurgy.

- Hoek, E., & Brown, E.T., 1988. The Hoek-Brown failure criterion – a 1988 update. Rock Engineering for Underground Excavations, Pro. 15th Canadian Rock Mech. Symp., (ed. J.C. Curran), 31-38. Toronto: Dept. of Civil Engineering, University of Toronto.
- Holmberg, R. and Persson, P.A., 1980. Design of tunnel perimeter blasthole patterns to prevent rock damage. Trans. Inst. Min. Metall., London, Vol. 89, pp. A37-40.
- Hudson Bay Mining and Smelting Co. Ltd., 1996. Flin Flon area stress. Internal report.
- Hudson Bay Mining and Smelting Co. Ltd., 2000. Drillhole deviation survey map.
- Hudson Bay Mining and Smelting Co. Ltd., 2001a. Map - Longitudinal view of the Callinan Mine orebody.
- Hudson Bay Mining and Smelting Co. Ltd., 2001b. Map - Longitudinal view of the Trout Lake Mine orebody.
- Hudson Bay Mining and Smelting Co. Ltd., 2001c. Map - Longitudinal view of the Ruttan Mine orebody.
- Hudson, J.A., & Harrison J.P., 1997. Engineering rock Mechanics – An introduction to the principles, Pergamon.
- Hutchinson, D.J. and Diederichs, M.S., 1996. Cablebolting in underground mines. BiTech Publishers Ltd. pp. 265-273.
- Kaiser, P.K., Falmagne, V., Suorineni, F.T., Diederichs, M., Tannant, D.D., 1997. Incorporation of rockmass relaxation and degradation into empirical stope design. CIM AGM 1997, Vancouver.
- Kirsch, G., 1898. Die Theorie der elastizitat und die bedürfnisse der festigkeitslehre, Veit. Ver. Deut. Ing., 42, pp. 797-802.
- Ko, C., 1986. Geology of the Trout Lake copper-zinc sulphide deposit, Hudson Bay Mine and Smelting Co. Ltd.. Unpubl. Co. Report.
- Laubscher, D.H., 1977. Geomechanics classification of jointed rock mass – mining applications. Trans. Inst. Min. Metall., 86, A1 – A8.
- Lauffer, H., 1958. Gebirgsklassifizierung für den stollenbau. geologie und bauwesen, Volume 24, Number 1, pp. 46-51.
- Liu, Q., 1998. Methods and tools for dilution control. Ground Control Bulletin, Issue No. 3, Winter '98-'99.

- HBMS, 2001. Longitudinal View of Callinan Mine Orebody. AutoCAD drawing, Department of engineering, Callinan Mine.
- HBMS, 2001. Longitudinal view of Trout Lake Mine orebody. AutoCAD drawing, Department of Engineering, Trout Lake Mine.
- Mah, S., Pakalnis, R., Poulin, R., Clark, L., 1996. Obtaining quality cavity monitoring survey data, CIM AGM.
- Martin, C.D., Yazici, S., Espley, S., and Tan, G., 2000. Using numerical models to quantify stope dilution. CIM AGM, Toronto, Ontario.
- Mathews, K.E., Hoek, E., Wyllie, D., and Stewart, S.B., 1981. Prediction of stable excavation spans for mining below 1000 metres in hard rock, Canada: CANMET, Dept. of Energy, Mines and Resources, DSS Serial No. OSQ80-00081, DSS File No. 17SQ.23440-0-9020.
- Mercer, J.K., 1980. Some aspect of blasting physics, Quarry Mine & Pit, Vol. 19, No.2.
- Merrill R. H., 1954. Design of underground mine opening, oil shale mine, Rifle, Colorado. Rep. Invest. U.S. Bur. Mines 5089, 56p.
- Miller, F., Potvin, Y., Jacob, D., 1992a. Cavity Monitoring System update and applications, 94th CIM AGM, Montreal, paper #106.
- Miller, F., Potvin, Y., Jacob, D., 1992b. Laser measurement of open stope dilution, CIM Bull., Vol. 85, Jul. – Aug.
- Milne, D., 1997. Underground design and deformation based on surface geometry, Ph.D Thesis, University of British Columbia, Vancouver, Canada.
- Milne, D., Hadjigeorinou, J., and Pakalnis, R., 1998. Rock mass characterization for underground hard rock mines.” Tunnelling and Underground Space Technology, Oct. 1998, vol. 13, no 4, pp 383-391.
- Milne, D., Pakalnis, R. and Lunder, P., 1996a. Approach to the quantification of hanging-wall behaviour, Trans. Inst. Min. Metal., Vol.105, pp. A69-A74.
- Milne, D., Pakalnis, R., and Felderer, M., 1996b. Surface geometry assessment for open stope design, North American Rock Mechanics Symposium, Montreal.
- Mines location map, 2001. Central Mine Engineering, Hudson Bay Mine and Smelting Co. Ltd.
- Morrison , R.G.K., 1970. A philosophy of ground control. Ontario Department of Mines. Toronto, pp. 40-59.

- New report shows offending drillers how to go straight – the hole truth and nothing but ..., Mining Construction, 1-97.
- Nickson, S.D., 1992. Cable support guidelines for underground hard rock mine operations. M.Sc. Thesis, University of British Columbia.
- NTC & Optech Inc., 1997. Cavity Monitory System (CMS) User Manual. Noranda Technology Centre and Optech Systems Inc..
- Obert, L., Duval, W., 1967. Rock mechanics and the design of structure in rock. John Wiley & Sons, Inc.
- Pakalnis, R., 1986. Empirical stope design at the Ruttan Mine, Sherritt Gordon Mines Ltd.. Ph.D. Thesis, University of British Columbia.
- Pakalnis, R., Poulin, R., Hadjigeorgiou, J., 1995a. Quantifying the cost of dilution in underground mines, SME Annual Meeting, Denver, CO.
- Pakalnis, R., Poulin, R., and Vongpaisal, S., 1995b. Quantifying dilution for underground mine operations, CIM AGM, Halifax, N.S.
- Palmström A., 1985. Application of the volumetric joint count as a measure of rock mass jointing. Int. symp. on Fundamentals of Rock Joints, Björkliden, Sweden.
- Palmström, A., 1995. RMi – a rock mass characterization system for rock engineering purposes. PhD thesis, University of Oslo, Department of Geology.
- Pande, G.N., Beer, G., & Williams, J.R., 1990. Numerical methods in rock mechanics, John Wiley & Sons Ltd.
- Peterson, J. and Tannant, D.D., 2001. Wall control blasting practices at the Ekati diamond mine. CIM Bulletin, Vol. 94, No 1050, May.
- Piché, A., Liu, Q., Tran, H., and Van Hijfte, L., 2000. Drilling and blasting research at the Noranda Technology Centre. CIM Bulletin, Vol. 93, No. 1039, April.
- Potvin, Y, Hudyma, M.R. and Miller, H.D.S., 1988. The stability graph method for open stope design. Presented at the 90th CIM AGM, Edmonton, Alberta, May 6th to May 12th.
- Potvin, Y. and Milne, D., 1992. Empirical cable bolt support design, proceedings Rock Support in Mining and Underground Construction. Pp. 269-275, Rotterdam: Balkema.

- Potvin, Y., 1988. Empirical open stope design in Canada. PhD. Thesis, University of British Columbia.
- Potvin, Y., Hudyma, M.R. and Miller, H.D.S., 1988. Stope design. NSERC Project #CRD-8612, Integrated Mine Design Project.
- Potvin, Y., Hudyma, M.R., and Miller, H.D.S., 1989. Design guidelines for open stope support. CIM Bulletin, 82, (926), pp. 53-62.
- Ran, J., 2002. Hanging wall sloughing mechanism in open stope mining, CIM Bulletin, Vol. 95, No. 1064, pp. 74-77.
- Page, C.H., Robert, S. and Kirsten, 1987. Controlled blasting for underground mining. Proceedings of the 13th Conference on Explosives and Blasting Technique, Society of Explosives Engineers. Miami, USA.
- Saada, A.S., 1974. Elasticity theory and applications. Pergamon Press Inc. ISBN 0-08-017972-X.
- Scoble, M.J., Moss, A., 1994. Dilution in underground bulk mining: Implications for production management, mineral resource evaluation II, methods and case histories, Geological Society Publication No. 79, pp. 95-108.
- Sepehr, K. and Stimpson, B., 1988. Roof deflections and sag in jointed, horizontally bedded strata – a numerical study. Rock Mech. And Rock Eng.. 21: 207-218.
- Speakman, D., Chornoby, P., Holmes, G. and Haystead, B. 1976. Geology of the Ruttan deposit. Internal Reports – Sherritt Gordon Mines.
- SPSS for windows software. 1989-1999. SPSS Inc.
- Stauffer, M.R., 1990. The Missi Formation: An Aphebian Molasse deposit in the Reindeer Lake zone of the trans-Hudson orogen. Canada. Geol. Assoc. Canada, Special Paper.
- Stimpson, B., 1989. Ultimate collapse of cross-jointed, thinly bedded horizontal roof strata. International Journal of Min. and Geol. Eng.. 7: 147-162.
- Suorineni, F.T., 1998. Effects of faults and stress on open stope design. PhD. Thesis, University of Waterloo.
- Suorineni, F.T., Tannant D.D. and Kaiser P.K., 1999. Fault factor for the stability graph method of open-stope. Trans. Instn Min. Metall. (Sect. A: Min. industry), 108, May-August.
- Syme, E.C., Bailes, A.H., 1993. Stratigraphic and tectonic settings of early proterozoic

volcanogenic massive sulphide deposits, Flin Flon, Manitoba. *Economic Geology*, Vol. 88.

- Wang, J., Milne, D., Yao, M. and Allen, G., 2002a. Factors influencing stope dilution at Hudson Bay Mining and Smelting, NARMS-TAC 2002, Hammah et al. (eds) University of Toronto, pp. 195-202.
- Wang, J., Milne, D., Yao, M. and Allen, G., 2002b. Quantifying the effect of hanging wall undercutting on stope dilution, CIM AGM, Vancouver, British Columbia.
- Wang, J., Milne, D., Yao, M., Allen, G. and Capes, G., 2003. Open stope exposure time and stope dilution, CIM –AGM 2003, Montreal
- Wiles, T., 1995. Map3D version 35 user's manual, Mine Modelling Limited, Copper Cliff, Ont.
- Willet, M., 2002. Dilution control practice at Trout Lake Mine. PowerPoint presentation. Trout Lake Mine, Flin Flon, Manitoba.
- Yang, R.L., Rocque, P., Katsabanis P. and Bawden, W.F., 1993. Blast damage study by measurement of blast vibration and damage in the area adjacent to blast hole, *Rock Fragmentation by Blasting*, Rossmanith (ed.), Balkema, Rotterdam.
- Yao, M., 2002 and 2003. Personal communications.
- Yao, X., Gary, A., and Willett, M., 1999. Dilution evaluation using Cavity Monitoring System at HBMS – Trout Lake Mine. CIM AGM, Calgary, Alberta.

APPENDIX I

BRIEF DESCRIPTION OF INDIRECT BOUNDARY ELEMENT METHOD (BEM) – FICTITIOUS STRESS METHOD

1. Introduction

Boundary Element Methods (BEM) are useful tools for stress analysis in rock engineering. There are two general types of BEM - direct boundary element method and indirect boundary element method. The direct boundary element method uses the weighted residual approach to obtain the governing equations to formulate boundary elements (Gipson, 1987). The indirect boundary element method uses fictitious stresses on the boundary to formulate boundary elements (Crouch & Starfield, 1983). This appendix is a brief review of fictitious stress method for two dimensional (2D) modelling.

2. Assumptions for the Application of the Method

The assumptions for using the indirect boundary element method – fictitious stress method (2D) are as follows (Hoek and Brown, 1980):

- a. the modelling material is homogeneous, isotropic and linear elastic;
- b. plane strain conditions;
- c. the medium is infinite, or closed by a finite external boundary of arbitrary shape;
- d. the medium may contain a number of holes of arbitrary shape;

- e. the loading may consist of any combination of uniform field stresses or uniformly distributed loads on the boundaries. Gravitational load is simulated by increasing the field stresses with depth.

These conditions cannot be met in the field. Rock does not exist in a perfectly homogeneous, isotropic or purely elastic state. For modelling purposes, a very large volume of rock is considered. It is assumed that the fractures and joints present in the rock mass break the rock into blocks, which can be treated like soil grains if a sufficiently large volume of material is considered. Figure I-1 from Hoek and Brown (1980) demonstrates this approach. This is an idealized approach required to sufficiently simplify rock mass properties for modelling purposes.

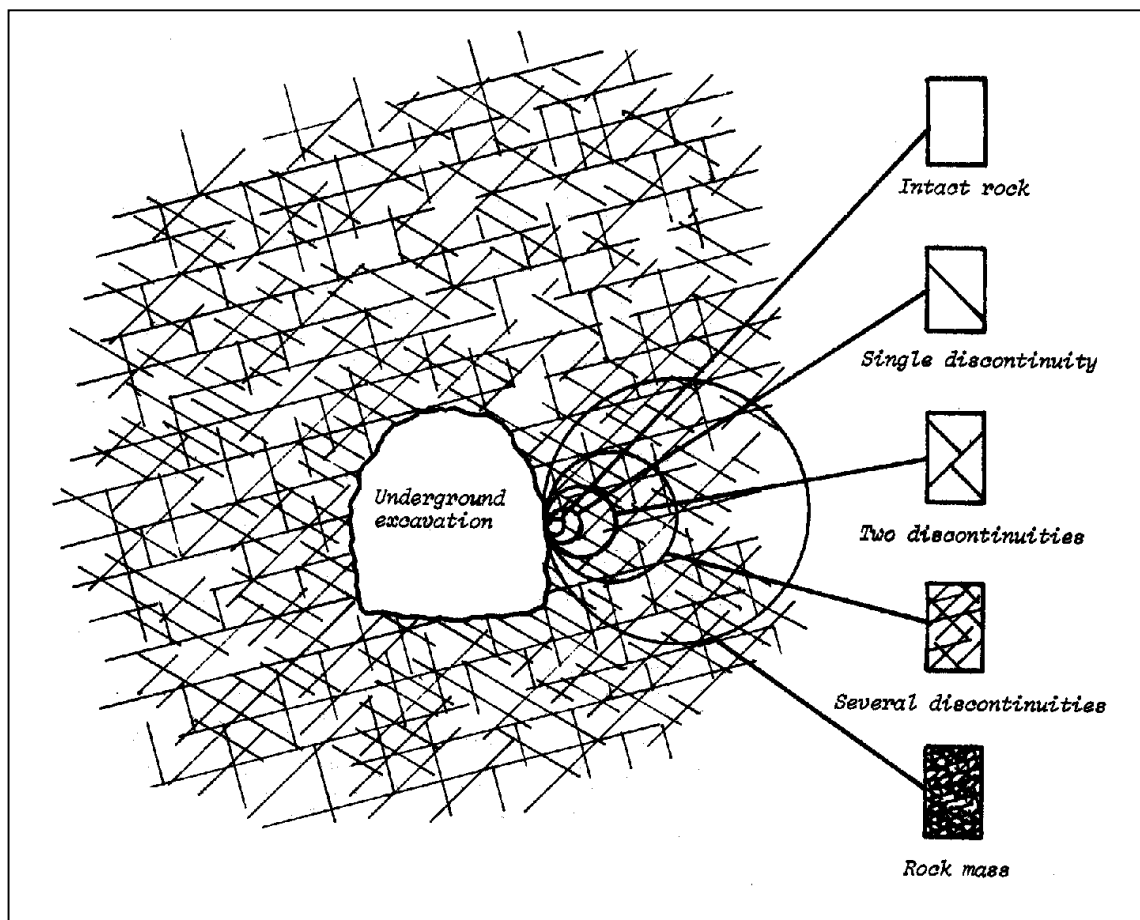


Figure I-1. Idealized diagram showing the transition from intact rock to a heavily jointed rock mass with increasing sample size (from Hoek and Brown, 1980)

3. The Principal of Indirect BEM

An example problem to be solved is as shown in Figure I-2, assuming we know the field stress p_v and p_h . The gravitational stress field can also be considered by giving the p_v (vertical stress) and horizontal stress to vertical stress ratio, K . Much of the following paragraph is taken from Hoek and Brown (1980).

Before an excavation is made, the stresses are evenly distributed in the rock medium (under the homogeneous, isotropic assumptions). The rock that is to be removed provides support for the surrounding rock. This support may be presented in terms of normal and tangential tractions (σ , τ) on the potential boundary of the excavation (Figure I-3). The magnitude of these tractions is the addition of the transformation of field stresses P_v and P_h in the normal and tangential directions to the potential boundary. The magnitude of these tractions will vary from point to point, depending on the orientation of the various parts of the potential boundary. When an excavation (hole) has been made, these tractions are reduced to zero (zero boundary stresses). These can be simulated as being equivalent to applying a system of negative tractions to the boundary of the excavation (Figure I-4). The resultant state of stress can then be considered as the superposition of two stress systems (Figure I-5):

- a. The original uniform stress state due to far field stress P_v and P_h ;
- b. The stresses induced by negative excavation boundary surface tractions ($-\sigma$, $-\tau$).

The problem now becomes to first determine the distribution of induced stresses corresponding to the negative boundary surface tractions.

To solve the problem, first assume that we have another infinite plate, which has a curved section as show in Figure I-6. The curve is divided into a series of elements and the elements are numbered consecutively, 1, 2, 3 ... N. The curve has the same shape as the curve in Figure I-4 which defines a excavation; however, it does not represent a boundary; it only marks the locations of the line segments in an infinite plate that are

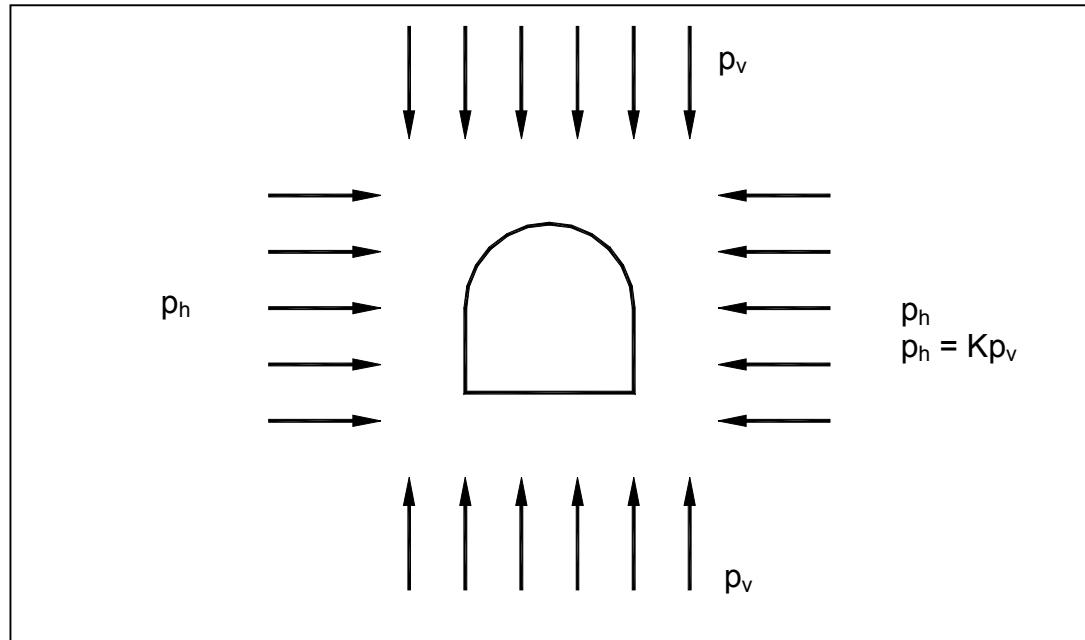


Figure I-2. The problem to be solved (after Hoek and Brown, 1980)

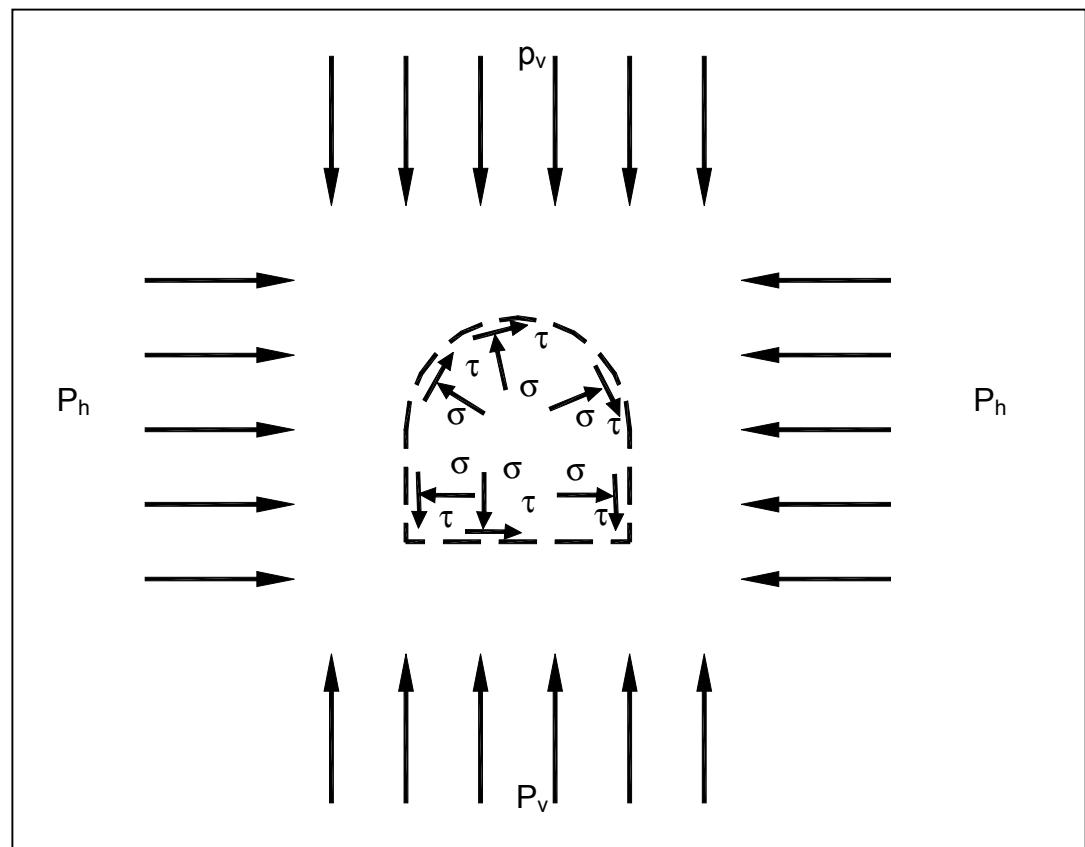


Figure I-3. Traction on potential boundary before excavation (after Hoek and Brown, 1980)

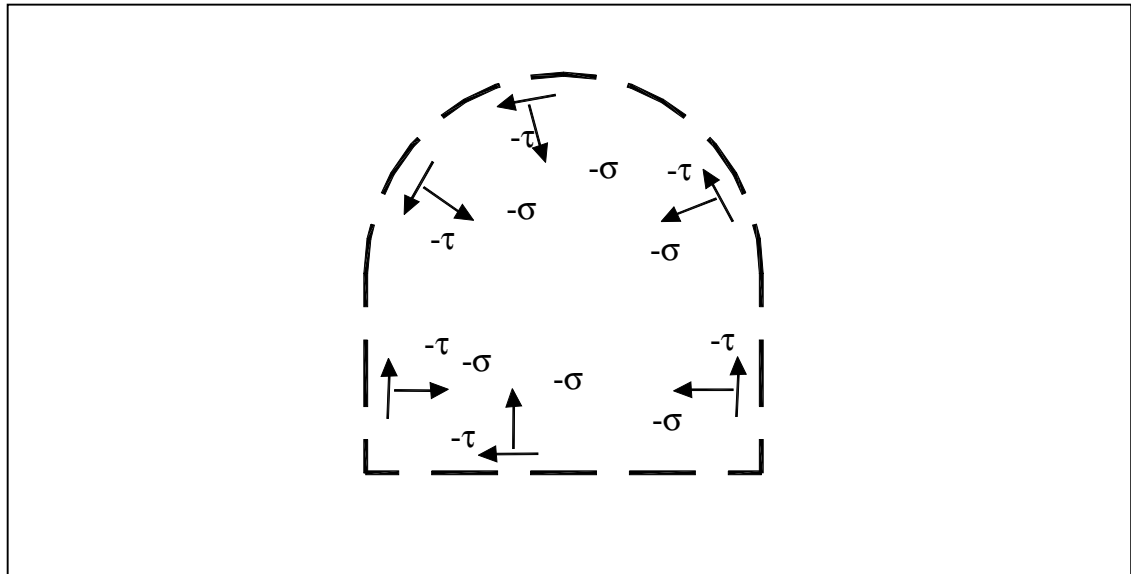


Figure I-4. Negative tractions representing effects of excavation (after Hoek and Brown, 1980)

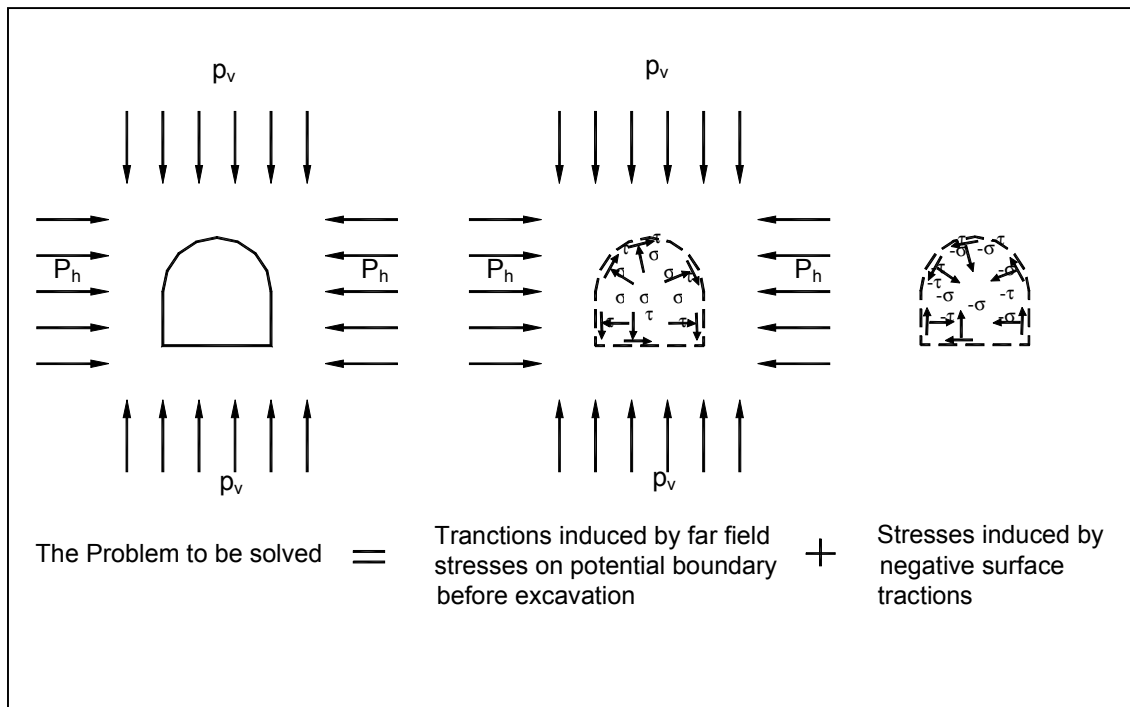


Figure I-5. The approach of solving of the problem - superposition

coincident with the boundary elements on the surface of the excavation in Figure I-4. We now imagine that constant resultant normal and shear stresses are applied to each of the N line segments along the curve. The normal and shear stresses applied to each segment are denoted as P_{nj} and P_{tj} . The stresses are referred to as fictitious stresses.

Since the stresses applied to each segment interact with each other, the stresses applied to the segments in no way correspond to the stresses applied to the boundary of the real plate. Adjustments must be made so that the normal and shear stresses (P_{nj} , P_{tj}) on each element are equal (but with opposite directions) to the corresponding normal and shear stresses (σ_j , τ_j). Standard numerical equations can be found from Crouch and Starfield (1983). The equations are:

$$\left. \begin{aligned} \sigma_i &= \sum_{j=1}^N A_{\sigma t}^{ij} P_t^j + \sum_{j=1}^N A_{\sigma\sigma}^{ij} P_n^j \\ \tau_i &= \sum_{j=1}^N A_{\tau t}^{ij} P_t^j + \sum_{j=1}^N A_{\tau\sigma}^{ij} P_n^j \end{aligned} \right\} \quad i=1 \text{ to } N \quad (\text{I-1})$$

Where, $A_{\sigma t}^{ij}$, $A_{\sigma\sigma}^{ij}$, $A_{\tau t}^{ij}$ and $A_{\tau\sigma}^{ij}$ are the boundary stress influence coefficients. The σ_i and τ_i can be calculated by using suitable transformation equations. They are related to field stress and the orientations of the line elements. By solving the above equations, we will have approximately solved the problem.

In the program, an iterative procedure is used to achieve the stress calculation adjustments. Starting with element 1, the stresses P_{n1} , P_{t1} are adjusted so that $\sigma_1 = -P_{n1}$ and $\tau_1 = -P_{t1}$. We then pass to elements 2, 3 to N in turn and do the similar adjustment. In correcting the values of σ and τ for any given element, we disturb the stresses on all the other elements, and hence the procedure must be continued for a series of cycles around the “boundary” until a pre-determined tolerance is reached.

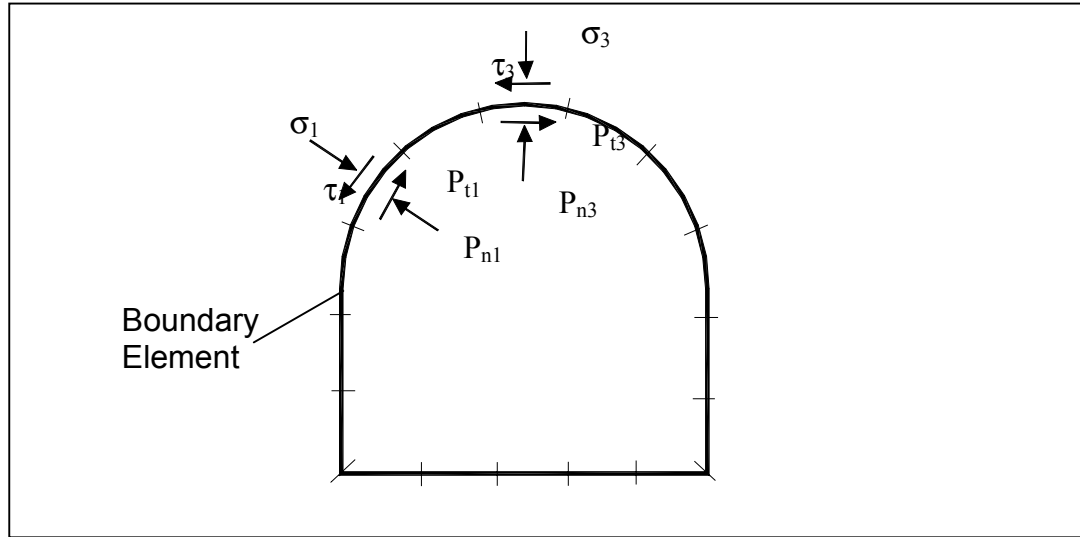


Figure I-6. Illustration of numerical model

Once this process is complete, the distribution of stresses σ_i and τ_i are identical to that of the stresses P_{ni} and P_{ti} . To compute the stresses at any point in the imaginary plate, all that has to be done is to sum the contributions of the various fictitious stresses P_{ni} and P_{ti} ($i = 1$ to N).

Once the stresses due to the negative surface tractions have been determined, they may be added to those of the original stress field (Figure I-5) to give the required stresses following excavation.

APPENDIX II - DATABASE

No.	Mine Name	Stope #	General Info (HW)						
			Strike Length, L (m)	Exposed Height, H (m)	H/L ratio	HR (m)	Dip (degree)	Ore Width (m)	N'
1	Callinan Mine	545-#1	20	26	1.3	5.7	37	3.5	14.2
2	Callinan Mine	580-2	20.3	23.4	1.2	5.4	44	7.3	16.4
3	Callinan Mine	580-3	20	15	0.8	4.3	49	9.9	18
4	Callinan Mine	605-3	32.8	14.2	0.4	5	37	3.6	14.2
5	Callinan Mine	630-6	11	40	3.6	4.3	37	3.6	14.2
6	Callinan Mine	630-7	11	40	3.6	4.3	37	3.6	14.2
7	Callinan Mine	865-5-1	57	26	0.5	8.9	41	5.9	32.3
8	Callinan Mine	865-1-2	22	24	1.1	5.7	56	5.8	39.4
9	Callinan Mine	885-1-1	26.5	33	1.2	7.3	57	3.3	40.2
10	Callinan Mine	885-1-2	25.5	26.4	1.0	6.5	60	5.3	42.5
11	Callinan Mine	885-1-3	33.4	33	1.0	8.3	50	6.7	35.2
12	Callinan Mine	910-1-2	26.8	31	1.2	7.2	75	9.6	54.7
13	Callinan Mine	910-1-3	26.8	32	1.2	7.3	71	11.8	51.3
14	Callinan Mine	910-7-1	13.9	22.2	1.6	4.3	47	2.4	16.6
15	Callinan Mine	920-7-1B	28.5	19.9	0.7	5.9	50	2.3	17.7
16	Callinan Mine	920-7-3	36	20	0.6	6.4	50	3.8	17.7
17	Callinan Mine	935-1-1	31	24	0.8	6.8	68	3.1	48.8
18	Callinan Mine	935-1-2	21	19.5	0.9	5.1	43	5.8	33.6
19	Callinan Mine	935-5-1	20.2	30	1.5	6	43	5.8	33.6
20	Callinan Mine	935-7-2	25	19	0.8	5.4	40	2.2	14.5
21	Callinan Mine	935-7-3	23	22	1.0	5.6	48	6.7	17
22	Callinan Mine	935-7-4	17	20	1.2	4.6	65	8	23.3
23	Callinan Mine	935-7-5	17	19	1.1	4.5	85	5	31.9
24	Callinan Mine	950-7-2	25	22	0.9	5.9	69	8.6	24.9
25	Callinan Mine	950-7-3	23	23	1.0	5.8	65	2.9	23.3
26	Callinan Mine	1075-2	29.5	30	1.0	7.4	45	20.4	20.1
27	Callinan Mine	1075-4	29.5	25.9	0.9	6.9	51	16.8	22.6
28	Callinan Mine	1075-5	16.5	28.4	1.7	5.2	48	8.9	21.3
29	Callinan Mine	1095-2	35.6	32	0.9	8.4	50	16.2	22.1
30	Callinan Mine	1095-6	29.2	26.8	0.9	7	42	4.3	18.9
31	Callinan Mine	1120-1	33	26.2	0.8	7.3	56	9.7	24.8
32	Callinan Mine	1100-2-4	15	10	0.7	3	39	9.3	3.8
33	Callinan Mine	1100-2-5	16.5	13	0.8	3.6	40	9.8	3.9
34	Callinan Mine	545-2	24	24	1.0	6	25	3.5	11.4
35	Callinan Mine	545-3	28	28	1.0	7	28	5.4	12
36	Callinan Mine	650-4	25	35	1.4	7.3	40	3.1	15.1
37	Callinan Mine	845-7-2	55	22	0.4	7.9	75	11.8	60
38	Callinan Mine	865-1-1	33	15	0.5	5.2	60	2.6	46.5
39	Callinan Mine	865-7-3	42	21	0.5	7	55	16.8	38.7
40	Callinan Mine	885-7-4	26	32	1.2	7.2	40	4.7	28.9
41	Callinan Mine	910-7-3	21	22	1.0	5.4	45	3.7	16
42	Callinan Mine	910-7-4	22	28	1.3	6.2	46	5	16.3
43	Callinan Mine	920-7-4	31	24	0.8	6.8	60	3.8	14.2
44	Callinan Mine	77-1100-2-1	18	23	1.3	5	24	11.2	2.9
45	Callinan Mine	865-1-1	33	15	0.5	5.2	60	2.6	35.4
46	Ruttan Mine	630-4B2	33.5	75	2.2	11.6	67	4.9	20.0
47	Ruttan Mine	540-12.5B	20	56	2.8	7.4	85	35	20.0
48	Ruttan Mine	440-0B2	28.6	44	1.5	8.7	75	13	20.1
49	Ruttan Mine	1050-29J6	23.5	67	2.9	8.7	70	24	15.0
50	Ruttan Mine	550-28JS	36	85	2.4	12.6	70	9.5	12.9
51	Ruttan Mine	440-5B2	19	47	2.5	6.8	65	13	14.6
52	Ruttan Mine	440-1B2	23	35	1.5	6.9	50	7	5.0
53	Ruttan Mine	590-14B	25	50	2.0	8.3	89	12	36.2
54	Trout Lake Mine	840-N9-4	21	40.2	1.9	6.9	66	3.4	10.5
55	Trout Lake Mine	950-W1-2	12.8	36.6	2.9	4.7	65	6	12
56	Trout Lake Mine	1070-W2-7	19	45	2.4	6.7	48	2.2	8.7
57	Trout Lake Mine	950-N12-1	22.2	38	1.7	7	60	4.2	8.1
58	Trout Lake Mine	810-N10-5	18.4	45.2	2.5	6.5	51	8.2	9.3
59	Trout Lake Mine	1040-H1-4	18.4	45.2	2.5	6.5	51	8.2	9.3
60	Trout Lake Mine	950-W1-4	24.4	37.6	1.5	7.4	60	4.7	11
61	Trout Lake Mine	950-N12-3	26.4	44.4	1.7	8.3	51	3.4	6.8
62	Trout Lake Mine	980-N11-1	20.3	34	1.7	6.4	56	3.9	7.1

APPENDIX II DATABASE

No.	Mine Name	Stope #	General Info (HW)						
			Strike Length, L (m)	Exposed Height, H (m)	H/L ratio	HR (m)	Dip (degree)	Ore Width (m)	N'
63	Trout Lake Mine	980-N12-2	30.9	40.6	1.3	8.8	52	1.9	7
64	Trout Lake Mine	950-W1-3	24	36.8	1.5	7.3	60	5.1	11
65	Trout Lake Mine	840-M3-2	21.6	38.6	1.8	6.9	60	6	9.5
66	Trout Lake Mine	1010-N9-1	31.6	45.2	1.4	9.3	58	3.2	7.1
67	Trout Lake Mine	980-N11-3	24	32	1.3	6.9	68	5.1	8.8
68	Trout Lake Mine	810-N10-4	24	39.2	1.6	7.4	61	4.4	11.1
69	Trout Lake Mine	870-N11-1	15.7	46.2	2.9	5.9	55	5.6	7
70	Trout Lake Mine	950-N12-2	24	41	1.7	7.6	58	5	7.8
71	Trout Lake Mine	980W1-6	39.7	36.8	0.9	9.5	71	2.5	13.2
72	Trout Lake Mine	900 M3 3	23.4	34	1.5	6.9	67	52	10.7
73	Trout Lake Mine	980 W1 2	22	36	1.6	6.8	59	5.6	10.8
74	Trout Lake Mine	1010N11 6	20.8	37.8	1.8	6.7	68	4.9	8.8
75	Trout Lake Mine	1010N9 2	17.4	42.8	2.5	6.2	65	4.8	8
76	Trout Lake Mine	980N11 2	23.7	31.2	1.3	6.7	67	5.3	8.7
77	Trout Lake Mine	980N12 3	23.8	40.6	1.7	7.5	51	5	6.8
78	Trout Lake Mine	865M3 3	18.4	44	2.4	6.5	47	4.8	7.4
79	Trout Lake Mine	1010N11 5	27	44	1.6	8.4	64	3.6	8.2
80	Trout Lake Mine	840M1 3	24	35.4	1.5	7.2	69	6	9.5
81	Trout Lake Mine	840N9-2	20.8	37.8	1.8	6.7	55	14.4	6.7
82	Trout Lake Mine	980N12 4	24.7	38.2	1.5	7.5	56	4.4	7.5
83	Trout Lake Mine	980W1 5	20.4	39.6	1.9	6.7	50	9.2	9.1
84	Trout Lake Mine	810N5 1	12.4	38.8	3.1	4.7	54	7.6	8.5
85	Trout Lake Mine	1070W2 6	22	41	1.9	7.2	51	3.4	7.3
86	Trout Lake Mine	10193	16.8	40	2.4	5.9	66	4.9	8.2
87	Trout Lake Mine	101114	20.6	46.2	2.2	7.1	53	6.5	6.7
88	Trout Lake Mine	10186	23.4	33.6	1.4	6.9	68	3.3	12.6
89	Trout Lake Mine	10181	24.8	38.4	1.5	7.5	62	7.6	11.4
90	Trout Lake Mine	8491	20.8	40.6	2.0	6.9	63	6	7.8
91	Trout Lake Mine	9883	14.2	34.6	2.4	5	59	6.3	10.8
92	Trout Lake Mine	8152	23.4	37.2	1.6	7.2	51	5.9	8
93	Trout Lake Mine	8454	19.8	37.4	1.9	6.5	77	8.5	12.6
94	Trout Lake Mine	81103	21.4	34.5	1.6	6.6	66	4.3	12.2
95	Trout Lake Mine	9884	24.2	40	1.7	7.5	50	6.6	9.1
96	Trout Lake Mine	8433	17.5	37	2.1	5.9	62	9.7	9.8
97	Trout Lake Mine	101113	19.3	42.6	2.2	6.6	62	9.9	7.9
98	Trout Lake Mine	98125	31.3	34.4	1.1	8.2	63	3.8	8.5
99	Trout Lake Mine	10182	20.8	37.5	1.8	6.7	62	8.9	11.4
100	Trout Lake Mine	8412	15.5	38	2.5	5.5	75	7.6	12.2
101	Trout Lake Mine	101122	25.8	33.4	1.3	7.3	50	3.5	6.7
102	Trout Lake Mine	8411	18.8	37	2.0	6.2	74	4.4	12
103	Trout Lake Mine	87112	30.5	44.6	1.5	9.1	75	4.6	9.9
104	Trout Lake Mine	81102	16.6	30.8	1.9	5.4	75	7.4	14.1
105	Trout Lake Mine	101112	19.6	42.7	2.2	6.7	64	5.4	8.2
106	Trout Lake Mine	10488	22.3	32.6	1.5	6.6	73	4.7	13.7
107	Trout Lake Mine	101123	27.4	37	1.4	7.9	55	3.4	7
108	Trout Lake Mine	10183	13.2	40.4	3.1	5	57	11.1	10.4
109	Trout Lake Mine	8792	17.2	39.1	2.3	6	73	10.7	9.2
110	Trout Lake Mine	8452	20	41.8	2.1	6.8	65	6.9	10.3
111	Trout Lake Mine	10184	27.8	42	1.5	8.4	54	5.2	9.8
112	Trout Lake Mine	7031	36.7	20.7	0.6	6.6	75	10	12.2
113	Trout Lake Mine	8753	15.4	39	2.5	5.5	70	10.5	11.2
114	Trout Lake Mine	10185	16	37	2.3	5.6	72	8.9	13.5
115	Trout Lake Mine	8793	19.8	36	1.8	6.4	66	9.4	8.2
116	Trout Lake Mine	8451\1	15	34	2.3	5.2	69	6.2	11.1
117	Trout Lake Mine	1048\2	13.8	37.4	2.7	5	61	6.5	11.1
118	Trout Lake Mine	8410\2	24.2	37.8	1.6	7.4	61	9.1	11.1
119	Trout Lake Mine	1048\1	26	34.4	1.3	7.4	62	7.2	11.4
120	Trout Lake Mine	7311	35.3	35	1.0	8.8	60	4.6	9.5
121	Trout Lake Mine	8791\4	27.4	39.4	1.4	8.1	58	6.7	7.1
122	Trout Lake Mine	8791\3	27.4	39.4	1.4	8.1	58	6.7	7.1
123	Trout Lake Mine	1048\5	14	34	2.4	5	64	8.2	11.8
124	Trout Lake Mine	8754	17.7	42	2.4	6.2	69	6.3	11.1
125	Trout Lake Mine	1078\1	20.5	34.9	1.7	6.5	63	8.4	11.6
126	Trout Lake Mine	8791\E	25.4	43	1.7	8	52	8.4	6.3
127	Trout Lake Mine	1048\3	21.5	40	1.9	7	54	12.7	9.8

APPENDIX II DATABASE

No.	Mine Name	Stope #	General Info (HW)						
			Strike Length, L (m)	Exposed Height, H (m)	H/L ratio	HR (m)	Dip (degree)	Ore Width (m)	N'
128	Trout Lake Mine	84105	37.6	33.4	0.9	8.8	66	10.8	12.2
129	Trout Lake Mine	84103	22	30	1.4	6.3	65	5.2	12
130	Trout Lake Mine	10782	20	30	1.5	6	58	10	10.6
131	Trout Lake Mine	87102	25	44	1.8	8	62	10	11.4
132	Trout Lake Mine	10486	23	35	1.5	6.9	72	4.3	13.5
133	Trout Lake Mine	10783	25	37	1.5	7.5	54	10.4	9.8
134	Trout Lake Mine	84104	20	30	1.5	6	60	5	11
135	Trout Lake Mine	10484	22	36	1.6	6.8	67	22.4	12.4
136	Trout Lake Mine	9051#1	30	35	1.2	8.1	64	7	10.1
137	Trout Lake Mine	6451b	28	32	1.1	7.5	63	8	10
138	Trout Lake Mine	6451	30	21	0.7	6.2	60	5.5	9.5
139	Trout Lake Mine	1010H1-4	24.7	25.5	1.0	6.3	65	6.9	10.3
140	Trout Lake Mine	875C2F-8	24	24.3	1.0	6	62	8.4	8.2
141	Trout Lake Mine	950N5-1	25	26	1.0	6.4	72	8.6	11.6
142	Trout Lake Mine	765C2-1	20	25.2	1.3	5.6	58	8	7.7
143	Trout Lake Mine	765C2-5	21	24.5	1.2	5.7	62	13	8.2
144	Trout Lake Mine	980N9-2	20.2	26.2	1.3	5.7	70	7.7	9.1
145	Trout Lake Mine	1040H1-6/7	45	27.1	0.6	8.5	55	5.2	8.2
146	Trout Lake Mine	810N10-7	24.8	31.4	1.3	6.9	57	9.6	10.4
147	Trout Lake Mine	950N9-2	20	26.9	1.3	5.7	80	6.5	10.6
148	Trout Lake Mine	950W1-6	23.5	28.5	1.2	6.4	60	6.8	9.5
149	Trout Lake Mine	980N11-6	17.4	27.4	1.6	5.3	78	5.4	12.8
150	Trout Lake Mine	920N12-3	22.5	23.3	1.0	5.7	58	5	9.9

APPENDIX II DATABASE

No.	Mine Name	Stope #	Undercutting						
			U/C Drift					O/C Drift	
			% of u/c along strike	Max. depth (m)	Avg. depth _strike (m)	u/c length along strike (m)	Avg.depth _u/c portion (m)	% of u/c along strike	Max. depth (m)
1	Callinan Mine	545-#1	0%	0	0.0	0.0	0.0	0.7	3.4
2	Callinan Mine	580-2	0%	0	0.0	0.0	0.0	0.8	2.3
3	Callinan Mine	580-3	10%	1.7	0.1	2.0	1.0	100%	1.5
4	Callinan Mine	605-3	80%	1.8	0.7	26.2	0.9	100%	1.8
5	Callinan Mine	630-6	50%	1	0.5	5.5	1.0	0%	0
6	Callinan Mine	630-7	0%	0	0.0	0.0	0.0	100%	0.7
7	Callinan Mine	865-5-1	100%	1.5	0.2	57.0	0.2	50%	1
8	Callinan Mine	865-1-2	30%	1	1.0	6.6	3.3	0%	0
9	Callinan Mine	885-1-1	100%	2	0.7	26.5	0.7	0%	0
10	Callinan Mine	885-1-2	0%	0	0.0	0.0	0.0	0%	0
11	Callinan Mine	885-1-3	10%	0.6	0.6	3.3	6.0	0%	0
12	Callinan Mine	910-1-2	0%	0	0.0	0.0	0.0	0%	0
13	Callinan Mine	910-1-3	0%	0	0.0	0.0	0.0	0%	0
14	Callinan Mine	910-7-1	100%	1.2	1.0	13.9	1.0	0%	0
15	Callinan Mine	920-7-1B	0%	0	0.0	0.0	0.0	100%	0.9
16	Callinan Mine	920-7-3	100%	2.5	1.1	36.0	1.1	60%	2
17	Callinan Mine	935-1-1	0%	0	0.0	0.0	0.0	0%	0
18	Callinan Mine	935-1-2	100%	1.3	1.0	21.0	1.0	100%	1
19	Callinan Mine	935-5-1	100%	4.2	2.1	20.2	2.1	0%	0
20	Callinan Mine	935-7-2	100%	1.6	0.9	25.0	0.9	0%	0
21	Callinan Mine	935-7-3	100%	3	1.4	23.0	1.4	100%	2.8
22	Callinan Mine	935-7-4	30%	3	0.2	5.1	0.7	0%	0
23	Callinan Mine	935-7-5	100%	4	3.5	17.0	3.5	100%	1
24	Callinan Mine	950-7-2	0%	0	0.0	0.0	0.0	0%	0
25	Callinan Mine	950-7-3	0%	0	0.0	0.0	0.0	0%	0
26	Callinan Mine	1075-2	80%	1.5	0.8	23.6	1.0	70%	1.5
27	Callinan Mine	1075-4	0%	0	0.0	0.0	0.0	0%	0
28	Callinan Mine	1075-5	60%	1	0.4	9.9	0.7	0%	0
29	Callinan Mine	1095-2	95%	1.6	1.0	33.8	1.1	0%	0
30	Callinan Mine	1095-6	0%	0	0.0	0.0	0.0	0%	0
31	Callinan Mine	1120-1	0%	0	0.0	0.0	0.0	0%	0
32	Callinan Mine	1100-2-4	0%	0	0.0	0.0	0.0	0%	0
33	Callinan Mine	1100-2-5	0%	0	0.0	0.0	0.0	100%	1.5
34	Callinan Mine	545-2	90%	7	2.0	21.6	2.2	0%	0
35	Callinan Mine	545-3	0%	0	0.0	0.0	0.0	0%	0
36	Callinan Mine	650-4	30%	5	1.2	7.5	4.0	60%	2.5
37	Callinan Mine	845-7-2	50%	2.5	1.1	27.5	2.2	0%	0
38	Callinan Mine	865-1-1	0%	0	0.0	0.0	0.0	0%	0
39	Callinan Mine	865-7-3	20%	2	0.2	8.4	1.0	0%	0
40	Callinan Mine	885-7-4	0%	0	0.0	0.0	0.0	0%	0
41	Callinan Mine	910-7-3	0%	0	0.0	0.0	0.0	0%	0
42	Callinan Mine	910-7-4	100%	1	0.5	22.0	0.5	0%	0
43	Callinan Mine	920-7-4	50%	3	1.5	15.5	3.0	0%	0
44	Callinan Mine	77-1100-2-	0%	0	0.0	0.0	0.0	0%	0
45	Callinan Mine	865-1-1	0%	0	0.0	0.0	0.0	0%	0
46	Ruttan Mine	630-4B2	100%	4	1.3	33.5	1.3	100%	1
47	Ruttan Mine	540-12.5B	0%	0	0	0.0	0.0	0%	0
48	Ruttan Mine	440-0B2	0%	0	0	0.0	0.0	0%	0
49	Ruttan Mine	1050-29J6	0%	0	0	0.0	0.0	0%	0
50	Ruttan Mine	550-28JS	0%	0	0	0.0	0.0	100%	4
51	Ruttan Mine	440-5B2	0%	0	0	0.0	0.0	0%	0
52	Ruttan Mine	440-1B2	0%	0	0	0.0	0.0	0%	0
53	Ruttan Mine	590-14B	0%	0	0	0.0	0.0	0%	0
54	Trout Lake Mine	840-N9-4	20%	0.4	0.1	4.2	0.5	20%	2
55	Trout Lake Mine	950-W1-2	57%	2.2	0.6	7.3	1.1	100%	1
56	Trout Lake Mine	1070-W2-7	20%	1.8	0.3	3.8	1.5	0%	0
57	Trout Lake Mine	950-N12-1	13%	1.2	0.1	2.9	0.8	80%	2.3
58	Trout Lake Mine	810-N10-5	63%	3.8	1.1	11.6	1.7	0%	0
59	Trout Lake Mine	1040-H1-4	0%	0	0.0	0.0	0.0	0%	0
60	Trout Lake Mine	950-W1-4	64%	3.8	1.2	15.6	1.9	60%	1.3
61	Trout Lake Mine	950-N12-3	37%	1.4	0.2	9.8	0.5	0%	0
62	Trout Lake Mine	980-N11-1	0%	0	0.0	0.0	0.0	0%	0

APPENDIX II DATABASE

No.	Mine Name	Stope #	Undercutting						
			U/C Drift					O/C Drift	
			% of u/c along strike	Max. depth (m)	Avg. depth _strike (m)	u/c length along strike (m)	Avg.depth _u/c portion (m)	% of u/c along strike	Max. depth (m)
63	Trout Lake Mine	980-N12-2	0%	0	0.0	0.0	0.0	0%	0
64	Trout Lake Mine	950-W1-3	70%	1.5	0.8	16.8	1.1	75%	2
65	Trout Lake Mine	840-M3-2	50%	6	1.5	10.8	3.0	0%	0
66	Trout Lake Mine	1010-N9-1	90%	0.7	0.4	28.4	0.4	100%	1.5
67	Trout Lake Mine	980-N11-3	62%	2.8	0.8	14.9	1.3	30%	2.5
68	Trout Lake Mine	810-N10-4	85%	2	0.8	20.4	0.9	0%	0
69	Trout Lake Mine	870-N11-1	65%	5.5	1.4	10.2	2.2	0%	0
70	Trout Lake Mine	950-N12-2	50%	1.4	0.6	12.0	1.2	0%	0
71	Trout Lake Mine	980W1-6	85%	10.2	2.2	33.7	2.6	20%	1.2
72	Trout Lake Mine	900 M3 3	15%	2.9	0.4	3.5	2.7	20%	1.2
73	Trout Lake Mine	980 W1 2	0%	0	0.0	0.0	0.0	0%	0
74	Trout Lake Mine	1010N11 6	0%	0	0.0	0.0	0.0	0%	0
75	Trout Lake Mine	1010N9 2	100%	1.5	0.6	17.4	0.6	25%	1.3
76	Trout Lake Mine	980N11 2	0%	0	0.0	0.0	0.0	0%	0
77	Trout Lake Mine	980N12 3	0%	0	0.0	0.0	0.0	15%	1.5
78	Trout Lake Mine	865M3 3	20%	2	0.4	3.7	2.0	25%	6
79	Trout Lake Mine	1010N11 5	0%	5.5	0.0	0.0	0.0	0%	0
80	Trout Lake Mine	840M1 3	0%	0	0.0	0.0	0.0	0%	0
81	Trout Lake Mine	840N9-2	15%	4.4	0.5	3.1	3.3	0%	0
82	Trout Lake Mine	980N12 4	90%	2.4	1.2	22.2	1.3	0%	0
83	Trout Lake Mine	980W1 5	0%	0	0.0	0.0	0.0	0%	0
84	Trout Lake Mine	810N5 1	60%	4	1.8	7.4	3.0	100%	1
85	Trout Lake Mine	1070W2 6	95%	2	0.7	20.9	0.7	90%	3
86	Trout Lake Mine	10193	50%	0.6	0.2	8.4	0.4	0%	0
87	Trout Lake Mine	101114	40%	0.6	0.1	8.2	0.3	0%	0
88	Trout Lake Mine	10186	25%	2.6	0.3	5.9	1.2	0%	0
89	Trout Lake Mine	10181	75%	4.2	1.0	18.6	1.3	50%	2
90	Trout Lake Mine	8491	50%	2.8	0.6	10.4	1.2	30%	3.5
91	Trout Lake Mine	9883	90%	0.5	0.2	12.8	0.2	60%	2
92	Trout Lake Mine	8152	50%	1.6	0.6	11.7	1.2	100%	1.5
93	Trout Lake Mine	8454	30%	2.4	0.6	5.9	2.0	0%	0
94	Trout Lake Mine	81103	100%	1.8	1.0	21.4	1.0	60%	1.2
95	Trout Lake Mine	9884	60%	1.8	0.4	14.5	0.7	0%	0
96	Trout Lake Mine	8433	10%	4	0.3	1.8	3.0	0%	0
97	Trout Lake Mine	101113	50%	3.6	0.9	9.7	1.8	0%	0
98	Trout Lake Mine	98125	0%	0	0.0	0.0	0.0	50%	3
99	Trout Lake Mine	10182	50%	1.2	0.5	10.4	1.0	0%	0
100	Trout Lake Mine	8412	0%	0	0.0	0.0	0.0	100%	3.5
101	Trout Lake Mine	101122	0%	0	0.0	0.0	0.0	0%	0
102	Trout Lake Mine	8411	0%	0	0.0	0.0	0.0	0%	0
103	Trout Lake Mine	87112	25%	1.4	0.2	7.6	0.8	0%	0
104	Trout Lake Mine	81102	55%	1.8	0.6	9.1	1.1	0%	0
105	Trout Lake Mine	101112	60%	1.3	0.6	11.8	1.0	10%	3
106	Trout Lake Mine	10488	0%	0	0.0	0.0	0.0	0%	0
107	Trout Lake Mine	101123	0%	0	0.0	0.0	0.0	0%	0
108	Trout Lake Mine	10183	0%	0	0.0	0.0	0.0	0%	0
109	Trout Lake Mine	8792	45%	8	1.1	7.7	2.4	0%	0
110	Trout Lake Mine	8452	50%	4	1.5	10.0	3.0	20%	2
111	Trout Lake Mine	10184	100%	2.7	1.8	27.8	1.8	0%	0
112	Trout Lake Mine	7031	100%	1.9	1.4	36.7	1.4	0%	0
113	Trout Lake Mine	8753	100%	1.8	1.2	15.4	1.2	70%	3
114	Trout Lake Mine	1018\5	20%	2	0.1	3.2	0.5	0%	0
115	Trout Lake Mine	8793	100%	1.8	0.6	19.8	0.6	30%	3
116	Trout Lake Mine	8451\1	100%	8	4.9	15.0	4.9	15%	4
117	Trout Lake Mine	1048\2	50%	1.6	0.5	6.9	1.0	60%	3
118	Trout Lake Mine	8410\2	100%	2.4	1.3	24.2	1.3	30%	1
119	Trout Lake Mine	1048\1	0%	0	0.0	0.0	0.0	100%	1.1
120	Trout Lake Mine	7311	0%	0	0.0	0.0	0.0	100%	3
121	Trout Lake Mine	8791\4	45%	1.8	1.0	12.3	2.2	0%	0
122	Trout Lake Mine	8791\3	45%	1.8	1.0	12.3	2.2	0%	0
123	Trout Lake Mine	1048\5	50%	3	0.8	7.0	1.6	0%	0
124	Trout Lake Mine	8754	100%	5.8	2.4	17.7	2.4	0%	0
125	Trout Lake Mine	1078\1	30%	2.2	0.5	6.2	1.7	100%	2
126	Trout Lake Mine	8791\E	0%	0	0.0	0.0	0.0	80%	5
127	Trout Lake Mine	1048\3	90%	10.1	2.7	19.4	3.0	100%	3.2

APPENDIX II DATABASE

No.	Mine Name	Stope #	Undercutting						
			U/C Drift					O/C Drift	
			% of u/c along strike	Max. depth (m)	Avg. depth _strike (m)	u/c length along strike (m)	Avg.depth _u/c portion (m)	% of u/c along strike	Max. depth (m)
128	Trout Lake Mine	84105	50%	1.6	0.6	18.8	1.2	0%	0
129	Trout Lake Mine	8410\3	60%	2.5	0.8	13.2	1.3	100%	3
130	Trout Lake Mine	1078\2	15%	1.5	0.1	3.0	0.7	0%	0
131	Trout Lake Mine	87102	70%	1.5	0.6	17.5	0.9	100%	2.5
132	Trout Lake Mine	10486	70%	3.5	1.5	16.1	2.1	80%	1
133	Trout Lake Mine	10783	100%	3	1.0	25.0	1.0	0%	0
134	Trout Lake Mine	84104	30%	3.5	0.6	6.0	2.0	0%	0
135	Trout Lake Mine	10484	0%	0	0.0	0.0	0.0	0%	0
136	Trout Lake Mine	9051#1	80%	3	1.2	24.0	1.5	40%	1.2
137	Trout Lake Mine	6451b	70%	3.5	2.0	19.6	2.9	0%	0
138	Trout Lake Mine	6451	20%	2	0.2	6.0	1.0	100%	3.5
139	Trout Lake Mine	1010H1-4	0%	0	0.0	0.0	0.0	50%	2.5
140	Trout Lake Mine	875C2F-8	20%	3	0.2	4.8	1.0	0%	0
141	Trout Lake Mine	950N5-1	30%	3	0.7	7.5	2.3	0%	0
142	Trout Lake Mine	765C2-1	50%	1.6	0.8	10.0	1.6	100%	0.7
143	Trout Lake Mine	765C2-5	0%	0	0.0	0.0	0.0	0%	0
144	Trout Lake Mine	980N9-2	55%	5	1.5	11.1	2.7	45%	2
145	Trout Lake Mine	1040H1-6/7	20%	2.2	0.3	9.0	1.5	0%	0
146	Trout Lake Mine	810N10-7	0%	0	0.0	0.0	0.0	0%	0
147	Trout Lake Mine	950N9-2	25%	2.5	0.3	5.0	1.2	0%	0
148	Trout Lake Mine	950W1-6	35%	2	0.6	8.2	1.7	0%	0
149	Trout Lake Mine	980N11-6	100%	2	1.6	17.4	1.6	30%	1
150	Trout Lake Mine	920N12-3	100%	3.5	2.0	22.5	2.0	35%	1

APPENDIX II DATABASE

No.	Mine Name	Stope #	Undercutting (cont.d)					
			O/C Drift (cont'd)			Overall		
			Avg. depth _strike (m)	u/c length along strike (m)	Avg. depth _u/c portion (m)	Portion of u/c along perimeter	Avg. depth in u/c portion (m)	Overall avg. depth u/c_strike (m)
1	Callinan Mine	545-#1	3	14.0	4.29	0.15	2.14	1.5
2	Callinan Mine	580-2	1.5	16.2	1.88	0.19	0.94	0.75
3	Callinan Mine	580-3	1.3	20.0	1.30	0.31	1.15	0.7
4	Callinan Mine	605-3	1.2	32.8	1.20	0.63	1.04	0.95
5	Callinan Mine	630-6	0	0.0	0.00	0.05	0.50	0.25
6	Callinan Mine	630-7	0.6	11.0	0.60	0.11	0.30	0.3
7	Callinan Mine	865-5-1	0.2	28.5	0.40	0.52	0.30	0.2
8	Callinan Mine	865-1-2	0	0.0	0.00	0.07	1.67	0.5
9	Callinan Mine	885-1-1	0	0.0	0.00	0.22	0.35	0.35
10	Callinan Mine	885-1-2	0	0.0	0.00	0.00	0.00	0
11	Callinan Mine	885-1-3	0	0.0	0.00	0.03	3.00	0.3
12	Callinan Mine	910-1-2	0	0.0	0.00	0.00	0.00	0
13	Callinan Mine	910-1-3	0	0.0	0.00	0.00	0.00	0
14	Callinan Mine	910-7-1	0	0.0	0.00	0.19	0.50	0.5
15	Callinan Mine	920-7-1B	0.6	28.5	0.60	0.29	0.30	0.3
16	Callinan Mine	920-7-3	0.8	21.6	1.33	0.51	1.22	0.95
17	Callinan Mine	935-1-1	0	0.0	0.00	0.00	0.00	0
18	Callinan Mine	935-1-2	0.5	21.0	0.50	0.52	0.75	0.75
19	Callinan Mine	935-5-1	0	0.0	0.00	0.20	1.05	1.05
20	Callinan Mine	935-7-2	0	0.0	0.00	0.28	0.45	0.45
21	Callinan Mine	935-7-3	1.2	23.0	1.20	0.51	1.30	1.3
22	Callinan Mine	935-7-4	0	0.0	0.00	0.07	0.33	0.1
23	Callinan Mine	935-7-5	0.8	17.0	0.80	0.47	2.15	2.15
24	Callinan Mine	950-7-2	0	0.0	0.00	0.00	0.00	0
25	Callinan Mine	950-7-3	0	0.0	0.00	0.00	0.00	0
26	Callinan Mine	1075-2	0.6	20.7	0.86	0.37	0.93	0.7
27	Callinan Mine	1075-4	0	0.0	0.00	0.00	0.00	0
28	Callinan Mine	1075-5	0	0.0	0.00	0.11	0.33	0.2
29	Callinan Mine	1095-2	0	0.0	0.00	0.25	0.53	0.5
30	Callinan Mine	1095-6	0	0.0	0.00	0.00	0.00	0
31	Callinan Mine	1120-1	0	0.0	0.00	0.00	0.00	0
32	Callinan Mine	1100-2-4	0	0.0	0.00	0.00	0.00	0
33	Callinan Mine	1100-2-5	0.8	16.5	0.80	0.28	0.40	0.4
34	Callinan Mine	545-2	0	0.0	0.00	0.23	1.11	1
35	Callinan Mine	545-3	0	0.0	0.00	0.00	0.00	0
36	Callinan Mine	650-4	0.7	15.0	1.17	0.19	2.58	0.95
37	Callinan Mine	845-7-2	0	0.0	0.00	0.18	1.10	0.55
38	Callinan Mine	865-1-1	0	0.0	0.00	0.00	0.00	0
39	Callinan Mine	865-7-3	0	0.0	0.00	0.07	0.50	0.1
40	Callinan Mine	885-7-4	0	0.0	0.00	0.00	0.00	0
41	Callinan Mine	910-7-3	0	0.0	0.00	0.00	0.00	0
42	Callinan Mine	910-7-4	0	0.0	0.00	0.22	0.25	0.25
43	Callinan Mine	920-7-4	0	0.0	0.00	0.14	1.50	0.75
44	Callinan Mine	777-1100-2-12	0	0.0	0.00	0.00	0.00	0
45	Callinan Mine	865-1-1	0	0.0	0.00	0.00	0.00	0
46	Ruttan Mine	630-4B2	0.5	33.5	0.50	0.31	0.90	0.9
47	Ruttan Mine	540-12.5B	0	0.0	0.00	0.00	0.00	0
48	Ruttan Mine	440-0B2	0	0.0	0.00	0.00	0.00	0
49	Ruttan Mine	1050-29J6	0	0.0	0.00	0.00	0.00	0
50	Ruttan Mine	550-28JS	3	36.0	3.00	0.15	1.50	1.5
51	Ruttan Mine	440-5B2	0	0.0	0.00	0.00	0.00	0
52	Ruttan Mine	440-1B2	0	0.0	0.00	0.00	0.00	0
53	Ruttan Mine	590-14B	0	0.0	0.00	0.00	0.00	0
54	Trout Lake Mine	840-N9-4	0.1	4.2	0.50	0.07	0.50	0.1
55	Trout Lake Mine	950-W1-2	0.8	12.8	0.80	0.20	0.93	0.7
56	Trout Lake Mine	1070-W2-7	0	0.0	0.00	0.03	0.75	0.15
57	Trout Lake Mine	950-N12-1	0.5	17.8	0.63	0.17	0.70	0.3
58	Trout Lake Mine	810-N10-5	0	0.0	0.00	0.09	0.87	0.55
59	Trout Lake Mine	1040-H1-4	0	0.0	0.00	0.00	0.00	0
60	Trout Lake Mine	950-W1-4	0.9	14.6	1.50	0.24	1.69	1.05
61	Trout Lake Mine	950-N12-3	0	0.0	0.00	0.07	0.27	0.1
62	Trout Lake Mine	980-N11-1	0	0.0	0.00	0.00	0.00	0

APPENDIX II DATABASE

No.	Mine Name	Stope #	Undercutting (cont.d)					
			O/C Drift (cont'd)			Overall		
			Avg.depth _strike (m)	u/c length along strike (m)	Avg. depth _u/c portion (m)	Portion of u/c along perimeter	Avg. depth in u/c portion (m)	Overall avg. depth u/c_strike (m)
63	Trout Lake Mine	980-N12-2	0	0.0	0.00	0.00	0.00	0
64	Trout Lake Mine	950-W1-3	1.6	18.0	2.13	0.29	1.64	1.2
65	Trout Lake Mine	840-M3-2	0	0.0	0.00	0.09	1.50	0.75
66	Trout Lake Mine	1010-N9-1	1.2	31.6	1.20	0.39	0.82	0.8
67	Trout Lake Mine	980-N11-3	0.7	7.2	2.33	0.20	1.81	0.75
68	Trout Lake Mine	810-N10-4	0	0.0	0.00	0.16	0.47	0.4
69	Trout Lake Mine	870-N11-1	0	0.0	0.00	0.08	1.08	0.7
70	Trout Lake Mine	950-N12-2	0	0.0	0.00	0.09	0.60	0.3
71	Trout Lake Mine	980W1-6	0.1	7.9	0.50	0.27	1.54	1.15
72	Trout Lake Mine	900 M3 3	0.1	4.7	0.50	0.07	1.58	0.25
73	Trout Lake Mine	980 W1 2	0	0.0	0.00	0.00	0.00	0
74	Trout Lake Mine	1010N11 6	0	0.0	0.00	0.00	0.00	0
75	Trout Lake Mine	1010N9 2	0.1	4.4	0.40	0.18	0.50	0.35
76	Trout Lake Mine	980N11 2	0	0.0	0.00	0.00	0.00	0
77	Trout Lake Mine	980N12 3	0.1	3.6	0.67	0.03	0.33	0.05
78	Trout Lake Mine	865M3 3	0.8	4.6	3.20	0.07	2.60	0.6
79	Trout Lake Mine	1010N11 5	0	0.0	0.00	0.00	0.00	0
80	Trout Lake Mine	840M1 3	0	0.0	0.00	0.00	0.00	0
81	Trout Lake Mine	840N9-2	0	0.0	0.00	0.03	1.67	0.25
82	Trout Lake Mine	980N12 4	0	0.0	0.00	0.18	0.67	0.6
83	Trout Lake Mine	980W1 5	0	0.0	0.00	0.00	0.00	0
84	Trout Lake Mine	810N5 1	0.5	12.4	0.50	0.19	1.75	1.15
85	Trout Lake Mine	1070W2 6	1.7	19.8	1.89	0.32	1.31	1.2
86	Trout Lake Mine	10193	0	0.0	0.00	0.07	0.20	0.1
87	Trout Lake Mine	101114	0	0.0	0.00	0.06	0.13	0.05
88	Trout Lake Mine	10186	0	0.0	0.00	0.05	0.60	0.15
89	Trout Lake Mine	10181	0.7	12.4	1.40	0.25	1.37	0.85
90	Trout Lake Mine	8491	0.7	6.2	2.33	0.14	1.77	0.65
91	Trout Lake Mine	9883	0.8	8.5	1.33	0.22	0.78	0.5
92	Trout Lake Mine	8152	1	23.4	1.00	0.29	1.10	0.8
93	Trout Lake Mine	8454	0	0.0	0.00	0.05	1.00	0.3
94	Trout Lake Mine	81103	0.6	12.8	1.00	0.31	1.00	0.8
95	Trout Lake Mine	9884	0	0.0	0.00	0.11	0.33	0.2
96	Trout Lake Mine	8433	0	0.0	0.00	0.02	1.50	0.15
97	Trout Lake Mine	101113	0	0.0	0.00	0.08	0.90	0.45
98	Trout Lake Mine	98125	1.5	15.7	3.00	0.12	1.50	0.75
99	Trout Lake Mine	10182	0	0.0	0.00	0.09	0.50	0.25
100	Trout Lake Mine	8412	2	15.5	2.00	0.14	1.00	1
101	Trout Lake Mine	101122	0	0.0	0.00	0.00	0.00	0
102	Trout Lake Mine	8411	0	0.0	0.00	0.00	0.00	0
103	Trout Lake Mine	87112	0	0.0	0.00	0.05	0.40	0.1
104	Trout Lake Mine	81102	0	0.0	0.00	0.10	0.55	0.3
105	Trout Lake Mine	101112	0	2.0	0.00	0.11	0.50	0.3
106	Trout Lake Mine	10488	0	0.0	0.00	0.00	0.00	0
107	Trout Lake Mine	101123	0	0.0	0.00	0.00	0.00	0
108	Trout Lake Mine	10183	0	0.0	0.00	0.00	0.00	0
109	Trout Lake Mine	8792	0	0.0	0.00	0.07	1.22	0.55
110	Trout Lake Mine	8452	0.1	4.0	0.50	0.11	1.75	0.8
111	Trout Lake Mine	10184	0	0.0	0.00	0.20	0.90	0.9
112	Trout Lake Mine	7031	0	0.0	0.00	0.32	0.70	0.7
113	Trout Lake Mine	8753	1.5	10.8	2.14	0.24	1.67	1.35
114	Trout Lake Mine	1018\5	0	0.0	0.00	0.03	0.25	0.05
115	Trout Lake Mine	8793	0.5	5.9	1.67	0.23	1.13	0.55
116	Trout Lake Mine	8451\1	0.2	2.3	1.33	0.18	3.12	2.55
117	Trout Lake Mine	1048\2	1.4	8.3	2.33	0.15	1.67	0.95
118	Trout Lake Mine	8410\2	0.5	7.3	1.67	0.25	1.48	0.9
119	Trout Lake Mine	1048\1	1	26.0	1.00	0.22	0.50	0.5
120	Trout Lake Mine	7311	1	35.3	1.00	0.25	0.50	0.5
121	Trout Lake Mine	8791\4	0	0.0	0.00	0.09	1.11	0.5
122	Trout Lake Mine	8791\3	0	0.0	0.00	0.09	1.11	0.5
123	Trout Lake Mine	1048\5	0	0.0	0.00	0.07	0.80	0.4
124	Trout Lake Mine	8754	0	0.0	0.00	0.15	1.20	1.2
125	Trout Lake Mine	1078\1	1.4	20.5	1.40	0.24	1.53	0.95
126	Trout Lake Mine	8791\E	3	20.3	3.75	0.15	1.88	1.5
127	Trout Lake Mine	1048\3	1.1	21.5	1.10	0.33	2.05	1.9

APPENDIX II DATABASE

No.	Mine Name	Stope #	Undercutting (cont.d)					
			O/C Drift (cont'd)			Overall		
			Avg.depth _strike (m)	u/c length along strike (m)	Avg. depth _u/c portion (m)	Portion of u/c along perimeter	Avg. depth in u/c portion (m)	Overall avg. depth u/c_strike (m)
128	Trout Lake Mine	84105	0	0.0	0.00	0.13	0.60	0.3
129	Trout Lake Mine	84103	1.7	22.0	1.70	0.34	1.52	1.25
130	Trout Lake Mine	10782	0	0.0	0.00	0.03	0.33	0.05
131	Trout Lake Mine	87102	1.7	25.0	1.70	0.31	1.28	1.15
132	Trout Lake Mine	10486	0.7	18.4	0.88	0.30	1.51	1.1
133	Trout Lake Mine	10783	0	0.0	0.00	0.20	0.50	0.5
134	Trout Lake Mine	84104	0	0.0	0.00	0.06	1.00	0.3
135	Trout Lake Mine	10484	0	0.0	0.00	0.00	0.00	0
136	Trout Lake Mine	9051#1	0.4	12.0	1.00	0.28	1.25	0.8
137	Trout Lake Mine	6451b	0	0.0	0.00	0.16	1.43	1
138	Trout Lake Mine	6451	2	30.0	2.00	0.35	1.50	1.1
139	Trout Lake Mine	1010H1-4	1	12.4	2.00	0.12	1.00	0.5
140	Trout Lake Mine	875C2F-8	0	0.0	0.00	0.05	0.50	0.1
141	Trout Lake Mine	950N5-1	0	0.0	0.00	0.07	1.17	0.35
142	Trout Lake Mine	765C2-1	0.5	20.0	0.50	0.33	1.05	0.65
143	Trout Lake Mine	765C2-5	0	0.0	0.00	0.00	0.00	0
144	Trout Lake Mine	980N9-2	0.6	9.1	1.33	0.22	2.03	1.05
145	Trout Lake Mine	1040H1-6/7	0	0.0	0.00	0.06	0.75	0.15
146	Trout Lake Mine	810N10-7	0	0.0	0.00	0.00	0.00	0
147	Trout Lake Mine	950N9-2	0	0.0	0.00	0.05	0.60	0.15
148	Trout Lake Mine	950W1-6	0	0.0	0.00	0.08	0.86	0.3
149	Trout Lake Mine	980N11-6	0.3	5.2	1.00	0.25	1.30	0.95
150	Trout Lake Mine	920N12-3	0.2	7.9	0.57	0.33	1.29	1.1

APPENDIX II DATABASE

No.	Mine Name	Stope #	Blasting					
			Drill hole size	Orientation (f-fanned p-parallel)	Dillhole offset from HW (Max/Min/Avg) (m)	Wall Control	# of blasts Slot//main	Powder Factor (lb/ton)
1	Callinan Mine	545-#1	2.5"	f	n/a	y	0	1
2	Callinan Mine	580-2	2.5"	f	1.5/0/.7	y	1//3	1.2
3	Callinan Mine	580-3	3"	f	1/0/.3	y	1//5	0.9
4	Callinan Mine	605-3	2"	p	0.5/0/.3	y		1.1
5	Callinan Mine	630-6	2.5"		0	y		1.1
6	Callinan Mine	630-7	2.5"	f	n/a	y		1.1
7	Callinan Mine	865-5-1	2.5"	f	n/a	y		1.4
8	Callinan Mine	865-1-2	3"	f	n/a	y		1.4
9	Callinan Mine	885-1-1	2.5	p	1/0/0.5	y		1.3
10	Callinan Mine	885-1-2	3"	f	n/a	y		1.3
11	Callinan Mine	885-1-3	2.5"	p	1/0/0.3	y		0.9
12	Callinan Mine	910-1-2	3"	p	1.5/0/0.5	y		1.2
13	Callinan Mine	910-1-3	3"	f	n/a	y		1.4
14	Callinan Mine	910-7-1	2.5"	p	1/-1/0.5	n		2.7
15	Callinan Mine	920-7-1B	2.5	p	1/0/0.5	y		2.5
16	Callinan Mine	920-7-3	2.5"	p	1.6/0/1	y	0	1.7
17	Callinan Mine	935-1-1	2.5"	p	1.2/0/0.5	y	/2	1.4
18	Callinan Mine	935-1-2	2.5"	f	n/a	y	1//3	0.9
19	Callinan Mine	935-5-1	2.5"	f	n/a	y		1.4
20	Callinan Mine	935-7-2	2.5"	p	1.8/0/0.6	n		1.9
21	Callinan Mine	935-7-3	2.5"	p	2/0/0.8	n		1.3
22	Callinan Mine	935-7-4	2.5"	p	1.5/0/0.6	n		1.1
23	Callinan Mine	935-7-5	2.5"	p	1.5/0/0.6	n		
24	Callinan Mine	950-7-2	3"	f	n/a	n		1.3
25	Callinan Mine	950-7-3	2.5"	f	n/a	n		
26	Callinan Mine	1075-2	2.5"	p	1/0/0.5	y	3	
27	Callinan Mine	1075-4	2.5"	f	n/a	y	5	1.2
28	Callinan Mine	1075-5	3"	f	n/a	y	1	
29	Callinan Mine	1095-2		f	n/a	y		
30	Callinan Mine	1095-6	2.5"	f	n/a	y	1//6	
31	Callinan Mine	1120-1	2.5"	f	n/a	n	8	0.7
32	Callinan Mine	1100-2-4	3.0"	f	n/a	n	4	1.8
33	Callinan Mine	1100-2-5	3.0"	f	n/a	y	3	1.4
34	Callinan Mine	545-2	2.5"	p	2/-2/.5	y	/5	1.2
35	Callinan Mine	545-3	2.5"	f	n/a	y	5	1.1
36	Callinan Mine	650-4	2.5"	f	n/a	y	4	0.9
37	Callinan Mine	845-7-2	3"	p	1/0/0.5	y	8	1
38	Callinan Mine	865-1-1	2.5"	f	n/a	y		
39	Callinan Mine	865-7-3	3"	f	n/a	y		
40	Callinan Mine	885-7-4	2.5"	f	n/a	y	6	1.1
41	Callinan Mine	910-7-3	2.5"	p	2/-1/.5	y	5	2
42	Callinan Mine	910-7-4	2.5"	p	1.4/0/0.7	y	7	1.2
43	Callinan Mine	920-7-4	3"	p	1/0/0.5	y	5	1.2
44	Callinan Mine	777-1100-2-12	2.5"	f	n/a	y	5	1.2
45	Callinan Mine	865-1-1	2.5"	f	n/a	y	5	1.3
46	Ruttan Mine	630-4B2	3"	f	n/a	y	6	
47	Ruttan Mine	540-12.5B	3"	f	n/a	y	6	
48	Ruttan Mine	440-0B2	3.6"	f	n/a	y	6	
49	Ruttan Mine	1050-29J6	3"	f	n/a	y	10	
50	Ruttan Mine	550-28JS	3"	p		y	7	
51	Ruttan Mine	440-5B2	3"	f	n/a	y	5	
52	Ruttan Mine	440-1B2	3.6"	f	n/a	y	4	
53	Ruttan Mine	590-14B	4.5"	f	n/a	y	6	
54	Trout Lake Mine	840-N9-4	4 1/2"	p	1.5/0/0.7	y	0//2	1.7
55	Trout Lake Mine	950-W1-2	5 1/2"	p	2/0.1/0.5	y	0//1	1.63
56	Trout Lake Mine	1070-W2-7	0	f	n/a	y	0//2	1.15
57	Trout Lake Mine	950-N12-1	0	p	1/0/0.5	y	//1	1.23
58	Trout Lake Mine	810-N10-5	0	f	n/a	y	2//2	1.3
59	Trout Lake Mine	1040-H1-4	3"	f	n/a	y	4//2	1.31
60	Trout Lake Mine	950-W1-4	4 1/2" L	p	1.2/0/0.6	y	//2	0.9
61	Trout Lake Mine	950-N12-3	4 1/2" L	f	n/a	y	2//2	0.7
62	Trout Lake Mine	980-N11-1	3"	f	n/a	y	2//2	0.9

APPENDIX II DATABASE

No.	Mine Name	Stope #	Blasting					
			Drill hole size	Orientation (f-fanned p-parallel)	Dillhole offset from HW (Max/Min/Avg) (m)	Wall Control	# of blasts Slot/main	Powder Factor (lb/ton)
63	Trout Lake Mine	980-N12-2	4 1/2" L	p	0.2/0.2/0.2	y	2//2	1.4
64	Trout Lake Mine	950-W1-3	0	f	0.5/0/0.25	y	2//1	1
65	Trout Lake Mine	840-M3-2	3"	f	n/a	y	3//2	0.8
66	Trout Lake Mine	1010-N9-1	4 1/2"	p	1.7/0/1	y	2//2	2.1
67	Trout Lake Mine	980-N11-3	4 1/2" L	p	2/0/0.6	y	2//2	1.3
68	Trout Lake Mine	810-N10-4	4 1/2" L	f	n/a	y	2//1	0.7
69	Trout Lake Mine	870-N11-1	3" & 4 1/2"	f	n/a	y	1//2	1
70	Trout Lake Mine	950-N12-2	4 1/2"	p	1.5/0/0.7	y	1//1	0.9
71	Trout Lake Mine	980W1-6	4 1/2" L	f	n/a	y	1//2	1
72	Trout Lake Mine	900 M3 3	3"	f	n/a	y	2//3	1.04
73	Trout Lake Mine	980 W1 2	4 1/2" L	f	n/a	y	2//1	1.05
74	Trout Lake Mine	1010N11 6	4 1/2" L	p	0	y	2//1	1.9
75	Trout Lake Mine	1010N9 2	4 1/2" L	f	n/a	y	2//1	1.5
76	Trout Lake Mine	980N11 2	3"	f	n/a	y	2//2	0.9
77	Trout Lake Mine	980N12 3	4 1/2" L	f	n/a	y	2//2	1
78	Trout Lake Mine	865M3 3	3"	f	n/a	y	2//2	0.72
79	Trout Lake Mine	1010N11 5	3", 4 1/2"	f	n/a	y	2//2	1
80	Trout Lake Mine	840M1 3	3"	f	n/a	y	1//2	0.8
81	Trout Lake Mine	840N9-2	3"	F	n/a	y	2//3	0.63
82	Trout Lake Mine	980N12 4	3"	f	n/a	y	2//1	0.9
83	Trout Lake Mine	980W1 5	3" & 4 1/2"	f	n/a	y	2//2	1.3
84	Trout Lake Mine	810N5 1	4 1/2 L	f	n/a	y	1//1	1.03
85	Trout Lake Mine	1070W2 6	3"	p	1.5/0/0.3	y	2//2	0.8
86	Trout Lake Mine	10193	3"	f	n/a	y	3//1	0.8
87	Trout Lake Mine	101114	4 1/2"	f	n/a	y	3//1	1.3
88	Trout Lake Mine	10186	0	f	n/a	y	0//3	0.7
89	Trout Lake Mine	10181	3"	f	n/a	y	2//2	0.65
90	Trout Lake Mine	8491	3"	p	2/0/.7	y	2//2	1
91	Trout Lake Mine	9883	3"	p	1.5/0/0.7	y	2//1	0.9
92	Trout Lake Mine	8152	4 1/2"		0	y	1//1	0.88
93	Trout Lake Mine	8454	4 1/2"	f	n/a	y	1//1	0.3
94	Trout Lake Mine	81103	3"	p	2/0/0.8	y	2//1	0.88
95	Trout Lake Mine	9884	3"	f	n/a	y	3//3	0.7
96	Trout Lake Mine	8433	3"	f	n/a	y	0	0.5
97	Trout Lake Mine	101113	4 1/2"	f	n/a	y	3//2	1.2
98	Trout Lake Mine	98125	3"	f	n/a	y	2//3	0.93
99	Trout Lake Mine	10182	4 1/2"		0	y	1//2	0.9
100	Trout Lake Mine	8412	0	f	n/a	y		1.03
101	Trout Lake Mine	101122	3"		0	y	2//2	1.3
102	Trout Lake Mine	8411	3"		0	y	2//2	1.33
103	Trout Lake Mine	87112	4 1/2"		0	y	2//4	1.94
104	Trout Lake Mine	81102	3"	p	1.6/0/0.8	y	2//1	0.82
105	Trout Lake Mine	101112	3"	f	n/a	y	1//1	1.4
106	Trout Lake Mine	10488	3"	f	n/a	y	1//1	1.14
107	Trout Lake Mine	101123	3"	f	n/a	y	2//2	1.2
108	Trout Lake Mine	10183	3"	f	n/a	y	2//2	0.45
109	Trout Lake Mine	8792	3"	p	2/-2/0.6	y	2//1	1
110	Trout Lake Mine	8452	4 1/2" L	f	n/a	y	2//1	1.2
111	Trout Lake Mine	10184	3"	f	n/a	y	2//2	0.7
112	Trout Lake Mine	7031	3"		0	y	1//2	0.95
113	Trout Lake Mine	8753	3"		0	y	use borehole	1.3
114	Trout Lake Mine	10185	3"	f	n/a	y	2//1	0.73
115	Trout Lake Mine	8793	3"	f	n/a	y	2//1	0.83
116	Trout Lake Mine	8451\1	4 1/2"	p	1.5/0/0.5	y	2//1	1.14
117	Trout Lake Mine	1048\2	3"	f	n/a	y	3//1	0.6
118	Trout Lake Mine	8410\2	4 1/2" L	f	n/a	y	2//1	1.04
119	Trout Lake Mine	1048\1	4 1/2", 2 1/2"	f	n/a	y	2//2	1.15
120	Trout Lake Mine	7311	3"	f	n/a	n		0.95
121	Trout Lake Mine	8791\4	3"		0	y	3//1	0.77
122	Trout Lake Mine	8791\3	3"	f	n/a	y	2//1	0.89
123	Trout Lake Mine	1048\5	3"	f	n/a	y	2//3	0.73
124	Trout Lake Mine	8754	4 1/2" L		0	y	2//2	0.88
125	Trout Lake Mine	1078\1	3"	p	0.8/0/0.5	y	2//1	1.1
126	Trout Lake Mine	8791\E	3"		0	y	3//3	0.9
127	Trout Lake Mine	1048\3	3"	p	1.2	0.7	2//2	0.61

APPENDIX II DATABASE

No.	Mine Name	Stope #	Blasting					
			Drill hole size	Orientation (f-fanned p-parallel)	Dillhole offset from HW (Max/Min/Avg) (m)	Wall Control	# of blasts Slot/main	Powder Factor (lb/ton)
128	Trout Lake Mine	84105	4 1/2" L	f	n/a	y	0//3	0.65
129	Trout Lake Mine	8410\3	4 1/2"	p	0.8/0/0.4	y	1//1	0.7
130	Trout Lake Mine	1078\2	3"	f	n/a	y	2//2	0.77
131	Trout Lake Mine	87102	3"	f	n/a	y	1//2	0.78
132	Trout Lake Mine	10486	3"	p	1.5/-2.5/0.4	y	2//2	1.2
133	Trout Lake Mine	10783	3"	p	1/0/0.5	y	2//2	0.7
134	Trout Lake Mine	84104	3", 3 8/5"	p	1/0/0.4	y	0//2	1.47
135	Trout Lake Mine	10484	3", 3 8/5"	f	n/a	y	2//6	0.67
136	Trout Lake Mine	9051#1	4 1/2"	p	2/0/0.9	y	1//2	1.12
137	Trout Lake Mine	6451b	3"	f	n/a	y	0//4	0.43
138	Trout Lake Mine	6451	3"	p	1.6/0/0.8	y	0//4	1.03
139	Trout Lake Mine	1010H1-4	3"	p	1.3/0/0.7	y	1//1	
140	Trout Lake Mine	875C2F-8	3 5/8"	p	2.5/0/0.9	y	0//2	0.65
141	Trout Lake Mine	950N5-1	3"	f	n/a	y	0//3	0.86
142	Trout Lake Mine	765C2-1	3 5/8"	p	1.5/0.2/0.9	y	0//2	1.03
143	Trout Lake Mine	765C2-5	3 5/8"	p	2/0.5/0.9	y	0//4	0.8
144	Trout Lake Mine	980N9-2	4 1/2"	p	1/0/.3	y	0//1	0.69
145	Trout Lake Mine	1040H1-6/7	3 5/8"	f	n/a	y	0//2	2.3
146	Trout Lake Mine	810N10-7	3"	p	1.3/.1/.6	y	2	1.26
147	Trout Lake Mine	950N9-2	3 5/8"	p	2.5/-1/.7	y	0//2	0.73
148	Trout Lake Mine	950W1-6	3"	f	n/a	y	0//2	
149	Trout Lake Mine	980N11-6	4 1/2"	p	1/0/0.5	y	0//2	
150	Trout Lake Mine	920N12-3	3"	p	1.5/0/.5	y	0//3	

APPENDIX II DATABASE

No.	Mine Name	Stope #	Stope situation				Time Opened (day)	HW Dilution	
			Stope config. Category	Lens	Adjacent mined	Adjacent filled		O/B Volume (m3)	ELOS Actual (m)
1	Callinan Mine	545-#1	1	s	f		37	1352	2.6
2	Callinan Mine	580-2	2	s	o	o	80	902.5	1.9
3	Callinan Mine	580-3	2	s	o	o	83	570	1.9
4	Callinan Mine	605-3	2	s	o	o	55	1350.7	2.9
5	Callinan Mine	630-6	5	s	b/o	b/o	38	176	0.4
6	Callinan Mine	630-7	2	s	o	o	38	176	0.4
7	Callinan Mine	865-5-1	5	s	b/o	b/o	52	1185.6	0.8
8	Callinan Mine	865-1-2	5	s	b/o	b/o	21	211.2	0.4
9	Callinan Mine	885-1-1	5	s	b/o	b/o	36	524.7	0.6
10	Callinan Mine	885-1-2	5	s	b/o	b/o	25	740.5	1.1
11	Callinan Mine	885-1-3	5	s	b/o	b/o	14	881.8	0.8
12	Callinan Mine	910-1-2	5	s	b/o	b/o	20	913.9	1.1
13	Callinan Mine	910-1-3	5	s	b/o	b/o	20	0	0
14	Callinan Mine	910-7-1	3	s	b	b	13	370.3	1.2
15	Callinan Mine	920-7-1B	3	s	b	b	12	1134.3	2
16	Callinan Mine	920-7-3	5	s	b/o	b/o	31	432	0.6
17	Callinan Mine	935-1-1	3	s	b	b	14	148.8	0.2
18	Callinan Mine	935-1-2	5	s	b/o	b/o	28	163.8	0.4
19	Callinan Mine	935-5-1	1	m	f		30	606.3	1
20	Callinan Mine	935-7-2	5	s	b/o	b/o	7	25	0.1
21	Callinan Mine	935-7-3	5		b/o	b/o	24	0	0
22	Callinan Mine	935-7-4	5	s	b/o	b/o	32	0	0
23	Callinan Mine	935-7-5	5	s	b/o	b/o	16	289	1
24	Callinan Mine	950-7-2	2	s	o	o	21	110	0.2
25	Callinan Mine	950-7-3	2	s	o	o	14	158.7	0.3
26	Callinan Mine	1075-2	2	s	o	o	95	2035.5	2.3
27	Callinan Mine	1075-4	2	s	o	o	60	916.9	1.2
28	Callinan Mine	1075-5	2	s	o	o	56	281.2	0.6
29	Callinan Mine	1095-2	2	s	o	o	68	529.7	0.6
30	Callinan Mine	1095-6	2	s	o	o	62	234.8	0.3
31	Callinan Mine	1120-1	3	s	b	b	55	1815.7	2.1
32	Callinan Mine	1100-2-4	5	s	b/o	b/o	12	15	0.1
33	Callinan Mine	1100-2-5	2	s	o	o	18	150.2	0.7
34	Callinan Mine	545-2	5	s	b/o	b/o	64	0	0
35	Callinan Mine	545-3	5	s	b/o	b/o	15	78.4	0.1
36	Callinan Mine	650-4	5	s	b/o	b/o	36	1575	1.8
37	Callinan Mine	845-7-2	5	s	b/o	b/o	75	121	0.1
38	Callinan Mine	865-1-1	3	m	b	b	21	148.5	0.3
39	Callinan Mine	865-7-3	5	s	b/o	b/o	30	176.4	0.2
40	Callinan Mine	885-7-4	5	s	b/o	b/o	22	0	0
41	Callinan Mine	910-7-3	2	s	o	o	31	277.2	0.6
42	Callinan Mine	910-7-4	5	s	b/o	b/o	17	369.6	0.6
43	Callinan Mine	920-7-4	2	s	o	o	16	297.6	0.4
44	Callinan Mine	777-1100-2-12	2	s	o	o	86	331.2	0.8
45	Callinan Mine	865-1-1	3	s	b	b	21	848.3	0.7
46	Ruttan Mine	630-4B2	2	s	o	o			0.6
47	Ruttan Mine	540-12.5B	2	m	o	o			0.2
48	Ruttan Mine	440-0B2	2	s	o	o			2
49	Ruttan Mine	1050-29J6	1	s	f				2.1
50	Ruttan Mine	550-28JS	2	s	o	o			3.4
51	Ruttan Mine	440-5B2	2	s	o	o			10
52	Ruttan Mine	440-1B2	2	s	o	o			0
53	Ruttan Mine	590-14B	5	s	b/o	b/o			0
54	Trout Lake Mine	840-N9-4	3	m	b/o	b/o	18	475	0.6
55	Trout Lake Mine	950-W1-2	2	m	o	o	15	75.9	0.2
56	Trout Lake Mine	1070-W2-7	5	s	b/o	b/o	22	41.8	0.1
57	Trout Lake Mine	950-N12-1	2	s	o	o	29	685.1	0.8
58	Trout Lake Mine	810-N10-5	6	s	a/b/o	a/b/o	54	1027.4	1.2
59	Trout Lake Mine	1040-H1-4	7	s	a/o	a/o	40	782.2	0.9
60	Trout Lake Mine	950-W1-4	5	m	b/o	b/o	18	1166.3	1.3
61	Trout Lake Mine	950-N12-3	5	s	b/o	b/o	27	3059.1	2.6
62	Trout Lake Mine	980-N11-1	5	m	b/o	b/o	40	731.6	1.1

APPENDIX II DATABASE

No.	Mine Name	Stope #	Stope situation				Time Opened (day)	HW Dilution	
			Stope config. Category	Lens	Adjacent mined	Adjacent filled		O/B Volume (m3)	ELOS Actual (m)
63	Trout Lake Mine	980-N12-2	2	m	os	os	57	2850.1	2.3
64	Trout Lake Mine	950-W1-3	6	m	a/b/o	a/b/o	32	1813.5	2.1
65	Trout Lake Mine	840-M3-2	1	m	f		12	112.8	0.1
66	Trout Lake Mine	1010-N9-1	2	s	o	o	13	1884.1	1.3
67	Trout Lake Mine	980-N11-3	5	m	b/o	b/o	15	97	0.1
68	Trout Lake Mine	810-N10-4	5	s	b/o	b/o	79	0	0
69	Trout Lake Mine	870-N11-1	5	m	b/o	b/o	65	273.6	0.4
70	Trout Lake Mine	950-N12-2	2	s	o	o	18	1031.9	1.1
71	Trout Lake Mine	980W1-6	5	m	b/o	b/o	65	273.6	0.4
72	Trout Lake Mine	900 M3 3	7	s	a	a	62	1461.8	1.8
73	Trout Lake Mine	980 W1 2	5	m	b/o	b/o	55	1164.7	1.5
74	Trout Lake Mine	1010N11 6	2	m	o	o	20	1646.8	2.1
75	Trout Lake Mine	1010N9 2	2	m	o	o	15	275.1	0.4
76	Trout Lake Mine	980N11 2	3	m	b	b	13	401.3	0.5
77	Trout Lake Mine	980N12 3	2	s	o	o	25	1288	1.3
78	Trout Lake Mine	865M3 3	3	s	b	b	30	307.1	0.4
79	Trout Lake Mine	1010N11 5	2	m	o	o	30	2505.6	2.1
80	Trout Lake Mine	840M1 3	2	s	o	o	32	749.9	0.9
81	Trout Lake Mine	840N9-2	5	m	b/o	b/o	32	98.8	0.1
82	Trout Lake Mine	980N12 4	5	s	b/o	b/o	41	1005.8	1.1
83	Trout Lake Mine	980W1 5	5	m	b/o	b/o	43	957.6	1.2
84	Trout Lake Mine	810N5 1	5	m	b/o	b/o	15	569.6	1.2
85	Trout Lake Mine	1070W2 6	3	s	b	b	90	544.9	0.6
86	Trout Lake Mine	10193	1	m	f	f	28	912.3	1.4
87	Trout Lake Mine	101114	2	m	o	o	16	1063.1	1.1
88	Trout Lake Mine	10186	2	s	o	o	8	622	0.8
89	Trout Lake Mine	10181	5	m	b/o	b/o	13	1100.4	1.2
90	Trout Lake Mine	8491	2	m	o	o	19	1598	1.9
91	Trout Lake Mine	9883	5	m	b/o	b/o	11	282.5	0.6
92	Trout Lake Mine	8152	5	m	b/o	b/o	26	1022.3	1.2
93	Trout Lake Mine	8454	5	s	b/o	b/o	41	276.9	0.4
94	Trout Lake Mine	81103	5	s	b/o	b/o	8	0	0
95	Trout Lake Mine	9884	3	m	b	b	88	3215.5	3.3
96	Trout Lake Mine	8433	2	s	o	o	26	335.4	0.5
97	Trout Lake Mine	101113	5	m	b/o	b/o	22	211.5	0.3
98	Trout Lake Mine	98125	2	s	o	o	9	781.4	0.7
99	Trout Lake Mine	10182	5	m	b/o	b/o	16	397.4	0.5
100	Trout Lake Mine	8412	2	m	o	os		258.8	0.4
101	Trout Lake Mine	101122	2	s	o	o	55	968.8	1.1
102	Trout Lake Mine	8411	5	m	b/o	b/o	10	1219.9	1.8
103	Trout Lake Mine	87112	5	m	b/o	b/o	22	1928	1.4
104	Trout Lake Mine	81102	5	s	b/o	b/o	15	92.2	0.2
105	Trout Lake Mine	101112	2	m	o	o	28	782.8	0.9
106	Trout Lake Mine	10488	2	s	o	o	31	51.6	0.1
107	Trout Lake Mine	101123	1	s	f		16	638.4	0.6
108	Trout Lake Mine	10183	5	m	b/o	b/o	37	507.8	1
109	Trout Lake Mine	8792	5	m	b/o	b/o	15	179.1	0.3
110	Trout Lake Mine	8452	7	s	a/b	a/b	29	1516.8	1.8
111	Trout Lake Mine	10184	5	s	b/o	b/o	21	2074.8	1.8
112	Trout Lake Mine	7031	2	s	o	o	73	197.5	0.3
113	Trout Lake Mine	8753	5	s	b/o	b/o	26	171.6	0.3
114	Trout Lake Mine	1018\5	5	m	b/o	b/o	65	526.2	0.9
115	Trout Lake Mine	8793	5	m	b/o	b/o	28	1473.1	2.1
116	Trout Lake Mine	8451\1	3	m	b	b	23	216.8	0.4
117	Trout Lake Mine	1048\2	4	s	b/bs	b/bs	9	252.9	0.5
118	Trout Lake Mine	8410\2	5	s	b/o	b/o	8	1896	2.1
119	Trout Lake Mine	1048\1	1	s	f		125	825.6	0.9
120	Trout Lake Mine	7311	3	s	b	b	21	591.3	0.5
121	Trout Lake Mine	8791\4	1	m	f		26	628.1	0.6
122	Trout Lake Mine	8791\3	5	m	b/o	b/o	29	628.1	0.6
123	Trout Lake Mine	1048\5	5	m	b/o	b/o	27	47.6	0.1
124	Trout Lake Mine	8754	3	s	b	b	6	1614.2	2.2
125	Trout Lake Mine	1078\1	2	s	o	o	8	407.8	0.6
126	Trout Lake Mine	8791\E	3	m	b	b	50	6098.1	5.6
127	Trout Lake Mine	1048\3	5	s	b/o	b/o	39	3440	4

APPENDIX II DATABASE

No.	Mine Name	Stope #	Stope situation				Time Opened (day)	HW Dilution	
			Stope config. Category	Lens	Adjacent mined	Adjacent filled		O/B Volume (m3)	ELOS Actual (m)
128	Trout Lake Mine	84105	5	s	b/o	b/o	10	0	0
129	Trout Lake Mine	84103	5	s	b/o	b/o	22	462	0.7
130	Trout Lake Mine	10782	2	s	o	o	29	86	0.1
131	Trout Lake Mine	87102	5	s	b/o	b/o	12	1053	1
132	Trout Lake Mine	10486	3	m	b	b	7	644	0.8
133	Trout Lake Mine	10783	1	s	f		16	1387.5	1.5
134	Trout Lake Mine	84104	3	s	b	b	4	662	1.1
135	Trout Lake Mine	10484	1	s	f		31	538	0.7
136	Trout Lake Mine	9051#1	1	m	f	n/a	26	3041	2.9
137	Trout Lake Mine	6451b	2	s	o	o	137	1164	1.3
138	Trout Lake Mine	6451	1	s	f			1613	2.6
139	Trout Lake Mine	1010H1-4	1	s	f		21	723	1.2
140	Trout Lake Mine	875C2F-8	2	s	o	o	31	287	1.1
141	Trout Lake Mine	950N5-1	1	m	f		20	287	0.4
142	Trout Lake Mine	765C2-1	3	s	b	b	23	743	1.5
143	Trout Lake Mine	765C2-5	5	s	b/o	b/o	30	1222	2.4
144	Trout Lake Mine	980N9-2	5	m	b/o	b/o	23	404	0.8
145	Trout Lake Mine	1040H1-6/7	2	s	o	o	86	2763	2.3
146	Trout Lake Mine	810N10-7	2	s	o	o	36	5857	2.3
147	Trout Lake Mine	950N9-2	5	m	b/o	b/o	12	74	0.1
148	Trout Lake Mine	950W1-6	5	m	b/o	b/o	33	742	1.1
149	Trout Lake Mine	980N11-6	5	m	b/o	b/o	49	1021	2.1
150	Trout Lake Mine	920N12-3	5	s	b/o	b/o	36	391	0.8

APPENDIX II DATABASE

No.	Mine Name	Stope #	Notes
1	Callinan Mine	545-#1	See CMS section.
2	Callinan Mine	580-2	Small HR and L/H ratio.
3	Callinan Mine	580-3	diminished ore at upper part of stope. Stope was not blasted through to overcut drift. HR should be smaller than calculated (about 2/3 of the calculated HR, e.g. HR=-5).
4	Callinan Mine	605-3	Small HR and L/H ratio. Possible stress and u/c problems.
5	Callinan Mine	630-6	Possibly u/c and stress effects
6	Callinan Mine	630-7	HW u/b. Favorable HW shape (HW curve out).
7	Callinan Mine	865-5-1	
8	Callinan Mine	865-1-2	
9	Callinan Mine	885-1-1	
10	Callinan Mine	885-1-2	Possibly stress problem
11	Callinan Mine	885-1-3	
12	Callinan Mine	910-1-2	
13	Callinan Mine	910-1-3	
14	Callinan Mine	910-7-1	stope lies in stress path. Maybe stress problem.
15	Callinan Mine	920-7-1B	
16	Callinan Mine	920-7-3	
17	Callinan Mine	935-1-1	Most likely ELOS due to U/C and O/C. Some blast damage in fan drilling area.
18	Callinan Mine	935-1-2	Possibly blast damage / higher stress
19	Callinan Mine	935-5-1	
20	Callinan Mine	935-7-2	
21	Callinan Mine	935-7-3	Very short strike length. Stress shadow.
22	Callinan Mine	935-7-4	Maybe High stress
23	Callinan Mine	935-7-5	o/b due to u/c (all o/b happened around u/c)
24	Callinan Mine	950-7-2	Small HR and L/H ratio.
25	Callinan Mine	950-7-3	Small HR and L/H ratio.
26	Callinan Mine	1075-2	
27	Callinan Mine	1075-4	
28	Callinan Mine	1075-5	
29	Callinan Mine	1095-2	
30	Callinan Mine	1095-6	Blast Damaged HW. See blast info sheet p10.
31	Callinan Mine	1120-1	No Blast Damage, No U/C. No stress Problem. Possible stress shadow (Middle zone #1 all stopes mined to date).
32	Callinan Mine	1100-2-4	stress problem (drillhole squeezed before blast loading)
33	Callinan Mine	1100-2-5	Small HR and L/H ratio.
34	Callinan Mine	545-2	
35	Callinan Mine	545-3	Stress problem (Squeezed drillholes)
36	Callinan Mine	650-4	Possibly stress problems
37	Callinan Mine	845-7-2	good blast, no stress problem, less u/c effect.
38	Callinan Mine	865-1-1	Possibly blast damage / higher stress
39	Callinan Mine	865-7-3	Water problem, possible stress problem.
40	Callinan Mine	885-7-4	
41	Callinan Mine	910-7-3	Small HR and L/H ratio.
42	Callinan Mine	910-7-4	Blast against fill stope 10185. No pillar between.
43	Callinan Mine	920-7-4	Poor blasting? Larger HR -bigger stress relaxation.
44	Callinan Mine	777-1100-2-1	curved (unfavorable) stope geometry. Stressed location?
45	Callinan Mine	865-1-1	Special case. This stope blast through to #2. #2 have very little ELOS. See paper file.
46	Ruttan Mine	630-4B2	
47	Ruttan Mine	540-12.5B	Maybe High stress
48	Ruttan Mine	440-0B2	
49	Ruttan Mine	1050-29J6	Good Blasts (blast records), stress shadow.
50	Ruttan Mine	550-28JS	Overblasting and poor HW shape (from blast log). Drillholes fanned into HW. (JW)
51	Ruttan Mine	440-5B2	May has stress problem due to mining sequence and stope location.
52	Ruttan Mine	440-1B2	
53	Ruttan Mine	590-14B	
54	Trout Lake Mine	840-N9-4	HW has little underbreak.
55	Trout Lake Mine	950-W1-2	
56	Trout Lake Mine	1070-W2-7	
57	Trout Lake Mine	950-N12-1	
58	Trout Lake Mine	810-N10-5	
59	Trout Lake Mine	1040-H1-4	Narrow ore body,
60	Trout Lake Mine	950-W1-4	
61	Trout Lake Mine	950-N12-3	lots of u/b.
62	Trout Lake Mine	980-N11-1	

APPENDIX II DATABASE

No.	Mine Name	Stope #	Notes
63	Trout Lake Mine	980-N12-2	stress problem (drillholes were squeezed before blast loading). Narrow orebody.
64	Trout Lake Mine	950-W1-3	Good example for overcut drift undercutting effects.
65	Trout Lake Mine	840-M3-2	Very good stope profile.
66	Trout Lake Mine	1010-N9-1	
67	Trout Lake Mine	980-N11-3	
68	Trout Lake Mine	810-N10-4	HW u/b and FW o/b.
69	Trout Lake Mine	870-N11-1	
70	Trout Lake Mine	950-N12-2	Squeezing ground, HW failing during mucking (From Blast log).
71	Trout Lake Mine	980W1-6	
72	Trout Lake Mine	900 M3 3	
73	Trout Lake Mine	980 W1 2	FW O/B ELOS=1.4m. HW has a little underbreak.
74	Trout Lake Mine	1010N11 6	FW O/B ELOS=1.8m
75	Trout Lake Mine	1010N9 2	vanished orebody. Almost half of the stope didn't break through to undercutting drift.
76	Trout Lake Mine	980N11 2	Not be considered to be a regular stope!
77	Trout Lake Mine	980N12 3	Large ore width.
78	Trout Lake Mine	865M3 3	stope may lay in stress shadow.
79	Trout Lake Mine	1010N11 5	Diminished orebody.
80	Trout Lake Mine	840M1 3	Cubex drill accuracy test stope. Controlled blast-buffer (2.5" stick, presplit 1.5")
81	Trout Lake Mine	840N9-2	A lots of dilution from back rather than from HW.
82	Trout Lake Mine	980N12 4	Possibly poor blast.
83	Trout Lake Mine	980W1 5	Maybe High stress
84	Trout Lake Mine	810N5 1	
85	Trout Lake Mine	1070W2 6	HW underbreak.
86	Trout Lake Mine	10193	
87	Trout Lake Mine	101114	
88	Trout Lake Mine	10186	funnel shaped stope.
89	Trout Lake Mine	10181	
90	Trout Lake Mine	8491	
91	Trout Lake Mine	9883	special case. Only upper half of the stope was mined.
92	Trout Lake Mine	8152	
93	Trout Lake Mine	8454	HW o/b & u/b exist at the same time
94	Trout Lake Mine	81103	
95	Trout Lake Mine	9884	
96	Trout Lake Mine	8433	
97	Trout Lake Mine	101113	
98	Trout Lake Mine	98125	No U/C, may has stress problem due to mining sequence location.
99	Trout Lake Mine	10182	FW O/B ELOS=1.4m. Sub-level between upper and lower drifts. Special case.
100	Trout Lake Mine	8412	Blasting problems-powder concentrated close to HW-hole faaned into HW
101	Trout Lake Mine	101122	
102	Trout Lake Mine	8411	
103	Trout Lake Mine	87112	only lower half of the stope was blasted.
104	Trout Lake Mine	81102	
105	Trout Lake Mine	101112	
106	Trout Lake Mine	10488	Possibly stress shadow.
107	Trout Lake Mine	101123	Stress, U/C effect possibly.
108	Trout Lake Mine	10183	Maybe stress problem
109	Trout Lake Mine	8792	little underbreak on both FW & HW.
110	Trout Lake Mine	8452	
111	Trout Lake Mine	10184	
112	Trout Lake Mine	7031	
113	Trout Lake Mine	8753	
114	Trout Lake Mine	10185	
115	Trout Lake Mine	8793	Maybe High stress
116	Trout Lake Mine	8451\1	
117	Trout Lake Mine	1048\2	Excellent HW
118	Trout Lake Mine	8410\2	blast damage?
119	Trout Lake Mine	1048\1	U/C effect mostly plus some degree of stress effect.
120	Trout Lake Mine	7311	Very short strike length. Stress shadow.
121	Trout Lake Mine	8791\4	
122	Trout Lake Mine	8791\3	
123	Trout Lake Mine	1048\5	Possibly stress problem
124	Trout Lake Mine	8754	
125	Trout Lake Mine	1078\1	
126	Trout Lake Mine	8791\E	
127	Trout Lake Mine	1048\3	

APPENDIX II DATABASE

No.	Mine Name	Stope #	Notes
128	Trout Lake Mine	84105	stress problem or poor blasting.
129	Trout Lake Mine	8410\3	Large N', Smaller HR and L/H ratio.
130	Trout Lake Mine	1078\2	stope may laid in stress shadow area.
131	Trout Lake Mine	87102	
132	Trout Lake Mine	10486	
133	Trout Lake Mine	10783	
134	Trout Lake Mine	84104	
135	Trout Lake Mine	10484	Hockey stick Stope, no U/C in u/c drift, Drillhole at lower half too close to HW (0m)
136	Trout Lake Mine	9051#1	
137	Trout Lake Mine	6451b	long strike length.
138	Trout Lake Mine	6451	Small HR and L/H ratio.
139	Trout Lake Mine	1010H1-4	Small HR and L/H ratio.
140	Trout Lake Mine	875C2F-8	the stope laid in stress path. Stress problem.
141	Trout Lake Mine	950N5-1	
142	Trout Lake Mine	765C2-1	Maybe stress problem
143	Trout Lake Mine	765C2-5	
144	Trout Lake Mine	980N9-2	
145	Trout Lake Mine	1040H1-6/7	maybe stress shadow (lower stress).
146	Trout Lake Mine	810N10-7	
147	Trout Lake Mine	950N9-2	
148	Trout Lake Mine	950W1-6	
149	Trout Lake Mine	980N11-6	Stress problem (Squeezed drillholes)
150	Trout Lake Mine	920N12-3	Small slot blasted for destress.

APPENDIX III

VARIATION OF THE DEPTH OF THE RELAXATION ZONE WITH LOCATION ON THE SURFACE EXPRESSED AS THE EFFECTIVE RADIUS FACTOR

The simulations conducted in Chapter 6 showed that the relaxation depth will change from location to location on a slope HW surface and that the stress ratio will change the relaxation depth significantly.

To better describe the relaxation depth change along slope HW surface, a term called the effective radius factor ERF (Milne et al., 1996a; Milne et al., 1996b) is introduced as follows:

ERF is a surface geometry parameter that equals half of the harmonic average radius (R_h) of a surface, measured from any point on the surface (Milne et al., 1996a; Milne et al., 1996b). Harmonic average radius is defined as the average distance from a location to the abutments and McGaughey suggested (Milne, 1997) that “this approximation of the average distance to the abutments could be better quantified by taking distance measurements to abutments at small angular increments (Milne, 1996)”. It is expressed as:

$$R_h = \frac{1}{\frac{1}{n} \sum_{\theta=1}^n \frac{1}{r_{\theta}}} \quad (\text{III-1})$$

where

R_h -Harmonic average radius,

r_θ --distance from any point within a surface to the abutments at angle θ , and

n - number of rays measured to the surface edge.

ERF has a maximum value at the center of a surface that is defined as the Radius Factor (RF) and the ERF value drops to zero at the abutments. ERF and RF are expressed as:

$$ERF = \frac{1}{2} R_h = \frac{0.5}{\frac{1}{n} \sum_{\theta=1}^n \frac{1}{r_\theta}} \quad (\text{III-2})$$

$$RF = \text{Max.} \left(\frac{1}{2} R_h \right) = \text{Max.} \left(\frac{0.5}{\frac{1}{n} \sum_{\theta=1}^n \frac{1}{r_\theta}} \right) \quad (\text{III-3})$$

Figure III-1 illustrates the ERF and RF calculation.

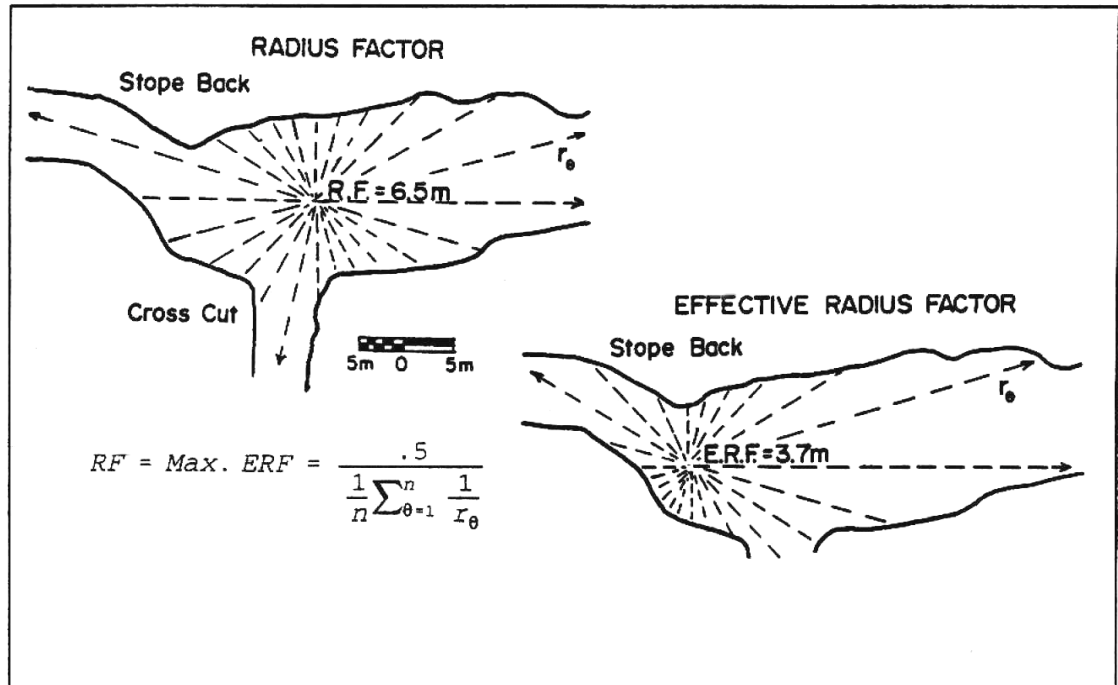


Figure III-1. An irregular stope back showing the calculated ERF value and RF value (from Milne et al., 1996)

In general, for a given location on a slope HW, an increase in the stress ratio, increases the depth of relaxation. For a lower stress ratio (e.g. $K \leq 1.5$) the depth of relaxation increases with the location moving from abutments to the centre of the surface and the centre of the surface has the maximum depth of relaxation. For a higher stress ratio (e.g. $K \geq 2.0$), the maximum depth of relaxation location will not be the centre of the surface but will occur between the abutments and the surface centre.

The following two example modelled results show the ERF change with the changing of location on the surface and the corresponding depth of relaxation for different stress ratios.

Figure III-2 shows how the effective radius factor value changes along the surface centre lines (A-A and B-B) for a 40m x 40m square shaped surface, measured at 2 metre interval. Figure III-3 shows the ERF value plotted against the distance from the centre of the surface. Figure III-3 shows that the maximum ERF is at the centre of the surface and the minimum ERF values are found at the boundary (abutments) of the surface.

Figure III-4 shows the ERF versus depth of relaxation on two mutual perpendicular axes for three stress regimes ($K=1.5$, $K=2.0$ and $K=2.5$) plots for the 40m x 40m square shaped surface.

For a rectangular shape, the ERF values along two perpendicular axes are different as shown in Figure III-5. Figure III-6 shows the ERF values plotted as a distance from the centre, measure along the two axes. The shapes of relaxation zone along the two perpendicular axes also have different shapes. Figure III-7 shows the depth of relaxation along the long axis of the 40 x 100m² rectangular shaped surface, corresponding to distance and ERF. Figure III-8 shows the depth of relaxation along short axes of the 40x100m² rectangular shaped surface corresponding to distance and ERF.

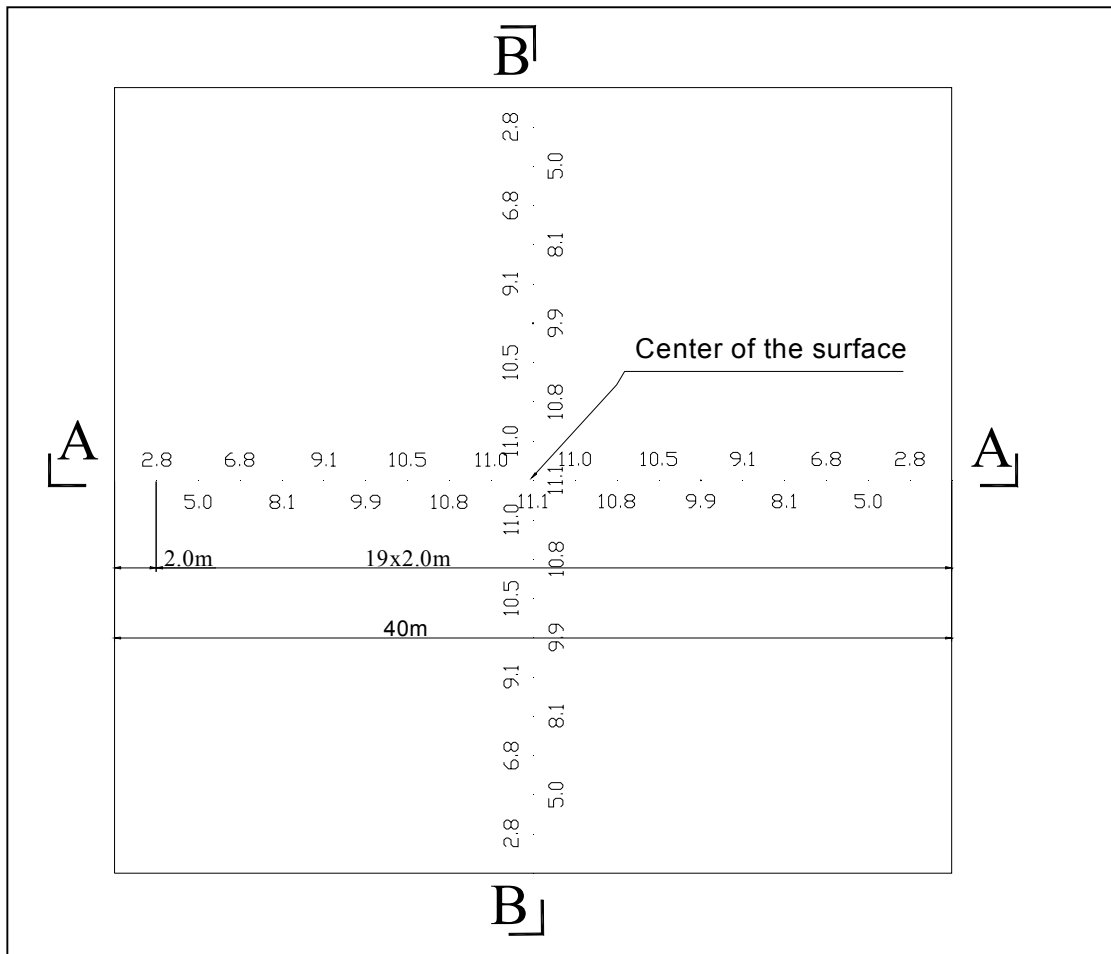


Figure III-2. Effective Radius Factor (ERF) values along centre lines of a 40m x 40m surface

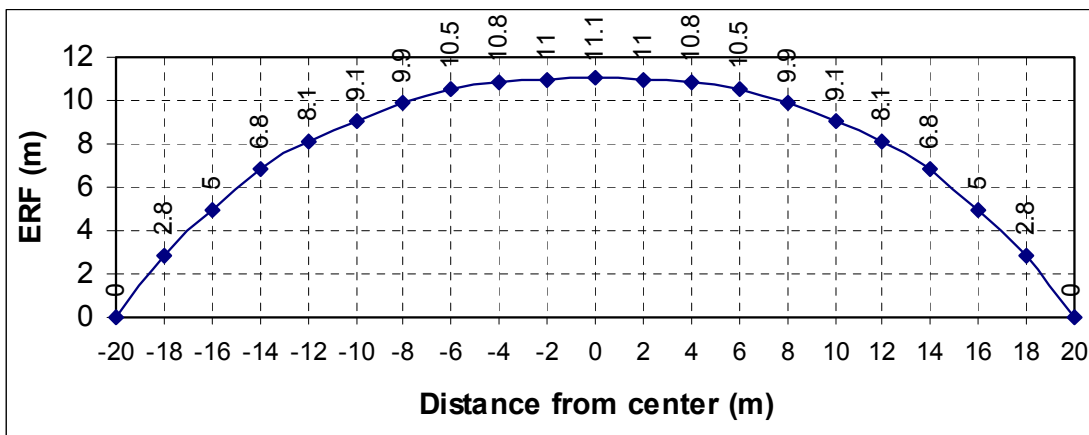


Figure III-3. Effective radius factor changes with the distance change along axes for a 40m x 40m rectangular surface

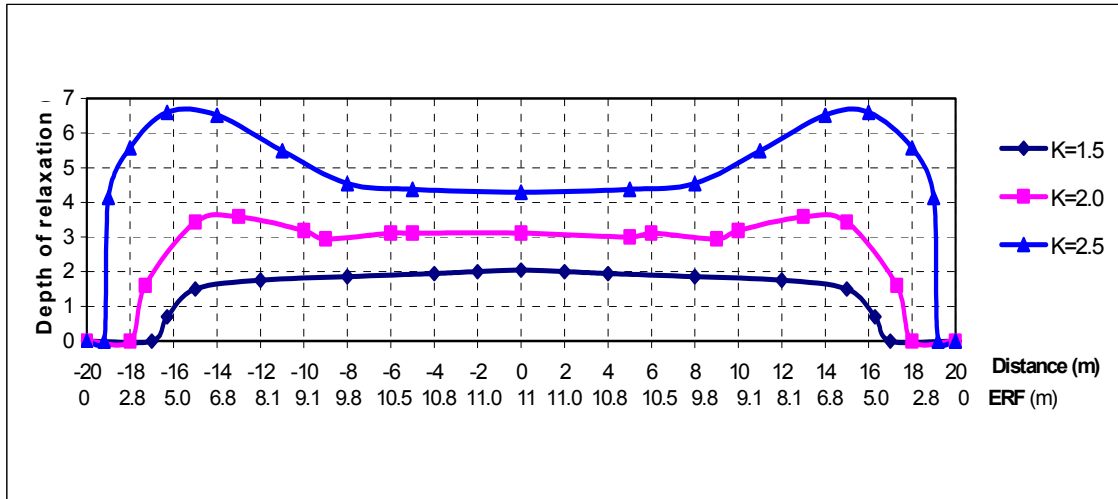


Figure III-4. Depth of relaxation along axes of a 40m x 40m square shaped surface corresponding to distance (from centre of the surface) and ERF

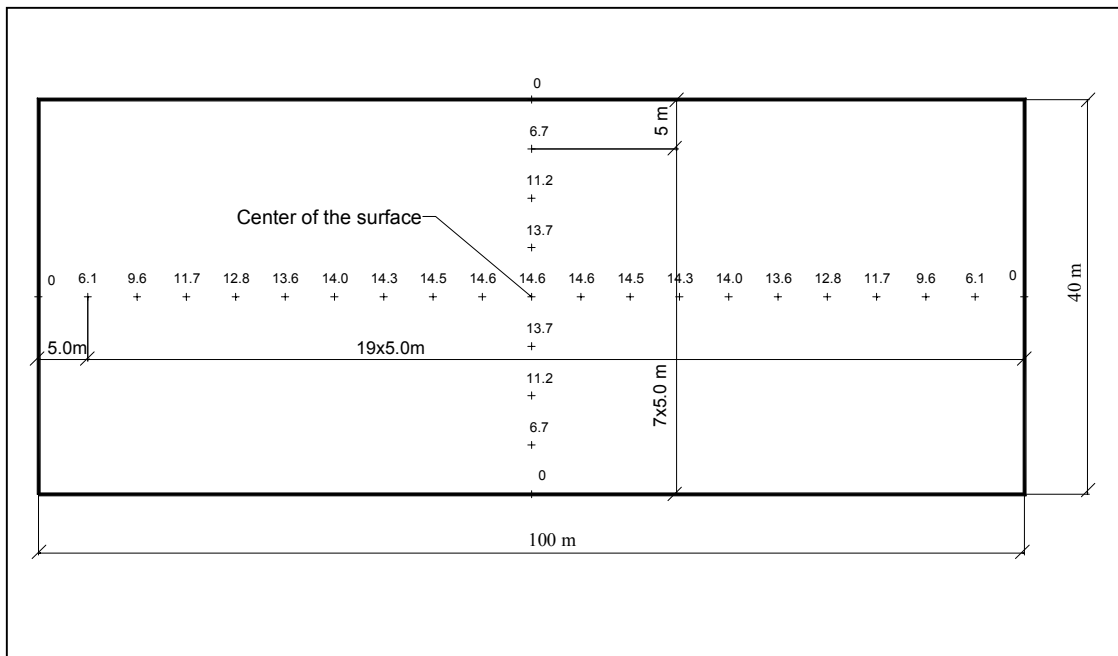


Figure III-5. ERF values along two mutual perpendicular axes, measured at 5 meters intervals, for a 40m x 100m rectangular surface

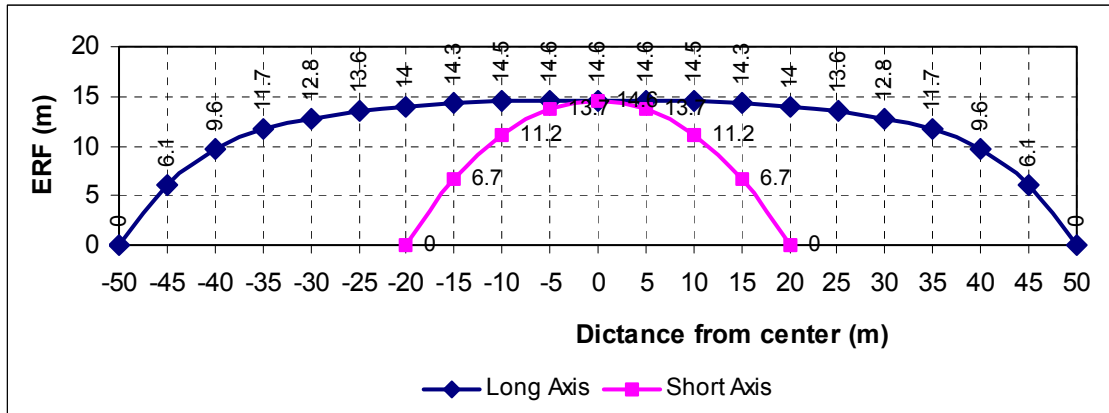


Figure III-6. ERF changes with the distance from the surface center along two axes for a 40m x 100 m rectangular surface

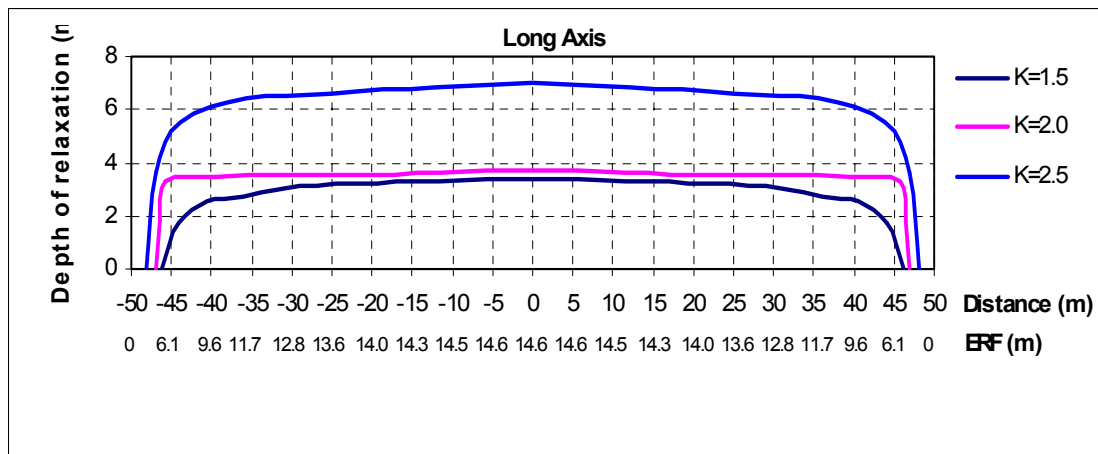


Figure III-7. Depth of relaxation along the long axis of a 40 x100m² rectangular shaped surface corresponding to distance from the centre or ERF

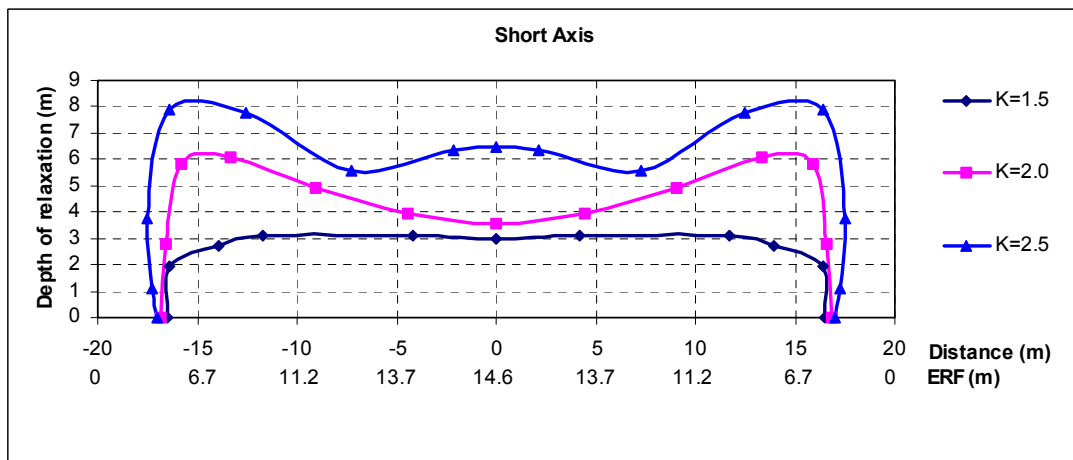


Figure III-8. Depth of relaxation along the short axis of a 40x100m² rectangular shaped surface corresponding to distance from the centre or ERF

Two factors could affect the variation of relaxation depth on a surface. One is the location on the surface which can be represented by Effective Radius Factor (ERF) and another is the stress factor as expressed as stress ratio K . The depth of relaxation at or near abutments is zero followed by a sudden increase away from abutments. For all types of surface shapes examined, the surface centre has the maximum relaxation depth for stress ratios equal to and less than 1.5. For stress ratio larger than 1.5 for circular shaped, square shaped surface as well as the rectangular shaped surface along short axis, the maximum depth of relaxation is not at the centre of the surface. The maximum depth of relaxation is between abutments and the centre of the surface.